Strathclyde Institute for Pharmaceutical and Biomedical Sciences Faculty of Science

Structural, functional and mechanistic analysis of the *Escherichia coli* ammonium transporter AmtB

Gaëtan Dias Mirandela

Thesis presented in fulfilment of the requirement for the degree of Doctor of Philosophy

October 2018

Declaration

This thesis is the result of the author's original research. It has been composed by the author and has not been previously submitted for examination which has led to the award of a degree.

The copyright of this thesis belongs to the author under the terms of the United Kingdom Copyright Acts as qualified by University of Strathclyde Regulation 3.50.

Due acknowledgement must always be made of the use of any material contained in, or derived from, this thesis.

Candidate

Signed:

Date:

Publications

Two papers have been published as a result of the work carried out during this project.

Most of their contents was used as material for the thesis. These are as follows and can be found printed at the back of this thesis in the Appendix section.

Dias Mirandela G, Tamburrino G, Ivanović MT, Strnad FM, Byron O, Rasmussen T, Hoskisson PA, Hub JS, Zachariae U, Gabel F, Javelle A. (2018) Merging In-solution X-Ray and Neutron Scattering Data Allows Fine Structural Analysis of Membrane-protein Detergent Complexes. *J. Phys. Chem. Lett.* **9**:3910–4.

Dias Mirandela G, Tamburrino G, Hoskisson PA, Zachariae U, and Javelle A. (2018) The lipid environment determines the activity of the *E.coli* ammonium transporter, AmtB. *FASEB J. in press. doi: 10.1096/fj.201800782R.*

Part of the study presented in the Chapter 4 of the thesis will be subject to publication and will be referred throughout this thesis as "Williamson *et al., in preparation*"

Williamson* G, Tamburrino* G, Dias **Mirandela* G**, Hoskisson PA, Pisliakov A, Boeckstaens M, Marini AM, Zachariae U and Javelle A "*Mechanism of action for the ammonium transporter AmtB*." *In preparation.*
*equally contributed

Acknowledgements:

I would like to thank first and foremost Dr. Arnaud Javelle who helped and guided me through this big adventure. He was, and still is, the best guide I had/have along my PhD. He taught me invaluable professional and personal lessons. All the work I have done during my PhD would not exist without him.
Un grand merci à toi pour ta générosité, patiente et ton partage de conaissance sur les Amt/Mep/Rh. Merci Arnaud pour les bon moments et discussions passés dans le labo, au téléphone et autour de binouses. Tout cela va énormément me manquer.

I also want to thank my second supervisor Prof. Paul Hoskisson who accepted a second Frenchie amongst the Micro-group. We are tough to deal with but always the first here in the morning. Thank you for the interesting questions and advice given during these 3 years.

I want to thank Prof. Iain Hunter for his excellent comments and suggestions along the project and for agreeing to be my internal examiner.

I would like to thank Prof. Gavin Thomas for giving me the opportunity to present my research and for agreeing to be my external examiner.

I would like to specially thank Dr. Frank Gabel who took the time to teach me everything I know about Small Angle Scattering techniques. He was a supportive pillar during my PhD project and he made me discover a real passion for Small Angle Scattering.

I would like to thank many people that helped throughout my PhD including: Dr. Giulia Tamburrino and Dr. Ulrich Zachariae for performing all the MD simulations; Dr. Milos Ivanochi and Prof. Hub S. Jochen for sharing their software: WAXSiS and its SANS version; Dr. Mélanie Boeckstaens and Dr. Anna-Maria Marini for the yeast complementation work and for supporting France during the World Cup; Prof. Olwyn Byron for teaching me the use of

Analytical Ultra Centrifugation technique; Dr. Kyle Dent and Dr. Martin Walsh for giving us access to EM facilities and for the acquisition of EM preliminary data.

I would like to thank the two companies Nanion Technologies and NanoTemper Technologies. In particular, Dr. André Bazzone of the former for his invaluable knowledge and for training me in the Solid Supported Membrane Electrophysiology technique and Dr. Pierre Soule of the latter for kindly teaching me how to use MicroScale Thermophoresis Technology.

I would like to thank Institut Laue Langevin and Diamond facilities and particularly: Dr. Anne Martel and Dr. Mark Tully for helping to reduce the SANS data collected and for helping with SAXS data analysis respectively.

I would like to thank Gordon Williamson for his help on this thesis work and also for trusting me enough as a mentor and as a friend. I am delighted to pass him the “Olympic flame” to continue working on Amt/Mep/Rh with Dr. Arnaud Javelle.
Mais ne serais-ce pas un petit bûcheron? Un de plus a ajouté à l’équipe!

I want to thank my previous students: Nikita, Rakhsana, Eilidh and Derek that brought new inputs to my work and a lot of fun in the lab. Thank you for being comprehensive, kind and invested in my project.

To everyone on level 6 floor (past and present members) for bringing science, fun and happiness. The best floor at SIPBS.

Special thanks to: Tiago Santos, Anna Birke, Mariam Badawi and César Bellota who gave Glasgow the best meaning I could ever imagine; Dr. Marie-Claire Dagher, Prof. Rob Ruigrok and Dr. Jérôme Dupuy who inspired me to become the person I am today; to my friends Tiphanie, Mickaël, Arnaud and Sylvain who were here from the beginning and who constituted my second

family; to Sylvia who supported me during my last year of PhD and to my lovely family: Jean-Marie, Christine, Arthur and Maud who have supported all of my professional and personal choices.

This thesis is dedicated to my grandfather Jean-Marie and my mother Christine.

Cette thèse est dédiée à mon grand-père Jean-Marie et à ma mère Christine.

Table of Contents

List of abbreviations

°C	degree Celsius
A solution	Activated solution
Å	Ångström
*Af*Amt1	*Archaeglobus fulgidus* ammonium transporter 1
Amt	ammonium transporter
AUC	Analytical ultracentrifugation
*Ca*Mep2	*Candida Albicans* Methylpermease 2
CMP	contrast match point
CV	column volume
DDM	n-Dodecyl-β-D-Maltopyranoside
DNA	deoxyribonucleic acid
dRTA	distal Renal Tubular Acidosis
*Ec*AmtB	*Escherichia coli* ammonium transporter
EM	Electron Microscopy
GFP	Green Fluorescent Protein
IMAC	Immobilised metal affinity chromatography
kcal	kilocalorie
kDa	kiloDalton
K_m	Michaelis constant
K_i	Inhibition constant
K_D	Dissociation constant
LB	Lysogenic broth medium
LDAO	n-Dodecyl-N, N-Dimethylamine-N-Oxide
LPR	Lipid protein ratio
mA	milliAmpere
MeA	methylammonium
Mep	methylammonium permease
MD	Molecular Dynamic
MSP	Membrane Scaffolding Protein
nA	nanoAmpere
NA solution	Non Activated solution
*Ne*Rh50	*Nitrosomonas europaea* Rhesus protein 50
OHSt	Overhydrated Hereditary Stomatocytosis
P(r)	Pair-distance distribution function
PAGE	polyacrylamide gel electrophoresis
PDB	protein databank
PDC	Protein Detergent Complex
pH	potential Hydrogen
pI	isoelectric point
PMSF	phenylmethylsulfonyl fluoride

PA	1-palmitoyl-2-oleoyl phosphate
PC	1-palmitoyl-2-oleoyl phosphatidylcholine
PE	1-palmitoyl-2-oleoyl phosphatidylethanolamine
PG	1-palmitoyl-2-oleoyl phosphatidylglycerol
PS	1-palmitoyl-2-oleoyl phospho-L-serine
R	radius
R^2	coefficient of determination
R_g	Gyration radius
R_{sat}	Saturation Constant
R_{sol}	Solublisation Constant
Rh	Rhesus
RMSD	Root Mean Square Deviation
RNA	ribonucleic acid
SANS	Small Angle Neutron Scattering
SAXS	Small Angle X-ray Scattering
*Sc*Mep2	*Saccharomyces Cerevisiae* Methylpermease 2
SDS	Sodium Dodecyl Sulfate
SEC	Size Exclusion Chromatography
SEC-MALS	Size Exclusion Chromatography Multiple Angle Light Scattering
SSME	Solid Supported Membrane Electrophysiology
TEMED	N, N, N', N'-tetramethylethylenediamine
Tris	2-amino-2-hydroxyméthyl-1,3-propanediol
x g	*x* gravity

Abstract

The exchange of ammonium across cellular membranes is an essential process in all kingdoms of life. Ammonium is a major source of nitrogen for bacteria, fungi, and plants, whereas in animal cells it is a cytotoxic waste metabolite, which must be excreted. The transport of ammonium is accomplished by the ubiquitous Ammonium transporter/Methylammonium permease/Rhesus (Amt/Mep/Rh) superfamily of membrane proteins. In addition to their fundamental role in facilitating the transport of metabolites, members of the Amt/Mep/Rh superfamily are important drivers of the virulence of infectious fungi. In humans, malfunctions of Rh proteins are linked to inherited haemolytic anaemia, stomatocytosis, and early onset depressive disorder, amongst many other human pathologies. Therefore, an improved understanding of the function of ammonium transporters has important medical implications alongside the elucidation of a central biological process. In spite of its general importance, a consensus on the pathway and mechanism of ammonium transport by this superfamily has not yet been achieved.
The overall aim of this project is to use *Escherichia coli* AmtB, the paradigmatic, most intensely studied member of the Amt/Mep/Rh protein family and an integrative approach combining molecular genetics, biochemistry, biophysics and molecular dynamic simulations to gain valuable structural and functional information on this important protein family.

A new in-solution structural approach combining Small Angle Neutron/X-ray Scattering with Molecular Dynamics simulation has been successfully developed providing a new tool to study membrane protein dynamics in solution. Moreover, a new mechanism for the deprotonation/translocation associated with ammonium transport through AmtB was suggested and demonstrated by using Solid Supported Membrane Electrophysiology (SSME) and Molecular Dynamics simulations on genetic variants. Furthermore, the influence of 1-palmitoyl-2-oleoyl phosphatidylglycerol (PG), a specific lipid known to structurally interact with AmtB, was assessed and it was suggested that this lipid is essential for translocation of ammonium across AmtB. Last but

not least, the electrophysiological technique developed on AmtB has been extended to study the bacterial Rh and fungal Mep proteins to explore whether the mechanism I propose for AmtB is a common feature for the Amt/Mep/Rh protein family.

Given the importance of this protein family in various fundamental biological processes and human diseases, this work may, in the long term, lead to the development of new therapeutic interventions.

Chapter 1: General Introduction

1.1 Membrane proteins and their importance

1.1.1 Biological membrane: The fluid mosaic model

Biological membranes are essential to cell metabolism as they provide four basic functions:

1- Separation: the membrane is a semi-permeable barrier, preventing polar and charged molecules from freely moving in and out of the cell.

2- Exchange: through membrane embedded proteins, the cell membrane allows the translocation of metabolites and macromolecules in and out of the cell.

3- Integration: The cellular membrane allows receptor-mediated signalling across the membrane and the propagation of electric signals along the lipid bilayer.

4- Metabolism: Biological membranes are essential for cell metabolism, in particular they are involved in harvesting, storage and conversion of cellular energy.

The general organisation of cellular membranes can be describe by a fluid-mosaic model proposed by Singer and Nicolson in the early 70's (Singer and Nicolson, 1972). In this model, as suggested by its name, the phospholipid bi-layer is dynamic, allowing the movement of membrane proteins in the plane or across the membrane. Membrane proteins can span the entire bilayer or be simply bound to the membrane surface, giving the appearance of a mosaic of proteins and lipids (**Figure 1.1**).

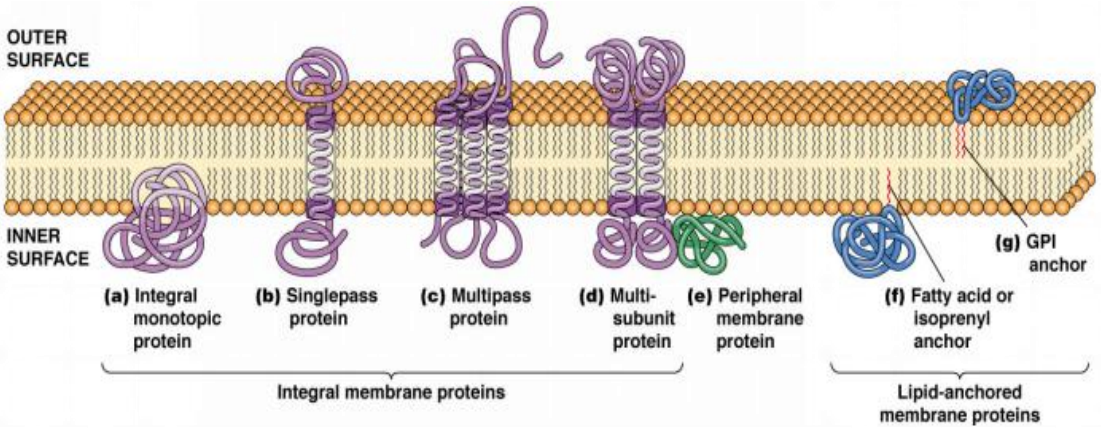

Figure 1.1 Representation of the different types of membrane protein insertions into a biological membrane. GPI: glycosylphosphatidylinositol (Figure from website (https://www.creative-biostructure.com/)).

Most living organisms possess a single membrane that surrounds the cytoplasm of each cell. However, bacteria have developed a more sophisticated “membrane system” in order to increase their viability in hostile environments (Silhavy *et al.,* 2010 and references therein). A staining assay was developed to differentiate bacteria in two sub-groups based on their cell envelope organisation (Schleifer and Kandler, 1972). The two sub-groups were the following:

1- Gram positive bacteria: composed of a thick peptidoglycan (30-100 nm) and of a single lipid bilayer.
2- Gram negative bacteria: possessed an outer and inner lipid bilayer that surrounded a thin peptidoglycan (few nm).

Both Gram positive and negative bacteria possess a peptidoglycan that acts as the “backbone” for the cells playing a crucial role in responding to osmotic pressure and attachment sites for proteins (Silhavy *et al.,* 2010).

The inner membrane of Gram negative and single membrane of Gram positive bacteria are phospholipid membranes that are present in all living organisms. However, the outer membrane in Gram negative bacteria, is only composed of glycolipids forming a “gel” called lipopolysaccharide (LPS). The LPS is ubiquitously distributed in all the outer membranes and functions in nutrient selectivity (semi-permeable membrane) and antigenicity during bacterial infections (Silhavy *et al.,* 2010 and references therein).

The *Escherichia coli* bacterium has been used as a Gram negative model organism for genetics, biological and biochemical studies due to its properties of being less biologically complex and easy to handle/modify. The outer membrane of *E.coli* contains two types of proteins: β-barrel protein and lipoprotein. The β-barrel protein is known to allow the diffusion of small molecules across the outer membrane while the role of lipoproteins remains uncertain. Finally the outer and inner membranes present in *E. coli* (and Gram negative bacteria in general) generate a compartment between the lumen and the cytoplasm called the periplasm, where enzymatic reactions such as antibiotic degradation occur (Silhavy *et al.,* 2010 and references therein).

1.1.2 Membrane transporters

Integral membrane proteins, and in particular membrane transporters, are the entry and exit routes for all nutrients, metabolic waste, hormones and drugs. They are involved in a wide variety of biological processes including photosynthesis, respiration, signal transduction, molecular transport and are also responsible for much of the communication between cells and their environment. In Gram negative bacteria, these types of integral membrane proteins are found in the inner membrane. Given the crucial importance of this enormous group of proteins in numerous fundamental biological processes, their medical relevance cannot be underestimated. Malfunctions of membrane transporters are involved in many common diseases, including heart disease, cancer, depression, Alzheimer's disease and cystic fibrosis (Hediger *et al.,* 2013). Membrane transporters sit at the surface of cells and are therefore readily accessible to small molecules circulating in the blood, hence they currently represent ~50% of drug targets (Overington *et al*., 2006). These medically critical proteins represent approximately 25% of all proteins (Krogh *et al*., 2001), and yet we know relatively little about them.

From the amino-acid sequences, 6 different classes of membrane transporters have been determined in *E. coli* (Elbourne *et al.,* 2016). The different classes encompass 634 transport proteins (December 2018 - http://www.membranetransport.org/transportDB2) scattered into 6 different sub-types: Secondary transporter, ATP-dependent, Ion channel, phosphotranferase system, outer membrane porins and unclassified. This classification system for the different membrane proteins is based on the amino-acid sequences. Hence this could lead to disparities between the classification assigned from the sequence data and the functional mechanism ascribed to a membrane protein from other data. An interesting example to illustrate the latest controversy is the Glycerol facilitator system. It was firstly hypothesised and demonstrated that the Glycerol facilitator (GlpF) from *E. coli* was transporting glycerol actively across the cellular membrane when expressed in oocytes (Maurel *et al.,* 1994). However it was demonstrated

subsequently that the expression of GlpF is enhancing the kinase activity of Glycerol kinase (GlpK) suggesting that metabolic trapping of glycerol by GlpK rather than an active transport from GlpF (Voegele *et al.,* 1993) was the reason for the apparent active transport, which was simply due to conversion of intracellular glycerol to glycerophosphate and not accumulation of intracellular glycerol *per se*..

Nonetheless, membrane proteins are notoriously challenging to study ***in vitro*** since they are designed to sit within the hydrophobic environment of the lipid bilayer. Membrane transporters are also flexible, undergoing substantial conformational changes during the substrate transport cycle (Moradi and Tajkhorshid, 2013, Alberts *et al.,* 2002). This means that their study at all levels, from structural, biochemical and functional characterisation, is highly challenging.

From a functional point of view, to maintain the membrane protein solubilised in aqueous solution requires the usage of detergent which can rapidly lead to destabilisation, unfolding or inactivation of the membrane protein. The strategy of reconstituting the membrane protein (after detergent solublisation/purification) into an *in vitro* "native" lipid environment became a highly recommended approach to study the "native" function/structure of membrane proteins (Cherezov *et al.,* 2009, Rigaud and Lévy, 2003). In **Chapter 4**, a new functional approach was undertaken to decipher the molecular mechanism of the ammonium transporter when reconstituted into liposomes. Additionally, in **Chapter 5**, the fine-tuning influence of the lipid environment composition on ammonium translocation mechanism was assessed. Very recently a "free detergent" approach has been used to study membrane proteins that are susceptible to the solubilisation process (Qiu *et al.,* 2018 and references therein).

From a structural point of view, in 1985, the first integral membrane protein structure, the photosynthetic reaction centre from *Rhodopseudomonas viridis,* was solved using x-ray crystallography (Deisenhofer *et al*., 1985) and since, structural analysis of integral membrane proteins has attracted tremendous

interest. However, obtaining structural information on integral membrane proteins using biophysical techniques such as crystallography remain challenging with only 787 unique protein structures deposited in the PDB database (June 2018 - http://blanco.biomol.uci.edu/mpstruc/). Moreover, the translocation cycle underpinning membrane transporter activity requires substantial conformational variability and in many cases, the static structural insight achieved by x-ray crystallography has proven insufficient to capture the essential functional information of these systems.

For this reason, there is considerable interest in the application of alternative methodologies, such as Small Angle Scattering (SAS) or cryo-electron microscopy (Cryo-EM) to structurally characterise membrane proteins. The development of such an alternative approach, combining SAS and molecular dynamic (MD) simulation to gain structural information on membrane proteins was a significant part of my project and is presented in detail (**Chapter 3**).

1.2 Importance of ammonium movement across biological membranes

Ammonium is the preferred nitrogen source for microbes and plants whereas in mammalian cells it represents a metabolic toxic waste that needs to be excreted (Andrade and Einsle, 2007, Wirén and Merrick, 2004). Hence, ammonium movement across biological membranes, whether it is uptake or excretion, is a process of fundamental importance in all living organisms. It had been generally accepted for years that ammonium acquisition by living organisms occurred by mere passive diffusion of NH_3 across the lipid bilayer at a rate of ~10^{-3} cm/s (Lande *et al*., 1995). However, the pKa value for the ammonium/ammonia (NH_4^+/NH_3) equilibrium is 9.25, hence at physiological pH, 99% of the ammonium is protonated (NH_4^+) (Bates and Pinching, 1950). Ions such as NH_4^+ cannot diffuse through the hydrophobic layer (**Figure 1.2**) because of the high energy cost to strip away the hydration shell (80 kcal/mol for NH_4^+) (Pearson, 1986, Cao *et al*., 2004). Therefore, transport systems are needed to efficiently translocate NH_4^+ across biological membranes.

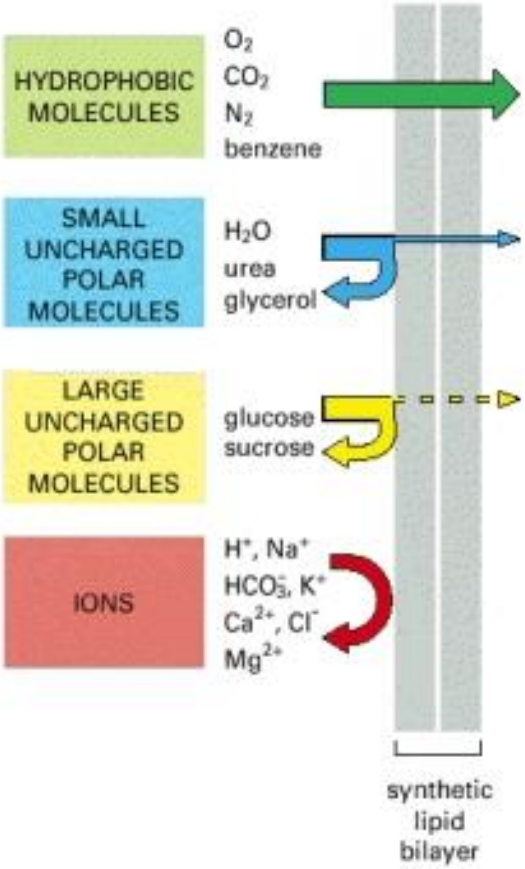

Figure 1.2 The relative permeability of a synthetic lipid bilayer to different classes of molecules adapted from (Alberts *et al.* 2002).

1.2.1 First evidence of the existence of specific ammonium transport system

Early studies suggested that a nonspecific amino-acid permease was expressed in the fungi *Penicillium chrysogenum* and *Aspergillus nidulans* under “nitrogen starvation conditions” (Hackette *et al*., 1970). Interestingly, these transport systems were inhibited by ammonium indicating, for the first time, that a specific ammonium permease system was present in *P. chrysogenum* and *A. nidulans* (Benko *et al*., 1969). The half-life of ^{13}N being 10 minutes, it is impossible to use $^{13}NH_4^+$ as a radioactive tracer to characterise the activity of ammonium transport systems. Hence, in a later study Hackette *et al*. used ^{14}C radio-labelled methylammonium (MeA) as an ammonium analogue to characterise the activity of the ammonium transporter in *P. chrysogenum* (Hackette *et al*., 1970). Crucially, Hackette *et al*. showed in this elegant work that ammonium was a potent competitive inhibitor of the MeA uptake activity. Since the K_i value for the ammonium inhibition of MeA transport activity (approximately 0.25 µM) was an order of magnitude lower than the K_m for MeA (1 mM) and because MeA cannot serve as a carbon or nitrogen source in *P. chrysogenum,* this uptake system was identified as an ammonium rather than MeA transporter (Hackette *et al*., 1970).

1.2.2 First identification of genes encoding for ammonium transport in *A. thaliana* and *S. cerevisiae*

1.2.2.1 Discovery of ammonium and methylammonium uptake systems

Following Hackette’s identification of an ammonium transport system in *P. chrysogenum* (Hackette *et al*., 1970), MeA accumulation assays were used to detect the presence of ammonium transporters in the bacterium *Klebsiella*

pneumoniae (Kleiner, 1982), *Escherichia coli* (Stevenson and Silver, 1977), nitrogen fixing-bacteria *Clostridium pasteurianum* (Kleiner and Fitzke, 1979), *Azotobacter vinelandii* (Laane *et al.*, 1980) and in the eukaryotic organism *Saccharomyces cerevisae* (Roon *et al.*, 1975), indicating the ubiquitous nature of these transport systems. In all these systems, it has been shown that MeA accumulated inside the cell (~1,000 fold) against its electrochemical gradient, which is the typical signature of an active transporter (Neverisky and Abbott, 2015). However, contradictory results were obtained concerning the energetics of the transport activity; in fungi, the activity has been shown to be pH and temperature dependant (Roon *et al*., 1975, Hackette *et al*., 1970), but independent in bacteria (Stevenson and Silver, 1977). Finally, the genes encoding *bona fide* ammonium transport systems were not isolated in these biochemical studies only and remained unidentified for a further 20 years.

1.2.2.2 Identification of the genes encoding ammonium transporters.

The first genetic evidence of ammonium transporter clusters started with the identification of 5 different loci specific to the ammonium uptake mechanism system in *Aspergillus nidulans* (Pateman *et al.,* 1973). In 1979 Dubois and Grenson showed that *S. cerevisiae* possesses at least 2 different ammonium transporter systems named Mep1 and Mep2 for Methylammonium permease (because their activity were characterised using ^{14}[C]MeA (Dubois and Grenson, 1979). Mep1 and Mep2 were characterised as low capacity/high affinity and high capacity/low affinity transport systems respectively. Two unlinked genetic mutations, *MEP1* and *MEP2* were identified to separately abolish the activity of these proteins, proving the existence of two distinct transporters (Dubois and Grenson, 1979). A strain (named 26972c) containing both *MEP1* and *MEP2* mutations was unable to grow in a medium containing 1 mM of ammonium as the sole nitrogen source. In 1994, Dr. Anne Marie Marini screened a low copy number plasmid library representing the total

genome of the *S. cerevisiae* strain Σ1278b to identify plasmids that allowed the complementation of the growth defect of the strain 26972c on a growth medium containing 1 mM ammonium as the sole nitrogen source (Marini *et al*., 1994). This lead to the first identification of a gene encoding a *bona fide* ammonium transporter (the gene was called *MEP1*) (Marini *et al*., 1994). In parallel and with the same approach, expressing a cDNA library from *Arabidopsis thaliana* in the *S. cerevisiae* strain 26972c, Dr. Olaf Ninnemann cloned *AMT1*, the first gene to be cloned encoding a plant ammonium transporter (Ninnemann *et al*., 1994). Later, it was hypothesised that *GmSAT1* gene was encoding for an ammonium transporter 1 in soy bean (Kaiser *et al.,* 1998). However, Marini *et al.,* demonstrated that *GmSAT1* expression in yeast lacking of all Mep proteins did not restore ammonium transport and the authors also demonstrated that *GmSAT1* expression plays a regulation role in the expression of Mep proteins (Marini *et al.,* 2000). Additionally, the sequence of *GmSAT1* does not contain any features commonly shared by Amt/Mep protein family but instead contains a helix-loop-helix domain typical of transcription factors (Marini *et al.,* 2000). In a more recent work, Kaiser's research group acknowledged that *GmSAT1* encodes for a transcription factor supporting Marini's work (Chiasson *et al.,* 2014).

The first bacterial homologue to be identified *via* database screening was the *amtA* gene (at that time called *amt*) of *Corynebacterium glutamicum* (Siewe *et al*., 1996). Since then, apart from rare exceptions, all bacterial genomes sequenced have revealed the presence of at least one gene encoding an Amt/Rh protein. In this regard it is interesting to note that nearly all of the genomes that do not encode for one of these proteins belong to pathogenic organisms, leading to the hypothesis that the absence of these genes reflect adaptation to specific niches within the host and is the consequence of reductive evolution (Thomas *et al*., 2000, Huang and Peng, 2005, McDonald *et al*., 2012, McDonald and Ward, 2016).

1.2.3 Identification of mammalian ammonium transporter genes

In 1997, using the *S. cerevisiae* Mep sequences in protein similarity searches, it was found that the human rhesus (Rh) proteins share 25% sequence similarity with the Amt/Mep transporter family (Marini *et al*., 1997b). The Rh proteins in mammals form a multimeric protein complex comprising two types of proteins: a polypeptide of 30 kDa (named Rh30) and a glycosylated protein of 50 kDa (named Rh50) (Huang, 1998, Matassi *et al*., 1998). The homology between Rh30 and Rh50 is 36%. In humans, two Rh30 proteins (RhD and RhCE) (Le van Kim *et al*., 1992, Avent *et al*., 1990, Cherif-Zahar *et al*., 1990) and three Rh50 (RhAG, RhBG and RhCG) have been identified (Avent and Reid, 2000). RhAG is mainly localised at the membrane of the erythrocytes forming the group antigen (Cherif-Zahar *et al*., 1996) while RhBG and RhCG are mainly found in the kidney, liver, central nervous system, testes and intestine (Weiner and Hamm, 2007). In 2000, it was suggested that the rhesus protein (Rh) represents the Amt/Mep orthologs in vertebrates as the human RhAG and RhCG proteins were able to functionally complement the growth defect of a *S. cerevisiae* knockout mutant, demonstrating that Rh50 protein can act as ammonium transport when expressed in yeast (Marini *et al.,* 2000). However, the functional context of Amt/Mep and Rh transporters is highly diverse: bacteria, fungi and plants use Amt/Mep proteins to scavenge ammonium from their environments for biosynthetic assimilation, whereas mammals use the Rh proteins for ammonium detoxification in erythrocytes, kidney and liver tissues (Neuhäuser *et al.,* 2014, Andrade and Einsle, 2007).

1.2.4 Phylogeny of Amt/Mep/Rh protein family

Since the identification of ammonium transporter genes in mammals by Marini and co-workers (Marini *et al*., 1997b), interest in the classification of the different members of the Amt/Mep/Rh has emerged. A first phylogenetic classification carried out in 2005 showed how Amt and Rh are related to each

other (Huang and Peng, 2005). After screening 111 Rh and 260 Amt proteins, it was observed that only 14% of identity existed between Amt and Rh proteins. This low identity between Rh and Amt proteins supports the hypothesis of an evolutionary divergence between the two families (**Figure 1.3**) (Huang and Peng, 2005).

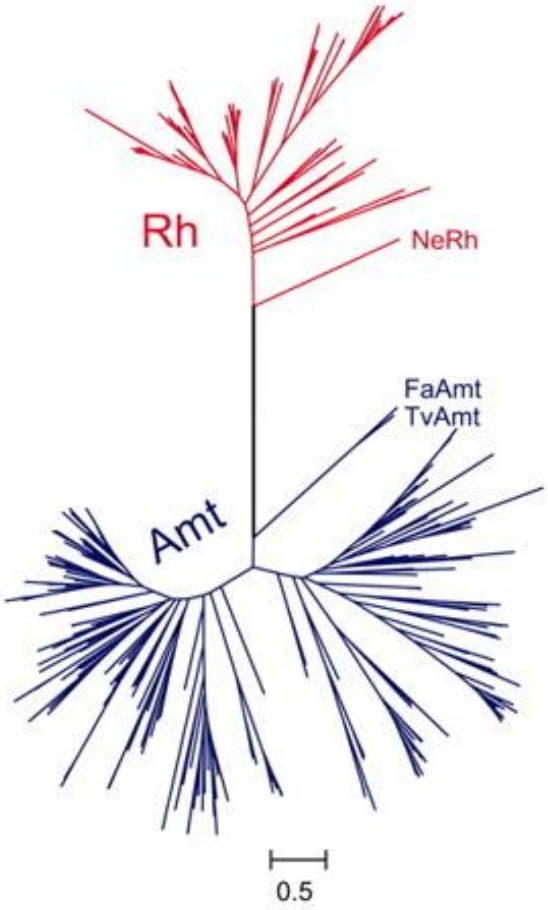

Figure 1.3 Rh and Amt are distant relatives: Maximum likelihood tree of Amt (blue) and Rh (red) proteins, *Ne*Rh (bacterial Rhesus), *Fa*AmtB/*Tv*AmtB (archael Amts) (Figure from Huang and Peng, 2005).

Interestingly, most vertebrates possess multiple copies of *Rh* but lack *AMT* genes (Huang and Peng, 2005). *Rh* genes were found in 41 species ranging from the chemolithotroph bacterium *Nitrosomonas europae* to mammals but were not found in archaea and vascular plants (Huang and Peng, 2005). Additionally, four different clusters for Rh proteins in vertebrates were identified: Rh30, RhAG, RhBG and RhCG while only two primitive clusters, Rhp1 and Rhp2 were identified in microbes, invertebrates and non-mammalian vertebrates. It was shown that RhAG and Rh30 share a common ancestor, different to the one shared by RhBG and RhCG. Rhp2 was defined as a non-mammalian cluster, conserved, and genetically stable due to its lack of introns. Moreover, it was demonstrated that Rhp2 is more closely related to the bacterial Rhesus 50 from *Nitrosomonas europaea* (*Ne*Rh50) and Rhp1 than the other Rh genes (Rh30, RhAG, RhBG and RhCG). On the other hand, Rhp1 is a more diverse cluster found in organisms expressing both Amt and Rh protein (Huang and Peng, 2005).

In a different work, Couturier and co-workers investigated the phylogeny of *AMT* from *Populus trichocarpa*, *A. thaliana* and rice (Couturier *et al*., 2007). It was shown that *P. trichocarpa* possessed 14 *AMT* genes instead of the 6 and 10 found in *A. thaliana* and rice, respectively. The 14 AMT proteins from *P. trichocarpa* were clustered in two major families (named AMT1 and AMT2) similar to what has been previously observed for *Rh* genes (Huang and Peng, 2005). AMT1 was described to be the most conserved cluster due to its lack of intron sequences in contrast to AMT2. The AMT1 cluster represents a high affinity transporter system (HATS) (with K_d ~10 µM for MeA) while the AMT2 cluster represents a low affinity transporter system (LATS) (Xiangjia *et al*., 2000). It was shown that LATS is solicited when ammonium concentration is high, while HATS works as a scavenging system when ammonium concentration is low. It appeared that the AMT2 cluster is more related to prokaryotic Amt while AMT1 is more related to plants and is mainly located in the roots, suggesting a scavenging function (Sohlenkamp *et al*. 2002),

In 2012, a phylogenetic study based on 513 genes from *AMT*, *MEP* and *Rh* have demonstrated that *AMT* genes were transferred vertically (parent

inherence) whereas *MEP* were transferred horizontally (between a donor and an acceptor from different species) (McDonald *et al*., 2012). It was shown that *AMT* genes from the eukaryotic domain belong to the prokaryotic *MEP* clade arguing for the existence of only two major ancestral clades: *MEP* and *Rh* (McDonald *et al*., 2012). However the crystal structures and activities measured on the different Amt/Mep/Rh challenged these concepts (**see section 1.3 and 1.4**).

1.2.5 Physiological and medical importance of the Amt/Mep/Rh proteins

Amt protein: The functional importance of the Amt/Mep/Rh family is highlighted by their central role in nitrogen metabolism in bacteria, fungi and plants. This will be further developed in **section 1.3.10** and for review see (Wirén and Merrick, 2004) and references herein.

Mep protein: Filamentation is a dimorphic transition often related to the virulence of pathogenic fungi, such as the human pathogens *Candida albicans* (Lo *et al*., 1997)*, Histoplasma capsulatum* (Maresca and Kobayashi, 1989), or *Cryptococcus neoformans* (Wickes *et al*., 1997). Analogously to the human pathogens, *S. cerevisiae* is also able to filament under nitrogen limitation by switching to an unipolar mode of budding, producing pseudohyphae which scavenge for nutrients in the environment (Gimeno *et al*., 1992). This occurs for instance when a limiting ammonium concentration is provided as sole nitrogen source. *S. cerevisiae* diploid cells deleted of the *MEP2* gene, encoding one of the three ammonium permeases, are no longer able to switch from budding to pseudohyphal growth in response to ammonium limitation (Lorenz and Heitman, 1998). Ammonium transport in *⊿MEP2* cells is largely unaffected and ensured by Mep1 and Mep3 paralogues. The Mep2-type ammonium transport protein has thus been assigned a sensor role in filamentous development in response to ammonium limitation (Lorenz and Heitman, 1998, Smith *et al*., 2003, Biswas and Morschhauser, 2005).

Rh protein: In humans, mutation in Rh genes are associated with numerous pathologies. RhAG mutations in red blood cells have been linked to recessive rhesus protein deficiency (Agre and Cartron, 1991) and Overhydrated Hereditary Stomatocytosis (Bruce *et al*., 2009) which is a rare dominantly-inherited haemolytic anaemia, characterised by leakage of important monovalent cations (K^+, Na^+) in red cell membranes (Ludewig *et al.,* 2001, Huang and Ye, 2010). In mice, RhCG mutations impair blood pH homeostasis and are associated with distal Renal Tubular Acidosis and male infertility (Biver *et al*., 2008). Rh proteins also play an essential role in the resorption of ammonium through the renal tubule epithelial cells in humans (Garvin *et al*., 1988). Finally, RhCG has been identified as a candidate gene for early-onset major depressive disorder (Verma *et al*., 2008).

1.3 Structural characterisation of ammonium transporters

1.3.1 Topology of ammonium transporters

The topology of the Amt protein was determined *in vivo* by genetic manipulation of the ammonium transporter AmtB in *E. coli* (Thomas *et al*., 2000). Two sets of complementary reporter proteins were produced in which either the alkaline phosphatase PhoA or the β-galactosidase LacZ, were fused to the C-terminus of each predicted TM helix. The principle of the methodology is that PhoA and LacZ are active when they are located in the periplasm or in the cytoplasm respectively, hence PhoA- and LacZ-fusions are alternatively active depending on the orientation of the preceding helix. Whereas the interpretation of LacZ activity assays was complicated by the tendency of LacZ to be cleaved off, the PhoA activity data was unambiguous and led to the development of the general topology of 11 transmembrane helices (TMH) with the N-terminus pointing in the periplasm and the C-terminus located in the cytoplasm. These results also suggested that the first theoretical TMH (amino acids 1-22) is a signal peptide cleaved off during the protein folding and/or

insertion into the membrane. Since then this general topology has been shown to be common to all Amt/Mep proteins. However, it has lately been shown the Rh protein possess 12 TMH with the N- and C-termini located in the cytoplasm (Lupo *et al*., 2007, Gruswitz *et al*., 2010).

1.3.2 Tertiary and Quaternary structure

The first evidence that Amt/Mep/Rh proteins may form oligomers came from the observation that, in *S. cerevisiae*, the expression of a non-functional Mep1 protein inhibits the transport activity of Mep2 and Mep3, indicating cross-talk between different Mep transporters (Marini *et al*., 2000), and similar observations have been reported for ammonium transporters of *Aspergillus nidulans* (Monahan *et al*., 2002). *E. coli* AmtB was the first Mep/Amt protein to be purified and by a combination of analytical ultracentrifugation (AUC) and size exclusion chromatography (SEC) analysis, it has been shown that the protein presents a trimeric organisation of 90 kDa when solubilised in the detergent n-Dodecyl-β-D-Maltoside (DDM) (Blakey *et al*., 2002). Ordered two-dimensional crystals of AmtB were obtained and the trimeric organisation was confirmed using cryo-electron microscopy and atomic force microscopy (Conroy *et al.,* 2004). In addition, it was shown that each monomer has a pseudo-two-fold symmetry (Conroy *et al*., 2004). Within the next few months, the high resolution structure of AmtB was solved independently in Prof. Robert Stroud's and Prof. Fritz Winkler's laboratories (Khademi *et al*., 2004, Zheng *et al*., 2004). During the last decade the structures of *Archaeglobulus fulgitus* Amt (*Af*Amt1), the Rh protein of *Nitrosomonas europaea* (*Ne*Rh50) and the human RhCG protein have been solved (Andrade *et al*., 2005, Lupo *et al*., 2007, Gruswitz *et al*., 2010). The trimeric nature is conserved in all these proteins, indicating the ubiquitous nature of this oligomeric arrangement in the Amt/Mep/Rh protein family.

1.3.3 *E. coli* AmtB protein

The high resolution structure of AmtB was solved and published in parallel by two different research groups with a resolution of 1.45 and 1.8 Å (Khademi *et al*., 2004, Zheng *et al*., 2004). AmtB crystallised as a trimer, as anticipated (Blakey *et al*., 2002, Conroy *et al.*, 2004), each monomer contained 11 transmembrane helices as predicted by Thomas *et al* (Thomas *et al*., 2000) and the structure of M1 to M10 reflects a quasi-twofold axis in the midplane of the membrane as anticipated by Conroy *et al.,* (Conroy *et al*., 2004). For each monomer, the helices M1, M6, M7 and M8 interact with the helices M1, M2 and M3 of the neighbouring monomer (**Figure 1.4**) (Khademi *et al.*, 2004, Zheng *et al.*, 2004). The structure of the 22 amino-acids constituting the C-terminal tail of AmtB was not resolved, certainly due to high flexibility. In line with this hypothesis, a later crystal structure of a complex in which the C-terminal extension of AmtB was stabilised by interacting with the P_{II} protein GlnK allowed the structure of the cytoplasmic extension to be solved (Conroy *et al*., 2007, Gruswitz *et al*., 2007). The C-terminal tail contains two short helices separated by a tight turn centred on residue Gly393 (**Figure 1.5**).

Crucially, the crystallographic structure led to the identification, at the centre of each monomer, of the substrate translocation pathway. The pathway contains four distinct structural features that may help in understanding the mechanism by which AmtB translocates ammonium **(Figure 1.6)** (Khademi *et al.,* 2004, Zheng *et al.,* 2004).

1- A binding site (S1) at the bottom of a water accessible periplasmic vestibule.

2- Below S1, a constriction or “gate” formed by two partly stacked phenyl rings that separate the S1 site from the pore.

3- The central part of the narrow and hydrophobic pore.

4- A cytoplasmic water accessible vestibule.

The identification of these structural features has several mechanistic implications both with regard to the mode of action of AmtB and the nature of the transported substrate (NH_4^+ or NH_3). I will now discuss each of these four structural features in detail.

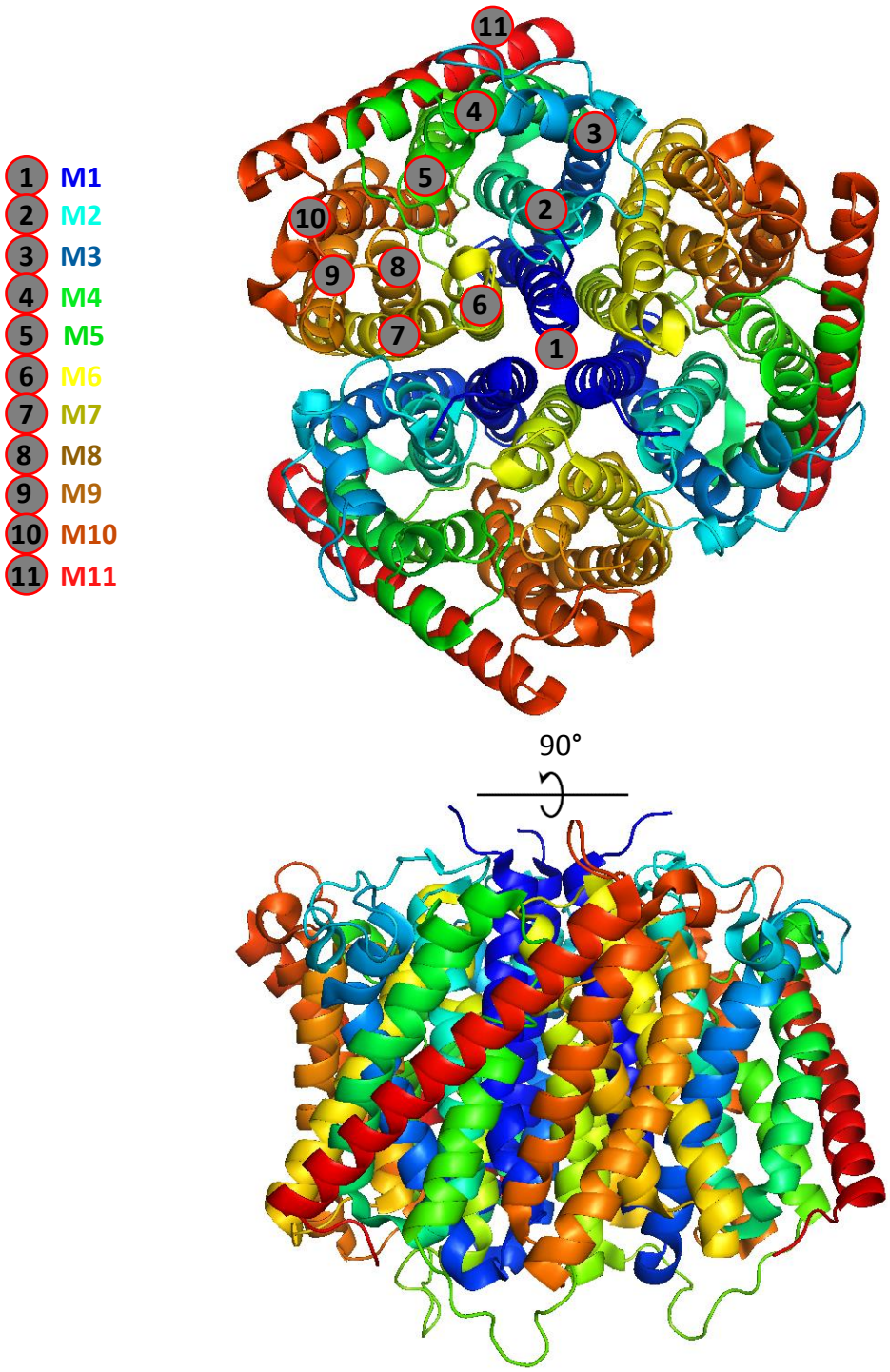

Figure 1.4 Top and side view of the structure of AmtB (1U7G). The circle numbers indicate the positions of the transmembrane α-helices from M1 to M11 (adapted from Khademi *et al.*, 2004).

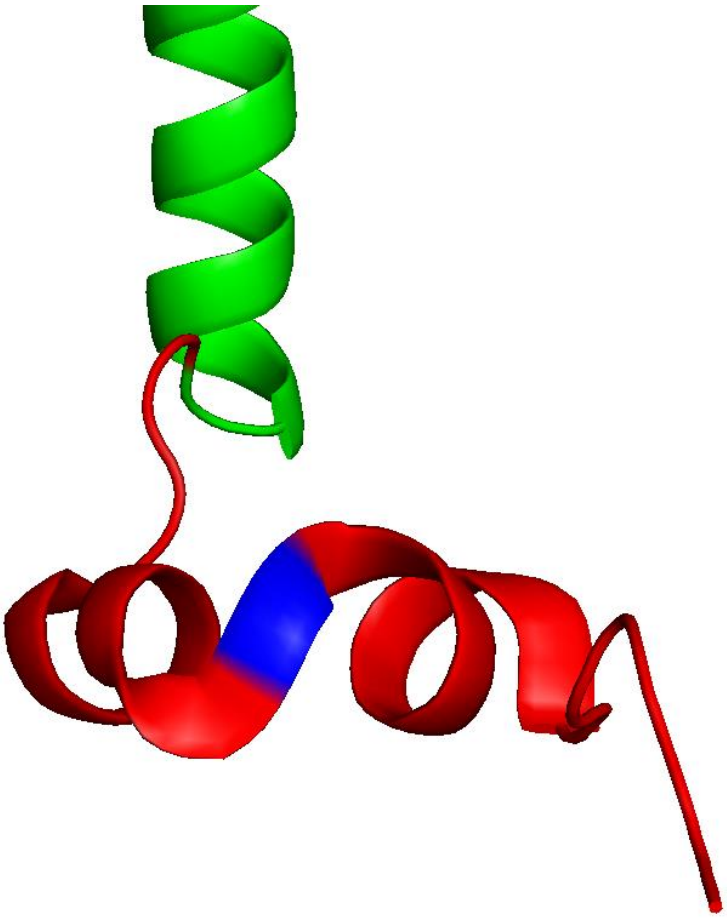

Figure 1.5 Structure of the C-terminal tail of AmtB as seen in the structure of AmtB-GlnK complex (PDB: 2NS1). The green transmembrane α-helix corresponds to M11, the red corresponds to the C-terminal tail, the blue residue corresponds to Gly393 (adapted from Gruswitz *et al.,* 2007).

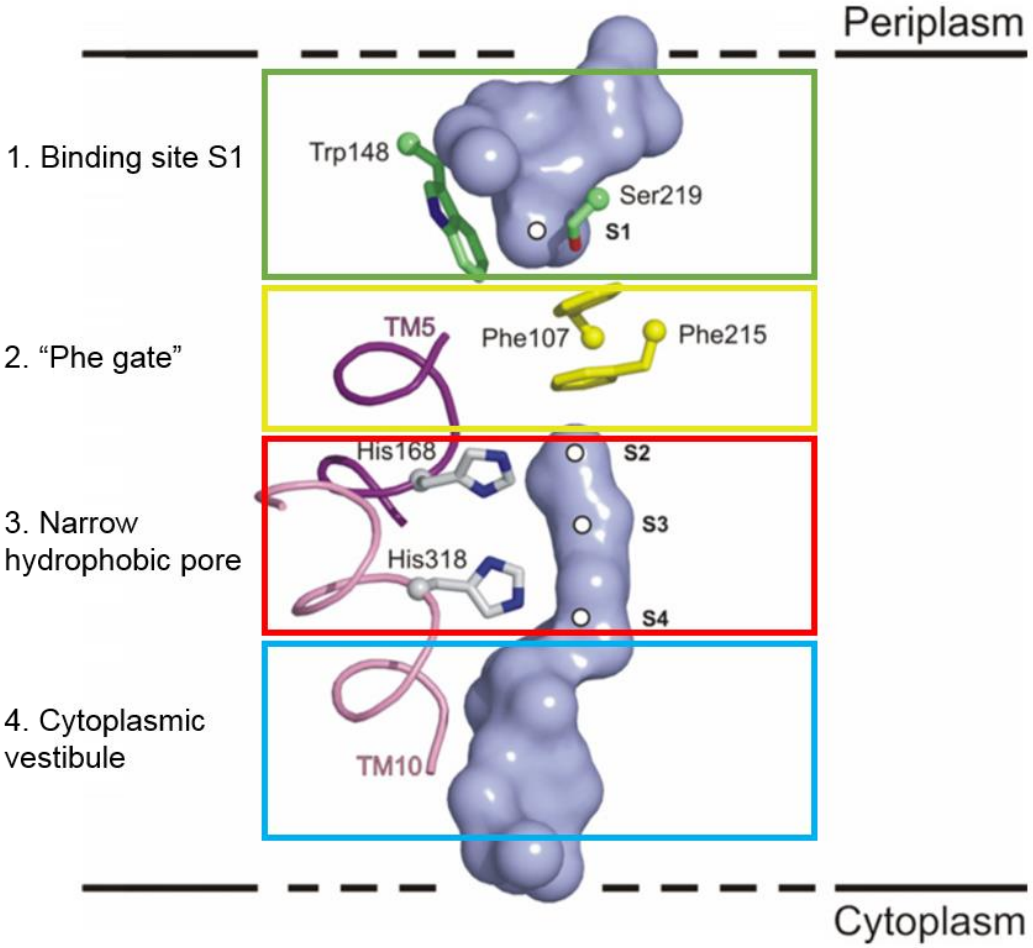

Figure 1.6 Translocation pathway of the AmtB from *E.coli* (adapted from Javelle *et al.*, 2007). The 4 structural features are represented: 1. S1 binding site (green box), 2. "Phe gate" (yellow box), 3. Narrow hydrophobic pore (red box) and 4. Cytoplasmic vestibule (blue box).

1.3.3.1 The periplasmic vestibule and S1 binding site

The first structural feature of the translocation pathway of AmtB is the S1 binding site. The residues delineating the specific binding site of ammonium are Trp148, Ser219 and Phe107. At the S1 site, NH_4^+ is potentially stabilised *via* the hydrogen bond with the O_γ of Ser219 and the formation of two π-cation-interactions with the ring of Phe107 and Trp148 (Khademi *et al*., 2004, Zheng *et al*., 2004). Functional studies done using ^{14}[C]MeA as ammonium analogue indicates that the binding affinity of the S1 site is in the micromolar range (Javelle *et al*., 2007). Moreover, it has been demonstrated using free energy calculations that the binding site has a greater affinity for NH_4^+ and NH_3 than for Na^+ and K^+ (Zheng *et al*., 2004), hence acting as a selective filter for passage of nonspecific cations and water (Winkler, 2006). The residue Asp160 in the vicinity of the S1 site is highly conserved across the Amt/Mep/Rh family indicating an essential function for ammonium binding and/or translocation (Thomas *et al*., 2000, Javelle *et al*., 2004, Marini *et al.,* 2006). However, the crystal structure of AmtB shows that Asp160 cannot access the bulk solvent, displaying only a structural role (Khademi *et al*., 2004), this is further discussed in paragraph 1.4.2.

From a functional and physiological point of view, this binding site may provide scavenging efficiency for ammonium, which is essential as the protein is only expressed under low ammonium conditions (Andrade and Einsle, 2007, Wirén and Merrick, 2004).

1.3.3.2 The “Phe Gate”

The second feature of the translocation pathway of AmtB is the “Phe gate”. Two stacked rings of the residues Phe107 and Phe215 completely block the translocation pathway between the S1 site and the hydrophobic pore, forming a “gate”. The opening diameter of the pore is 1.2 Å suggesting that the two

Phe residues are dynamic to allow the passage of the substrate (Khademi *et al*., 2004, Zheng *et al.,* 2004).

1.3.3.3 The hydrophobic pore

The central part of the narrow pore (1.2x20 Å) is formed by residues in the transmembrane helices (TMH) 1, 3 and 5 and in the pseudo-symmetrical TMH 6, 8, and 10. The pore is predominantly hydrophobic, suggesting a high energy barrier for the conduction of NH_4^+. The side chains of two highly conserved histidine residues protrude into the lumen of the pore with their δ nitrogen atoms linked by an hydrogen bond, forming what has been named the “twin-His” motif (Javelle *et al*., 2006). The almost complete conservation of this twin-His motif in the protein family strongly indicates an important functional role. Interestingly, three electron densities, named Am2, 3 and 4 have been identified in the vicinity of the twin-His motif (Khademi *et al.,* 2004). The authors claimed that these densities were only present in the $(NH_4)_2SO_4$-soaked crystal, hence ammonium and ammonia molecules were mapped inside. Crucially, this result was not reproduced by others and the same densities were observed in the absence of ammonium, leading to the conclusion that these densities correspond to water molecules (Zheng *et al*., 2004, Javelle *et al*., 2006, Javelle *et al*., 2008).

1.3.3.4 Cytoplasmic vestibule

At the cytoplasmic end of the translocation pathway, a water accessible vestibule was identified. In contrast to the periplasmic vestibules, no clear binding site can be identified. Moreover, Zheng *et al*, have crystallised AmtB in two different spatial groups, in which the conformation of the intracellular vestibule was not identical. This observation reveals that the cytoplasmic vestibule can exist in different conformations whose functional significance is still not known (Zheng *et al*., 2004).

1.3.4 Other Amt/Mep/Rh structures

This section will focus on the main differences between the structure of AmtB and the structures of other members of the family published since 2004.

High resolution structures of different Amt/Mep/Rh proteins have been solved over the last 13 years for *Archaeglobus fulgidus* ammonium transporter 1 *Af*Amt1 (Andrade *et al*., 2005), *Kuenenia stuttgartiensis* Amt5 (Pfluger *et al*., 2018), *S. cerevisae* and *C. albicans* Mep2 (van den Berg *et al*., 2016), *Nitrosomonas europaea* Rhesus protein *Ne*Rh50 (Lupo *et al*., 2007), and *Homo sapiens* Rhesus protein RhCG (Gruswitz *et al*., 2010). The α-helical transmembrane domains are highly conserved but slight structural differences can be observed in the extracellular loops and the C-terminal tail.

1.3.4.1 *A. fulgitus* Amt1

The structure of *Af*Amt1 was solved in 2005 (Andrade *et al*., 2005). The general topology of AmtB and *Af*Amt1 are highly similar, however, *Af*Amt1 does not possess a signal sequence. The two-fold axis present in the crystal structure of *Af*Amt1 (between helices 1-5 to 6-10) is similar to AmtB. No electron densities were found in the hydrophobic pore of *Af*Amt1 upon ammonium soaking, in contrast to the electron densities observed in the structure of AmtB.

*Af*Amt1 was crystallised in the presence of Xenon gas. Xenon acts as an anomalous signal of 7 electrons potentially helping to solve the phase during data processing. Xenon revealed 3 strong and 1 weak binding sites in the putative translocation pathway of *Af*Amt1. Xenon electron density appeared at the exact same position as the electron density observed in the crystal structure of AmtB, assigned to ammonia or water molecules. In addition, Xenon molecules are hydrophobic, hence the position of the Xenon in the

crystal structure supports the hypothesis of NH_3 conduction (Andrade *et al*., 2005).

The structure of the *Af*Amt1 C-terminal tail was solved and the superposition with the C-terminal tail of AmtB, as seen in the AmtB/GlnK complex, revealed an identical conformation.

1.3.4.2 Bacterial *Ks*Amt5

The roles of ammonium transporters in the regulation of nitrogen metabolism have been widely discussed over the last years (Tremblay and Hallenbeck, 2009). *Kuenenia stuttgartiensis* is an anaerobic ammonium oxidation bacterium possessing an “ammonium transporter” named *Ks*Amt5. The C-terminal tail of *Ks*Amt5 contains a potential histidine kinase (HK) domain, highly similar to the HK domain present in bacterial two component systems, suggesting a new function of these Amt proteins as an ammonium sensor (Pfluger *et al*., 2018). The transmembrane structure of *Ks*Amt5 is very similar to AmtB and *Af*Amt1 (Khademi *et al*., 2004, Andrade *et al*., 2005, Pfluger *et al*., 2018). The HK domains of *Ks*Amt5 were not resolved due to its high flexibility. Interestingly, the *Ks*Amt5 structure revealed that the translocation pathway is blocked by the bulkier side chain of the residues Phe27, Tyr30 and Phe34 and by a shift of the twin-His motif position of 0.8 Å (Khademi *et al*., 2004, Zheng *et al*., 2004, Andrade *et al*., 2005, Javelle *et al*., 2007). In addition, the activity of *Ks*Amt5 measured using Solid Supported Membrane Electrophysiology (SSME) (see **Chapter 2**, **section 2.4.2**) indicates that the protein only binds but does not translocate ammonium across the lipid bilayer (Pfluger *et al*., 2018).

1.3.4.3 Fungal Mep *Sc*Mep2 and *Ca*Mep2

In 2016, the structures of Mep2 from *S. cerevisae* (*Sc*Mep2) and *C. albicans* (*Ca*Mep2) were solved at 3.2 and 1.5 Å respectively (van den Berg *et al*., 2016). Both structures were similar (Carbon alpha root mean square deviation [C-α r.m.s.d] of 0.7 Å when aligned) with the exception of the N- and C-terminal parts. However, 3 major structural differences were observed between the Mep2 and the bacterial Amt structures (van den Berg *et al.,* 2016).

1- An extended N-terminus of ~25 residues interacting with the extra-cellular loop 5 (ECL5) of the neighbouring monomer creating a wider ammonium binding site.

2- A strong hydrogen bond between the residues Thr53 (located at the C-terminal tail of the TMH1) and His348 (second highly conserved twin-His residue). This hydrogen bond creates a “closed state” never observed in bacterial Amt structures.

3- The C-terminus region does not physically interact with the core of the protein resulting in an elongated conformation of the tail not observed in bacterial Amt structures.

1.3.4.4 *Nitrosomonas europae* protein Rh50

In silico topological analysis has shown that Amt and Rh proteins possess 11 and 12 transmembrane α-helices (TMH) respectively (Marini *et al*., 1997b). The structure of the human RhCG protein confirmed the presence of 12 THM (**see section 1.3.9**) (Gruswitz *et al.,* 2010). Surprisingly, the structure of the *Nitrosomonas europae* Rh50 (*Ne*Rh50) reveals only 11 TMH and it has been hypothesised that the extra TMH was cleaved off when *Ne*Rh50 was expressed in *E.coli* (Lupo *et al*., 2007). The general structural organisation of *Ne*Rh50 is closely related to the bacterial Amt, in particular the conserved trimeric nature which contradicts the previous assumption that Rh proteins were tetramers (Eyers *et al.,* 1994). This confirmed the ubiquitous nature of the oligomeric state across the protein family. The S1 binding site found in bacterial Amts is missing in the *Ne*Rh50 structure (**Figure 1.7**) but the "Phe-gate" and the hydrophobic nature of the pore are conserved. The positions of the two Phe rings in the gate are parallel in Amt but perpendicular in Rh proteins (**Figure 1.7**). The Phe86 is tilted in *Ne*Rh50 compared to Amt protein and allows a water molecule to be deeply docked (~2 Å). The flip of the Phe86 residue, the substitution of Thr273 in AmtB for a Gly251 in *Ne*Rh50 and the increased distance between TMH4 and 6 widens the pore of *Ne*Rh50. In addition, a tilt of the second Phe favours the passage of NH_4^+/NH_3 in *Ne*Rh50 compare to the bacterial Amt. The potential functional implication of this structural variation between bacterial Amt and Rh protein is still unclear.

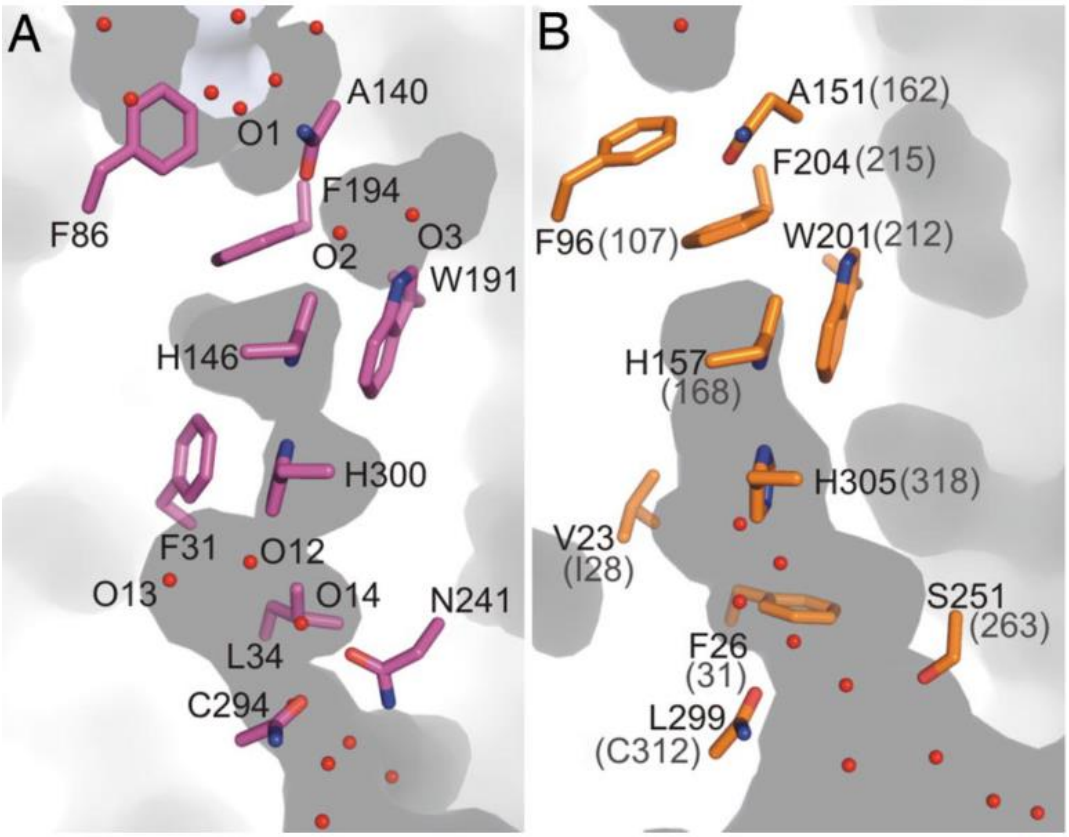

Figure 1.7 Comparison of the translocation pathway between **(A)** Amt1 from *A. fulgitus* (from Andrade *et al.,* 2005) or **(B)** Rh50 from *N. europaea* (Lupo *et al.,* 2007) (Figure from Lupo *et al.*, 2007).

1.3.4.5 Mammalian Rhesus RhCG

The crystal structure of the human RhCG has been resolved at a resolution of 2.1 Å (Gruswitz *et al*., 2010). The quasi two-fold axis, with respect of the lipid bilayer observed in the Amt protein is conserved. Unlike its bacterial homologue *Ne*Rh50, RhCG contains 12 TMH and the extra N-terminal TMH lies at the interface of each trimeric subunit (Gruswitz *et al*., 2010).

As observed in the Rhesus protein from *N. europaea* (*Ne*Rh50), no S1 binding site is present in the RhCG structure but the residues Glu166, Asp218, Asp278 and Glu329 may create a NH_3 recruitment site. The Asp177 residue, corresponding to the Asp160 residues in AmtB is conserved in the structure of RhCG, suggesting an essential functional role (Javelle *et al.*, 2004, Khademi *et al.*, 2004). The pore of RhCG is highly hydrophobic, suggesting the conduction of NH_3 rather than NH_4^+ (Gruswitz *et al*., 2010). Finally, a common feature specific to the Rh (RhCG and *Ne*Rh50) proteins is a “shunt” on the cytoplasmic face of the proteins (**Figure 1.8**). The function of this particular structural feature is still unclear, but it has been hypothesised that it may represent an alternative path for NH_4^+ entry, and NH_3 delivery into the hydrophobic portion of the pore (**Figure 1.8**).

To summarize this **section 1.3.4** “**Other Amt/Mep/Rh structures**”, the high expectations to elucidate the transport mechanisms from all the Amt/Mep/Rh 3D structures have not been met to date, as all the structures are very similar and show the same inward-facing state of the protein. There are no significant differences in the crystal structures of Amt, Mep and Rh proteins that can clearly account for the functional differences between transporter-like (Amt/Mep) and channel-like (Rh) activity.

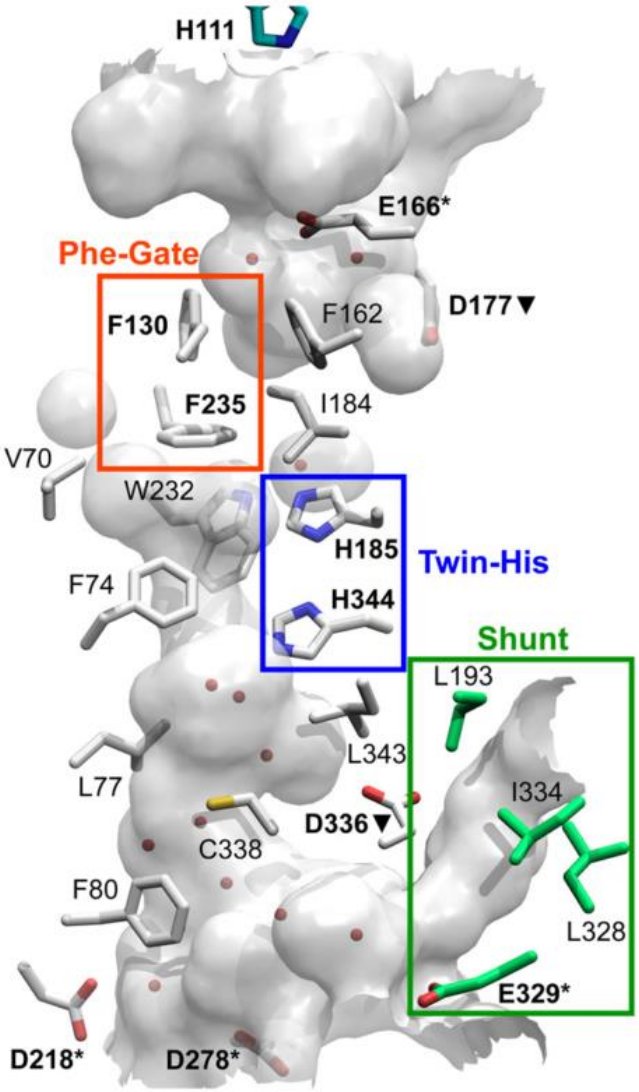

Figure 1.8 Translocation pathway of the human RhCG protein (from Gruswitz *et al.,* 2010). The red, blue green boxes are corresponding to the “Phe gate”, twin-His motif and shunt motif respectively.

1.3.5 Regulation of *E.coli* AmtB expression and activity

1.3.5.1 The NtrB/NtrC two component system

The control of nitrogen assimilation in *E. coli* is mediated by the two component system NtrB/NtrC. The system was originally described in *Klebsiella pneumoniae* (Stanley *et al.,* 1974) but it is now known to be present in most proteobacteria with only few exceptions (Huergo *et al*., 2013). The general mechanism of the NtrB/NtrC system is presented in **Figure 1.9**. The regulatory system acts at the transcriptional and post-translational level. Herein, the different blocks composing the NtrB/NtrC system will be described.

One of the first enzyme involved in ammonium assimilation is glutamine synthetase (GS). GS catalyses the conversion of ammonium and glutamate into glutamine by hydrolysing ATP (Shwu-Huey *et al*., 1995). The enzyme is regulated by GlnE, a bifunctional enzyme containing a C-terminal adenylyl-transferase and an N-terminal adenyl-removase domain. The activity of GlnE is under the regulation of the P_{II}-type protein GlnB. *E. coli* encodes two P_{II} proteins: GlnK and GlnB. The P_{II} proteins are one of the most widely distributed families of signal transduction proteins and are pivotal players in the control of nitrogen metabolism in bacteria and archaea (Huergo *et al*., 2013). The P_{II} proteins form homotrimers with a compact barrel-like shape. A flexible loop, named “T-loop”, protrudes from the upper face of the barrel. In *E. coli*, the P_{II} proteins interact with their protein targets, including GlnE, AmtB and NtrB, through T-loop contacts. The activity of P_{II} proteins is dependent on binding the effectors ATP, ADP and 2-oxoglutarate (2-OG).

1- When the cytoplasmic concentration of ATP and 2-OG is high, both effectors bind to GlnK/GlnB, stabilising a T-loop conformation in which the highly conserved Tyr51 residue is exposed (Truan *et al*., 2010). In this conformation, the Tyr51 residue can be urydylylated in *E. coli* by a bifunctional uridylyl-transferase/uridylyl-removase enzyme named

GlnD (Son and Rhee, 1987). Once uridylylated, GlnK/GlnB can't interact with their target.

2- When the cytoplasmic concentration of 2-OG and ATP is low, only ADP is bound to GlnK/GlnB and the conformation of the T-loop changes which results in the interaction the P_{II} proteins with their target proteins GlnE, AmtB and NtrB (Jiang and Ninfa, 2007).

The activity of the bifunctional uridylyl-transferase/uridylyl-removing enzyme GlnD is regulated by the cytoplasmic concentration of glutamine and 2-OG. In the presence of glutamine/absence of 2-OG, the urydylylase activity is stimulated while in absence of glutamine/presence of 2-OG, the urydylyltransferase activity is dominant (Jiang *et al*., 1998, Rhee *et al*., 1985, Huergo *et al*., 2013).

At the transcriptional level, nitrogen assimilation is regulated by the two component system NtrC/NtrB. NtrC is a homodimer composed by a N-terminal phosphorylation site, an AAA^+ ATPase domain for transcription and a C-terminal DNA binding domain (Huergo *et al*., 2013). NtrB is also a homodimer with each monomer consisting of a N-terminal sensor domain, a central core phosphotransferase and phosphatase domain, and the C-terminal histidine kinase domain (Huergo *et al*., 2013).

In the section below, the activity of the NrtB/NrtC system will be described (**Figure 1.9**).

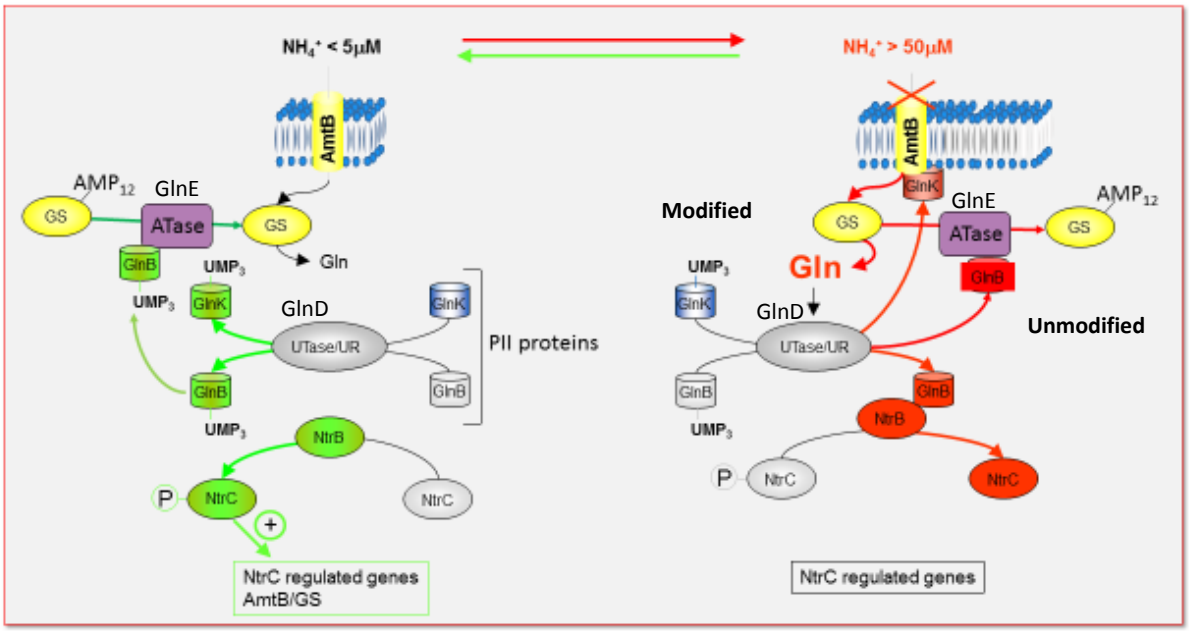

Figure 1.9 Regulation of NtrB/NtrC two components system in *E. coli* at the transcriptional and post-translational level (adapted from Javelle *et al.*, 2004).

Under nitrogen limitation conditions (Figure 1.9, left panel):

When the extracellular ammonium concentration is low, the intracellular glutamine concentration decreases and the cellular 2-OG and ATP concentrations increase.

1-Post-translational regulation: In absence of glutamine, the urydylyl transferase activity of GlnD dominates, leading to the formation of GlnK-UMP_3 and GlnB-UMP_3. GlnB-UMP_3 interacts with GlnE which stimulates the adenylylremovase activity of GlnE. The unmodified GS is active and assimilates ammonium to glutamine, meanwhile GlnK-UMP_3 does not interact with AmtB, ensuring NH_4^+ uptake.

2-Transcriptional regulation: GlnB-UMP_3 does not interact with NtrB, which inhibits NtrB autophosphorylation. The NtrB histidine kinase activity phosphorylates NtrC promoting NtrC dimerisation. The NtrC dimer binds to the promoters of the target genes, increasing the transcription of *glnA* and *amtB*, encoding for GS and AmtB respectively.

Under ammonium excess conditions (Figure 1.9, right panel):

An increase of the external ammonium concentration results in an increase of the intracellular glutamine concentration and a low concentration of 2-OG and ATP.

***1-Post-translational regulation*:** In the presence of glutamine, the urydylylase activity of GlnD dominates which de-modifies GlnK and GlnB. GlnB activates the adenylyltransferase activity of GlnE, which modifies the GS into GS-AMP_{12}. GS-AMP_{12} is inactive, which decreases the intracellular glutamine concentration. Meanwhile, GlnK interacts with AmtB blocking the import of NH_4^+ (the mechanism of the AmtB-GlnK interaction is detailed in 1.3.5.2.1).

2-Transcriptional regulation: Unmodified GlnB binds to NtrB which activates NtrB phosphatase activity. NtrC is dephosphorylated, leading to the inactivation of the transcription of the genes under its regulation.

1.3.5.2 Regulation of AmtB activity by GlnK and specific lipids

In this part, the interaction of GlnK with AmtB and the interaction of AmtB with the lipidic environment will be discussed.

1.3.5.2.1 AmtB/GlnK complex

It was originally suggested that *amtB* and *glnK* are functionally associated due to the proximal location (pairing) of the two genes in the bacterial genome (Thomas *et al*., 2000). It was later shown that after a 30 mM ammonium pulse (named “ammonium shock”), GlnK relocalised from the cytoplasm to the inner-membrane and that this was dependent on the presence of AmtB (Coutts *et al*., 2002). The AmtB-GlnK complex formation was further studied and it has been shown that after an ammonium shock GlnK and AmtB can be co-purified (Javelle *et al*., 2004). It has been demonstrated that intracellular ATP and 2-OG control the association/dissociation of the AmtB-GlnK complex (Durand and Merrick, 2006, Radchenko *et al*., 2010). In addition, after a non-physiological increase of ammonium concentration outside the cell, GS will synthesise a lot of glutamine. The sudden increase of glutamine synthesis will result in the death of the cells due to rapid drop of the ATP concentration. However, after the ammonium pulse, the glutamine production is stopped after 10 seconds. To explain the regulation mechanism, Stadtman *et al.* obtained two purified forms of the GS: one adenylylated that is sensitive to feedback inhibition and one non-adenylylated which is not. This discovery demonstrated the importance of enzyme regulations to avoid cell death under non-physiological ammonium pulse (Stadtman, 2001) and references therein.

The X-ray structure of the GlnK-AmtB complex has been simultaneously resolved by two different groups (Conroy *et al*., 2007, Gruswitz *et al*., 2007). GlnK and AmtB form a $GlnK_3$:$AmtB_3$ complex at a ratio 1:1. Interestingly, the C-terminal tail of AmtB and the T-loop of GlnK are structurally defined in the complex (Conroy *et al*., 2007, Gruswitz *et al*., 2007) whereas they were not in

the individual crystal structures (Khademi *et al.*, 2004, Zheng *et al*., 2004). The T-loop of GlnK in the complex is composed of 2 anti-parallel β-strands and this conformation allows a perfect fitting of the loop into the cytoplasmic vestibule of AmtB. The conserved Arg47 in the T-loop of GlnK form two hydrogen bonds with the highly conserved AmtB residue Ser263 and Asp313, which physically block the pore (**Figure 1.10**) (Conroy *et al.,* 2007, Gruswitz *et al*., 2007).

Surprisingly, the GlnK Tyr51 residue, which can be uridylylated, is not accessible in the AmtB-GlnK complex, indicating that the covalent de-modification of GlnK does not play a key role in the complex disassembling. Three molecules of ADP were found to bind into the three effector binding sites of GlnK in complex with AmtB, which indicates that ATP/ADP binding is a key step in the complex formation/disassembling (Conroy *et al.,* 2007, Gruswitz *et al*., 2007). The structure also reveals two pockets at the base of the T-loop in GlnK and a third in the interface between the T-loop and the vestibule of AmtB. Using docking software, it has been demonstrated that 2-OG molecules fit into each pockets (Gruswitz *et al*., 2007). The physiological relevance of the putative 2-OG binding sites have been tested *in vivo* and it has been shown that after an ammonium shock, the concentration of 2-OG and the ATP/ADP ratio decreased (Radchenko *et al*., 2010). In addition, it was shown that the affinity of GlnK for AmtB decreased when 2-OG is present and the presence of the Mg^{2+} ion seems to be essential for the dissociation of the complex *in vitro* (Heinrich *et al*., 2006). This information lead to the hypothesis that the uridylylation of GlnK occurs upon ADP binding and that the uridylylation is not necessary to disassemble the complex (Radchenko *et al*., 2010).

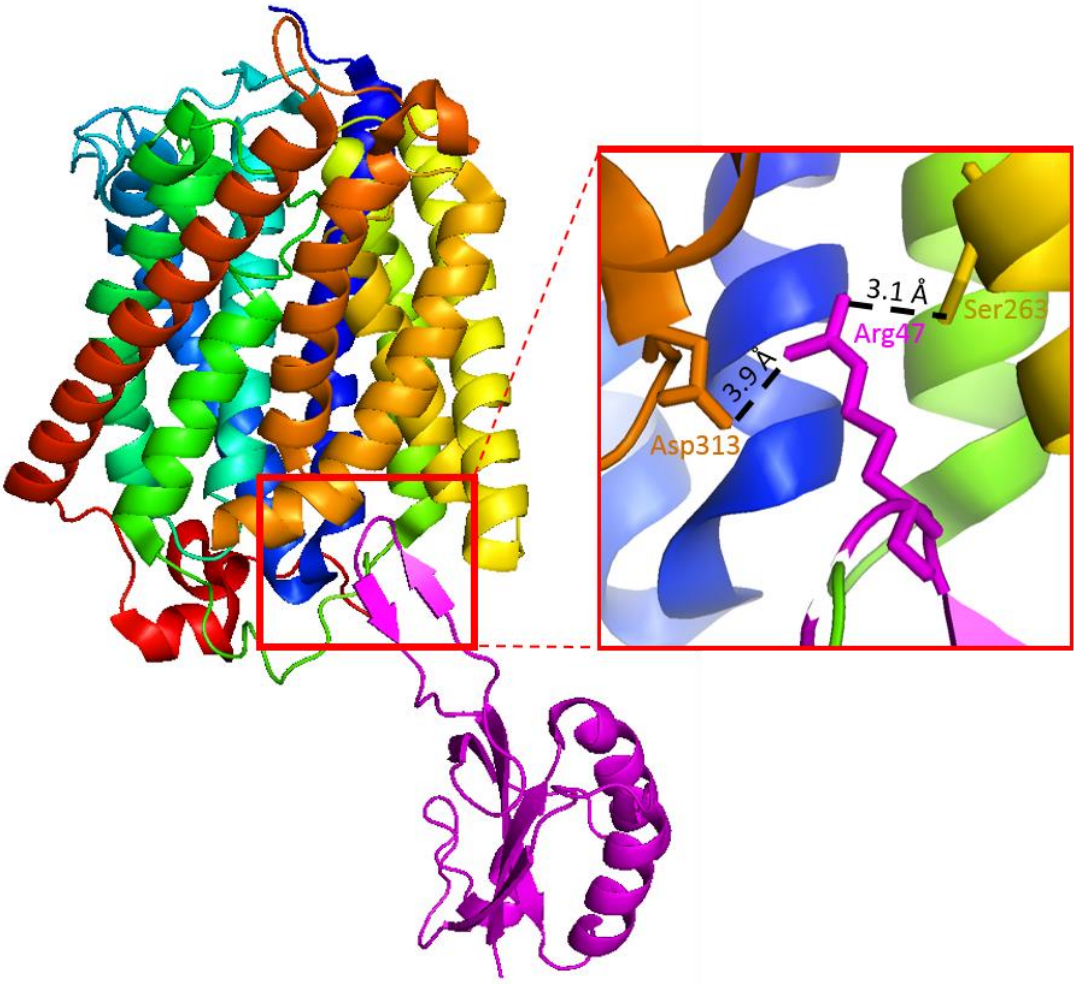

Figure 1.10 Side view of the structure of the AmtB-GlnK complex (PDB: 2N1S). The structure of AmtB is displayed in rainbow and the structure of GlnK is displayed in magenta. The red box illustrates a zoom-view of the interaction area. The black dash-lines correspond to the hydrogen bond distance between the residues (adapted from Gruswitz *et al.*, 2007).

1.3.5.2.2 Regulation of AmtB *via* lipid interaction

Specific lipid binding sites have been identified in AmtB using mass spectroscopy (Laganowsky *et al*., 2014). It has been demonstrated that cationic lipids such as cardiolipin and phosphatidyl-glycerol (PG) help to stabilise AmtB in a concentration dependent manner whereas anionic phosphatic acid (PA), phosphatidyl-choline (PC) and zwitterionic phosphatidyl-serine (PS) and phosphatidyl-ethanolamine (PE) have no effect (Laganowsky *et al*., 2014). To further investigate the role of the lipids, AmtB was crystallised in the presence of PG, and 8 PG specific binding sites located at the outer leaflet were identified (**Figure 1.11**) (Laganowsky *et al*., 2014). In the crystal structure, PG molecules formed hydrogen bonds with the Asn72 residue and a water bridge with Asn79 residue and a $AmtB^{Asn72Ala/Asn79Ala}$ variant was not able to bind PG (Cong *et al*., 2016, Laganowsky *et al*., 2014).

Furthermore, two lines of evidence strongly indicate that PG binding triggers conformational rearrangement of AmtB:

1- Recently, a method to determine the thermodynamics of AmtB-PG interactions using native MS has been developed. The thermodynamics for the binding of PG to AmtB is entropically unfavourable (Cong *et al*., 2016). This counterintuitive result can only be explained if PG binding triggers some molecular rearrangement.
2- The crystal structure of AmtB reveals that several residues are repositioned to interact with the phospholipid bilayer upon PG binding (Laganowsky *et al*., 2014). However, no functional relationships have been reported between PG binding and AmtB activity so far. This aspect has been part of my PhD project and the results are presented **Chapter 5**.

How lipid binding events affect the complex formation between AmtB and GlnK has been studied (Cong *et al*., 2017) and it has been shown that:

1- The increase of lipid binding events modulate the dissociation constant of the complex AmtB/GlnK.

2- It was suggested that PC, PE and PG lipids were positively contributing to the stabilisation of the AmtB-GlnK complex whereas PA lipid was enhancing the dissociation of the complex (K_D from 50 µM to 80 µM).
3- Using PG as a lipid model, it was shown a hydrophobic tail of 12 and 16 carbons provided a positive allosteric modulation on the complex AmtB/GlnK while a 14-carbon tail did not stabilise the complex. This suggested that the lipid binding sites in AmtB are lipid size dependent.

This study emphasised the importance of the chemical properties of the lipids on the stability of the AmtB-GlnK complex leading to a new vision for membrane protein complex formation.

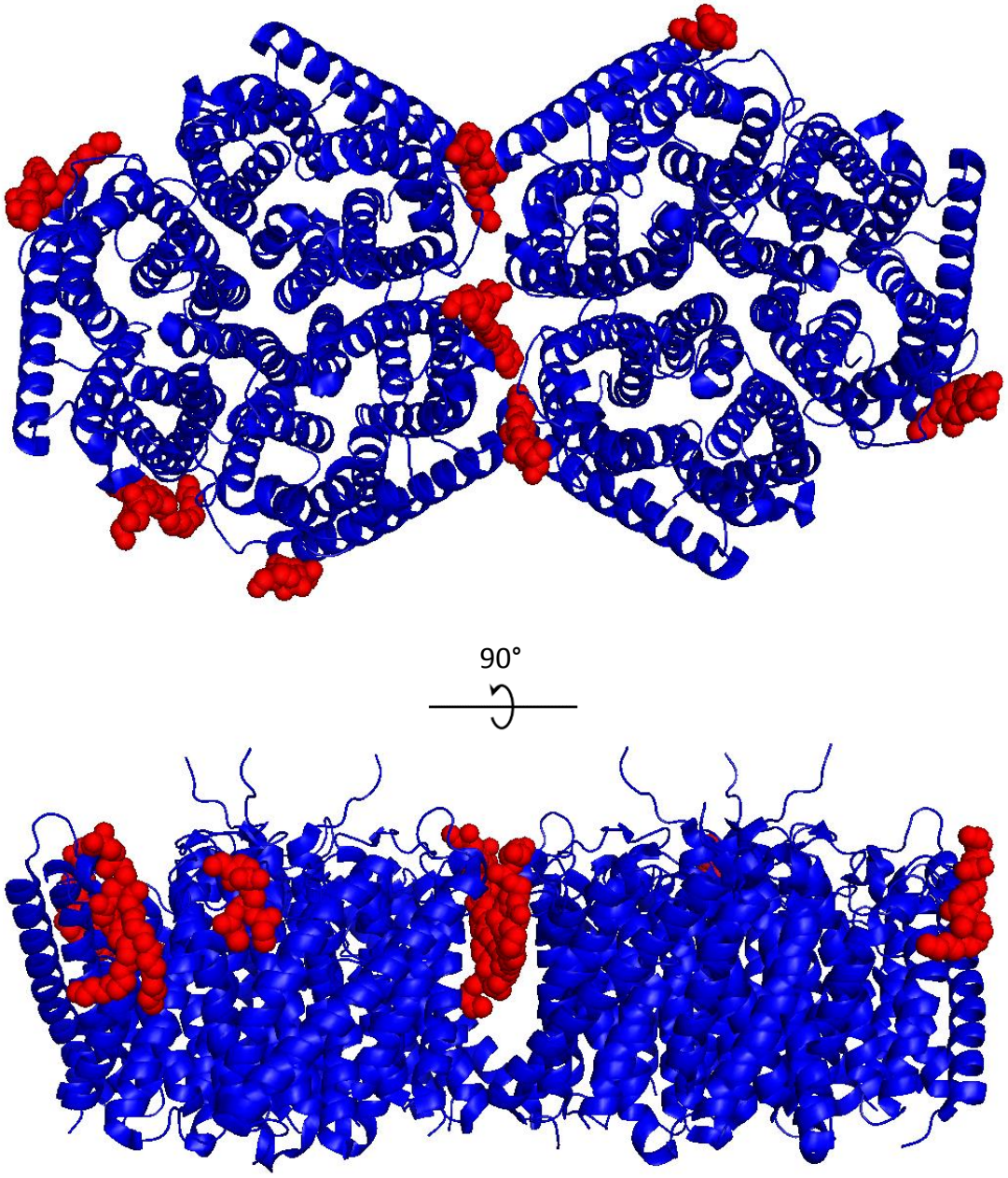

Figure 1.11 Structure of AmtB with PG bound. AmtB is represented in blue and the PG lipids in red (adapted from Laganowsky *et al.,* 2014).

1.4 Functional characterisation of Amt/Mep/Rh protein

1.4.1 General mechanism of transport

Since the first characterisation of an ammonium transport activity in *P. chrysogenum* using ^{14}[C]MeA as a tracer (Hackette *et al*., 1970), *in vivo* and *in vitro* MeA uptake has been widely used in numerous biological systems to characterised Amt/Mep transporters (Wirén and Merrick, 2004, Andrade and Einsle, 2007, Javelle *et al*., 2007). From these functional studies, two conflictual hypotheses concerning the general mechanism of transport emerged:

1- The measurement of MeA accumulation *in vivo* supported the hypothesis that Amt proteins were acting as strict MeA/NH_4^+ uniporters in *Rhyzobium etli* (Tate *et al*., 1998), *C. glutamicum* (Meier-Wagner *et al*., 2001), *S. cerevisae* (Marini *et al*., 1997a), *Oryza sativa* ($^{13}NH_4^+$ uptake) (Wang *et al*., 1993) and the ectomychorizal fungi *Hebeloma cylindosporum*/*Paxillus involutus* (Javelle *et al*., 2001, Javelle *et al*., 2003).

2- The second hypothesis, based on growth experiments, stated that Amt/Mep proteins act as bidirectional "NH_3 gas-channel" in *E. coli* (Soupene *et al*., 1998) and *S. cerevisiae* (Soupene *et al*., 2001).

Subsequently, patch-clamp electrophysiology was used to measure ammonium transport into *Xenopus* expressing plant AMT and human Rh proteins. It was shown that AMT1;1 from *Lycopersicon esculentum* acts as an electrogenic NH_4^+ uniporter (Ludewig *et al*., 2002), the human RhAG and RhBG as electroneutral NH_4^+/H^+ antiporter or NH_3 uniporter (Westhoff *et al*., 2002, Ludewig, 2004) whereas RhCG acts as an electrogenic NH_4^+ uniporter (Bakouh *et al*., 2004). Noteworthy, conflicting results have been obtained concerning RhCG: using stopped flow spectrophotometry to measure the pH variation upon ammonium pulse inside erythrocyte vesicles (Ripoche *et al*.,

2004), recombinant kidney cells (Zidi-Yahiaoui *et al*., 2005) and liposomes containing purified RhCG (Mouro-Chanteloup *et al*., 2010) it was concluded that RhCG acts as a NH_3 channel.

Finally, it has to be noted that few studies argued that the human Rh proteins were channels for both CO_2 and NH_3. I will not discuss this aspect in this thesis, but see the recent review (Endeward *et al*., 2017) and references therein.

To summarise, the plethora of functional studies aimed at elucidating the mechanism of ammonium transport by the Amt/Mep/Rh proteins has led to considerable controversy, concerning both the general mechanism of transport (channel *versus* transporter) and the substrate translocated (NH_3 v.s. NH_4^+) (Javelle *et al*., 2007). The dispute was most certainly the result of the lack of quantitative kinetic data characterising the activity of Amt/Mep/Rh proteins at the single channel level. Essentially all functional studies were carried out using intact cells or cell-derived vesicles. In all of these systems, the parameters measured to analyse ammonium conduction (pH change, electric current, uptake of labelled analogue) are likely to be affected by other physiological phenomena, requiring careful controls. The other consideration is that the functional difference between Amt/Mep and Rh protein may reflect the physiological roles of these proteins – Amt/Mep transporters in bacteria, fungi and plants are essential to scavenge ammonium from the environment, whereas the Rh proteins are involved in ammonium excretion.

The year 2004 marked a breakthrough in the Amt/Mep/Rh field with the publication of the structure of AmtB and the expectation to finally elucidate the mechanism of ammonium transport. However as we will see, this high expectation has not been met. The structure of AmtB revealed four distinct and non-symmetrical features in the ammonium translocation pathway, namely the S1 binding site, the “phe-gate”, the hydrophobic pore and the cytoplasmic vestibule (**see section 1.3**) (Khademi *et al*., 2004, Zheng *et al*., 2004, Javelle *et al*., 2007). These conserved non-symmetrical structural features suggested a unidirectional transport system, in strong disagreement with the bi-directional mechanism suggested by Soupene and co-workers (Soupene *et al*., 1998,

Soupene *et al*., 2001, Soupene *et al*., 2002). In addition, an *in vitro* pH-dependant fluorophore assay was developed to characterise AmtB transport activity (Khademi *et al*., 2004). The fluorophore (5-carboxy fluorescin) was trapped inside liposomes containing AmtB. The intensity of the fluorescence varied proportionally with the pH. After a rapid ammonium pulse, an alkalinisation was observed inside the liposome, suggesting that AmtB facilitated the diffusion of NH_3 (Khademi *et al.,* 2004). Crucially however, a study presented evidence that clearly questions the reliability of this assay (Javelle *et al.,* 2007). In 2011, Westerhoff's research group supported the view that AmtB could acts as a NH_3 active transporter or NH_4^+ facilitated diffusion system (Boogerd *et al.,* 2011). The authors hypothesised that if AmtB is an active NH_3 transporter, the transporter will have to be 10 times more efficient than the natural NH_3 permeation across the *E. coli* membrane (estimated to be around 1000 µm/s) (Boogerd *et al.,* 2011). Even if the previous condition is respected, Boogerd *et al* argued that AmtB transport activity will not be sufficient to explain the growth of *E. coli* at low NH_4^+/NH_3 concentration (10-50 µM) (Boogerd *et al.,* 2011). This work supported the view that AmtB should acts as an active NH_4^+ or NH_3/H^+ transporter at low NH_4^+/NH_3 concentration (Boogerd *et al.,* 2011). Finally, the authors emphasised that there is a lack of experimental evidences to conclude if AmtB transports NH_3 or NH_4^+ (Boogerd *et al.,* 2011).

In 2014, the first reliable *in vitro* assay to measure Amt/Mep/Rh protein came with the elegant work done in Prof. Susana Andrade's laboratory (Wacker *et al.,* 2014). In this study, the author reconstituted a purified ammonium transporter from *A. fulgidus* (*Af*Amt1) in liposomes and measured its activity using the solid supported membrane electrophysiology (SSME) technology. The proteoliposomes containing *Af*Amt1 were adsorbed on solid supported membrane (SSM) composed of a gold-coated sensor chip with an alkylmercaptane monolayer and a lipids monolayer on top. The SSM system creates a capacitively coupled system which allows the measurement of an electrogenic voltage generated by transporters into liposomes (Bazzone *et al*., 2013). Using this assay, it was hypothesised that *Af*Amt1 acts as an

electrogenic transporter (Wacker *et al*., 2014). The charge displacement associated with the translocation of ammonium suggest a NH_4^+ uniport or NH_3/H^+ symport transport mechanism. As detailed previously, the crystal structure of AmtB revealed that each monomer possessed a hydrophobic central pore which prevents the movement of a charge (Khademi *et al.*, 2004). Therefore, it is puzzling to reconcile this misaligned functional information, which supports the view that AmtB activity is associated with a charge translocation, and the structural data that indicates that a charge translocation through the pore is thermodynamically extremely unfavourable.

1.4.2 Functional characterisation of AmtB variants

Multiple functional studies and molecular dynamic simulation, aiming at elucidating the transport mechanism of AmtB at the molecular level have been done in the past 15 years.

1.4.2.1 S1 Binding site and Phe gate

Using *in vitro* MeA uptake, it was shown that Phe107Ala, Trp148Ala and Ser219Ala variants possessed a higher transport activity compared to the WT (Javelle *et al.,* 2008). This somewhat counterintuitive result indicates that ammonium binding at the S1 site represents a thermodynamic barrier. To corroborate these findings and assess more directly the loss of the S1 site, inhibition assays were done using the monovalent cation Tl^+, which has been shown to bind at the S1 site in the x-ray structure of AmtB (Javelle *et al*., 2008). Tl^+ (0.5 mM) completely inhibits MeA (0.02 mM) uptake activity, whereas no inhibition was observed in a Phe107Ala/Trp148Ala/Ser219Ala variant. All together, these results indicated that the S1 site may be biologically significant at very low substrate concentrations. Later on, it has been shown by analysis the growth rate of cells expressing AmtB variants that the S1 site was not required for AmtB function but instead served to optimise its performance (Hall and Kustu, 2011).

In 2006, a couple of MD studies used calculation of the free energy binding at low and high pH to determine the dynamics of the binding mechanism (Luzhkov *et al.*, 2006, Nygaard *et al.*, 2006). It was demonstrated that NH_4^+ binding was favourable compared to NH_3 at the S1 site by more than 20 kcal/mol. At the S1 site, NH_4^+ is stabilised by cation-π interaction with the aromatic rings of Trp148, Phe107 and hydrogen bonds with the residues Asp160 and Ser219 (Luzhkov *et al.,* 2006). A slightly different binding mechanism for NH_4^+ at the S1 site, was also proposed, involving hydrogen bonds with the Ser219 hydroxyl group and Ala162 carboxyl group and one

hydrogen bond with a polarised water molecule stabilised by the residue Gln104 (Bostick and Brooks, 2007).

1.4.2.2 Deprotonation mechanism

The hydrophobicity of the AmtB pore does not allow a charge to pass through. Thus, in between the S1 site and the entry of the hydrophobic pore, NH_4^+ has to be deprotonated and three hypotheses are currently considered.

1.4.2.2.1 Deprotonation at the binding site *via* a water molecule

The first hypotheses about the deprotonation of ammonium was proposed by Khademi and co-workers (Khademi *et al*., 2004). When NH_4^+ bound to the S1 site (**Figure 1.6**), the NH_4^+/NH_3 pKa decreased below 6 which favours the deprotonation of NH_4^+ by a water molecule. Khademi and co-workers did not detect a proton translocation through the pore, thus they concluded that after the deprotonation, the proton was released back in the periplasmic vestibule of AmtB (Khademi *et al*., 2004). In agreement with this view, it has been argued that the deprotonation occurred before reaching the hydrophobic pore, based on a Michael-Menten kinetics model (Winkler, 2006). In this model, it was estimated that the limiting concentration for normal growth in an *E.coli ⊿amtB* strain was below 100 nM. Using a simple diffusion limiting model, it was estimated that AmtB transports 60 molecules per second at 100 nM which is very slow compared to the substrate diffusion through a channel, classically estimated between 10^6-10^8 molecules per second per channel. The author hypothesised that the binding site was essential for the recruitment of ammonium to provide sufficient ammonium to the cell and that the most likely deprotonation occurs at the binding site *via* water molecules (Winkler, 2006). The proton should be released in the periplasm. I will show, however, that this model can now be formally rejected (**see Chapter 4**).

1.4.2.2.2 Deprotonation via the Asp160 residue

The second possibility is that the deprotonation occurs at the S1 site but the proton acceptor is the residue Asp160. Multiple Amt/Mep/Rh proteins sequence alignment showed that the residue Asp160 (in AmtB) is highly conserved within the Amt/Mep/Rh protein family, indicating a potential functional role (Thomas *et al.,* 2000, Javelle *et al*., 2004, Marini *et al*., 2006). It was demonstrated, using *in vivo* MeA uptake, that a $AmtB^{Asp160Ala}$ variant was inactive, whereas a $AmtB^{Asp160Glu}$ mutant was capable of maintaining 70% of the WT activity, suggesting that the Asp160 residue is not essential for AmtB activity (Javelle *et al.*, 2004). In addition, It was shown, in *S. cerevisae*, that the Asp182 residue of Mep2 (corresponding to the Asp160 in *E. coli*) played a key role in MeA binding (Marini *et al.,* 2006). In contradiction, the AmtB x-ray structure revealed that the distance between the Asp160 residue and the binding site is not favourable for a direct interaction with the substrate (Khademi *et al*., 2004, Zheng *et al*., 2004). However, a later MD simulation study showed that the Asp160 residue, separated by 8 Å from the binding site, was able to interact with ammonium (Luzhkov *et al*., 2006). Hence it remains an open question whether the Asp160 residue is involved in the deprotonation of NH_4^+.

1.4.2.2.3 Deprotonation at the Phe gate

It has been shown that the Phe107Ala mutation has no effect on AmtB activity but that a $AmtB^{Phe215Ala}$ variant was inactive (Javelle *et al.,* 2008). Replacing the Phe215 with His, Gln, Ser or Trp residue did not restore AmtB activity. This result demonstrated the importance of the Phe215 residue and it was assumed that the deprotonation of ammonium occurs at the "Phe gate" position (Javelle *et al*., 2008). However, no evidence of the direct role of the residue Phe215 in the deprotonation has been obtained so far.

1.4.2.2.3 Deprotonation at the S2 site

In 2006 an MD study on the AmtB from *E.coli* indicated that the carbonyl group of the Ala162 residue can be orientated either toward the S1 or S2 site (**Figure 1.6**), forming a H-bond with NH_4^+ (Nygaard *et al.,* 2006). This result suggested that the Ala162 residue acted as a "substrate guide" to move NH_4^+ from the binding site across the "Phe gate" to the S2 site (**Figure 1.12**, step 1). The deprotonation mechanism proposed is that NH_4^+ is translocated between the S1 and S2 site by the movement of Ala162 which becomes perfectly aligned with the Gly163:NH bond by interacting with the O_δ of the Asp160 residue (Nygaard *et al.,* 2006) **(Figure 1.12**, step 2). This new configuration allowed the deprotonation of the NH_4^+ by the Ala162 residue and the proton transfer to Asp160. Once a proton has been transferred from NH_4^+ to the O_δ Asp160, all amino acids involved become neutral and the C-O-H group of Ala162 is re-orientated toward the S1 binding site (**Figure 1.12**, step 3). The proton is subsequently released in the periplasmic vestibule *via* a water molecule (**Figure 1.12**, step 4). (Nygaard *et al.,* 2006).

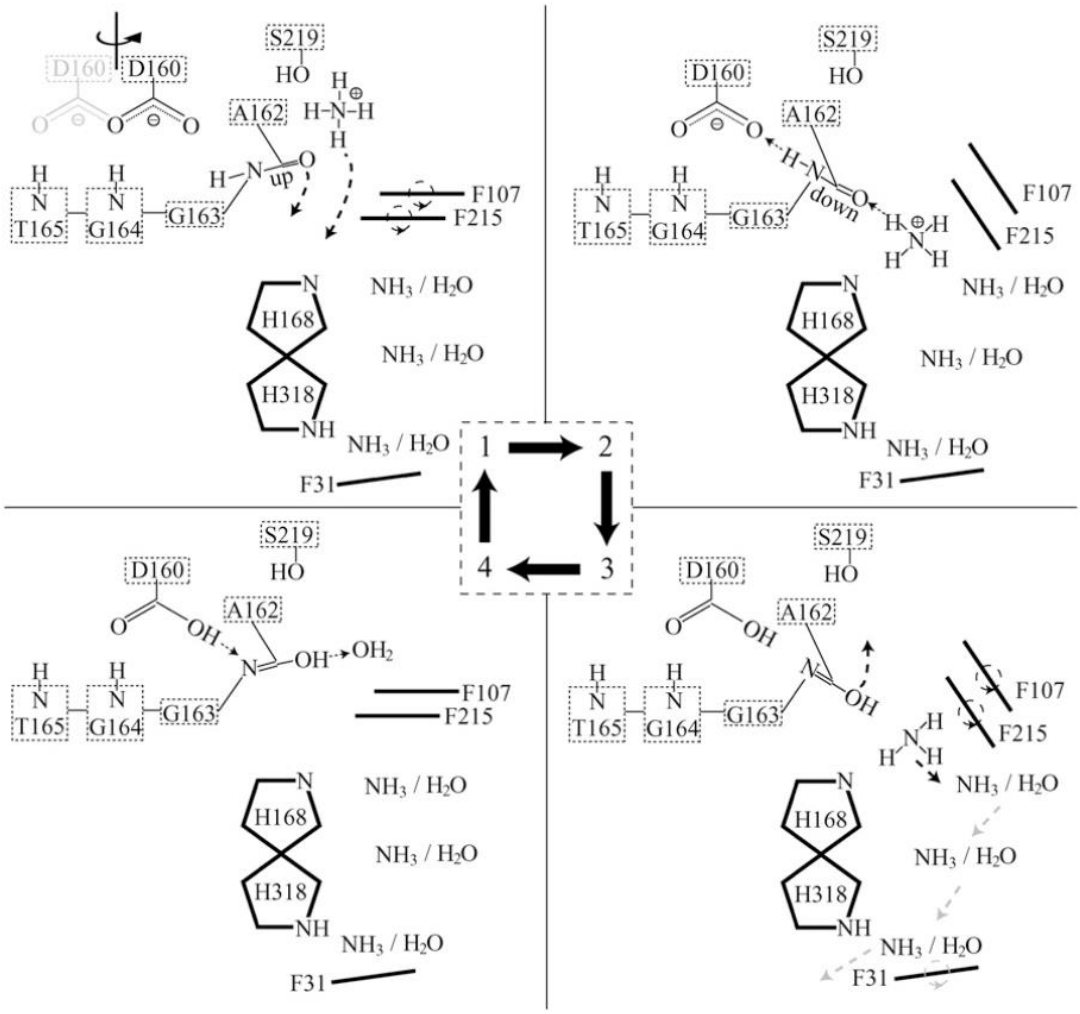

Figure 1.12 Molecular dynamic simulation of NH_4^+ deprotonation *via* Asp160 (Figure from Nygaard *et al.,* 2006).

Using MD simulations, it has been shown that a wire composed of 3 water molecules was present inside the pore of AmtB (position S2-S4, **Figure 1.6**) (Lamoureux *et al*., 2007). Using potential mean force calculations, the authors have suggested that the deprotonation occurs at the S2 site. Two mechanisms have been proposed 1- deprotonation *via* the His168 residue, and transfer of the proton in the lumen *via* the twin-His motif or 2- deprotonation by the water molecule present in the vicinity of the S2 site and transfer of the proton in the lumen through the water wire *via* a Grotthuss mechanism (Lamoureux *et al*., 2007).

However, in 2013, a study combining MD with functional assays (using growth experiments or MeA uptake) challenged the hypothesis of deprotonation *via* the His168 residue. Numerous variants of the twin-His motif of AmtB and Mep2 from *S. cerevisae* were analysed. AmtB His168Ala or His318Ala variants and Mep2 His194Ala or His348Ala variants were capable to complement the growth defect of a yeast *⊿MEP* strain on minimal medium containing 1 mM of ammonium as sole nitrogen source but were unable to transport MeA (Wang *et al*., 2013). This apparent discrepancy in between growth analysis and MeA uptake was explained by MD simulations (Wang *et al*., 2013). The hydrophobic environment created by a substitution of the His168 to an Ala residue allows MeA, but not ammonium, to form a hydrogen bond with the His318 residue (Wang *et al.,* 2013). This explained why the variant cannot translocate MeA but is still active when ammonium is use as a substrate (Wang *et al.,* 2013). It was concluded that His168 is not essential for AmtB activity, hence for NH_4^+ deprotonation. This work also emphasised that MeA is not a suitable substrate to answer mechanistic questions concerning AmtB function (Wang *et al*., 2013).

1.4.2.3 Free energy calculation: conduction of NH_3 versus NH_4^+

Using free energy calculations, it was shown that positions S2, S3 and S4 (**Figure 1.6**), were thermodynamically extremely unfavourable for NH_4^+ ($\triangle G_{deprotonation} < 103$) (Bostick and Brooks, 2007). In agreement, an energetic barrier of ~10 kcal/mol for NH_4^+ compared to NH_3 was calculated at position S3-S4 (Luzhkov *et al.*, 2006). These results strongly suggest that NH_3 is translocated through the hydrophobic pore. Subsequent MD simulation studies, using the same approaches, agreed with this hypothesis (Yang *et al*., 2007, Lamoureux *et al*., 2007, Wang *et al*., 2010).

Aims and objectives of the PhD project

As discussed, the plethora of functional and MD simulation studies aimed at elucidating the mechanism of ammonium transport by the Amt/Mep/Rh proteins has led to considerable controversy. Several high resolution structures of Amt/Mep/Rh proteins have been solved but unfortunately the high expectations to elucidate the transport mechanisms from these structures have not been met to date. All the structures are very similar when generated in the presence or absence of ammonium and show the same inward-facing state of the proteins. Hence, the exact mechanism of ammonium transport by Amt/Mep/Rh proteins remains largely elusive and controversial. In this context, the aim of my PhD project was to elucidate the transport mechanism of the Amt protein and establish whether the mechanism is conserved through the Amt/Mep/Rh family. To achieve my aim, I have exploited the tractable model systems AmtB of *E. coli* and subsequently extended the studies to the Rh50 protein from *N. europaea* and Mep2 from *S. cerevisiae*. A multidisciplinary and integrated approach, combining molecular genetics, biochemistry, biophysics, electrophysiology and computational biology has been used to fulfil the four specific objectives presented in the **Chapters 3-6**:

1- Combine small angle Neutron/X-ray scattering (SANS/SAXS) and molecular dynamic (MD) simulation to gain structural information of AmtB in solution.

2- Characterise the general mechanism of AmtB using Solid Supported Membrane Electrophysiology (SSME).

3- Elucidate the mechanism of ammonium conduction using SSME and MD simulation.

4- Explore the functional role of the lipid environment on AmtB activity.

Chapter 2: Materials and Methods

2.1 Molecular biology

2.1.1 Media preparation

Bacterial strains and media composition used during this work are presented in **Table 2.1** and **2.2** respectively.

All media were autoclaved at 121ºC for 15 minutes and antibiotic solutions filtered with a 0.22 µm filter (**Table 2.1**).

2.1.2 Chemically competent cells preparation

A single colony of the appropriate strain was inoculated in 5 mL LB and grown overnight at 37ºC under shaking. The next day 100 mL of LB medium were incubated with 1 mL of the overnight culture and grown for 2 hours at 37ºC until OD_{600} reached 0.5. The culture was then transferred to sterile centrifuge tubes and after incubation for 30 min on ice, the cells were pelleted. The supernatant was removed and the cells re-suspended in 30 mL of ice cold sterile 0.1 M $CaCl_2$ and left on ice for 30 min, after which a second centrifugation step was performed. The cells were re-suspended in 8 mL ice cold 0.1 M $CaCl_2$ + 15% glycerol, snap-frozen in liquid nitrogen and stored at -80ºC.

2.1.3 Heat-shock transformation

0.1 µg of the plasmid DNA was added to 50 µL of competent cells, incubated for 15 minutes on ice and heat-shocked at 42ºC for 45 seconds and left on ice for 5 minutes. 1 mL of LB was added and the cells were incubated for at least

1.5 hours at 37^{o}C before they were plated on LB medium supplemented with the appropriate antibiotic (**Table 2.2**) and incubated overnight at 37^{o}C.

Table 2.1: Genotype of *E.coli* bacterial strains used.

Strain	Genotype	Reference
DH5α	F– Φ80lacZΔM15 Δ(lacZYA-argF) U169 recA1 endA1 hsdR17 (rK–, mK+) phoA supE44 λ– thi-1 gyrA96 relA1	(Hanahan, 1983)
BL21 (DE3)	F- ompT gal dcm lon hsdSB(rB- mB-) λ(DE3) pLysS(cmR)	(Studier *et al.,* 1990)
C43 (DE3)	F- ompT gal dcm lon hsdSB (rB -mB -) λ(DE3)	(Miroux *et al.,* 1996)
GT1000	*rbs lacZ::IS gyrA hutCK ΔglnKamtB*	(Coutts *et al.,* 2002)

Table 2.2: Media preparation.

Name of the medium	Composition	Reference
ZYP-5052	1 mM MgSO4 2% (v/v) 50x5052 5% (v/v) 20xNPS	Studier, 2005
ZY	10 g/L N-Z amine 5 g/L yeast extract	
50x5052	0.5 M $(NH_4)_2SO_4$ 1 M KH_2PO_4 1 M Na_2HPO_4	
20xNPS	25% (w/v) glycerol 2.5% (w/v) glucose 10% (w/v) lactose	
Luria Bertani	10 g/L tryptone 5 g/L yeast extract 10 g/L NaCl	Sambrook *et al.*, 1989
Terrific Broth	12 g/L tryptone 24 g/L yeast extract 10% (v/v) salt solution	Tartof, 1987
Salt solution	0.16 M KH_2PO_4 0.54 M K_2HPO_4	
M9 Minimum media	0.2% (v/v) glucose 0.2 mg/mL glutamine 1 mM $MgSO_4$	Elbing and Brent, 2002
M9 medium	6 g/L Na_2HPO_4 3 g/L KH_2PO_4 0.5 g/L NaCl	
Ampicillin Chloramphenicol Kanamycin	100 µg/ml 34 µg/ml (in ethanol) 34 µg/ml	

2.1.4 Plasmid DNA purification

Cells were grown overnight in LB supplemented with the appropriate antibiotics (**Table 2.2**) and plasmids were purified using QIAprep Miniprep Kit® (Qiagen) according to manufacturer's instructions. Briefly, cells were pelleted by centrifugation and lysed under alkaline conditions. Lysates were separated from cell debris by centrifugation and subsequently DNA was bound to the QIAprep silica membrane. RNA and proteins were washed off of the column using high salt buffer. Finally, DNA plasmid was eluted in water.

2.1.5 Site directed mutagenesis

The site directed mutagenesis was done using QuikChange II Multi Site-Directed Mutagenesis kit (Agilent Technologies), according to the manufacturer's instructions. The mutant constructions made and primers used are listed **Table 2.3** and **2.4**. Briefly, after PCR, the template DNA was digested with 10 Units of DpnI enzyme at 37ºC for 30 minutes and the amplified plasmid transformed into XL10-Gold cells.

Table 2.3: Plasmids used for this study.

Plasmids	Antibiotic marker	Reference
pET22b (+)	Ampicilin	Novagen
pET28a (+)	Kanamycin	Novagen
pDR195	Ampicilin	(Rentsch *et al*., 1995)
pZheng (pET22b-AmtB(His)6)	Ampicilin	(Zheng *et al*., 2004)
pAJ2024 (AmtB(His)6 S219A)	Ampicilin	(Javelle *et al*., 2008)
pAJ2039 (AmtB(His)6 H168D)	Ampicilin	(Javelle *et al*., 2006)
pAJ2035 (AmtB(His)6 S219A/F107A/W148A)	Ampicilin	(Javelle *et al*., 2008)
pDA7 (pESV2-*Ne*Rh50(His)6)	Chloramphenicol	(Cherif-Zahar *et al*., 2007)
pGDM1 (pZheng-AmtBTEV(His)6)	Ampicilin	this study
pGDM2 (pZheng-AmtBH168A/H318A)	Ampicilin	this study
pGDM3 (pZheng-AmtBH168D/H318E)	Ampicilin	this study
pGDM4 (pZheng-AmtBD160A)	Ampicilin	this study
pGDM5 (pZheng-AmtBD160E)	Ampicilin	this study
pGDM6 (pAJ2024-AmtBS219A/H168A/H318A)	Ampicilin	this study
pGDM7 (pDR195-S219A)	Ampicilin	this study
pGDM8 (pDR195-H168D)	Ampicilin	this study
pGDM9 (pDR195-D160A)	Ampicilin	this study
pGDM10 (pDR195-D160E)	Ampicilin	this study
pGDM11 (pDR195-H168D/H318E)	Ampicilin	this study
pGDM12 (pDR195-H168A/H318A)	Ampicilin	this study
pGDM13 (pDR195-S219A/H168A/H318A)	Ampicilin	this study
pGDM14 (pZheng-AmtBN72A)	Ampicilin	this study
pGDM15 (pZheng-AmtBN79A)	Ampicilin	this study

Table 2.4: Primers used for this study.

Primer	Direction	Nucleotide sequence
*Ec*AmtB H168A	Forward	GGTGGCACCGTGGTGGCCATTAACGCCGCAATC
*Ec*AmtB H368A	Forward	TGTCTTCGGTGTGGCCGGCGTTTGTGGCATT
*Ec*AmtB H168D	Forward	GGTGGCACCGTGGTGGATATTAACGCCGCAATC
*Ec*AmtB H368E	Forward	TGTCTTCGGTGTGGAGGGCGTTTGTGGCATT
*Ec*AmtB D162A	Forward	CTCACGGTGCGCTGGCCTTCGCGGGTGGCACC
*Ec*AmtB D162E	Forward	CTCACGGTGCGCTGGAGTTCGCGGGTGGCACC
*Ec*AmtB N72A	Forward	CGTTTGGTGAGGGCGCCAACTTCTTCGGCAA
*Ec*AmtB N79A	Forward	TCTTCGGCAACATTGCCTGGTTGATGCTGAA
*Ec*AmtB TEV seq	Reverse	CTGAAAATACAAGTTCTCCGCGTTATAGGCATTCT CGCCGTGGCTGTTGACATC
*Ec*AmtB TEV seq	Forward	AACTTGTATTTTCAGGGCGAACAAGCACAACAGCC GGCCCAGGCTGATCTCGAGC
*Ec*AmtB XhoI cleaving site	Forward	AGTCCTCGAGATGAAGATAGCGACGATAAAA
*Ec*AmtB BamHI cleaving site	Reverse	AGTCGGATCCTCACGCGTTATAGGCATTCTC

Nucleotides mutated/added from the original sequence are in red

2.1.6 Cloning AmtB for expression in yeast

We used the plasmid pDR195 (Rentsch *et al.*, 1995) to express *amtB* in yeast. AmtB expression is under the control of the promoter of the housekeeping plasma membrane ATPase gene PMA1.

20 ng of plasmid DNA from pZheng, pAJ2024, pAJ2039, pGDM2, pGDM3, pGDM4, pGDM5 and pGDM6 constructions (**Table 2.3**) were amplified by PCR reaction using KOD Hotstart DNA polymerase (Merck Millipore) according to the manufacturer's instructions. The primers AmtB XhoI and BamHI (**Table 2.4**) were used for the PCR reaction. After the PCR, 1 µg of amplified DNA products and 2 µg of pDR195 vector (**Table 2.3**) were digested using XhoI and BamHI (Promega Corporation) (5 units of enzyme/µg of DNA) at 37°C for 1h. Digested DNA samples were run on 2% agarose gels in TAE buffer (**Table 2.5**) at 100V/cm for 1 hour. The DNA was extracted from the gel using the kit Wizard® SV Gel and PCR clean-up system (Promega Corporation) according to the manufacturer's protocol. For the ligation reaction, 50 ng of digested insert and vector (pDR195) DNA were mixed to an insert:vector molar ratio of 5:1. T4 DNA ligase (Promega) was used to ligate the digested insert and vector DNA. The reaction volume was 10 µL and the ligation reaction was done overnight at 4°C. Finally, 5 µL of ligated product was transformed into DH5α using the Heat-shock technique (**see section 2.1.3**).

Table 2.5: Buffer composition used for this study.

Name of the buffer	Composition
Resuspension buffer	50 mM Tris-HCl pH 8 500 mM NaCl 10% Glycerol 160 µM phenylmethylsulfonyl fluoride 10 µg/ml DNase
Solubilisation buffer	50 mM Tris-HCl pH 8 500 mM NaCl 10% Glycerol 2% DDM or 2% LDAO
Buffer A IMAC	50 mM Tris-HCl pH 8 500 mM NaCl 10% Glycerol 0.03% DDM or 0.09% LDAO
Buffer B IMAC	50 mM Tris-HCl pH 8 500 mM NaCl 10% Glycerol 500 mM Imidazole 0.03% DDM or 0.09% LDAO
Buffer A IMAC TEV	50 mM Tris-HCl pH 8 300 mM NaCl 10% Glycerol
Buffer B IMAC TEV	50 mM Tris-HCl pH 8 300 mM NaCl 10% Glycerol 500 mM Imidazole
Buffer gel filtration	50 mM Tris-HCl pH 7.8 100 mM NaCl 0.03% DDM or 0.09% LDAO
Stripping solution	100 mM EDTA 500 mM NaCl
Nickel solution	100 mM $NiSO_4$
Cobalt solution	100 mM $CoCl_2$
10% SDS-PAGE Resolving gel (for 2 gels)	32.5% (v/v) 30% Acrylamide/0.8% bis-Acrylamide 25% (v/v) Solution 2 SDS-PAGE 41.4% (v) H_2O 1% (v/v) of 10% ammonium persulfate 0.1% (v/v) TEMED
12.5% SDS-PAGE Resolving gel (for 2 gels)	41% (v/v) 30% Acrylamide/0.8% bis-Acrylamide 25% (v/v) Solution 2 SDS-PAGE 32.9% (v/v) H_2O 1% (v/v) of 10% ammonium persulfate 0.1% (v/v) TEMED

SDS-PAGE Stacking gel (for 2 gels)	15% (v/v) 30% Acrylamide/0.8% bis-Acrylamide 30% (v/v) Solution 3 SDS-PAGE 60% (v/v) H_2O 1% (v/v) of 10% ammonium persulfate 0.1% (v/v) TEMED
Solution 2 SDS-PAGE	1.5 M Tris-HCl pH 8.8 0.3% SDS
Solution 3 SDS-PAGE	0.5 M Tris-HCl pH 6.8 0.3% SDS
10X running buffer pH 8.3	30 g/LTris-base 144 g/L glycine 1% (w/v) SDS
Loading blue 6X	2% SDS 10% glycerol 0.001 bromophenol blue 0.0625 M Tris-HCl pH 6.8 5% β-mercaptoethanol
Staining buffer	0.1% Coomassie Brilliant blue R-250 50% methanol 10% acetic acid
Destaining buffer	40% methanol 10% acetic acid
2% agarose gel	20 g/L of agarose TAE buffer 1 µg/ml of ethidium bromide
TAE buffer	40 mM Tris-HCl 20 mM acetic acid 1 mM EDTA
Liposome buffer	100 mM potassium phosphate pH 7.6 300 mM KCl
Non-activated solution	100 mM potassium phosphate 300 mM KCl
Activated solution	100 mM potassium phosphate 100 mM KCl 200 mM $NH_4^+Cl^-$ / 200 mM Methylammonium/ 200 mM NaCl
Non-activated solution sodium	100 mM sodium phosphate 300 mM NaCl
Activated solution sodium	100 mM sodium phosphate 100 mM NaCl 200 mM $NH_4^+Cl^-$ / 200 mM Methylammonium/ 200 mM KCl 200 mM NH4+Cl- / 200 mM Methylammonium/ 200 mM KCl

2.2 Protein over-expression and purification

2.2.1 *E.coli* AmtB

2.2.1.1 Over-expression

AmtB(His_6), cloned into the pET22b vector (**Table 2.3**), was overproduced in the C43(DE3) strain. A single colony containing pET22b-AmtB was used to inoculate an overnight culture of LB (**Table 2.2**). The next morning, twelve litres of the auto induction medium ZYP-5052 (**Table 2.2**), were inoculated at OD_{600} 0.02 using the overnight culture, grown at 30 °C, 210 rpm for 19 hrs and harvested at 7,000 x g (JLA9.1000 rotor, Beckman), 4°C for 30 min. The cell pellet was washed and resuspended (10 mL of buffer/g of cells) using resuspension buffer (**Table 2.5**).

2.2.1.2 Membrane preparation

E. coli membranes were isolated according to (Blakey *et al.*, 2002). Cells were broken by three passage through a French press (20 kpsi). The outer membrane and unbroken cells were pelleted by centrifugation at 23,000 x g, 4 °C for 40 min (JA30-50 rotor, Beckman). The supernatant was then removed and the inner membrane was collected by ultracentrifugation at 170,000 x g, 4 °C for 1.5 hrs (Ti60/Ti45 rotor, Beckman). The membranes were stored at -20 °C.

2.2.1.3 Immobilised metal affinity chromatography

The membrane was solubilised using solubilisation buffer to a ratio 0.1 mg/mL (**Table 2.5**) for 2 hrs at 4°C under gentle agitation and the non-solubilised material was collected by ultracentrifugation (170,000 x g, 4 °C) for 45 minutes.

To reduce the DDM concentration, which could harm the protein, the solubilised membrane was diluted 2 times with IMAC buffer A (**Table 2.5**) and loaded on to an IMAC column (Hitrap HP 1mL, Ge Healthcare) using an ÄKTA pure FPLC system (Ge Healthcare). The resin was previously loaded with cobalt and equilibrated with IMAC Buffer A with detergent (**Table 2.5**). The hexa-histidine tag at the C-terminal tail of AmtB interacts with the cobalt by electron coordination. AmtB was purified in DDM at a final concentration of 0.03% (w/w).

The protein was eluted from the IMAC column by increasing the concentration of imidazole gradually. Imidazole acts as a competitive inhibitor binding to cobalt, thus preventing the sharing of electrons between cobalt and the histidine-tag (Bornhorst and Falke, 2000). Elution fractions were collected with a fraction collector and the absorbance at 280 nm was monitored during the purification. Elution fractions were loaded on a 10% sodium dodecyl sulfate polyacrylamide (SDS) gel to monitor the presence of AmtB. Elution fractions containing AmtB were pooled and concentrated to 5 mg/mL and further purified by size-exclusion chromatography (Superdex 200).

2.2.1.4 IMAC column regeneration

IMAC columns were regenerated by sequentially passing 5 column volume (CV) of water, stripping solution, water, nickel or cobalt solution, water and finally 20% ethanol. The compositions of these solutions are described (**Table 2.5**).

2.2.1.5 Size exclusion chromatography

Size-exclusion chromatography allows the separation of proteins as a function of their hydrodynamic property. The column used was a Superdex S200 15/30 GL (Ge Healthcare) which can resolve proteins with a molecular mass from 600 to 10 kDa. The calibration of the column was performed using the standards kit from Biorad containing bovine thyroglobulin (670 kDa), bovine γ-globulin (158 kDa), chicken ovalbumin (44 kDa), horse myoglobin (17 kDa) and vitamin B_{12} (1.35 kDa). The size-exclusion chromatography was performed in gel filtration buffer (**Table 2.5**) using an ÄKTA pure purification system (Ge Healthcare).The elution fractions were analysed on a SDS-PAGE gel to confirm the presence of AmtB and assess the purity of the samples. AmtB was concentrated to 10 mg/mL and kept at 4°C.

2.2.2 *N. europaea* Rhesus protein 50

2.2.2.1 Over-expression of the *N. europaea* Rhesus protein 50

*Ne*Rh50(His_6) cloned into the pDA7 vector (**Table 2.3**), was overproduced in the GT1000 strain (**Table 2.1**). A single colony of GT1000 containing pDA7 (**Table 2.3**) was used to inoculate an overnight culture in LB (**Table 2.3**). The next morning, 12 litres of M9 minimum medium (**Table 2.2**), were inoculated at OD_{600} 0.02 using the overnight culture, grown at 30 °C, 210 rpm for 19 hrs and harvested at 7,000 x g (JLA9.1000 rotor, Beckman) 4°C for 30 min. The cell pellet was washed and resuspended (10 mL of buffer/g of cells) using resuspension buffer (**Table 2.5**).

The protocols used for membrane preparation and purification of the *Ne*Rh50 protein were strictly the same as the purification of AmtB with the only

exception that the detergent used was 0.09% (w/w) of n-Dodecyl-N, N-Dimethylamine-N-Oxide (LDAO) (**Table 2.5**).

2.2.3 Tobacco Etch Virus (TEV) cysteine protease

2.2.3.1 Over-expression of the Tobbaco Etch Virus (TEV) cysteine protease

TEV(His_7) cloned into the pET22b vector (**Table 2.3),** was overproduced in the Rosetta (DE3) pLysS strain. A single colony of Rosetta (DE3) pLysS containing pET22b-TEV(His_7) was used to inoculate an overnight culture of LB (**Table 2.3**). The next morning, 2 litres of LB medium (**Table 2.2**), were inoculated at OD_{600} 0.02 using the overnight culture. After reaching an OD_{600} 0.4, 1 mM of IPTG was added to the cultures to induce the TEV overexpression at 25°C, 210 rpm for 19 hrs and harvested at 7,000 x g (JLA9.1000 rotor, Beckman) 4°C for 30 min. The cell pellet was washed and resuspended (10 mL of buffer/g of cells) using resuspension buffer (**Table 2.5**). The cytosolic fraction was collected after high-speed centrifugation at 23,000 x g, 4 °C for 40 min (JA30-50 rotor, Beckman).

2.2.3.2 Purification

The cytosolic fraction was loaded on to an IMAC column (Hitrap HP 1mL, Ge Healthcare). The resin was previously loaded with nickel and equilibrated with Buffer A IMAC TEV (**Table 2.5**). The protein was eluted from the IMAC column by increasing the concentration of imidazole gradually. IMAC chromatography was performed using an ÄKTA pure purification system (Ge Healthcare). Elution fractions were collected with a fraction collector and the absorbance at 280 nm was monitored during the purification. Elution fractions were loaded on

a 10% SDS-PAGE to monitor the presence of TEV. Elution fractions containing TEV protein were pooled, concentrated to 5 mg/mL then diluted with buffer IMAC A TEV (**Table 2.5**) in order to reduce the quantity of imidazole. The TEV protein was concentrated to 5 mg/mL, aliquoted, snap-frozen with liquid nitrogen and stored at -80°C.

2.2.6 SDS-PAGE

The principle of SDS-PAGE was previously described by (Laemmli, 1970). Briefly, a SDS-PAGE gel (Biorad MiniPROTEAN® cell) was used to monitor the presence of proteins in elution fractions and to assess the purity of our samples. Sodium dodecyl sulfate (SDS) is an anionic detergent which denatures and negatively charges proteins. The proteins linearised by SDS separates according to their molecular mass. The sample was mixed with the loading buffer and loaded onto the gel (**Table 2.5**). The gels were run at 27V/cm for 1 hour, stained 30 min and destained for 3 hours. The composition of the buffers are described in **Table 2.5**.

2.2.7 Determination of the Protein concentration

Protein concentration was determined using the 280nm specific absorbance related to the presence of aromatic amino-acids. The molar extinction coefficient was determined based on the amino-acid sequence of the protein and by using the online informatics tool ExPASy ProtParam (Gasteiger *et al.*, 2005). The absorbance at 280nm was measured using a Nanodrop 2000/2000c spectrophotometer (ThermoFisher Scientific) and the concentration of the protein was determined using Beer-Lambert law. The extinction molar coefficients used to calculate protein concentrations are given in **Table 2.6**.

Table 2.6: Properties and amino-acids sequence of the protein over-expressed.

Protein name	Main sequence	MW (KDa)	Epsilon (L.mol-1.cm-1)	Reference
*Ec*AmtB	APAVADKADNAFMMICTALVLFMT IPGIALFYGGLIRGKNVLSMLTQVT VTFALVCILWVVYGYSLAFGEGNN FFGNINWLMLKNIELTAVMGSIYQ YIHVAFQGSFACITVGLIVGALAER IRFSAVLIFVVVWLTLSYIPIAHMV WGGGLLASHGALDFAGGTVVHIN AAIAGLVGAYLIGKRVGFGKEAFK PHNLPMVFTGTAILYIGWFGFNAG SAGTANEIAALAFVNTVVATAAAIL GWIFGEWALRGKPSLLGACSGAI AGLVGVTPACGYIGVGGALIIGVV AGLAGLWGVTMLKRLLRVDDPCD VFGVHGVCGIVGCIMTGIFAASSL GGVGFAEGVTMGHQLLVQLESIAI TIVWSGVVAFIGYKLADLTVGLRV PEEQEREGLDVNSHGENAYNAE QAQQPAQADLEHHHHHH	44.4	66140	Uniprot number: C3TLL2 (Apweiler *et al*., 2004)
*Ne*Rh50	MSKHLCFTAFSSIALFLLCFSSWA SAVAPAEINEARLVAQYNYSINILA MLLVGFGFLMVFVRRYGFSATTG TYLVVATGLPLYILLRANGIFGHAL TPHSVDAVIYAEFAVATGLIAMGA VLGRLRVFQYALLALFIVPVYLLNE WLVLDNASGLTEGFQDSAGSIAIH AFGAYFGLGVSIALTTAAQRAQPI ESDATSDRFSMLGSMVLWLFWP SFATAIVPFEQMPQTIVNTLLALCG ATLATYFLSALFHKGKASIVDMAN AALAGGVAIGSVCNIVGPVGAFVI GLLGGAISVVGFVFIQPMLESKAK TIDTCGVHNLHGLPGLLGGFSAILI VPGIAVAQLTGIGITLALALIGGVIA GALIKLTGTTKQAYEDSHEFIHLA GPEDEHKAERLVLEAKTEIQGLKN RIDAAVLSAKSEG	44.6	38515	Uniprot number: Q82X47
TEV	GHHHHHHHGESLFKGPRDYNPIS STICHLTNESDGHTTSLYGIGFGP FIITNKHLFRRNNGTLLVQSLHGVF KVKNTTTLQQHLIDGRDMIIIRMPK DFPPFPQKLKFREPQREERICLVT TNFQTKSMSSMVSDTSCTFPSSD GIFWKHWIQTKDGQCGSPLVSTR DGFIVGIHSASNFTNTNNYFTSVP KNFMELLTNQEAQQWVSGWRLN ADSVLWGGHKVFMVKPEEPFQP VKEATQLMNRRRRR	28.6	32095	

2.3 Liposomes/proteoliposomes preparation

2.3.1 Lipids preparation

All lipid stock solutions (Avanti polar lipids) were dried out first under nitrogen flow for 1 hour and subsequently 2 hours under vacuum in a desiccator. The dried lipid films were rehydrated in liposome buffer (**Table 2.5**) at 5 mg/mL to form multilamellar liposomes.

2.3.2 Liposomes formation

The multilamellar liposomes were extruded 13 times using a Mini-extruder (Avanti polar lipids) mounted with a 0.1 µm filter pore (Avanti polar lipids) to obtain a unimodal size distribution solution of unilamellar liposomes.

2.3.3 Determination of the R_{sat} and R_{sol} constants for AmtB reinsertion

Optimal insertion of membrane proteins into liposomes occurs upon destabilisation of liposomes using detergent (triton X-100 in this study), at a detergent/lipid ratio between the onset of solubilisation, R_{sat} and the total solubilisation, $R_{sol,}$ of the lipids (Rigaud *et al.*, 1995, Rigaud *et al.*, 1988, Rigaud, 2002, Paternostre *et al.*, 1988). The addition of detergent disrupts lipid-lipid interactions, which results in a more permeable bilayer and these structures are more receptive to protein insertion. The turbidity of the lipososmes solution increases as the lipososme become more saturated with detergent, until R_{sat} is reached, then decreases until the total solubilisation of the lipids is achieved (R_{sol}). Hence, to determine the R_{sat} and R_{sol} constants of the lipososmes, 1 µL Triton X-100 at 25% was sequentially added to 500 µL of

liposomes (5 mg/mL) and the absorbance at 400 nm was measured. The optimum amount of Triton X-100 for protein insertion was determined to be 1 µL of Triton X-100 at 25% (w/v) per mg of lipid.

2.3.4 Insertion of the membrane protein into the liposomes

AmtB/*Ne*Rh50/*Sc*Mep2 (5 mg/mL) was mixed with the liposomes/Triton X-100 mixture at a lipid:protein ratio (LPR) of 5:1, 10:1 or 50:1 (**see Chapter 4**) and incubated for 30 minutes under gentle agitation at 4°C. The Triton X-100 was removed by adsorption onto hydrophobic beads (SM-2 Biobeads, BioRad) to allow the insertion of AmtB/*Ne*Rh50/*Sc*Mep2 inside the lipid bilayer (Galián *et al.*, 2011). The biobeads were prepared according to the manufacturer's instructions and added to a beads:detergent ratio (w/w) of 20. The biobeads were incubated at 4°C under gentle rotation for 2 hours, removed and new biobeads were added and the mixture left on a rotating wheel overnight at 4°C.

2.3.5 Proteoliposomes washing step by ultra-centrifugation

After the overnight incubation with SM-2 Biobeads, the proteoliposomes were diluted 10 times in the liposome buffer (**Table 2.5**), collected by ultracentrifugation at 200,000 g, 4ºC for 30 minutes, re-suspended in 6 mL of liposome buffer (**Table 2.5**) and the operation repeated two times. Finally, the proteoliposomes were resuspended in 500 µL of liposome buffer (5 mg/mL of lipids), aliquoted in 100 µL and stored at -80ºC.

2.3.6 Size determination by Dynamic Light Scattering

The average diameter of the liposome solution was determined using a Zetasizer Nano ZS (Malvern instruments). The technique uses the principle of

Dynamic Light Scattering that was previously described by the Stokes-Einstein equation regarding the relationship between the size and the diffusion of a particle (von Smoluchowski, 1906, Sutherland, 1905, Einstein, 1905). The motion of the particle was directly recorded *via* static light scattering detectors placed at certain angles. An auto-correlation function was used in order to determine the particle size distribution (Malvern instruments). The refractive index and absorption set up for liposomes during the data acquisition were 1.490 and 0.010 respectively.

2.3.7 Orientation of the protein inserted in the liposomes

2.3.7.1 Orientation of the protein using purification matrix

To examine the orientation of AmtB inserted in the liposomes, we analysed the proteoliposomes by IMAC (Vitrac *et al.*, 2013). If all AmtB proteins are inserted in a right-side-out (RSO) orientation in a liposome, all the C-terminal affinity tag should not be accessible, hence the proteoliposomes should flow through the IMAC matrix. By contrast, if an AmtB protein is inserted inside-out (IO) in the proteoliposomes, then the His-tag should be accessible and the proteoliposomes are expected to bind the matrix and thus be present in the elution fraction. As a control, we treated the proteoliposomes in parallel with DDM to solubilise AmtB and analyse it by IMAC using identical conditions as for the analysis of the proteoliposomes without DDM. For the analysis, 160 µL of proteoliposomes (5 mg/mL) treated with or without 2% DDM were incubated with 100 µL of Ni-affinity resin (Ni-Sepharose High Performance, GE healthcare) at 4ºC for 1 hour. The supernatant was collected after centrifugation and the resin was washed 4 times using 50 µL of non-activated buffer (**Table 2.6**). The proteoliposomes were eluted in NA buffer containing 500 mM imidazole. 15 µL of each fraction was mixed with 5 µL of loading blue buffer and analysed by SDS-PAGE.

2.3.7.2 Orientation of the protein using TEV protease

Another method to determine the orientation of AmtB in the proteoliposomes is to treat them using the TEV protease according to the procedure previously described (Wacker *et al.,* 2014). AmtB proteins containing a TEV cleavable site inserted between the C-terminal tail and the His tag (plasmid pGDM1, **Table 2.3**) was inserted into liposomes according to the procedure described in 2.3.1. The proteoliposomes were treated with the TEV protease to a ratio of 5:1 (w/w) overnight at 4°C with 2 mM of β-mercaptoethanol. As a control the same digestion experiment was done using pure AmtB protein and proteoliposomes solubilised by 1.25% of Triton X100. If AmtB is orientated right-side-out (RSO), the TEV protease will not have access to the TEV-cleavable site, however, if AmtB is orientated inside-out (IO), the TEV protease will cleave the hexa-hisitidin tag (~20 amino-acids lacking) leading to the shortening of the protein.15 µL of each digestion sample was mixed with 5 µL of loading blue buffer and analysed by a gel gradient SDS-PAGE (Novex™ 4-20% Tris-Glycine Mini Gels, ThermoFisher Scientific).

2.4 Protein functional assays

Membrane proteins solubilised in detergent have a tendency to lose their activity, thus to ensure AmtB retains activity two techniques have been used during this study: MicroScale Thermophoresis (MST) and Solid Supported Membrane Electrophysiology (SSME) on the protein solubilised in detergent or reconstituted in liposomes.

2.4.1 MicroScale Thermophoresis

MicroScale Thermophoresis technology (Baaske *et al.*, 2010) was used to measure the AmtB-ammonium binding affinity. The experiments were performed using a Monolith NT.115 and Monolith NT.LabelFree (NanoTemper Technologies). AmtB was labelled with the kit Monolith His-Tag Labeling Kit RED-tris-NTA according to the manufacturer's instructions (NanoTemper Technologies). AmtB (110 µM) was mixed with 98 µL of gel filtration buffer (**Table 2.5**) containing 16 different NH_4^+ concentrations ranging from [6.1 µM to 200 mM] and loaded into 16 hydrophobic coating grade capillaries. The K_d calculated from the MST measurement has been obtained using the MO.Affinity Analysis software v2.2.4 (NanoTemper Technologies).

2.4.2 Solid supported membrane electrophysiology (SSME)

Principle of the assay: the proteoliposomes are adsorbed to a solid supported membrane (SSM) on a gold coated sensor chip of 3 mm, forming an electrode. AmtB/*Ne*Rh50/*Sc*Mep2 activity was measured by a fast solution exchange without and with substrate. If AmtB/*Ne*Rh50/*Sc*Mep2 activities are electrogenics it is generated a charge translocation which can be measured at the electrode *via* capacitative coupling. The maximum amplitude of the signal was used for Michaelis-Menten analysis while the shape of the transient was used to calculate the turnover rate of transport.

2.4.2 1 Preparation of the sensors

3-mm gold coated sensors were prepared according the procedure described by Nanion Technologies GmbH. 50 µL of 0.5 mM octadecanethiol prepared in iso-propanol was used to coat a thiol layer on the gold surface of the sensor for 30 minutes. The sensors were rinsed three times with 10 mL of iso-propanol

and 10 mL of deionised water. Sensors were dried by tapping them on a tissue and 1.5 µL of 1,2 diphytanoyl-sn-glycerol-3-phosphocholin (7.5 µg/µL, prepared in n-decane) was applied to the gold surface. The sensor was immediately filled with non-activated solution at pH 7 (**Table 2.5**) in order to form the solid supported membrane. The proteoliposomes were defrosted and sonicated in a sonication bath (U300H Ultrawave Precision ultrasonic cleaning) at 35 Watts for 1 minute. The proteoliposomes were diluted 10-fold using a non-activated solution at pH 7. 10 µL of the diluted proteoliposomes solution was applied to the sensor. Sensors with proteoliposomes were centrifuged at 2500 g for 30 minutes prior to the measurement. The sensors were stable for 3 days at 4ºC.

2.4.2.2 Measurement and signal analysis

The sensors' quality was checked by determining their capacitance and conductance as if the SSM is not formed correctly, the capacitance and conductance values are close to the pure gold sensor (~75nF and ~40nS respectively). However, for sensors with an ideal SSM the capacitance and conductance values should be ~15-30nF and <5nS respectively. When the parameters did not fulfil these requirements, the sensors were discarded. The activities of AmtB/*Ne*Rh50/*Sc*Mep2 were measured by sequentially passing 200 µL of a non-activated (NA) and activated (A) solution that contained the substrate to be tested (**Table 2.5**). At the end of the measurement, the sensor was rinsed automatically with 1 mL of NA solution.

2.4.2.3 Kinetics

A serial dilution in between the non-activated and activated solution was made to obtain an activated solution containing an ammonium/methylammonium concentration ranging from 98 µM to 200 mM. The maximum amplitude of the signal measured at each ammonium concentration was fitted according to the Michael-Menten kinetics and the kinetics parameters (K_m, V_{max}) were determined using the software Graphpad PRISM v6.

2.4.2.4 Decay time

The decay time of the exponential phase of the transient current, which is proportional to the velocity of the complete transport turnover, was measured by fitting the raw data to a one phase exponential decay function (**equation 2.1**) from the maximum height of the peak up to the plateau region (**Figure 2.1**) using the software OriginPro 2017 (OriginLab).

$$y = y_0 + A_1 e^{-x/t_1} \qquad (\mathbf{2.1})$$

Where y is the amplitude in (nA), y_0 is the maximum amplitude, x is the time in seconds, t_1 the rate constant. The decay time value (λ) = 1/ t_1.

The different transient currents were normalised and a comparison based on their peak shape was done.

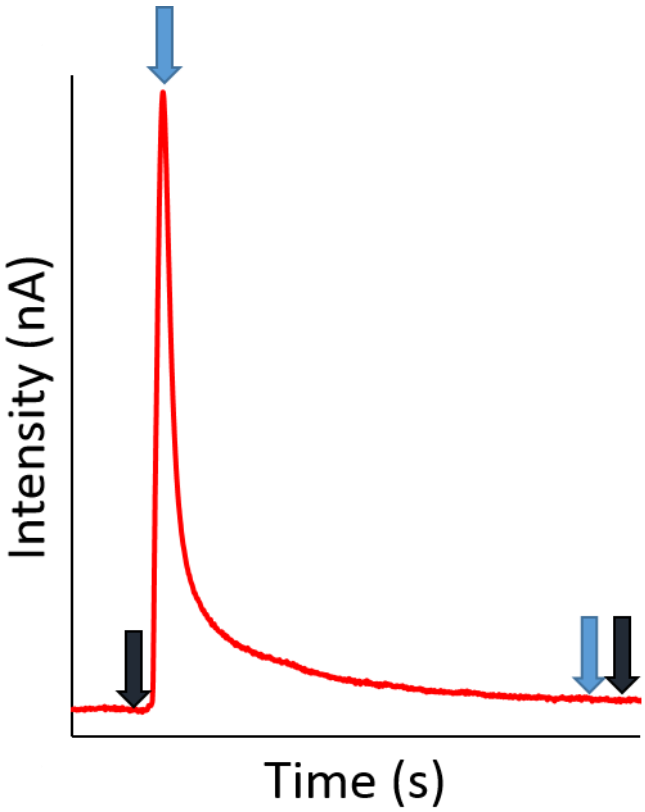

Figure 2.1 Typical electrophysiological current recorded during the experiment. Blue arrows represent the area used for the exponential decay time measurement, black arrows represent the area used for the integral calculation.

2.4.2.5 Current reconstruction

The transient current measures both pre-steady and steady state current (**see Chapter 4**), however, as outlined by Mager and collaborators, the current can be mathematically reconstructed, by analysing the system as an electrical circuit (Mager *et al.*, 2011). By using the **equation 2.2**, it is possible to extract $I_p(t,V_p)$ which is the steady state current of the transporter from I(t) which is the pre-steady state and steady state combined (**Figure 2.2**)**.**

$$I_p(t,0) = (1 + \frac{C_p}{C_m})\left\{I(t) + (k_0 + k_\infty)\int_0^t I(t)dt\right\} \qquad (\mathbf{2.2})$$

The term (k_0+k_∞) was simplified to 1/t_1 (Mager *et al.*, 2011).

The integral from (*t*,0) has been calculated using OriginPro 2017 (OriginLab) by setting the area from the beginning of the maximum peak current up to the plateau baseline (**Figure 2.1**).

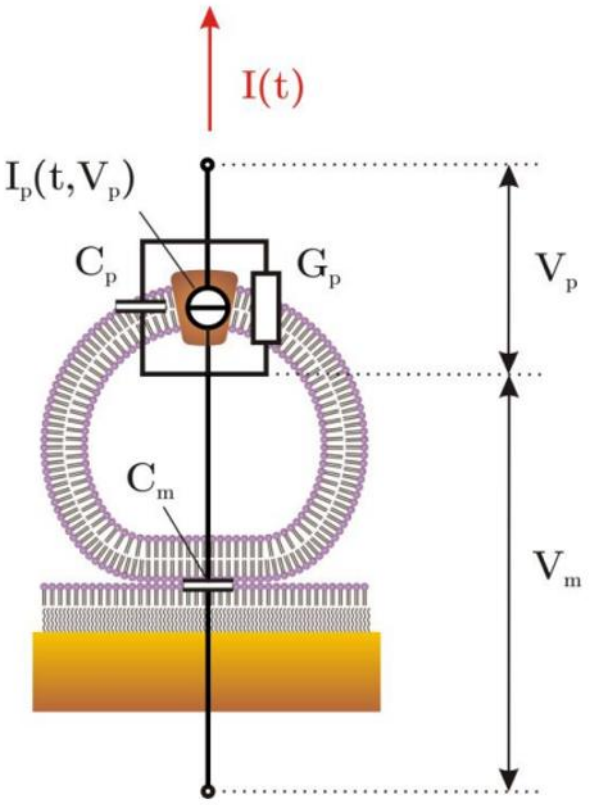

Figure 2.2 Schematic representative of a proteoliposome adsorbed on a SSM layer. The different electric parameters used for the current reconstruction are displayed in the figure (Mager *et al*., 2011).

2.5 Protein biophysical characterisation

2.5.1 Size exclusion chromatography multiple angle light scattering (SEC-MALS)

SEC-MALS analysis of the AmtB-DDM complex was carried out using Superdex 200 10/300 column (Ge Healthcare) mounted on an Agilent 1100 HPLC system. 70 µL of AmtB at 75 µM in gel filtration buffer (**Table 2.5**) was injected at a flow rate of 0.5 mL/min. Light scattering, refraction index and absorbance at 280 nm were measured using a multi angle light scattering mini DAWN TREOS detector (Wyatt Technology), a refractometer Optilab T-rEX detector (Wyatt Technology) and a Jasco UV-2077 Plus UV/vis spectrophotometer (Jasco, GmbH) respectively. We used the ASTRA software package version 5.3.2.10 (Wyatt Technologies) to import the signals from the three detectors and analysed the data according to (Slotboom *et al.*, 2008). The dn/dc used for the AmtB was calculated from its amino-acid sequence (**Table 2.6**).

2.5.2 Analytical Ultra-Centrifugation

AmtB at 10, 22 and 87 µM was submitted to sedimentation velocity using a Beckman Coulter Optima XL-I analytical ultracentrifuge mounted with an An-50 Ti 4-hole rotor (49000 rpm at 4°C). The reference buffer used was the gel filtration buffer (**Table 2.5**) without detergents. Data were acquired every 6 min for 12 hrs, with interference and absorbance optics and were subsequently analysed using SEDFIT (Schuck, 2000) with the continuous c(s) distribution model. SEDNTERP was used to determine the molar mass (46647 g/mol) and the partial specific volume (0.749 mL/g) of AmtB. The partial specific volume of DDM used was 0.82 mL/g. The viscosity (1.567 cP) and the density (1.00557 g/mL) of the gel filtration buffer (**Table 2.5**) were determined using

SEDNTERP. The ratio of detergent bound to the protein and the molecular weight of the complex were calculated using a method described previously (Ebel, 2011).

2.6 Small Angle Scattering

2.6.1 Theory

The elastic scattering of an X-ray/neutron beamline by biological macromolecules can be described as illustrated **Figure 2.3**. The SAS patterns are typically represented as the logarithm of scattered intensity as a function of the magnitude of the scattering vectors.

The s is defined by the **equation 2.3**

$$s = \frac{4\pi \sin\theta}{\lambda} \qquad (\mathbf{2.3})$$

Where *s* is the scattering vector, 2θ the scattering angle and λ the wavelength of the X-ray/neutron used (Blanchet and Svergun, 2013).

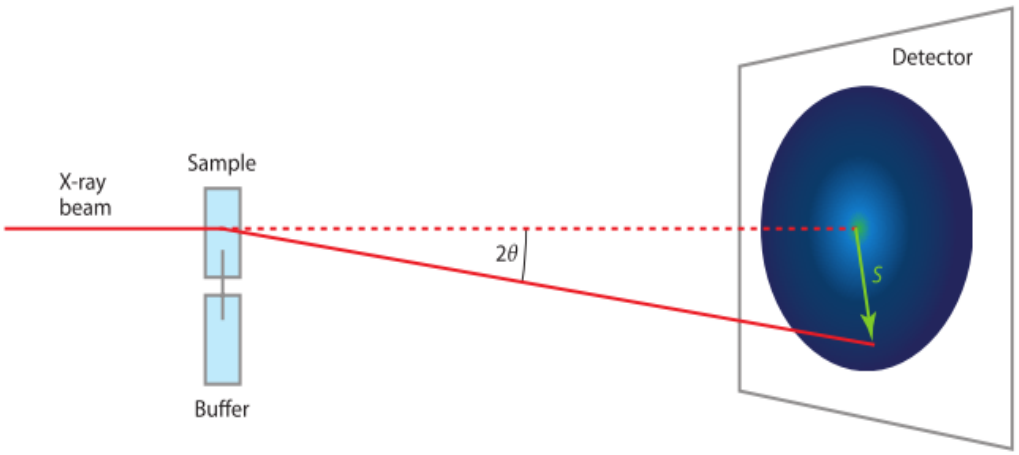

Figure 2.3 Set up of a classic Small Angle X-ray scattering experiment (Blanchet and Svergun, 2013).

2.6.2 Size exclusion chromatography coupled with small angle X-ray scattering (SEC-SAXS)

SEC-SAXS experiments were conducted at 25ºC at the B21 beamline at Diamond Light Source (Didcot, U.K.). The light source generates 10^{11} photons/second with a wavelength (λ) in between 0.0038 to 0.42 $Å^{-1}$. The detector was set up at a fixed distance of 4.014 meters. 45 µL of AmtB sample (111 µM) in 0.03% DDM was injected in a size-exclusion chromatography column (Superdex S200 10/300, GeHealthcare) at a flow of 0.05 mL/min. 15 frames of the elution peak corresponding to the membrane protein were averaged and subtracted from the running buffer using ScÅtter software. 57 frames corresponding to the buffer curve were averaged prior to the subtraction. SAXS data were collected in 255 time frames with 3 s per frame (13 min in total). The scattering images were averaged and the buffer scattering intensities subtracted using the program ScÅtter and the same program was used to evaluate the radius of gyration (R_g). The data-collection parameters are presented in **Table 2.7** (Dias Mirandela *et al.*, 2018).

Table 2.7: Collection parameters for SANS and SEC-SAXS experiment.

	from SEC-SAXS	**from SANS batch**
Instrument/data processing	B21 BioSAXS Diamond Light Source synchrotron beamline (UK)	D22 beamline Institut Laue-Langevin Neutron source with a multidetector (3He) 16K resolution elements
Beam geometry (mm)	1 X 5	55 x 40
Camera length (m)	4.014	4/4 offset
Flow (ml/min)	0.05	N/A
Wavelength (Å)	0.99	4.5 < λ/Å < 40 (for Δλ/λ = 10 %)
s range ($Å^{-1}$)[a]	0.0022 to 0.42	0.045 to 0.4
Exposure time (s)	3 (every 5 seconds)	~3600 to 10800/sample
Sample configuration		cell path of 1 mm
Concentration range ($mg \cdot mL^{-1}$)	see main text	see main text
Temperature (K)	298	279.15

2.6.3 Small Angle Neutron Scattering

2.6.3.1 Data acquisition and reduction

To ascertain the reproducibility and the quality of our measurements, two independent sets of SANS data were measured (September 2016 and March 2018) using two batches of AmtB purified independently. SANS experiments were conducted at 6^0C using the large dynamic range diffractometer D22 at the Institut Laue-Langevin (Grenoble, France) in Hellma® quartz cuvettes 100QS with 1 mm optical pathlength. 300 µL of samples at a concentration of 110 µM were extensively dialysed (3 times 12 hrs) against the size-exclusion chromatography buffer (50 mM Tris pH 7.8, 100 mM NaCl, 0.03% DDM and D_2O as required) and used for the SANS experiment. The final dialysis buffer was used in the SANS experiment as the reference and subtracted from the protein signal. The samples were recorded at a 4 m/4 m detector/collimator distance, using a neutron wavelength of 6 Å. For each condition, H_2O/D_2O buffers, the empty beam, an empty quartz cuvette as well as a boron sample (electronic background) were measured. Exposure times varied between 20 min (empty cell, boron) and 3 hours for the protein samples and buffers. Transmissions were measured for 1 min. The raw data were reduced (detector efficiency, electronic background and angular averaging) using a standard ILL software package. Finally, the corrected scattered intensities $I(Q)$ ($Q=(4\pi/\lambda)\sin\theta$, where 2θ is the scattering angle, from the different Q-ranges and the respective buffer signals were subtracted using the program PRIMUS from the ATSAS suite (Franke *et al*., 2017). The data-collection parameters are presented in **Table 2.7**.

2.6.3.2 Contrast match point determination

The contrast match point of DDM was experimentally determined by measuring SANS contrast series of DDM (5 mg/mL) at 0, 20, 40, 60, 80 and 100 % D_2O and used to plot $(I(0)/(T_sC))^{1/2}$ as a function of percentage of D_2O in the solvent (T_s is the measured sample transmission). The DDM contrast match point (22.2%) was determined by the intersection of a linear fits through all points with the abscissa as previously described (Compton *et al*., 2011).

2.6.4 Overall parameters

2.6.4.1 Guinier approximation

The Guinier approximation (**equation 2.4**) equation was used to determine the gyration radius (R_g) at small *s* values of the small angle scattering data by assuming that $s \times R_g < 1.3$ (Rice, 1956).

$$I(Q) \approx I(0)\exp\left(-\frac{1}{3}R_G^2 Q^2\right) \qquad (\mathbf{2.4})$$

Q is the wave vector. I is the scattering intensity and I(0) is the forward scattering intensity at Q=0.

2.6.4.2 GNOM

The software GNOM was used to generate the pair distance distribution function P(r) using an indirect Fourier transformation (Svergun, 1992). The D_{max} used was equal to 3 times the R_g estimated by Guinier approximation.

2.6.5 *Ab-initio* modelling

2.6.5.1 DAMMIN

To obtain low resolution models using the small angle scattering data, the program DAMMIN was used (Svergun, 1999). P1 and P3 symmetry fold were used and spherical, oblate or prolate volumes were imposed during the modelling runs. All the other parameters of the DAMMIN software were set up by default.

2.6.5.2 Memprot

In order to visualise the position of the DDM corona around AmtB, an *ab-initio* model has been generated using the software memprot (version 1.7) and by following the procedure previously described by (Berthaud *et al.,* 2010). The two experimental input files used were the AmtB crystal structure 1U7G (Khademi *et al.,* 2004) and the SAXS data. The following searching parameters were set up according to (Berthaud *et al.*, 2012) (**Figure 2.4**). In this modelling, the geometrical parameters used were: a = 29 – 39 Å (1 Å/step), b = 34 – 44 Å (1 Å/step), t = 5 – 7 Å (0.5 Å/step), e = 1.100 – 1.200 Å (0.01 Å/step). The best model had the following settings: a = 33 Å, b = 35 Å, t = 6 Å, e = 1.090 (**Figure 2.4**). The chi^2 of the best model against the experimental X-ray scattering data was 1.9.

The molecular weight of the DDM corona in the memprot model was calculated by subtracting the molecular weight of the trimeric AmtB from the total molecular weight of the protein-detergent complex obtained using CRYSOL (Svergun *et al.*, 1995). The molecular weight of the trimeric form of AmtB was estimated using the amino-acid sequence. It was estimated that 326 DDM molecules were forming the corona around the AmtB trimer.

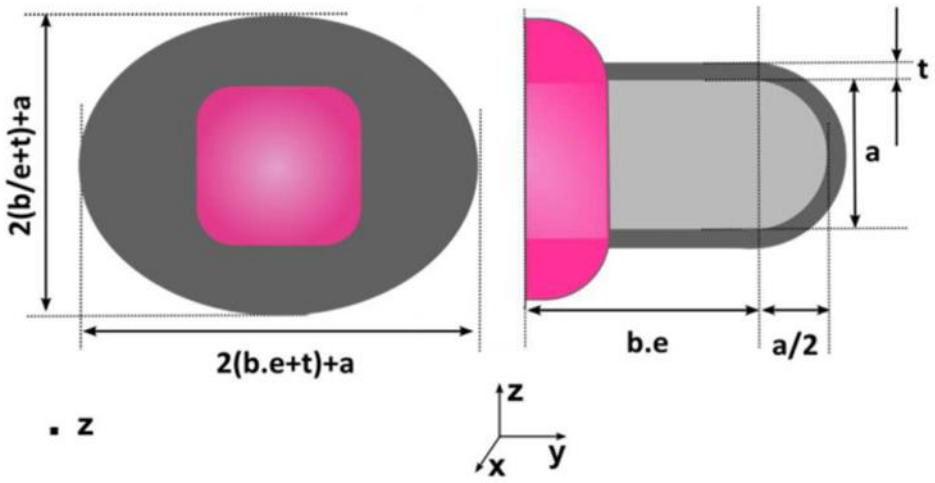

Figure 2.4 Schematic representation of the different parameters used during the detergent torus modelling by the software Memprot (Berthaud *et al*., 2012).

2.6.5.3 MONSA

The multiphase volumetric analysis using MONSA (Reyes *et al.*, 2014, Svergun, 1999) (extended version of DAMMIN) was used to obtain a three phase dummy atom model of the AmtB-DDM complex reporting the protein, DDM head and DDM tail phases respectively. The analysis was done using all SAS (SAXS and SANS at 0, 22, 42 and 60 % D_2O) data. The parameters used for the analysis were **1-** the volume of the AmtB trimer (calculated from the amino acid sequence using the *Biomolecular Scattering Length Density Calculator* available on line (http://psldc.isis.rl.ac.uk/Psldc). The volume obtained was 166,864 $Å^3$ **2-** the volume of the 320 molecules of DDM head and tail (112,000 $Å^3$ and 108,800 $Å^3$ respectively) (Breyton *et al.*, 2013). The SEC-MALS, AUC and SAXS analysis shows that AmtB is trimeric (**see Chapter 3**), hence a P3 symmetry constraint was applied. The MONSA analysis (200 annealing steps) was done using DAMESV (Reyes *et al.*, 2014, Svergun, 1999) models. At least 10 models were generated, superimposed and checked for constituency. All models were very similar in size and shape for all three phases.

Chapter 3: In solution structural analysis of AmtB

Aim and objectives

Structural characterisation of membrane transporters currently relies mainly on high-resolution structures, which in some cases do not account for their conformational changes. This is particularly true for Amt proteins as all the structures published so far did not reveal any obvious conformational differences when generated in the presence or absence of ammonium. In-solution small angle x-ray and neutron scattering (SAXS/SANS) have become popular methods to characterise the structure of membrane proteins solubilised by detergents. Hence, the aim of the study presented in this chapter was to develop an approach to obtain structural information of AmtB in solution. The novelty of the methology is to combine SAXS and SANS data analysis. The specific objectives were to:

1- Solubilise AmtB in the detergent DDM and quantify the detergent present in the corona surrounding the transporter.
2- Use SAXS data and *ab-initio* modelling to obtain models of the AmtB-DDM complex in solution.
3- Conduct molecular dynamic simulations to obtain atomistic models of the AmtB-DDM complex and use the information obtained in objectives 1 and 2 to validate a plausible atomistic model.
4- Combine SAXS and SANS data and conduct a multiphase analysis to obtain structural information on the phase density of the detergent surrounding AmtB.

I would like to point out that the majority of the results presented in this chapter have been published in *The Journal of Physical Chemistry Letters* (see **appendix A**):

> **Dias Mirandela G**, Tamburrino G, Ivanović MT, Strnad FM, Byron O, Rasmussen T, Hoskisson PA, Hub JS, Zachariae U, Gabel F, Javelle A. (2018) Merging In-solution X-Ray and Neutron Scattering Data

Allows Fine Structural Analysis of Membrane-protein Detergent Complexes. *J. Phys. Chem. Lett.* **9**:3910–14

3.1. Introduction

The predominant view is that Amt proteins act as electrogenic transporters for ammonium, whereas Rh proteins act as passive NH_3 (ammonia) channels. From a functional perspective, the catalytic cycle of transporters (Amt-like) involves selective binding of the substrate and subsequent conformational changes to translocate the substrate against its electrochemical gradient. On the other hand, channels (Rh-like) facilitate the translocation of the substrate down the electrochemical gradient, which involves relatively little energetic interaction between the channel protein and its substrate and no major conformational rearrangement (Andrade and Einsle, 2007, Wirén and Merrick, 2004). There are no significant differences in the crystal structures of Amt and Rh protein that can clearly account for the functional differences between a transporter-like and a channel-like activity. Moreover, the structures of Amts proteins did not reveal any obvious conformational differences when generated in the presence or absence of ammonium (Khademi *et al.*, 2004, Zheng *et al.*, 2004, Javelle *et al*., 2007) whereas compelling evidence points towards a conformational rearrangement associated with the translocation cycle. Ammonium-fluorescent sensors were developed by inserting circularly-permutated GFP into extra-loops of plant and yeast Amt/Mep proteins (De Michele *et al.*, 2013). Pulses of ammonium to yeast cells expressing these sensors triggered a variation of the fluorescence intensity, indicating structural rearrangement of Amt/Mep proteins (De Michele *et al.*, 2013). Additionally, the existence of open and closed states for Amts and Mep has been substantiated by demonstrating allosteric feedback inhibition of transport activity by phosphorylation of the cytosolic C-terminus (van den Berg *et al.*, 2016, Loqué *et al.*, 2007). However, to date, no structural data are available to describe these conformational changes. Thus, it is timely to explore a new approach

and extend the reach of new and rapidly developing biophysical techniques to solve the fundamental mechanistic questions about the Amt/Mep/Rh protein family. In this chapter, I will present a new methodological approach, combining low resolution structural techniques such as Small Angle x-ray Scattering and Small Angle Neutron Scattering (SAXS/SANS) coupled with atomistic molecular dynamic simulations to obtain structural information on AmtB in solution.

3.2 Purification of AmtB from *E. coli*

Small Angle Scattering (SAS) experiments are very demanding in terms of sample quality (Trewhella *et al.*, 2017, Jeffries *et al.*, 2016), therefore, before recording SAS data, I ascertained that our samples were monodisperse and that AmtB was pure, stable and critically, active in detergent.

3.2.1 Immobilised Metal Affinity Chromatography

AmtB was overexpressed in *E. coli* C43(DE3) cells and the membrane fractions were isolated and solubilised in 2% DDM. After ultracentrifugation, the supernatant was loaded on a Histrap column loaded with cobalt (**see Chapter 2** for technical details). The column was washed with 10 mL of IMAC A buffer (**see Table 2.5, Chapter 2**) containing 40 mM imidazole in order to wash out unspecific proteins bound. AmtB was subsequently eluted using a constant imidazole gradient [40-500 mM] over 20 mL. The elution fractions were analysed on a SDS-PAGE gel to assess the presence and purify of AmtB in the sample (**Figure 3.1, insert**). The absorbance at 280 nm on the chromatograph indicated that AmtB bound to the column started to elute between 100 to 200 mM of imidazole (**Figure 3.1**). SDS-PAGE gel analysis revealed one major band, between 100-130 kDa in the elution fraction. This band represents ~90% of the total amount of protein indicating a good purity

of AmtB. The theoretical molecular weight of AmtB monomer is around 44 kDa hence these data suggested that AmtB runs as a trimer in the SDS-PAGE gel. It should be noted that anomalous migration of membrane proteins on SDS-PAGE is common and is likely due to the anomalous SDS-loading capacity and partial unfolding of the hydrophobic domains (Rath *et al.*, 2009).

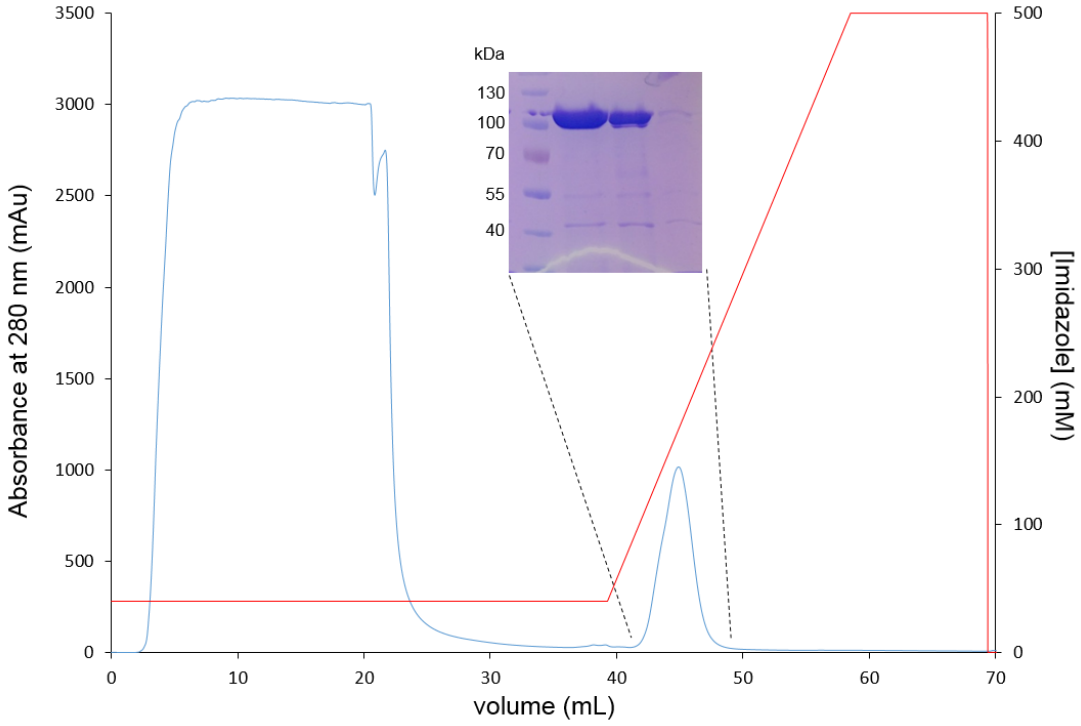

Figure 3.1 Purification of AmtB by IMAC. A_{280nm} (blue), imidazole concentration (red). (***Insert***) 12.5% SDS-PAGE analysed of the fractions present under the elution peak.

3.2.2 Size exclusion chromatography

After the IMAC purification, the elution fractions containing AmtB were collected, concentrated to 5 mg/mL and injected on a Superdex 200 10/300 size-exclusion chromatography (SEC) column. The SEC elution profile shows that there is no protein present in the void volume showing no sign of protein aggregation. A single symmetrical peak was observed indicating that the sample is monodisperse (**Figure 3.2**). The fractions under the elution peak were analysed by SDS-PAGE gel revealing that the sample was pure (**Figure 3.2**). The second protein band observed at around 55 kDa corresponds to AmtB monomer (**Figure 3.2 insert**). To ascertain AmtB stability, the SEC analysis was repeated after each SAS experiment (~12 days after the first size-exclusion chromatography) **(Figure 3.2**). The chromatograms before and after the SAS experiments were identical Indicating that AmtB was stable throughout the SAS data acquisitions (see **section 3.4 and 3.6**).

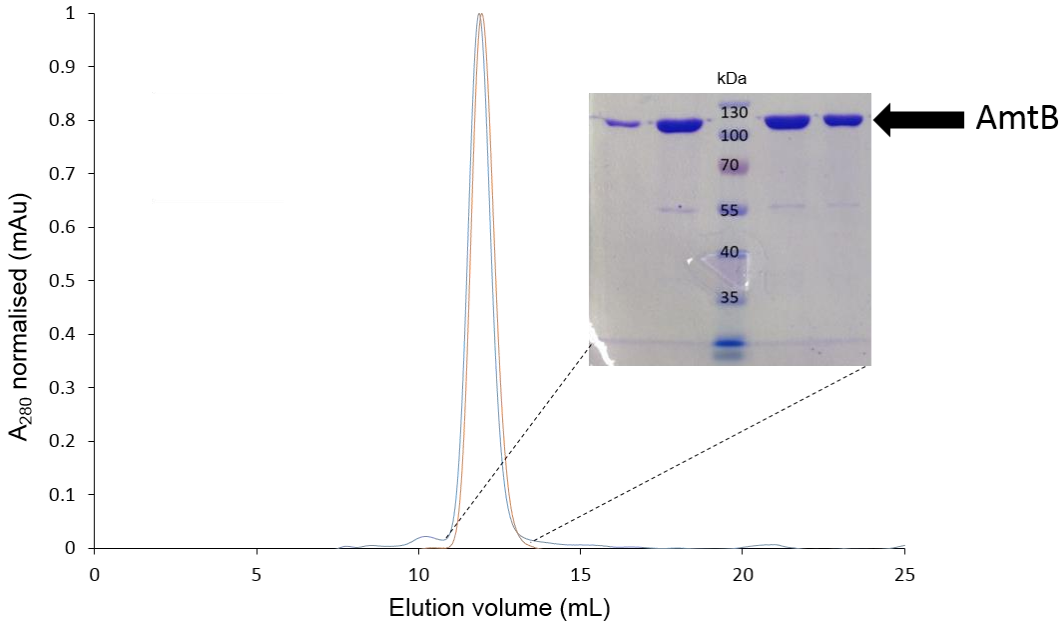

Figure 3.2 Size exclusion chromatography profile of AmtB solubilised in 0.03% DDM before (blue) and after SAS experiment (orange). (***Insert***) 12.5% SDS-PAGE analysis of the fractions present under the peak.

3.2.3 Functional characterisation of AmtB using MicroScale Thermophoresis

Membrane proteins have a tendency to lose their activity when purified in detergent. Previous structural and functional studies have identified a binding site for NH_4^+ at the bottom of the periplasmic vestibule of AmtB (S1 site) (Khademi *et al.,* 2004, Zheng *et al.,* 2004). In order to ascertain that purified AmtB is correctly folded and active, I have measured NH_4^+ binding using microscale thermophoresis (MST). MST is a technique which measures the motion of particles under a temperature gradient (Jerabek-Willemsen *et al.*, 2014). Briefly, an infrared laser is used to create a microscopic temperature gradient of 2-6°C on the middle of the capillary containing the protein to be analysed. A fluorescence detector measures the movement of the protein in the microscopic temperature gradient. Upon ammonium binding, the hydration shell of AmtB changes which modifies the hydrodynamic properties of the protein, thus its movement in the microscopic temperature gradient. The change in AmtB movement is proportional to the ammonium concentration which allows the quantification of the binding affinity (Jerabek-Willemsen *et al.,* 2014).

For the MST measurements, 110 µM of AmtB was loaded on 14 capillaries previously loaded with a buffer containing different ammonium concentrations ranging from 6.1 µM to 200 mM. After placing the capillaries in the Monolith NT.115, the difference of the normalised fluorescence between the bound AmtB at various ammonium concentrations and unbound AmtB was used to generate a binding curve (**Figure 3.3**). The normalised fluorescence varied proportionally to the ammonium concentration (**Figure 3.3**). The data were fitted to a standard 1:1 binding model using MO.Affinity Analysis software v2.2.4 and a K_D of 0.6 mM was estimated. This result indicates that the purified AmtB seems correctly folded and active under my experimental conditions. However due to the difficulty of measuring a MST signal on membrane protein solubilised in detergent and in presence of substrate, the result presented only indicates a tendency for a K_D.

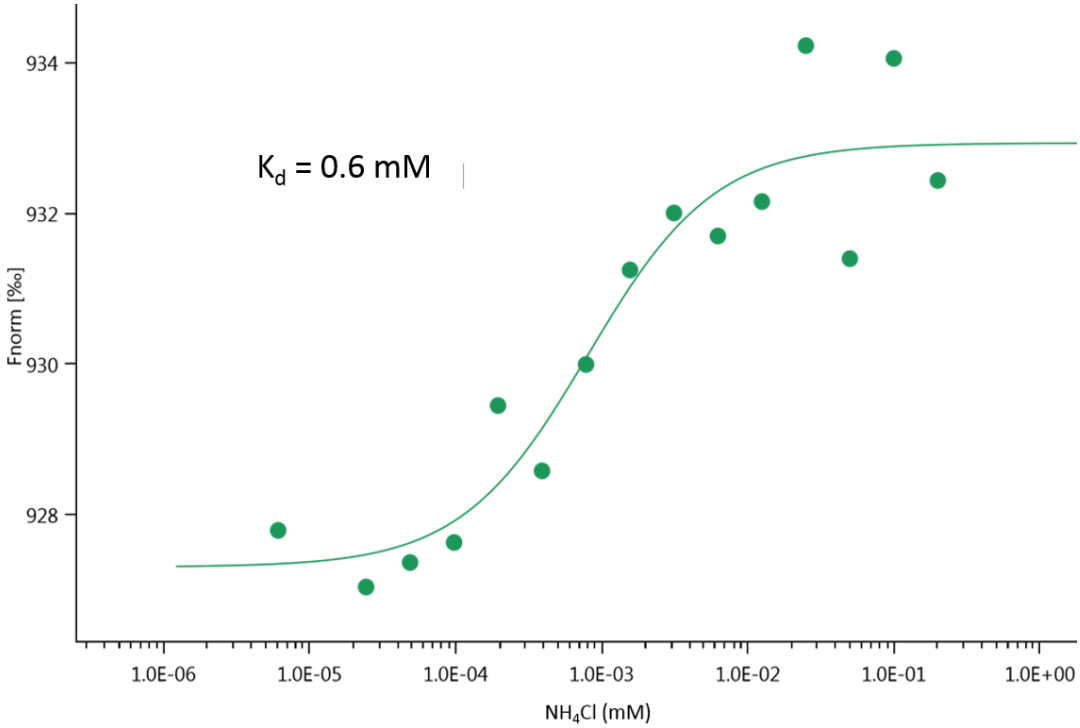

Figure 3.3 Determination of AmtB-NH_4^+ binding affinity in DDM using MicroScale Thermophoresis. The difference of normalised fluorescence induced by thermophoresis between AmtB in presence and in absence of substrate is plotted against ammonium concentration.

3.3 Biophysical characterisation of AmtB-DDM complex

A membrane protein purified in detergent is a complex sample containing the protein/detergent complexes (PDC), mixed micelles and detergent monomers. Unfortunately, SEC analysis is not sufficient to ascertain the mass monodispersity of the sample, the absolute mass of the PDC and the mass of the protein in the PDC, all these parameters being essential to analyse SAS data with confidence. To analyse the monodispersity and obtain the absolute mass of the PDC I have used two independent and complementary techniques: Analytical ultracentrifugation (AUC) and Size Exclusion Chromatography coupled with Multi-Angle Light Scattering measurements (SEC-MALS).

3.3.1 Size-exclusion chromatography multiple angle light scattering (SEC-MALS)

I will not describe here the SEC-MALS technology in detail, all the theoretical background and practical aspects of static light scattering analysis of membrane proteins have been remarkably reviewed in (Slotboom *et al.*, 2008). My sample containing AmtB was injected in a Superdex 200 10/300 in line with UV, light scattering (LS) and refractive index (RI) detectors. As previously observed (**Figure 3.2**), the absorbance at 280 nm displayed a single symmetrical peak (**Figure 3.4**). DDM does not absorb at 280 nm therefore no free DDM micelles are detected by UV. However, the excess DDM micelles are detected as a small peak at an elution volume of 14.5 mL by the RI and the LS detectors (**Figure 3.4**). The combine analysis of UV, RI and LS shows that the molecular weight of the AmtB-DDM complex (257.2 kDa) was constant within the elution peak. It also demonstrates that the molecular weight of AmtB in the complex is 144.4 kDa clearly indicating a trimeric oligomeric state and that the quantity of detergent in the AmtB-DDM complex represents 145 kDa which correspond to ~285 molecules of DDM (**Figure 3.4**).

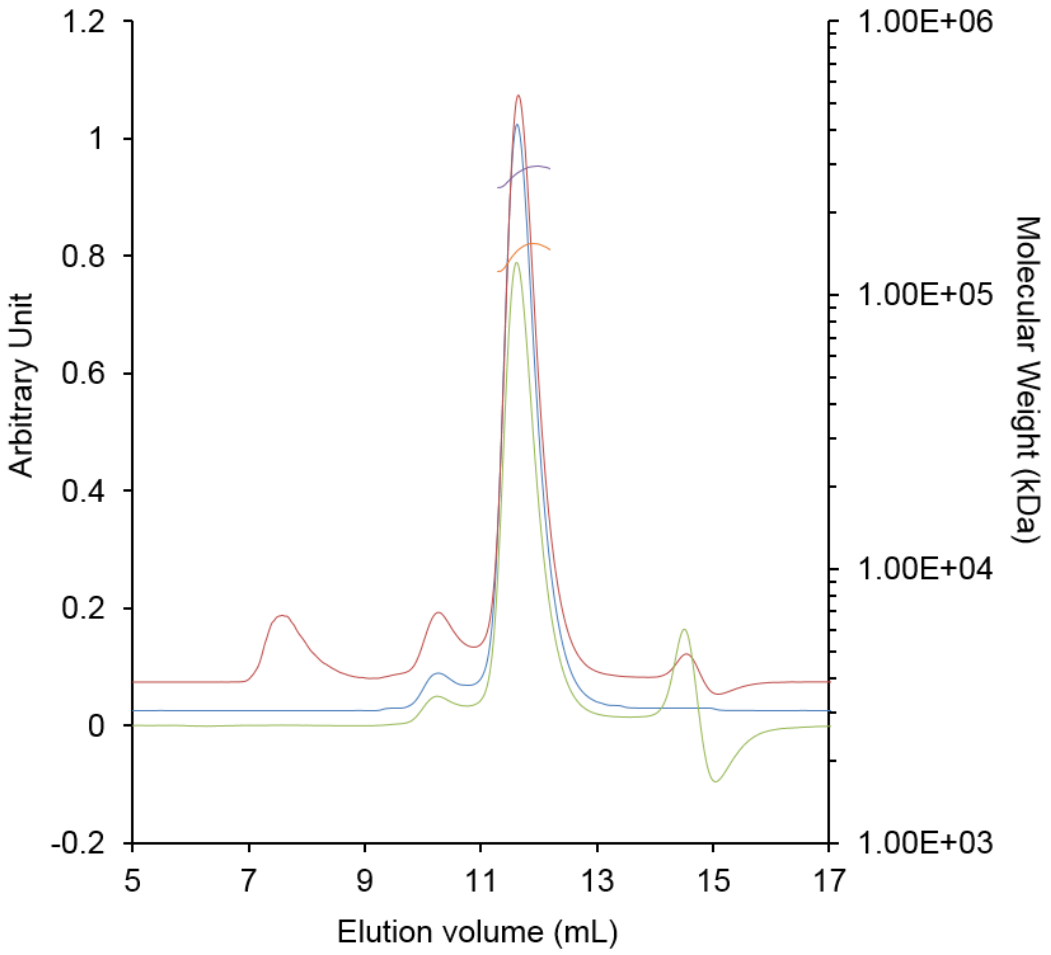

Figure 3.4 Size exclusion chromatography multiple angle light scattering analysis of AmtB solubilised in 0.03% DDM. A_{280nm} (blue), light scattering (red), refractive index (green), total molecular weight (purple) and the protein molecular weight (orange).

3.3.2 Analytical ultracentrifugation (AUC)

I have used AUC (sedimentation velocity) to independently obtain the absolute mass of the PDC. The absorbance at 280 nm and interference scans are presented **Figure 3.5**, panel A and B respectively. The residuals observed for both absorbance and interference were ~6% and well distributed around zero, indicating the good quality of the measurements and of the fit. After applying a continuous distribution of the Lamm equation to the different scans for the absorbance and the interference signals, a sedimentation coefficient at 20°C ($C_{w,20}$) in water was calculated **(Figure 3.5, panel C**). The ($C_{w,20}$) profiles obtained from the absorbance and the interference signals showed one major symmetrical peak at 10 $S_{20,w}$. The two additional peaks observed for the interference signal were due to a side-effect of the meniscus (25 $S_{20,w}$) or to free DDM detergent molecules (4 $S_{20,w}$) (Ebel, 2011). These result supported the view that AmtB behaves as a single and monodisperse biological particle in solution. The interference signal analysis (according to (Ebel, 2011)) allows calculation of the respective contribution of the protein and the detergent in the AmtB-DDM complex. I have determined that the PDC mass was 312 kDa, containing 148.8 kDa of AmtB (trimer) and 163.7 kDa of DDM (321 molecules) (**Table 3.1** and **section 3.3.3**).

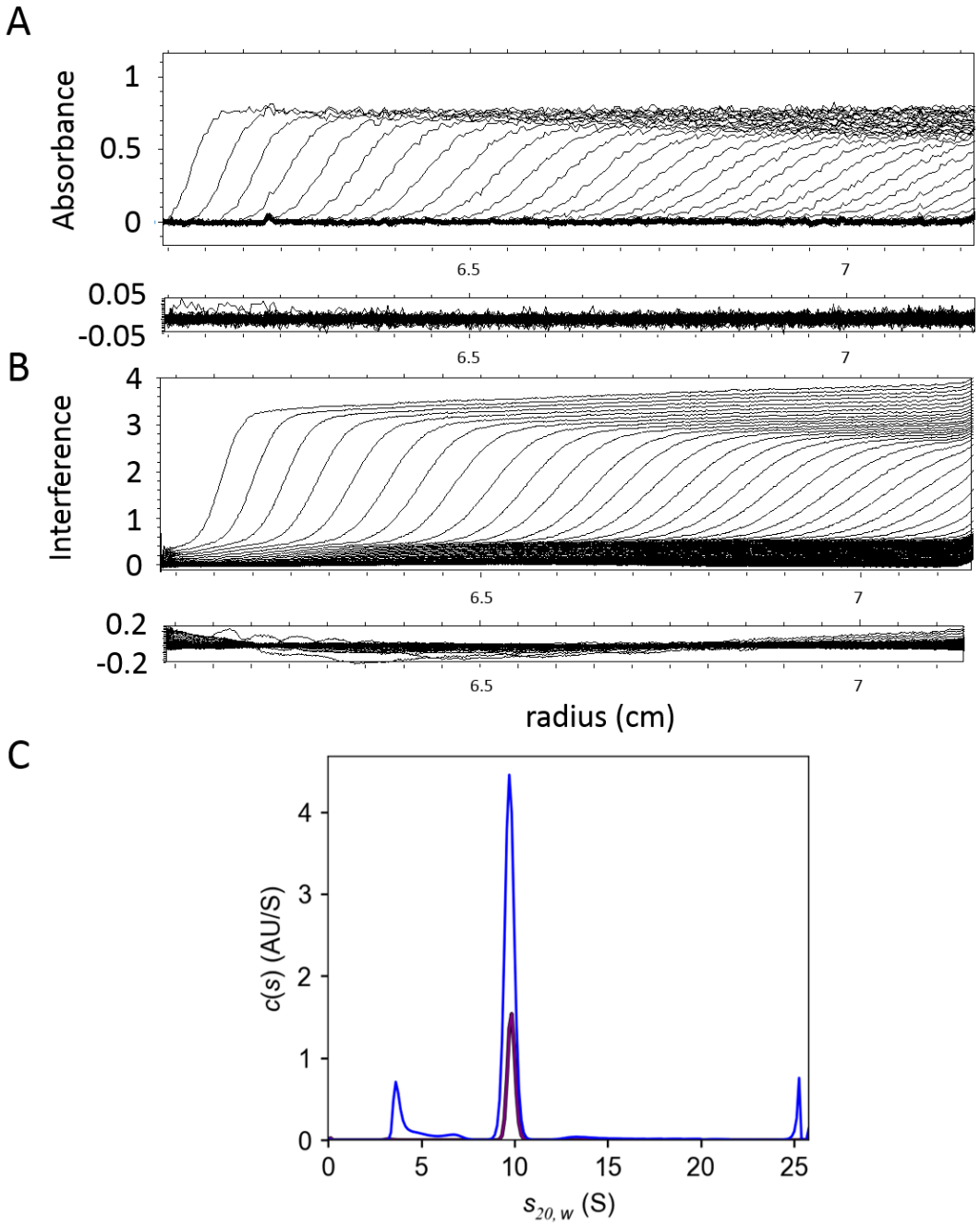

Figure 3.5 AUC profiles **(A)** absorbance at 280 nm and **(B)** interference signals of analytical ultra-centrifugation sedimentation profile of AmtB solubilised in 0.03% DDM. **(C)** Superposition of the c(s) distributions expressed at 20°C in water (blue: A_{280nm}, purple: Interference) (Dias Mirandela *et al*., 2018).

To further understand if the trimeric organisation of AmtB in the PDC was dependent on the protein concentration, different sedimentation coefficients were calculated from the absorbance and interference signal for 3 different protein concentrations (10, 22 and 87 µM) (**Figure 3.6**). As shown in **Figure 3.6**, the sedimentation coefficient calculated using the interference or absorbance data did not depend on AmtB concentration. This result demonstrated that the trimeric state of AmtB is not protein concentration dependant, which is important to analyse the SAS data with confidence.

3.3.3 Comparison of the molecular weight obtained by SEC-MALS and AUC

The molecular weights calculated using SEC-MALS and AUC are summarised in **Table 3.1**. These results support the view that AmtB was organised as a trimer in solution. The quantity of DDM bound to the trimeric form of AmtB was estimated to be between 270 to 320 DDM molecules depending on the technique used. These results are in agreement with the previous DDM characterisation study on AmtB which demonstrated that 265 DDM molecules were bound to the trimeric form of AmtB (Blakey *et al.,* 2002).

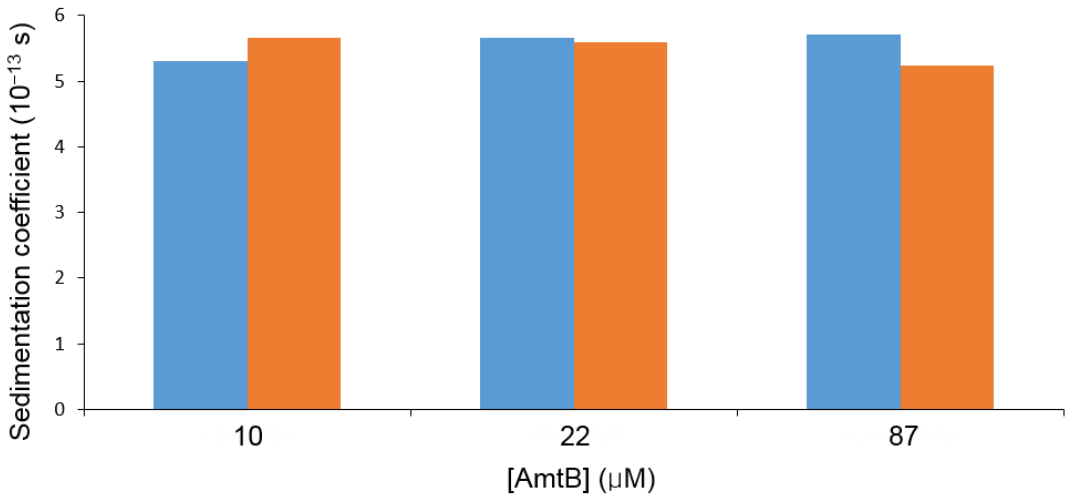

Figure 3.6 Influence of the protein concentration on the sedimentation coefficient. A_{280nm} (blue), Interference (orange).

Table 3.1 Molecular weights of the complex AmtB-DDM obtained using SEC-MALS and AUC.

	M_w AmtB-DDM	M_w AmtB	M_w DDM	DDM molecules
SEC-MALS	287.2±16.7	144.4±11.1	142.8±5.9	285±12
AUC	312.6±14.5	148.8±6.8	163.7±0.7	321±1

3.4 SEC-SAXS

Having thoughtfully characterised the AmtB sample, I have subsequently collected experimental synchrotron SAXS data (B21 bioSAXS beamline at the DIAMOND Synchrotron) following size-exclusion chromatography (SEC-SAXS) to obtain structural information of the AmtB–DDM complex in solution. I will present the data acquisition and analysis (**section 3.4.1**). Subsequently, the SEC-SAXS data have been used to obtain models of the AmtB-DDM complexes using two different *ab-initio* approaches:

1- *ab-initio* modelling using the software DAMMIN (**section 3.4.2**)

2- geometrical coarse-grained *ab-initio* modelling (**section 3.4.3**)

3.4.1 Data acquisition and analysis

The SAXS data were collected after size-exclusion chromatography. The absorbance profile at 280 nm shows a symmetrical peak showing that the hydrodynamic radius of the AmtB-DDM complex follows a uninominal distribution (**Figure 3.7**).The gyration radii (Rgs) of the AmtB-DDM complex calculated, using the Guinier approximation, are constant across the elution peak (~45 Å) proving that the size of the complex is homogenous in solution. All the 15 scattering curves corresponding to the elution peak in **Figure 3.7**, were merged to obtain an average SAXS experimental curve (**Figure 3.8**). This average curve was subsequently used to perform the modelling and data analysis described in this chapter.

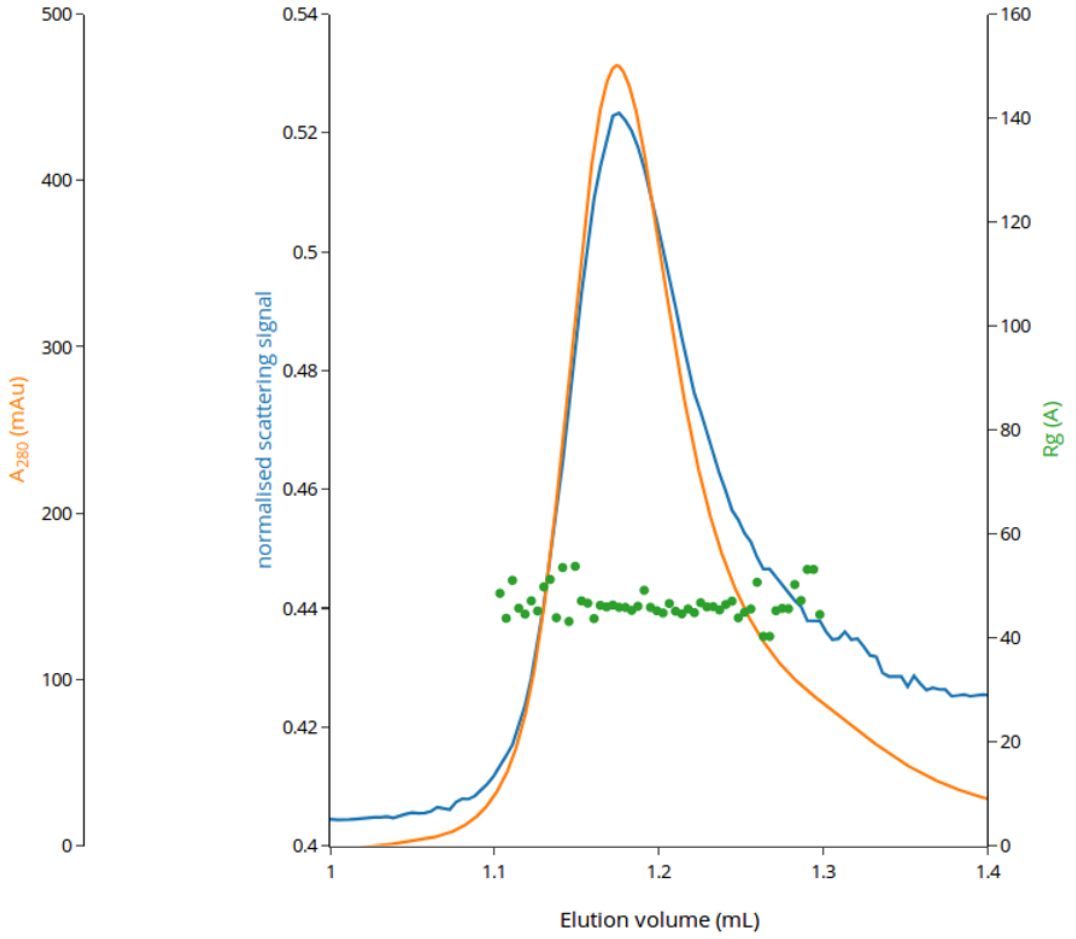

Figure 3.7 SEC-SAXS elution profile of AmtB. The OD at 280 nm (orange), x-ray scattering intensities (blue), radius of gyration (Rg) (green dot) are represented.

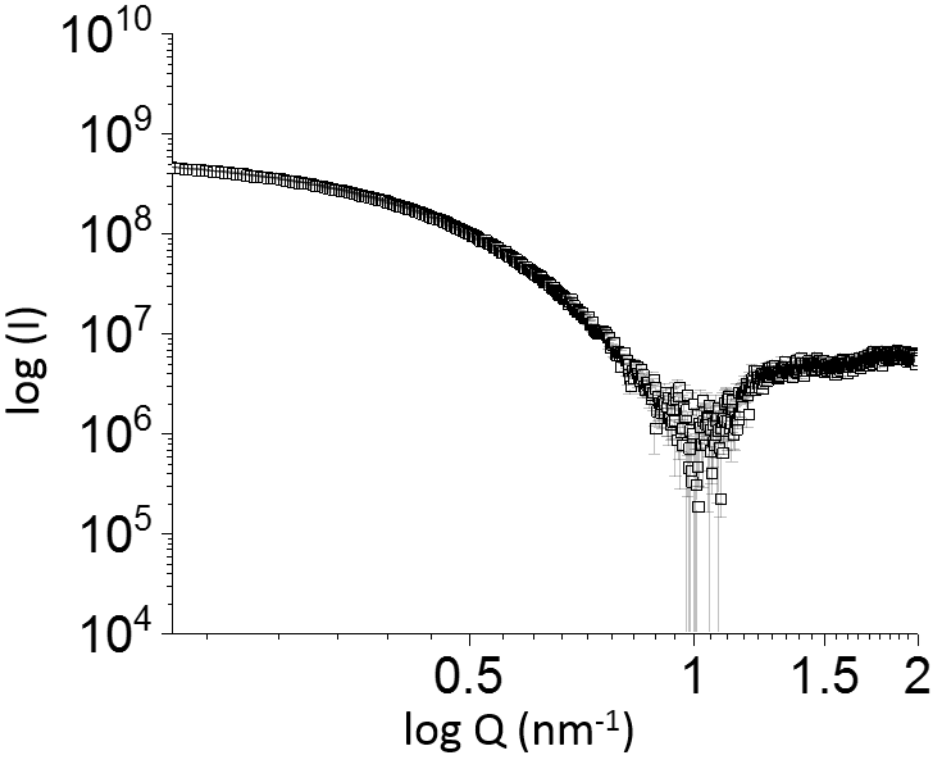

Figure 3.8 Average of the small angle scattering curves obtained from the SEC-SAXS measurements.

3.4.2 *Ab-initio* modelling using DAMMIN software

The program DAMMIN uses small angle x-ray scattering data to obtain the *ab initio* low resolution shape of randomly oriented protein-detergent complexes (PDC) in solution (Franke *et al*., 2017). The average of scattering curves (**Figure 3.8**) was used to perform *ab-initio* modelling using DAMMIN. The only parameters imposed were the symmetry (none or P3) and the shape of the expected model (none or oblate). The P3 symmetry was used because I have shown that AmtB forms a stable trimer in solution (see **sections 3.3.1-3.3.3**) and the oblate parameter was used because it corresponds to the overall shape of the x-ray crystal structure of AmtB (PDB 1U7G) (Khademi *et al.,* 2004). Ten models were averaged and filtered using different programs from the ATSAS package (DAMSEL, DAMSUP, DAMAVER and DAMFILT) (Franke *et al*., 2017). All the models display a conserved dense "core" consisting of a high beads density whereas the peripheral beads density shows slight variation (**Figure 3.9**). In order to validate the accuracy of the models, computed SAXS curves for each of the models presented in **Figure 3.9** has been generated using the software CRYSOL (Svergun *et al.,* 1995) and compared to the experimental SAXS data. For clarity, the experimental SAXS curve in **Figure 3.9**, panel B was plotted without the experimental errors (see **Figure 3.8** in which experimental errors are plotted). Chi^2 value was used as a statistical parameter to test the goodness of the fit for each theoretical SAXS curve against the experimental data. The chi^2 obtained for the default, oblate shape, symmetry P3 and symmetry P3/oblate shape parameters were 9, 7, 43 and 3.4 respectively. Hence, the oblate shape helped to slightly improve the fit of the model against the experimental data as the chi^2 decreased from 9 to 7. In contrast, the symmetry P3 model does not fit between 0 to ~0.8 nm^{-1} resulting in a ~5 times increase of the chi^2 compare with the model obtained using default parameters (**Figure 3.9**). Combining P3 symmetry and oblate shape drastically increases the quality of the fit between calculated curve and experimental data with a chi^2 of 3.4 (**Figure 3.9**). Not surprisingly, these results showed that a symmetry P3 and an oblate shape were the best modelling

parameters required to compute models using the software DAMMIN. The superimposition of the crystal structure of AmtB with the core of the P3/oblate model shows a fairly good fit (**Figure 3.10**). The radius of the AmtB trimer and of the core of the DAMMIN model, calculated using the software PyMOL, were 64 and 68 Å respectively. This result suggested that the core observed in the PDC model corresponds to the position of AmtB.

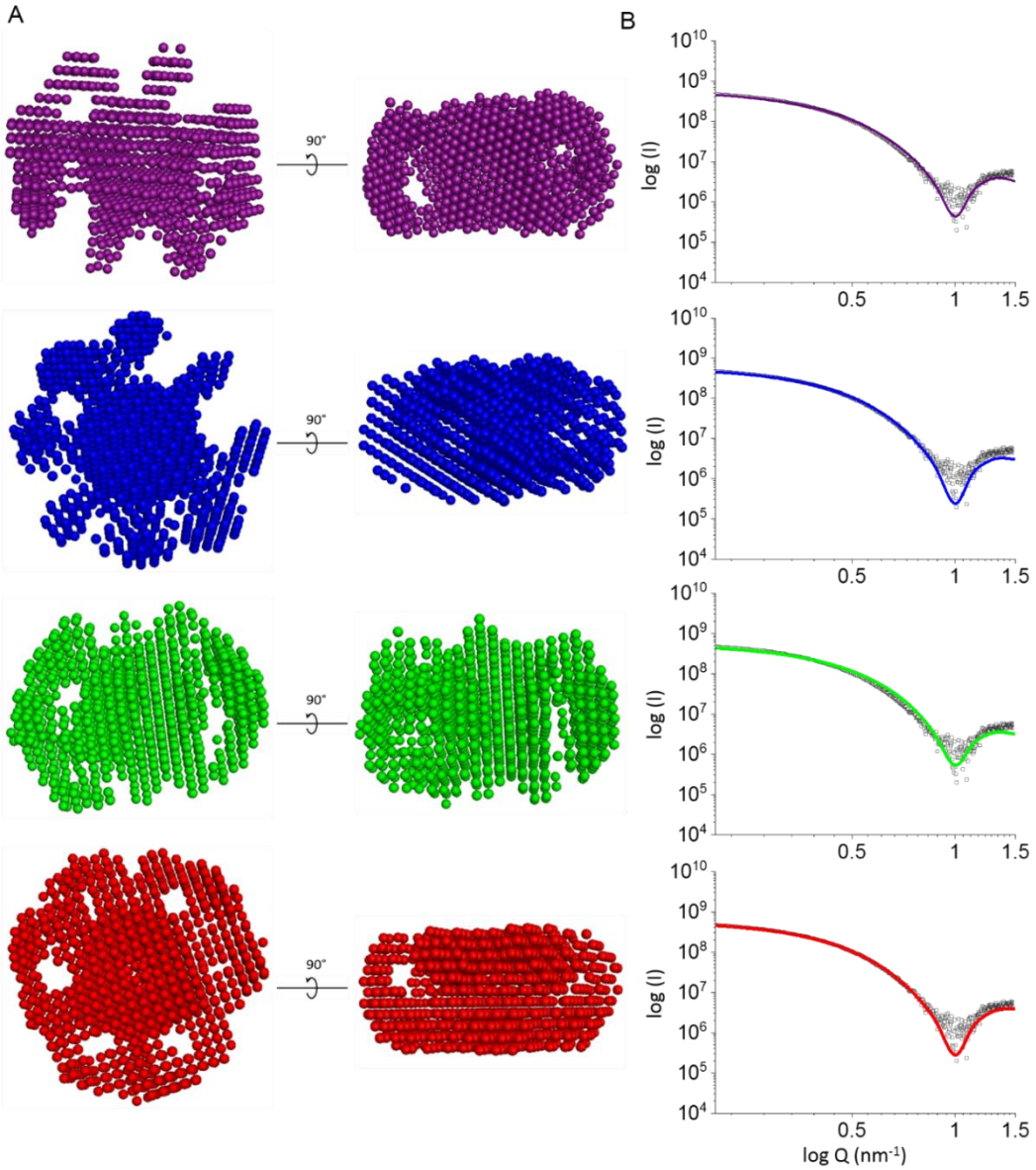

Figure 3.9 (A): Top and side view of DAMMIN averaged models computed using default (purple), oblate (blue), P3 (green) and P3/oblate (red) restrictions. **(B)**: Comparison of the theoretical SAXS curve calculated from the DAMMIN models against the experimental data. The restrictions applied were default (purple), oblate (blue), P3 (green) and P3/oblate (red).

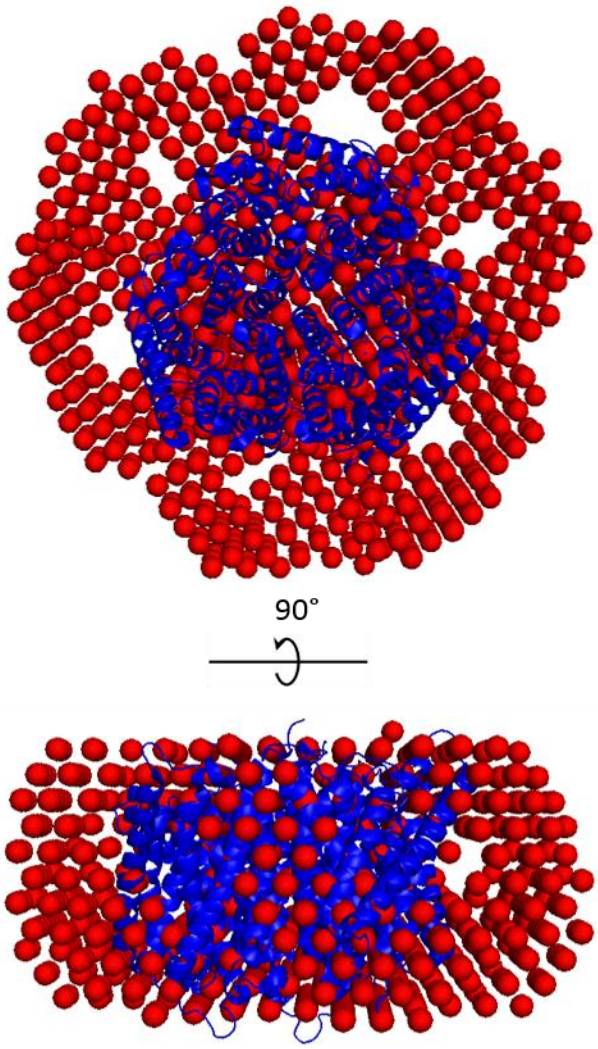

Figure 3.10 Alignment of the averaged DAMMIN model with the structure of AmtB. The DAMMIN model was computed using P3 symmetry/oblate shape (red). The AmtB trimeric structure (1U7G) is displayed as blue cartoon.

3.4.3 *Ab-initio* modelling using coarse-grained approach

Next, we used a coarse-grained procedure combining the crystal structure of AmtB (1U7G, Khademi *et al.,* 2004) with the experimental SAXS curve to generate an independent *ab-initio* model of the PDC. Memprot is a software used to generate a torus shape for the detergent corona surrounding membrane proteins (Perez and Koutsioubas, 2015). The software optimizes step by step the values of the four geometric dimensions, a, b, e and t (**Figure 3.11**) that define the shape of the detergent corona. One geometrical parameter was modified at a time during the modelling, resulting in a total of 12,705 models (Perez and Koutsioubas, 2015). A theoretical scattering curve using CRYSOL (Svergun *et al.,* 1995) was generated for each of the 12,705 models and compared to the experimental SAXS data. For each model, the chi^2 value was used as a statistical parameter to evaluate the goodness of the fit between the experimental and theoretical scattering curve. The best model possesses a detergent corona with the following geometry: a = 33 Å, b = 35 Å, t = 6 Å, e = 1.090 Å (**Figure 3.12**).

In addition, Memprot provided a volume occupancy of the protein and the detergent corona based on the beads model (**Figure 3.12A**) (Breyton *et al.*, 2013). Hence, by knowing 1-the volume of the AmtB trimer based on the crystal structure (166800 $Å^3$) and 2- the volume of a DDM molecule (690 $Å^3$ (Breyton *et al.*, 2013)), it was possible to calculate that the detergent torus contained 301 molecules of DDM, in good agreement with our AUC and SEC-MALS analysis (**section 3.3**).

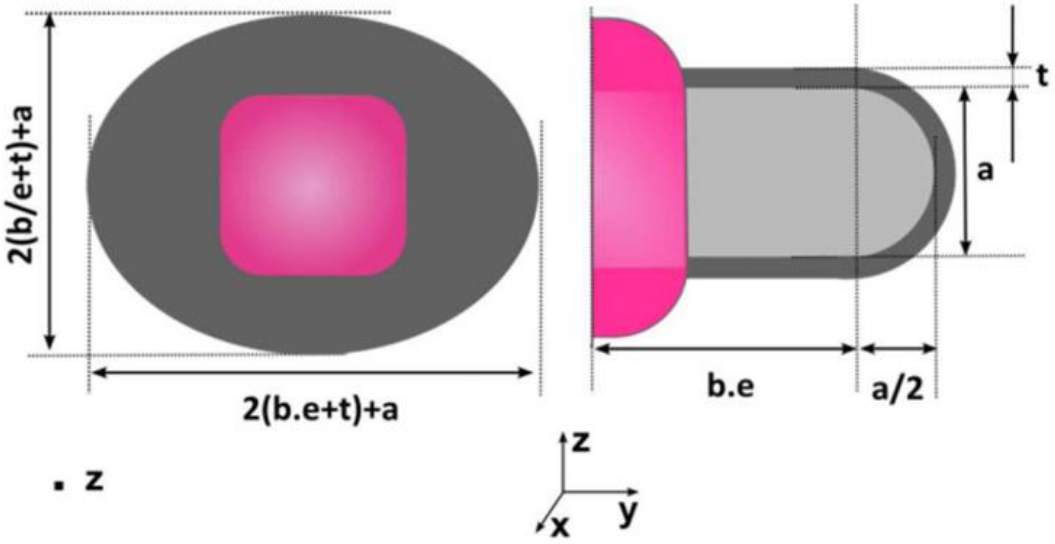

Figure 3.11 Schematic representation of the geometrical parameters used during the detergent torus modelling by the software Memprot (Berthaud *et al*., 2012). The protein and detergent position are coloured in purple and grey respectively.

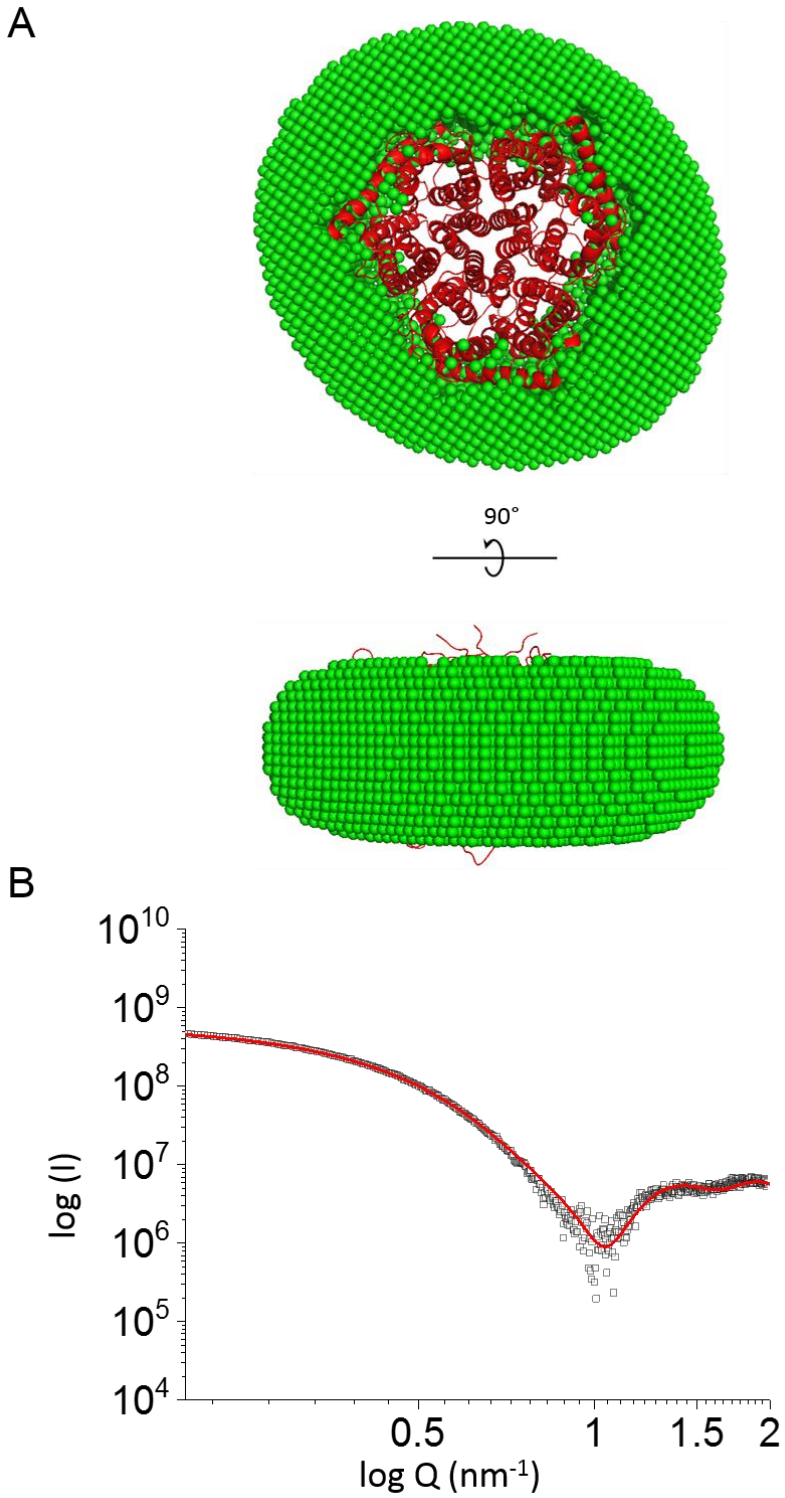

Figure 3.12 Top and side view of the best model computed using Memprot. **(A)** The trimeric crystal structure of AmtB (1U7G) is represented in red cartoon and the detergent corona bead model is represented in green. The values of the geometrical parameters describing the shape of the detergent corona (**Figure 3.11**) are: a = 33 Å, b = 35 Å, t = 6 Å, e = 1.090 Å. **(B)** Comparison of the experimental (symbols) and Memprot computed (red line) SAXS curves (chi^2: 1.9).

3.5 Molecular dynamic simulations

We next exploited atomistic molecular dynamics (MD) simulations to obtain atomistic models of the AmtB-DDM complex and score them against the experimental SAXS data. These studies have been made in close collaboration with the laboratory of Dr. Ulrich Zachariae from the University of Dundee. The simulations have been conducted by Dr. Giulia Tamburrino. The computational work has been informed by, and in turn feedback information to, the experimental studies presented here.

3.5.1 MD models

We have demonstrated that AmtB is a trimer in solution and the SEC-MALS and AUC analysis (**sections 3.3.1-3.3.3**) indicates that the detergent corona around AmtB is likely to include between 260 and 320 DDM molecules. Hence, using CHARMM-GUI Membrane Builder plugin and GROMACS 5.1.1 software package CHARMM36 force field (Dias Mirandela *et al.,* 2018), molecular dynamic (MD) simulations of AmtB surrounded by a coronas containing 260, 280, 300, 320, 340 and 360 detergent molecules were conducted. As an example, the MD simulation model corresponding to 320 DDM molecules is presented **Figure 3.13**. The simulations indicate that the protein-detergent complexes are stable, and although some reorientation of DDM was observed during the equilibration, no dissociation of detergent molecules from the protein was detected after 20 ns of simulation time. The atomistic model clearly shows that the DDM molecules adopted the typical toroidal shape reported for other protein-detergent complexes (Chen and Hub, 2015, Berthaud *et al.,* 2012), with their hydrophilic heads facing the aqueous solution and their hydrophobic tails oriented toward the inside of the complex.

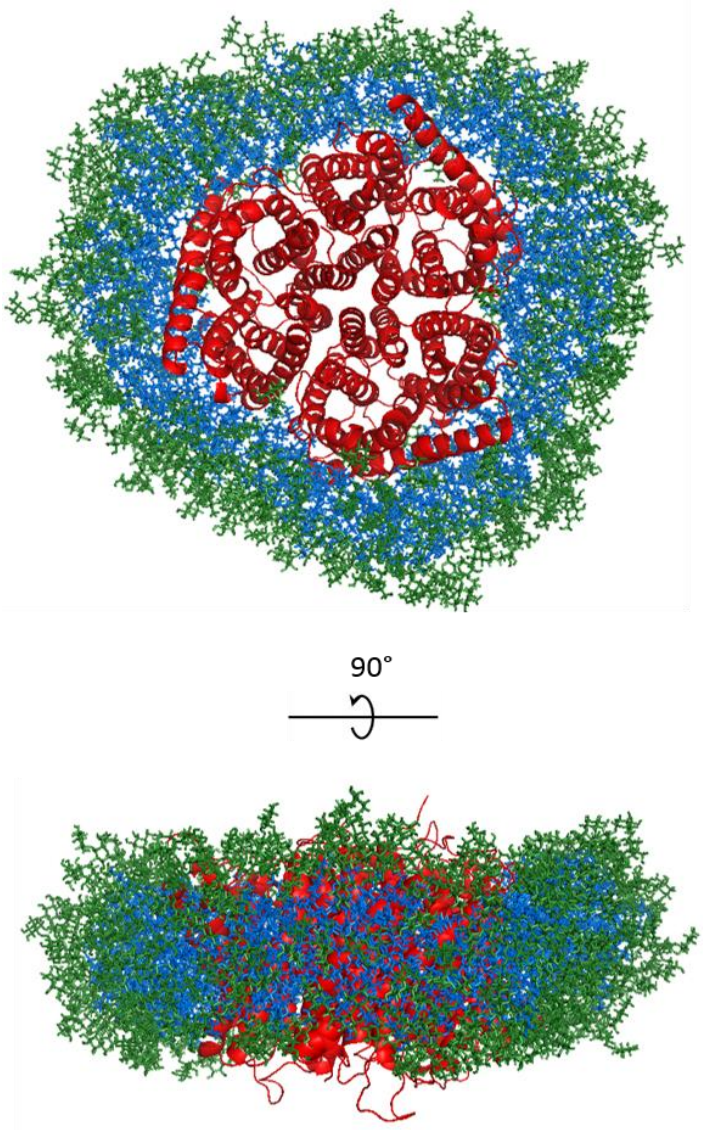

Figure 3.13 Top and side view of a MD model at 320 DDM molecules based on the trimeric 1U7G crystal structure of AmtB from *E.coli* (green: Stick representation of DDM molecule heads, blue: Stick representation of DDM molecule tails red: Cartoon representation of the 1U7G crystal structure).

3.5.2. Validation of the atomistic model

To discriminate the accuracy of the different MD models of the PDC containing between 260-320 molecules of DDM, theoretical SAXS curves were generated using the software WAXSiS and fitted to the experimental SAXS data. This part of my PhD project has been done in close collaboration with Prof. Jochen Hub (Saarland University, Germany). WAXSiS is a software used to generate theoretical SAXS curves based on an atomic model. In contrast to CRYSOL, WAXSiS calculates SAXS curves by accounting for explicit-solvent (Knight and Hub, 2015) whereas CRYSOL implicitly calculates the solvent contribution. The theoretical scattering curves obtained for the 260, 280 and 300 DDM molecules models deviate from the experimental data within the Q=1-2 nm^{-1} range. The residual plot clearly shows that increasing the number of detergent molecules from 260 to 320 improved the quality of the fit, but above 320 molecules the quality of the fit decreased (**Figure 3.16**). The best fit between the calculated curve and experimental data was clearly obtained for the PDC model containing 320 molecules of DDM (**Figure 3.16**). These results suggest that the MD model generated with 320 DDM molecules is the more accurate representation of the biological sample used to measure the experimental SAXS data. To further discriminate between the different MD models, I have calculated their gyration radii (R_gs) using the Guinier approximation. The Rgs calculated from the Guinier plot for the models containing between 260-300 molecules of DDM (43.1 - 44.5 Å) are lower than the Rg calculated from the experimental data (45.5 Å). In contrast, the Rgs calculated for the models containing between 340 and 360 molecules of DDM (47.8 and 48.6 Å) are greater (**Figure 3.17**). Remarkably, the Rg calculated from MD model containing 320 molecules of DDM (45.6Å) is almost identical to the Rg derived from the experimental data (**Figure 3.17**). These results confirmed that the overall dimension of the simulated PDC containing 320 molecules of DDM is identical to the AmtB-DDM complex in solution.

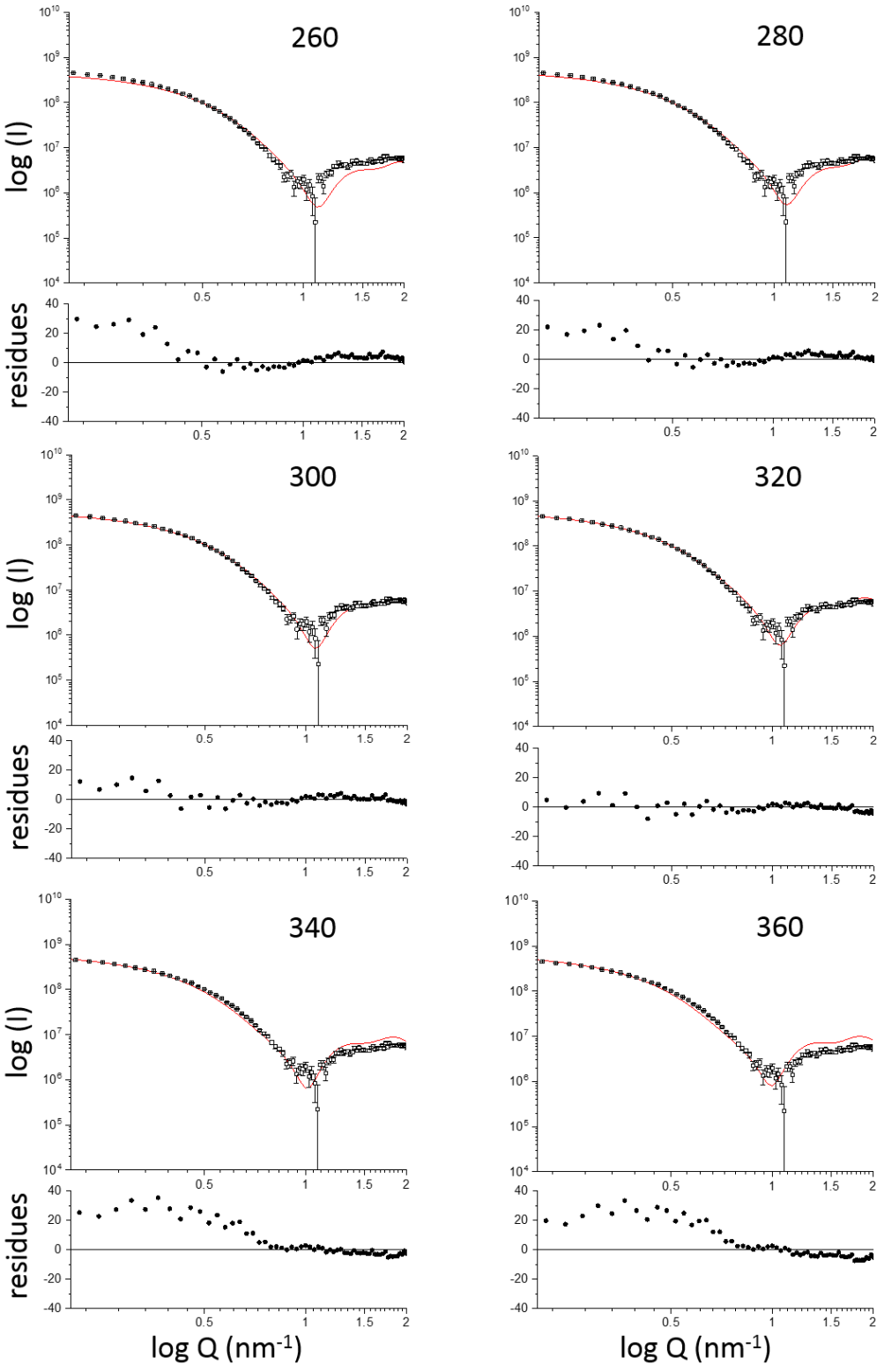

Figure 3.14 Comparison of the experimental (symbols) and computed (red line) SAXS curves of the AmtB-DDM complex containing between 260 and 360 DDM molecules. Below each graph, the residual error plot expressed as the experimental minus computed scattering intensity.

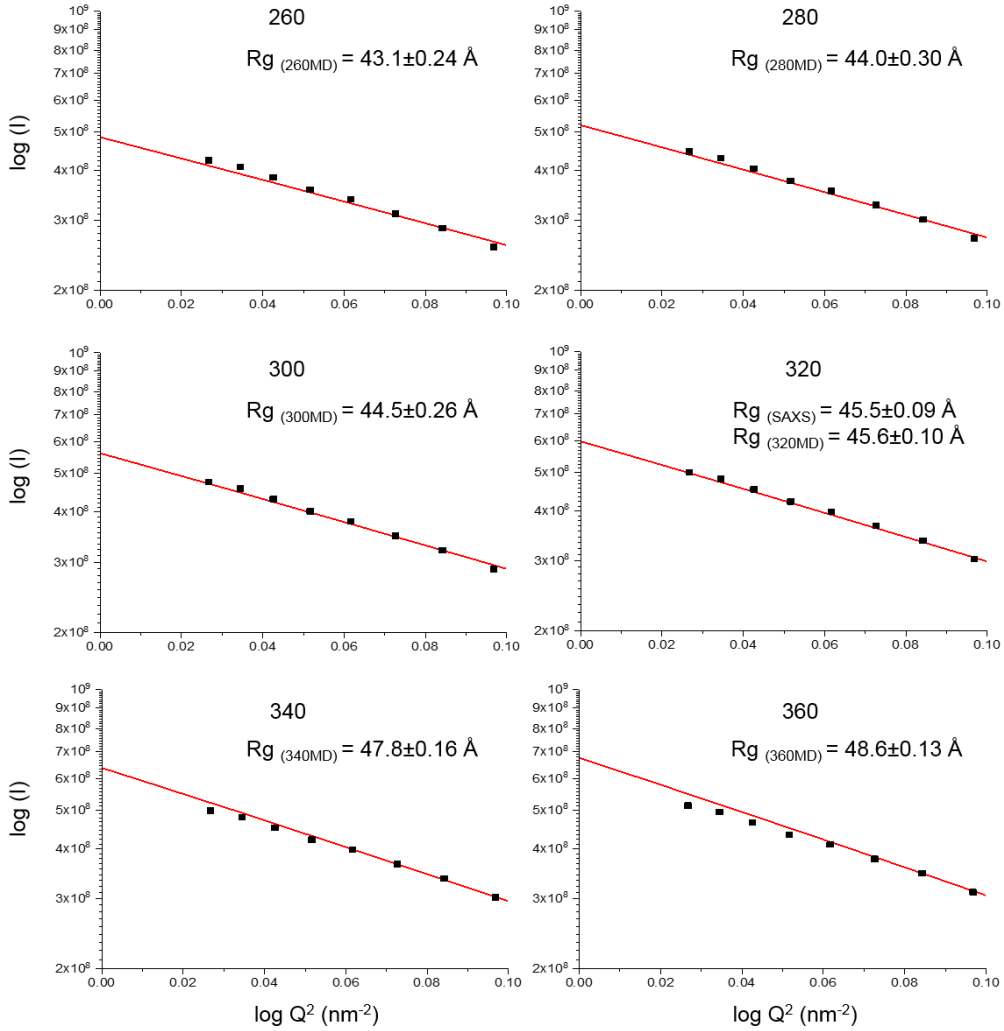

Figure 3.15: Guinier plot comparison of the experimental (symbols) and computed (red line) SAXS curves of the AmtB-DDM complex containing between 260 and 360 DDM molecules (Dias Mirandela *et al.*, 2018).

3.6 SANS analysis

It is important to note that the overall information content of SAXS is relatively low, and thus agreement between experimental and back-calculated curves may be insufficient to serve as unambiguous evidence for a structural model (Petoukhov and Svergun, 2015). Specifically, in the context of a protein-detergent complex, SAXS data reports on the overall shape of the complex, whereas they do not provide independent information on the individual contributions from the protein and the detergent corona. Therefore, I employed SANS together with contrast variation to more firmly validate the computational model (**sections 3.6.1-3.6.3**). In a second step I have merged our complete SAXS and SANS data and conducted a multiphase volumetric analysis of the complex using the software MONSA (Reyes *et al.*, 2014, Svergun, 1999) to capture detailed structural information on the complex without using the crystal structure of AmtB (**section 3.6.4**).

3.6.1 Contrast match point determination of the DDM

The fundamental difference between SANS and SAXS is that x-rays interact with the electronic cloud of atoms whereas neutrons interact with the nuclei. Thus, the neutron scattering pattern from a hydrogen or a deuterium atom are different. The exchange of hydrogen to deuterium in biological macromolecules, by varying the ratio of H_2O/D_2O in the buffer, affects how the molecules scatter neutrons. The scattering length density (SLD) is a measure of the strength of the interaction of a neutron beamline with a given nucleus. At the right H_2O/D_2O ratio, when the SLD of a molecules matches the SLD of the buffer, the molecule becomes “invisible” to neutrons: this is the contrast match point (CMP) expressed in % of D_2O (**Figure 3.16**). I was aiming at distinguishing AmtB from the detergent in the Amt-DDM complex in SANS analysis using a CMP approach. To determine the CMP of DDM, the scattering intensities of a pure DDM solution was measured in a buffer containing different D_2O concentrations (**Figure 3.17**).

I have plotted the square root of the absolute scattering intensity against the concentration of D_2O and the data have been fitted using a linear regression (**Figure 3.17**). The CMP of the DDM, 22% D_2O, was defined by the intersection between the linear regression and x-axis of the plot.

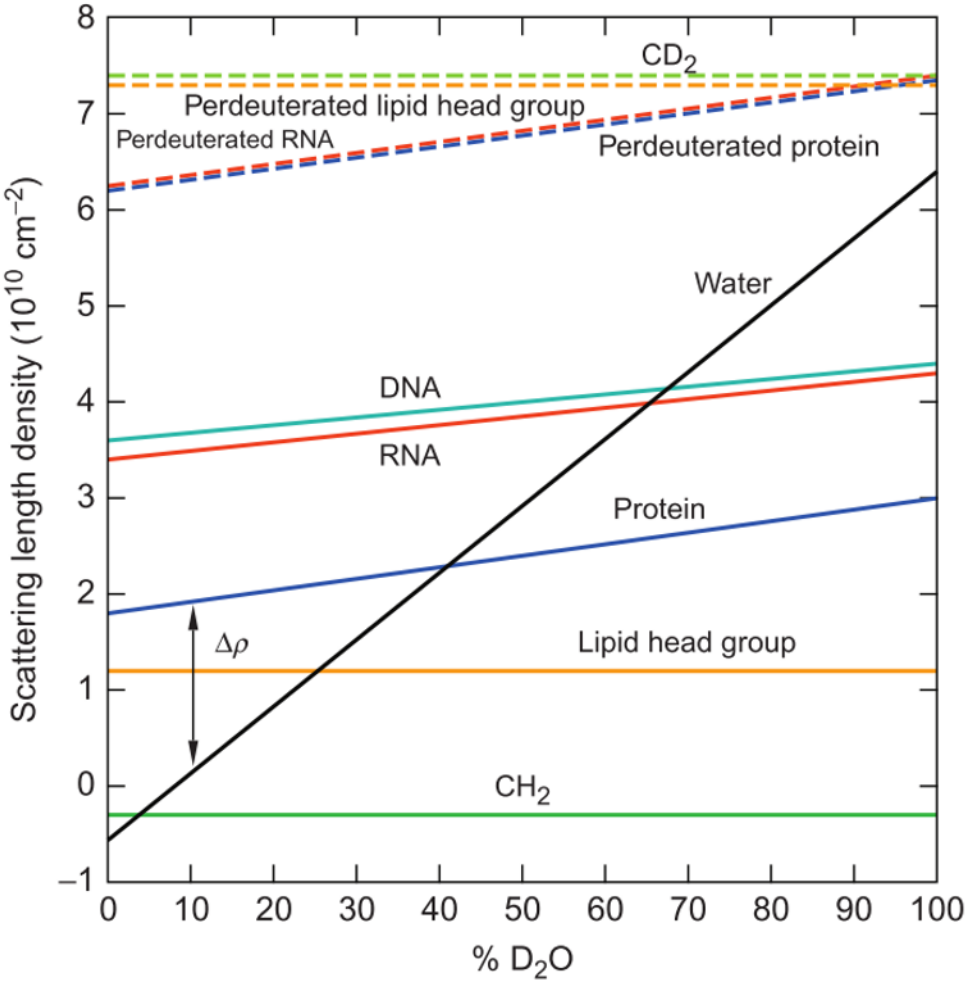

Figure 3.16 Schematic example of contrast match point variation for different biological macromolecules (Zaccai *et al.*, 2016).

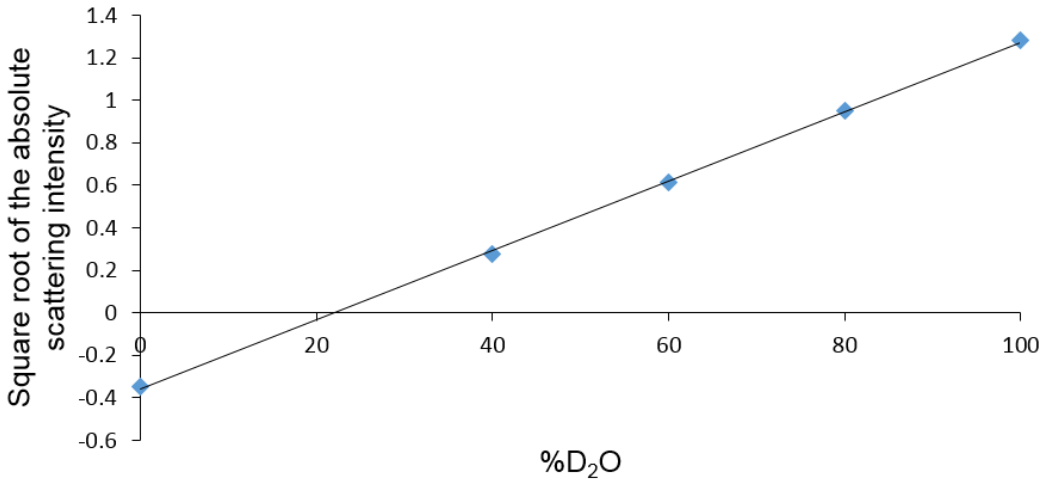

Figure 3.17 Contrast match point determination of DDM. Square root of the absolute scattering intensity as a function of the $\%D_2O$ in the buffer.

3.6.2 SANS data collection

We collected SANS data at four contrast points (0%, 22%, 42% and 60% (v/v) D_2O) to differentiate between the individual components of the protein-detergent complex. To ensure that the samples were stable over the course of the SANS experiment, I analysed the hydrodynamic behaviour of the proteins before and after the SANS measurements by analytical size exclusion chromatography. No differences were observed in the elution profile, confirming the stability of the protein during the SANS experiment (see **Figure 3.2** in **section 3.2.2**). To ascertain the reproducibility and the quality of the SANS measurements, I have measured two independent sets of data in September 2016 and March 2018 using two batches of AmtB purified independently and the two datasets were found to be identical within the limits of the observed experimental noise (**Figure 3.18**). It has previously been shown that in the absence of D_2O in the buffer, neutron scattering from DDM micelles originates primarily from the hydrophilic head groups (Oliver *et al.*, 2017). I have calculated (see **section 3.6.1**) the overall contrast match point of DDM to be at 22% D_2O, while the contrast match point for typical proteins is around 42% D_2O (Zaccai *et al.*, 2016, Breyton *et al.*, 2013). Consequently, the scattering contribution is dominated by the protein and the DDM hydrophilic head group in a buffer containing 0% D_2O, by the protein at 22% D_2O and by the complete detergent corona at 42% D_2O (**Figure 3.18**). The two scattering curves measured in September 2016 and March 2018 present exactly the same shape for the conditions at 0, 22 and 42% D_2O (**Figure 3.18**). This result shows that the overall organisation of the complex AmtB-DDM did not change in between the two datasets (**Figure 3.18**). A complementary SANS curve was measured at 60% D_2O in March 2018 to improve the quality of my modelling process. Usually SANS data is noisy and by increasing the concentration of D_2O, the signal becomes even noisier. The experimental errors measured for all the datasets were very low at a Q range below 1 nm^{-1} illustrating the quality of the data.

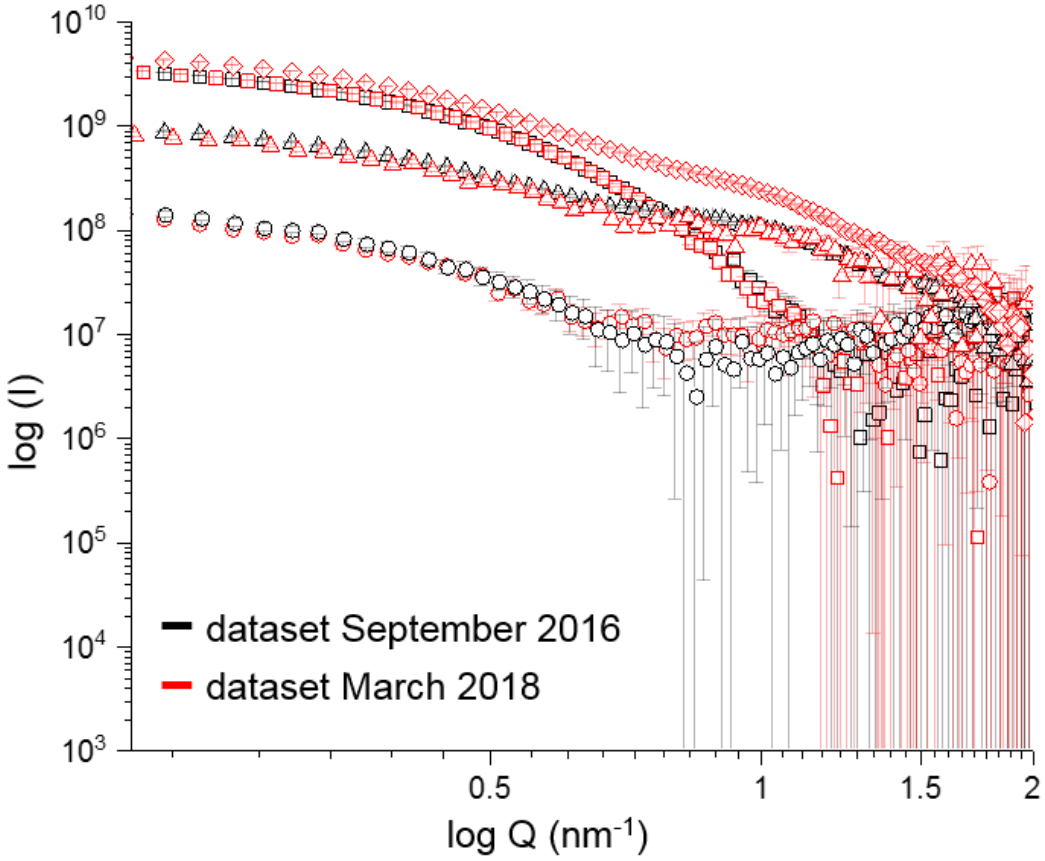

Figure 3.18: Comparison of the two SANS dataset measured in September 2016 (black) and March 2018 (red) at (□) 0% D_2O, (○) 22% D_2O, (△) 42% D_2O and (◇) 60% D_2O.

3.6.3 Validation of the MD models using SANS data

To compare the experimental neutron scattering data with the MD-generated models (see **section 3.5**), SANS curves were calculated using WAXSiS for 9000 individual configurations observed during 70-160 ns MD trajectories of each of the complexes. To this end, using my SANS dataset, Prof Jochen Hub extended the WAXSiS software, originally developed for SAXS predictions, to also allow SANS predictions with explicit-solvent models at various D_2O concentrations. I have fitted the experimental curves of the MD models containing 260-360 molecules of DDM to the calculated curves following $I_{fit} = f \cdot I_{exp} + c$, thereby accounting for scattering contributions from the incoherent background with the fitting parameter c (**Figure 3.19-24**). However, neither the hydration layer nor the excluded volume were adjusted. The residual plot indicates that all SANS data sets were best fitted by the curves calculated for the model incorporating 320 molecules of DDM (**Figure 3.22**). Hence, the SANS and SAXS data consistently validates our MD model with 320 DDM molecules. The good agreement between experimental and computed SANS curves indicates that the MD model describes accurately the hydrophobic and hydrophilic phase of the detergent ring as well as the position of AmtB inside the corona. Hence, the computed approach is validated by the experimental SAXS/SANS data, demonstrating that precise atomic details can be derived from a combined approach using MD/SAS combined analysis.

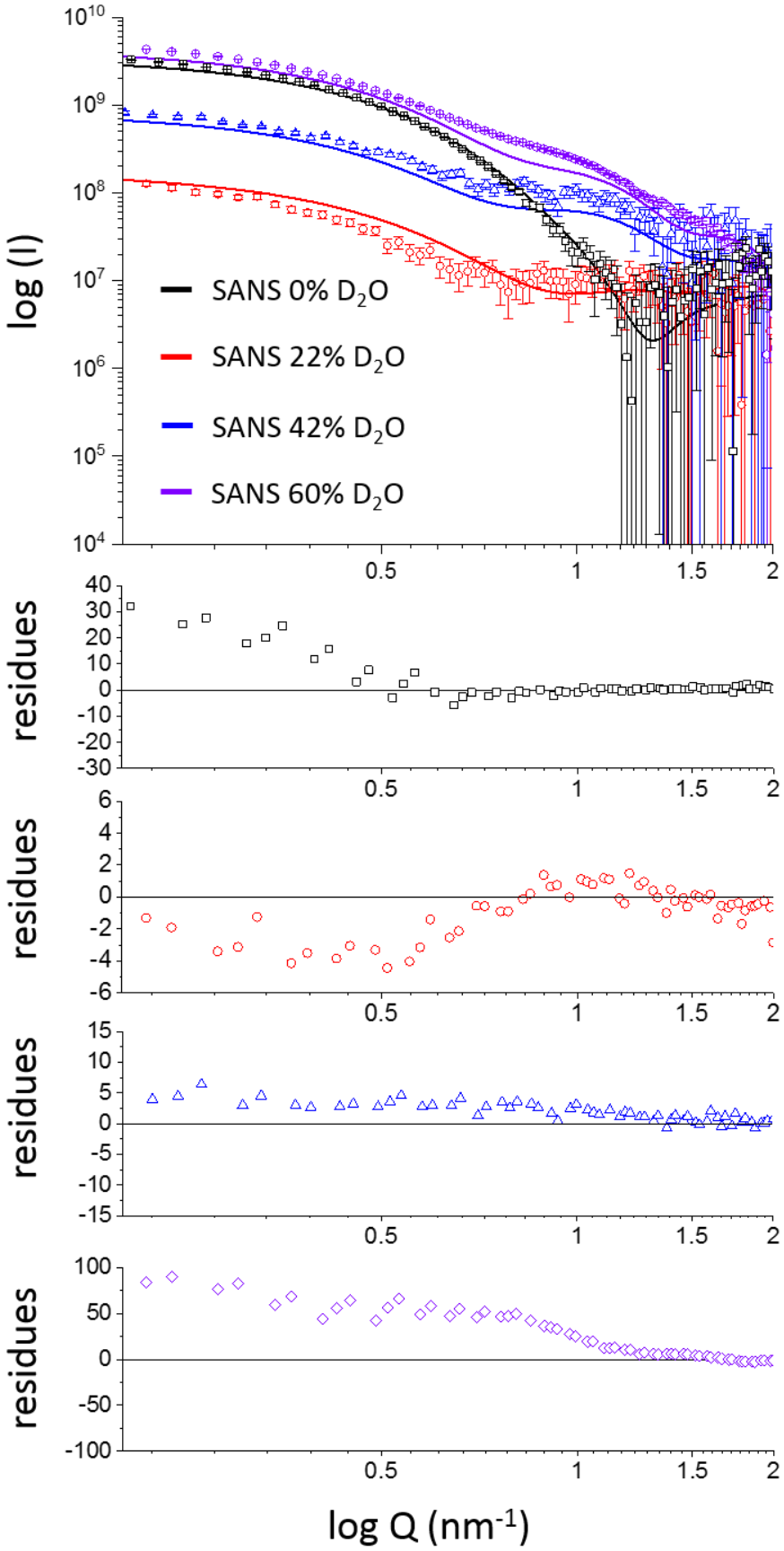

Figure 3.19 Comparison of the experimental (symbols) and computed SANS (lines) for the MD model at 260 DDM molecules. Below each graph, the residual error plot expressed as the experimental minus computed scattering intensity.

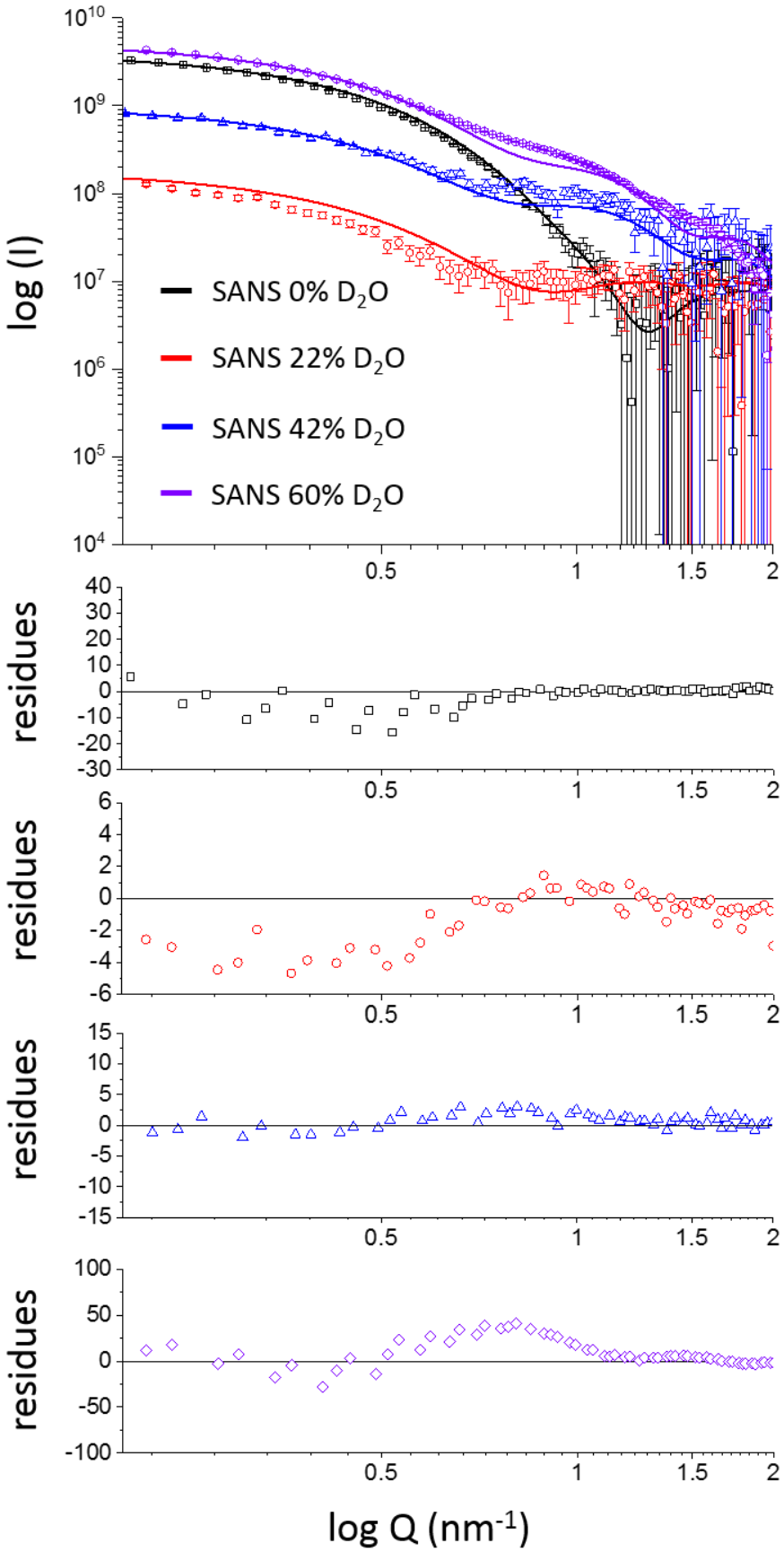

Figure 3.20 Comparison of the experimental (symbols) and computed SANS (lines) for the MD model at 280 DDM molecules. Below each graph, the residual error plot expressed as the experimental minus computed scattering intensity.

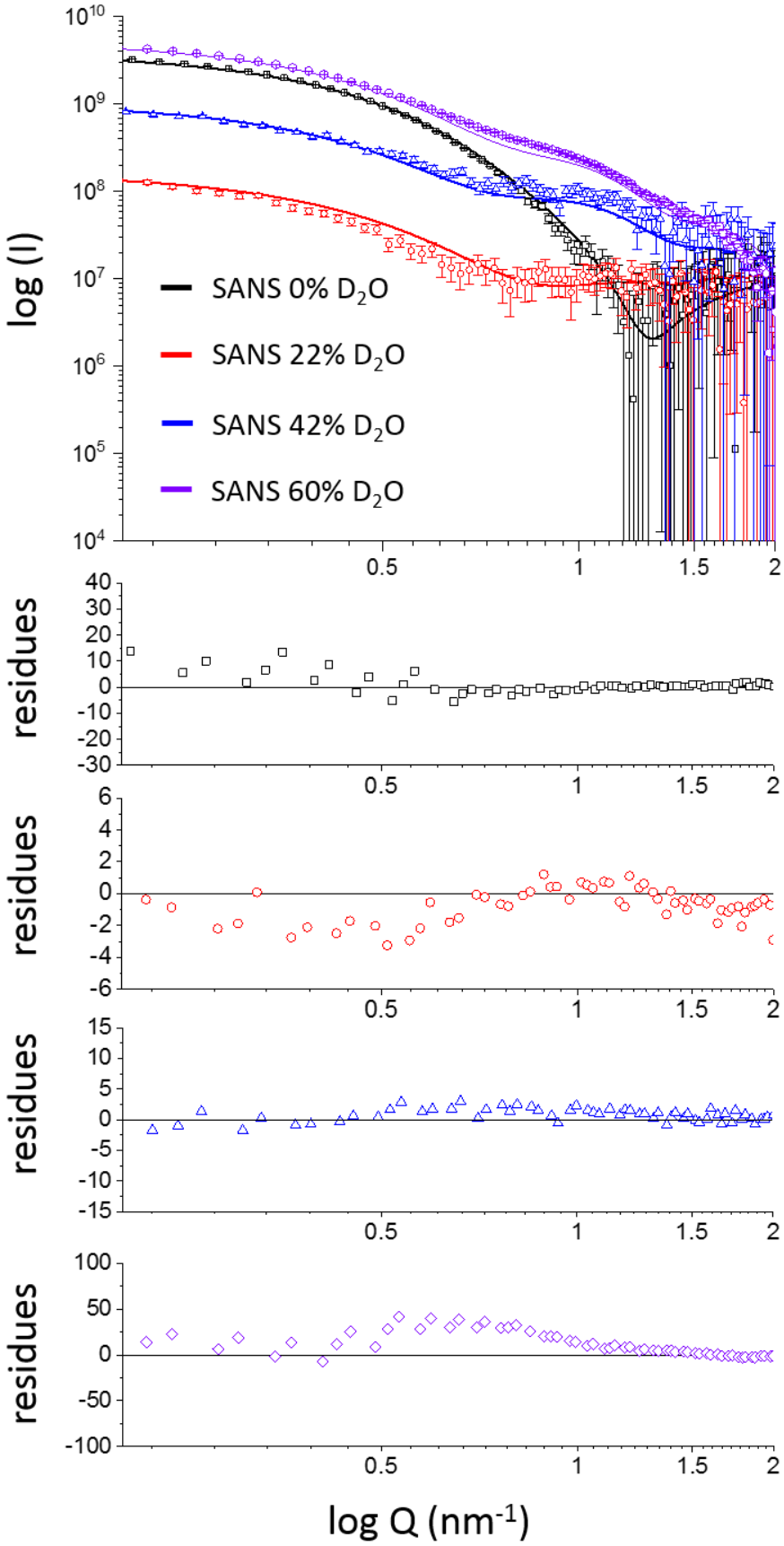

Figure 3.21 Comparison of the experimental (symbols) and computed SANS (lines) for the MD model at 300 DDM molecules. Below each graph, the residual error plot expressed as the experimental minus computed scattering intensity.

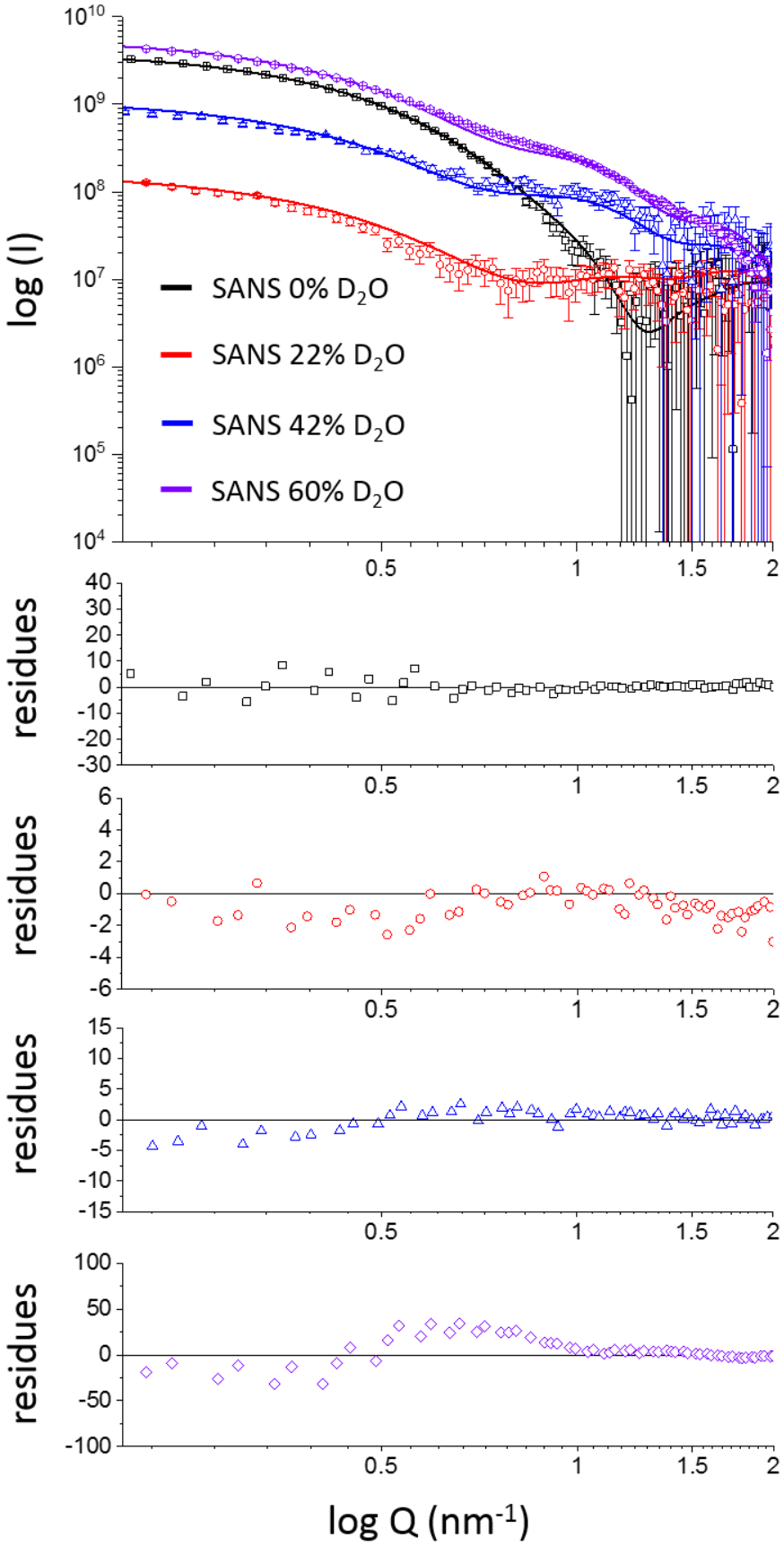

Figure 3.22 Comparison of the experimental (symbols) and computed SANS (lines) for the MD model at 320 DDM molecules. Below each graph, the residual error plot expressed as the experimental minus computed scattering intensity.

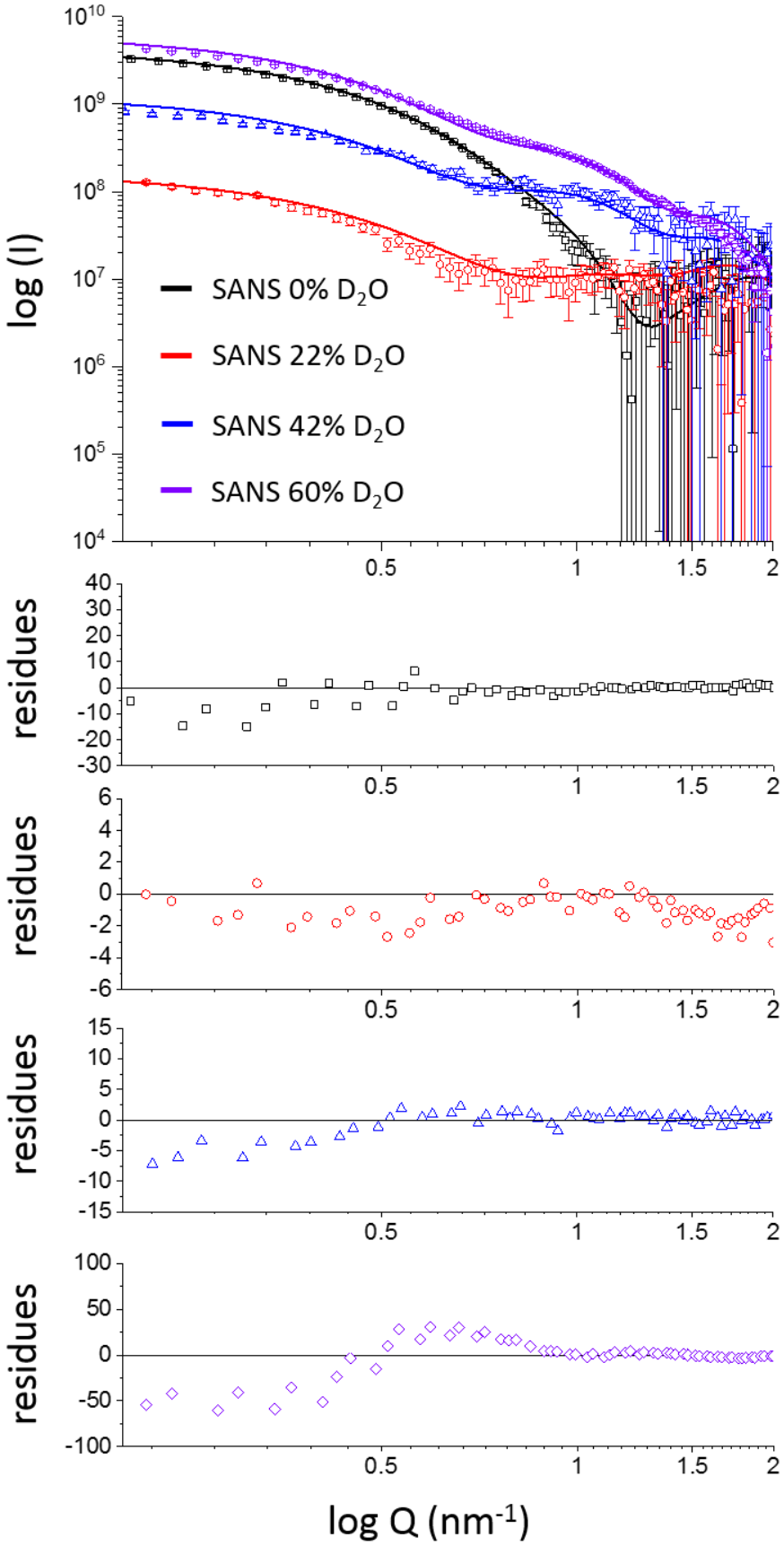

Figure 3.23 Comparison of the experimental (symbols) and computed SANS (lines) for the MD model at 340 DDM molecules. Below each graph, the residual error plot expressed as the experimental minus computed scattering intensity.

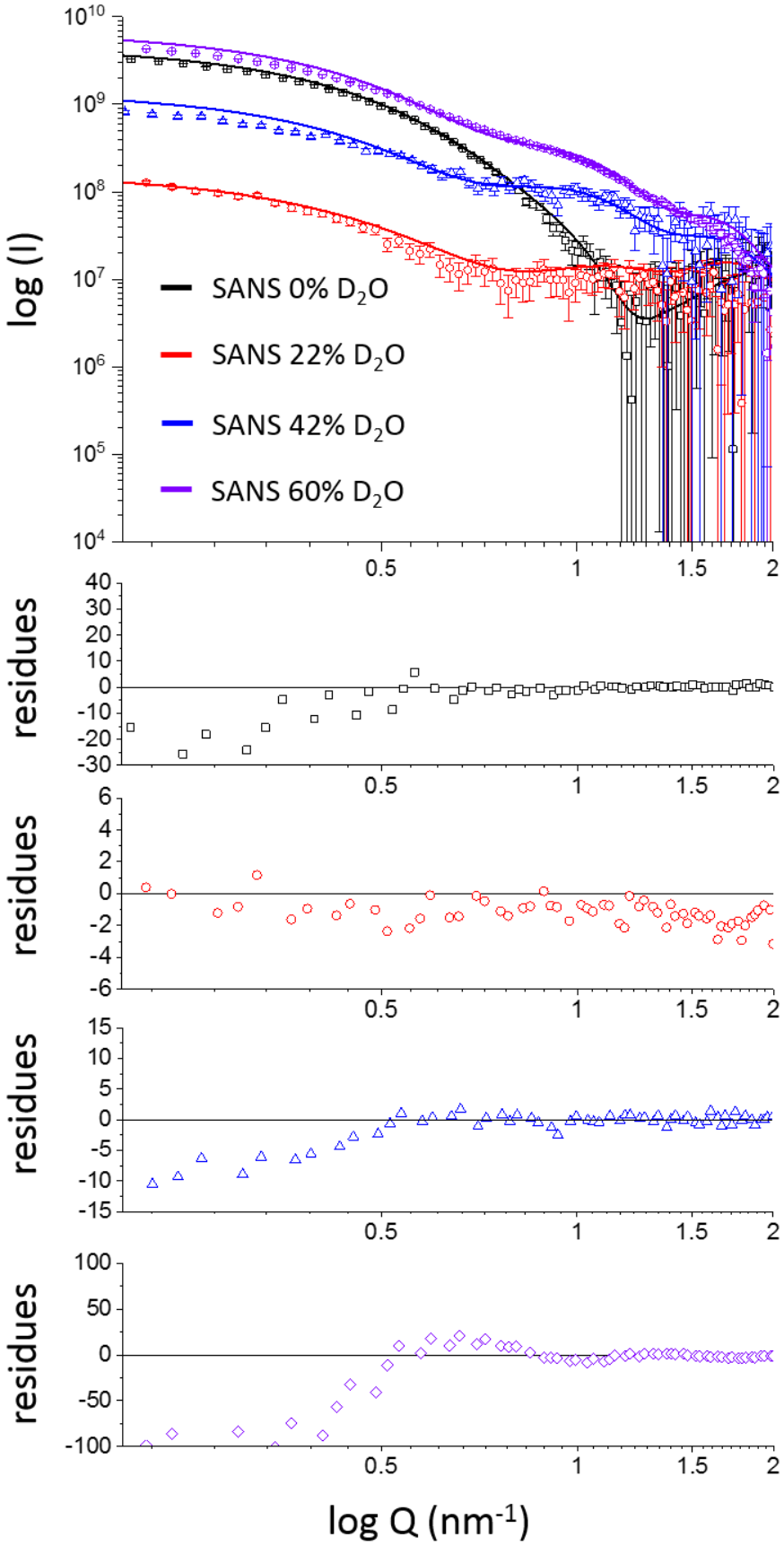

Figure 3.24 Comparison of the experimental (symbols) and computed SANS (lines) for the MD model at 360 DDM molecules. Below each graph, the residual error plot expressed as the experimental minus computed scattering intensity.

3.6.4 *Ab initio* modelling using multiphase software MONSA

In the MD/SAS combined approach presented in paragraphs 3.5.1, 3.5.2 and 3.6.3, the crystal structure of AmtB was used to produce the MD trajectories, which precludes the possibility of applying this combined approach to membrane proteins of unknown structure. I therefore applied an independent "MD-free" approach to obtain a full *ab-initio* model that captures detailed structural information on the complex without using the crystal structure of AmtB. To achieve this, I have merged the complete SAXS and SANS data and conducted a multiphase volumetric analysis of the complex using the software MONSA (Reyes *et al.*, 2014, Svergun, 1999). MONSA is an extended version of the software DAMMIN that I have used to obtain AmtB-DDM models from SAXS data (see paragraph 3.4.2). MONSA is used for multiphase bead modelling which allows simultaneous fitting of multiple curves from x-ray and neutron contrast variation series. MONSA reads multiple data sets and information about the contrasts and volume fractions of the protein and detergent phases in the AmtB-DDM particle. Hence, it is possible not only to separate the scattering signal from the protein and the DDM but also to distinguish the hydrophilic heads from the hydrophobic tails of the DDM. The scattering length density I have used to calculated the various phase of the PDC during the MONSA-modelling process are presented in **Table 3.2**. Assuming the volume of a DDM molecule to be 690 $Å^3$ (350 $Å^3$ and 340 $Å^3$ for the head and the tail respectively) (Breyton *et al.*, 2013), I have imposed a volume of 112,000 $Å^3$ and 108,800 $Å^3$ for the hydrophilic and hydrophobic phases of the 320 DDM molecules. The volume of AmtB (166,864 $Å^3$) was calculated based on its amino acid sequence alone using the *Biomolecular Scattering Length Density Calculator* available on line (http://psldc.isis.rl.ac.uk/Psldc). Since the trimeric nature of AmtB in solution was confirmed by my SEC-MALS and AUC analyses (see paragraph 3.3.1-3.3.2), I have imposed a P3 symmetry for the complex. Crucially, all this information can be readily obtained for any membrane protein solubilised in detergent, using widely accessible and complementary biophysical techniques

(e.g. SEC-MALS/AUC in this study). Ten MONSA runs (**Figure 3.25**) were performed and all the models look nearly identical, which demonstrates the robustness of the modelling step. A representative MONSA model with the crystal structure of AmtB docked is shown in **Figure 3.26**. The model faithfully reflects both the size and shape of the MD-generated model. The protein envelope is a good representation of the crystallographic structure of AmtB and is confined inside the detergent corona. Importantly, the joint use of both SAXS and multiple SANS datasets allowed the head- and tail-groups of the detergent corona to be distinguished and place them correctly with respect to the protein surface and solvent. Such detailed insight is usually not achieved with *ab initio* models unless additional contact restraints are applied (Koutsioubas, 2017). The detergent ring fits the contours of the protein and the positions of the two detergent phases (head- and tail-groups) are particularly clear. The hydrophobic phase is strictly contained between AmtB and the hydrophilic ring, with only the tails of DDM being in contact with the hydrophobic surface of the transmembrane domain. Hence, without using deuterated protein or detergent, and without information about the 3D structure of AmtB, the combination of SAXS and SANS data captures the essential structural details contained in membrane-protein detergent complexes in solution.

To assess and validate the multiphase modelling approach using MONSA, I have fitted the theoretical SANS and SAXS curve generated for one of the 10 models (model boxed in **Figure 3.25**) to the experimental SANS/SAXS dataset (**Figure 3.26**). I have used chi^2 as a statistical parameter to test the goodness of the fit for each theoretical SANS and SAXS curves against the experimental dataset. The chi^2 obtained for the SANS condition at 0, 22, 42, 60% D_2O and SAXS curve were 1.19, 0.44, 1.09, 4.01 and 1.72 respectively. The chi^2 values showed that the MONSA model perfectly fits the experimental SANS and SAXS dataset.

Table 3.2 Scattering length density contribution of the protein, hydrophilic heads and hydrophobic tails of the detergent at different H_2O/D_2O conditions.

	Protein	Hydrophilic heads of DDM	Hydrophobic tails of DDM
0% D2O	2.33	2.41	0.15
22% D2O	1.04	1.34	-1.38
42% D2O	-0.14	0.36	-2.77
60% D2O	-1.20	-0.52	-4.03
X-ray (electron scattering)	2.43	5.13	-1.35

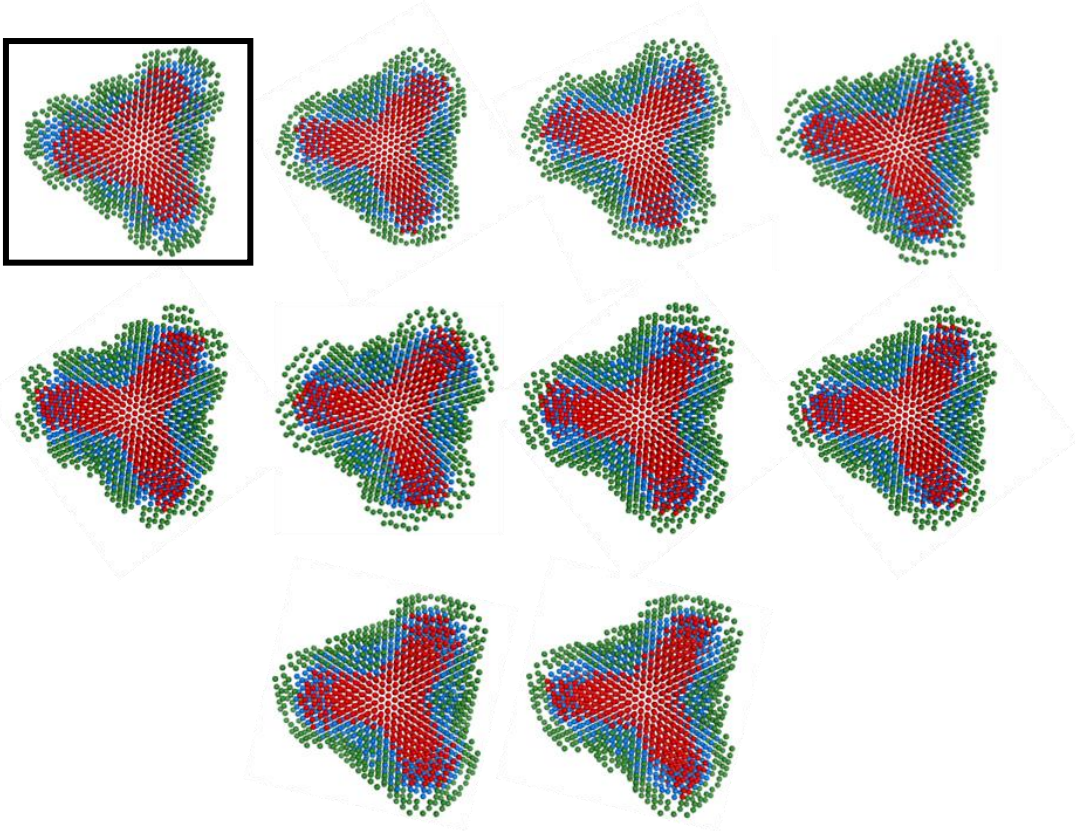

Figure 3.25 Top view of 10 different MONSA multiphase modelling using the SAXS and SANS data. The phase corresponding to the protein is represented by red beads, the hydrophilic and hydrophobic detergent density are represented by green and blue, respectively. The model in a box was used for SAS curves analysis.

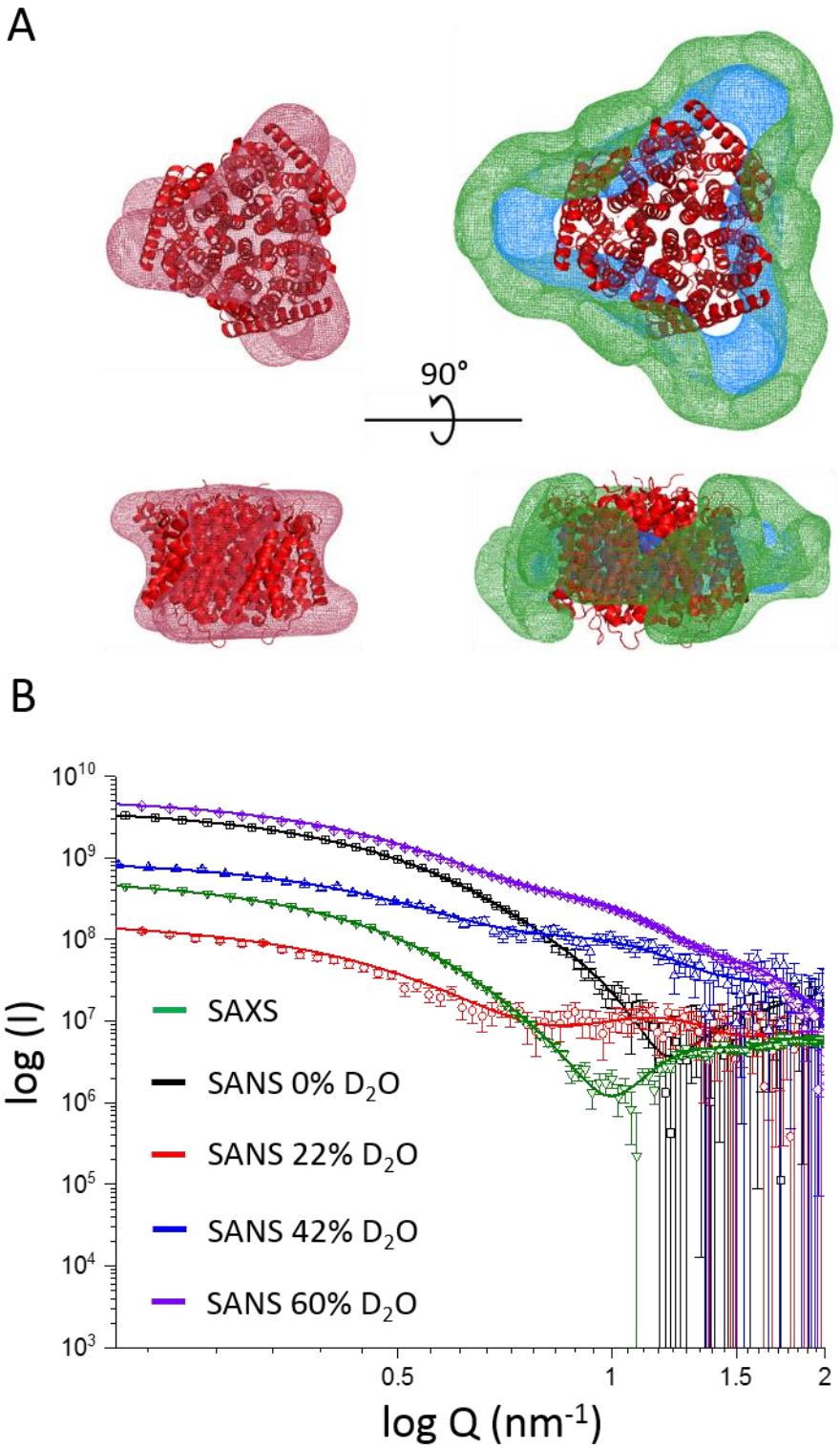

Figure 3.26 (A) MONSA multiphase model obtained using the SAXS and SANS data. **(B)** Fit of the MONSA model against the experimental SAXS data (inverted green triangle), SANS 0% (black square), 22% (red circle), 42% (blue triangle) and 60% (purple diamond) D_2O curves.

3.6.5 Structural comparison between the experimental and computational models

To compare the computational and experimental modelling approaches, I have superimposed the atomic model generated by MD simulations for AmtB at 320 DDM molecules with the experimental multiphase MONSA model (**Figure 3.27**). The positions of the hydrophobic tails and hydrophilic heads of the DDM in computational and experimental models are identical. This result emphasised that the multiphase experimental model I have obtained accurately describes the position of the detergent molecules. Thus, the accuracy of the low resolution experimental model is in agreement with the atomic computed model validating this combined approach.

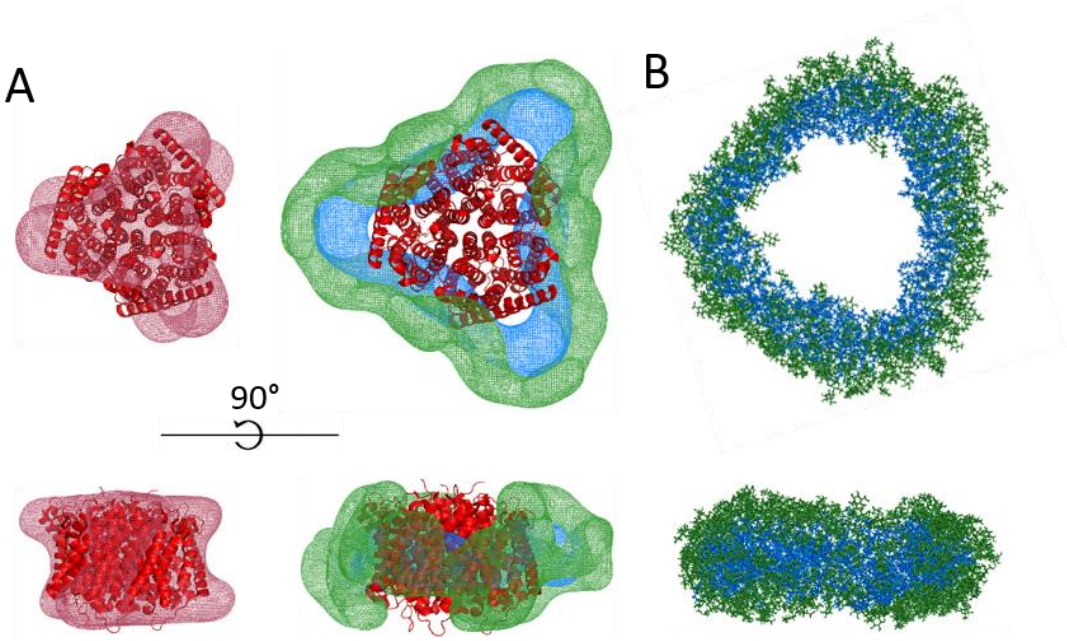

Figure 3.27 (A) MONSA multiphase modelling using the SAXS and SANS data. **(B)** Molecular dynamic model of the detergent (320 molecules) surrounded AmtB. The phase corresponding to the protein is represented in red mesh, the hydrophilic and hydrophobic detergent densities are represented in green and blue, respectively.

3.7 Discussion

The difficulty of handling membrane transporters has made it difficult to solve their structures and in numerous cases, crystallographic structures gave little, if any, information on the dynamics of the protein as exemplified by the Amt/Mep/Rp transporter family. Thus, it is timely to explore new approaches and extend the reach of new and rapidly developing SAS technologies to solve fundamental mechanistic questions about membrane transporter and channel function.

SAXS studies: In this part of my PhD project, I aimed to use SAXS to obtain structural information of AmtB in solution. In structural maps obtained by SAXS methods on membrane proteins, the detergent shell that encompasses the hydrophobic domains of the protein forms a continuous region of density. Thus, distinguishing the protein from the detergents is particularly problematic as the software used to analyse SAXS data assumes a homogenous repartition of the electron density in the PDC. To overcome this challenge, the software memprot has been developed to obtain a torus ellipsoid shape representing the detergent corona around the membrane protein (Perez and Koutsioubas, 2015). However, the use of memprot presents several limitations: 1-the high resolution structure of the membrane protein is necessary for the modelling process and 2- it as to be assumed that the crystal structure describes the overall conformation of the protein in solution (Berthaud *et al*., 2012, Perez and Koutsioubas, 2015). Memprot is a useful software to generate a coarse grained model of detergent molecules that surround membrane proteins but the resolution is low. I have therefore complemented the SAXS analysis with SANS studies combined with atomistic modelling.

SANS/CMP studies: The use of neutron instead of x-ray in scattering experiments allows us to distinguish the different components of a heterogeneous complex, for example a protein-protein, protein-RNA or protein-detergent complex (Gabel, 2015, Mahieu and Gabel, 2018). So far,

contrast match point is the most common approach to distinguish the different components of protein complexes by SANS:

1- Using deuterated proteins (Zaccai *et al.,* 2016) or deuterated detergents (Oliver *et al.,* 2017). However, producing deuterated macromolecules is time and not cost effective. In addition, deuterated media are often toxic to bacteria, leading to decreased protein yields (Xie and Zubarev, 2014). Finally commercially available deuterated detergents are extremely expensive, for example 0.5 g of deuterated DDM costs around £2,200.

2 - Using a deuterated lipid/protein in nanodiscs (Ritchie *et al.,* 2009). In this system a disc of lipid bilayer is stabilised using a membrane scaffold protein (MSP) forming a nanodisc (Ritchie *et al.,* 2009). The membrane protein is then inserted into the disk. The lipids and MSP used are usually deuterated allowing a "stealth carrier" formation, hence the scattering signal of the membrane protein can be isolated and measured independently in a "native" lipid environment (Maric *et al.,* 2014). This "stealth carrier" tool was developed by Prof. Lise Arleth and was successfully applied to obtained structural information on cytochrome P450 (Skar-Gislinge *et al.,* 2015) and bacteriorhodopsin (Kynde *et al.,* 2014). However, using deuterated macromolecules and lipids are problematic (see point 1 above).

Crucially, all the SAS analysis describe so far needs a-priori knowledge of the 3D structure of the membrane proteins. To overcome this bottleneck, I have merged my SAXS and SANS data and conducted a multiphase analysis using MONSA. This is the first time that such methodology has been applied to analyse a protein-detergent complex.

SANS/SAXS multiphase analysis: Even if the crystal structure of a membrane protein is not available, SANS measurements at different contrast match points can be used to provide low resolution structural insights as exemplified by the Slc26/SuIP family of transporters (solute carrier/sulfate transporter) (Compton *et al*., 2011, Compton *et al*., 2014). In these studies, the authors, without any information on the structure of the Slc26/SuIP transporter family, used SANS to show that these transporters dimerise in solution via their

transmembrane domain helices (TMH) and that the cytoplasmic Sulphate Transporter and AntiSigma factor antagonist (STAS) domain projects away from the TMH domain and is not involved in the dimerisation. These data were later confirmed by the first high resolution structure of a member of the Slc26/SuIP transporter family (Geertsma *et al.*, 2015). In our approach, we pushed further the boundaries of using the SAS technique at different contrast match points by performing a multiphase analysis using MONSA software (Svergun, 1999). In this modelling experiment, we merged SAXS and SANS data, without using deuterated protein/detergent to obtain unprecedented structural information on the phase density of the detergent, in particular to distinguish head- and tail-groups in the assembled membrane protein−detergent complexes. The advantage of this approach lies in the fact that it does not require information on the 3D structure of the protein, which opens up the possibility of applying this methodology to a wide range of important membrane proteins that have remained inaccessible to high resolution structural analysis. A software was developed in order to optimise *ab-initio* modelling using multiple SAS datasets. Dr. Koutsioubias recently developed an algorithm to generate a multiphase coarse-grained model capable of distinguish protein, detergent tails/heads and the solvent. Models generated with this algorithm are based on different SAXS/SANS datasets (similar to MONSA software) (Koutsioubas, 2017, Svergun, 1999). The same study showed that one scattering dataset is not enough for accurate *ab-initio* modelling. Hence, the increment of SANS datasets at different contrast match points substantially improves the fidelity of the model obtained, which is in agreement with our approach (Koutsioubas, 2017).

Future development of SAS approaches to study membrane protein dynamics:

SAXS/SANS are not able to determine atomic-resolution models of proteins *de novo* but are instead best used to validate or discard hypotheses on the structures based on *a priori* information. Thus, the combination of MD and SAS techniques provided a tool to study the dynamics of a known atomic model. Comparing the theoretical scattering curves from atomic computed models

against experimental data may help to improve our understanding of the dynamics of a transport system. An example of this application was the study undertaken by Dr. Frank Gabel and co-workers on the membrane transporter FhaC (Gabel *et al.,* 2014). In this study, the authors were able to probe fine structural details of the protein in the presence of detergent, such as the position of the N-terminal *α* helix and discard several potential conformations obtained by MD simulations. The authors, however, did not combine SANS and SAXS analysis. Our integrated approach demonstrates that combining SAXS, SANS, and iterative simulations provides much more detailed structural information than each of the methods alone. It is my belief that a hybrid approach, combining in solution SAS techniques and *in silico* modelling, will allow the description of conformational changes of membrane proteins in solution, induced by ligand or cofactor binding.

Software development for SAS analysis: A critical aspect of computing SAS data from MD simulation is that most of the software that generates theoretical scattering curves is based on an implicit solvent layer calculation of the atomic model (Knight and Hub, 2015). This means that dummy atoms are used to estimate the hydration layer of atomic model and implicit solvent calculation often leads to overestimation of the fit between experimental and computed scattering curves (Knight and Hub, 2015). Therefore, Prof. Jochen S. Hub created a software (WAXSiS) capable to explicitly calculate the hydration layer based on SAXS data (Knight and Hub, 2015, Chen and Hub, 2014). Using my dataset, the software has been extended to account for SANS data and therefore opens up this software package for future projects including both SAXS and SANS scattering data.

Combinations of SANS, SAXS and MD simulations have remained underexploited by the scientific community. In this context, this work represents a significant advancement in data acquisition, model validation, development of new software, and multiphase volumetric analysis to firmly establish SAS technology as a standard method for membrane protein structural biology

Chapter 4: Functional analysis of AmtB

Aims and objectives

The study presented in this chapter focuses on using an electrophysiological technique named Solid Supported Membrane Electrophysiology (SSME) to unravel *in vitro* the molecular mechanism of the *E.coli* ammonium transporter AmtB. To this end, I have characterised the activity of wild type AmtB and variants affected in the S1 binding site and in the hydrophobic pore (**see section 1.3.3 in Chapter 1**).

In parallel to the *in vitro* experiments, I used a yeast *in vivo* complementation assay to confirm our SSME analysis. This *in vivo* study was done in collaboration with Dr. Mélanie Boeckstaens and Dr. Anna-Maria Marini (Université Libre de Bruxelles).
My objectives were to:

1- Insert AmtB into liposomes and characterise the proteolipososmes obtained (size, protein content and orientation).

2- Develop an assay to measure the activity of AmtB using solid supported membrane electrophysiology (SSME).

3- Decouple and characterise the ammonium binding and translocation activity of AmtB by analysing the activity of variants affected in the S1 site or the hydrophobic pore.

The study presented in this Chapter and in Chapter 5 is the subject of two publications: one published in *FASEB Journal* (see **appendix B**) and one in preparation:

Dias Mirandela G, Tamburrino G, Hoskisson PA, Zachariae U, and Javelle A. (2018) The lipid environment determines the activity of the *E.coli* ammonium transporter, AmtB. *FASEB J. in press. doi: 10.1096/fj.201800782R*

Williamson* G, Tamburrino* G, Dias **Mirandela* G**, Hoskisson PA, Pisliakov A, Boeckstaens M, Marini AM, Zachariae U and Javelle A "*Mechanism of action for the ammonium transporter AmtB*." *In preparation.*

*equally contributed

4.1. Introduction

As stated in the introduction of this thesis, the *E. coli* ammonium transporter AmtB is the model system of choice to investigate ammonium uptake in the ubiquitous Amt/Mep/Rh protein family. AmtB is structurally well characterised, with more than 20 high resolution structures reported in the Protein Data Bank (PDB) to date. Despite this wealth of structural information, the ammonium transport mechanism has not yet been unravelled since all the structures show a very similar conformation irrespective of the presence or absence of ammonium. Moreover, the functional studies undertaken during the last two decades to elucidate the mechanistic of ammonium transporters led to controversial conclusions (**see Chapter 1, section 1.4**).

Recently, the activity of the ammonium transporter 1 from *A. fulgitus* (*Af*Amt1) has been characterised using Solid Supported Membrane Electrophysiology (SSME) (Wacker *et al.,* 2014). It was experimentally demonstrated for the first time that *Af*Amt1 was electrogenic indicating the translocation of NH_4^+ or NH_3 and H^+ (Wacker *et al.*, 2014). This functional breakthrough challenged all the crystal structure analyses so far showing that the pore of Amt/Mep/Rh proteins is hydrophobic (Khademi *et al*., 2004, Zheng *et al*., 2004, Andrade *et al*., 2005, Javelle *et al*., 2007, Javelle *et al*., 2008, van den Berg *et al*., 2016). To confirm that Amt proteins are electrogenic transporters, I have investigated the activity of the ammonium transporter B from *E.coli* using SSME technology. Additionally, I have measured the activity of AmtB variants affected in the S1 binding site and the hydrophobic pore (Javelle *et al*., 2008, Javelle *et al*., 2006,

Wang *et al*., 2013).

4.2 Proteoliposomes formation and characterisation

Having successfully characterised and purified AmtB solubilised in DDM (**Chapter 3**), I have reconstituted AmtB into an artificial liposome.

4.2.1 Destabilisation of the liposomes

To facilitate the insertion of AmtB, the liposomes need to be destabilised using detergent (Triton X-100). To this end, Triton X-100 is added sequentially to the liposome solution to progressively destabilise the lipid bilayer. The liposomes swell due to the insertion of detergent inside their membranes until reaching the onset of saturation (R_{sat}). When the R_{sat} limit is reached, further addition of detergent starts to solubilise the liposomes until reaching the onset of solubilisation (R_{sol}) (Rigaud *et al*., 1995, Rigaud *et al*., 1988, Rigaud, 2002, Paternostre *et al*., 1988).

To experimentally determine R_{sat} and R_{sol}, 1 µL Triton X-100 at 25% was sequentially added to 500 µL of liposomes (5 mg/mL) and the absorbance at 400 nm was monitored. The turbidity of the liposome solution increases with the addition of detergent as the liposomes become more saturated and swell. The turbidity stopped to increase after 4 µL (0.39 M) of Triton X-100 was added (R_{sat} reached). After R_{sat}, the addition of detergent decreased the absorbance until the total solubilisation of the lipids was achieved (R_{sol}) (Figure 4.1). Hence, the optimum amount of detergent for protein insertion was 1.56 µM of Triton X-100 per mg of lipid.

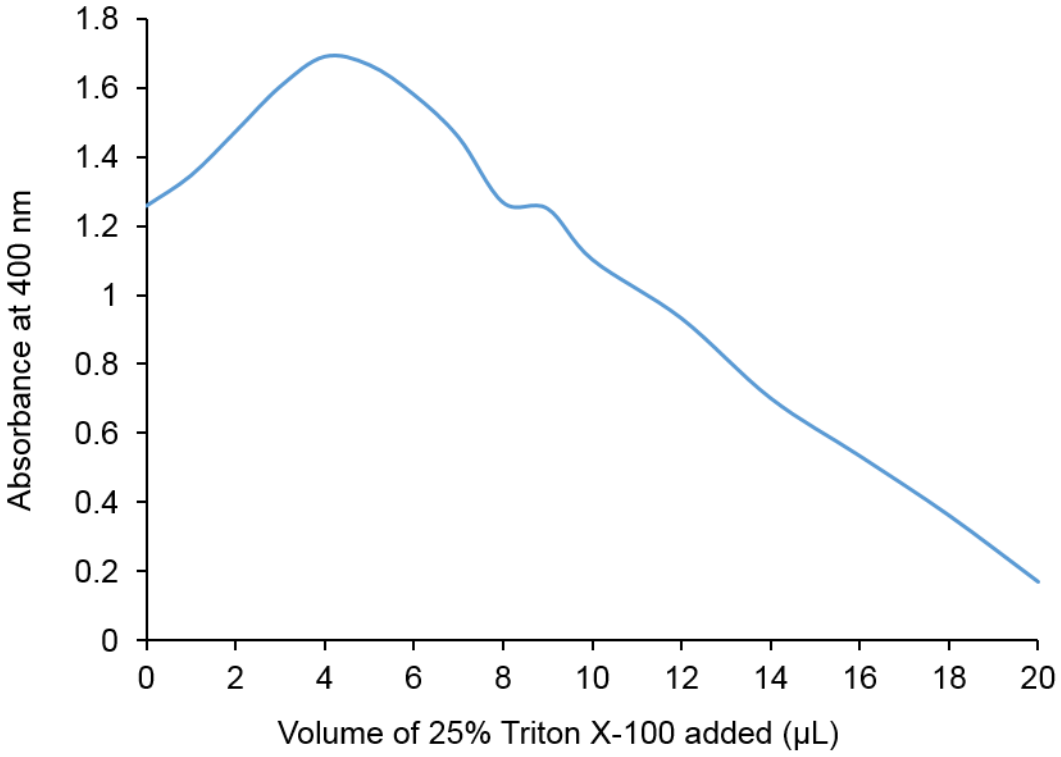

Figure 4.1 R_{sat} and R_{sol} constant determination of *E.coli* polar lipid:PC 2:1 (w/w) liposomes using Triton X-100 at 25%.

4.2.2 AmtB insertion in the liposomes

To ensure that AmtB was inserted, I have analysed the liposomes by SDS-PAGE. As previously described in **Chapter 2**, pure AmtB solubilised in DDM (5 mg/mL) was mixed into the liposomes/Triton X-100 mixture (see **section 4.2.1**). Subsequently, Triton X-100 and DDM were removed by adsorption onto hydrophobic beads (SM2 Biobeads, BioRad) to allow the insertion of AmtB inside the lipid bilayer (Galián *et al*., 2011). After an overnight incubation with SM-2 Biobeads, the proteoliposomes were diluted 10 times in liposome buffer (**see Chapter 2, Table 2.5**), collected by ultracentrifugation at 200,000 g, 4ºC for 30 minutes, and re-suspended in 6 mL of liposome buffer (as a washing step). This operation was repeated two times. Finally, after the last ultracentrifugation step, the pellet containing the proteoliposomes was re-suspended in 500 µL of liposome buffer (5 mg/mL of lipids). At each step of the process, the liposomes were analysed by SDS-PAGE gel to ensure that the protein was correctly inserted into the lipid bilayer (**Figure 4.2**). If the protein is completely inserted, no protein should be found in the wash fractions. The result presented in **Figure 4.2** shows that no protein was found in the washing fractions. The protein was only found in the proteoliposomes indicating that AmtB was inserted into the lipid bilayer.

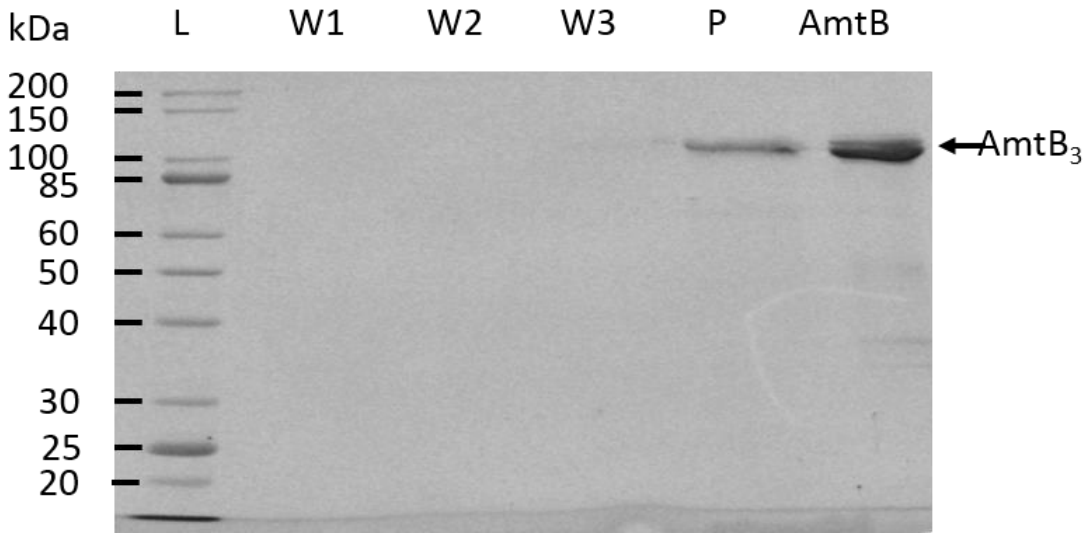

Figure 4.2: SDS-PAGE Coomassie Blue-stained gel. L; ladder, W1-3; washing fraction 1-3, P; proteoliposomes, AmtB; 5 µg of pure AmtB used for the reconstitution in the proteoliposomes.

4.2.3 Size distribution of the liposomes and proteoliposomes

The size of the liposomes and proteoliposomes were determined using dynamic light scattering (DLS).

The motion of the liposomes in the buffer was directly recorded *via* a static light scattering detector placed at certain angles. An auto-correlation function was used in order to determine the particle size distribution. The DLS analysis confirmed that liposomes and proteoliposomes follow a unimodal size distribution with a mean diameter of 110 nm, hence the insertion of AmtB did not affect the size distribution (**Figure 4.3**). In addition, the DLS profiles indicate that empty liposomes and proteoliposomes do not form aggregates. Taken together, these results show that I am able to directly compare the transient charge displacement, characterising the translocation of NH_4^+ through the membrane/AmtB in the empty liposomes/proteoliposomes respectively.

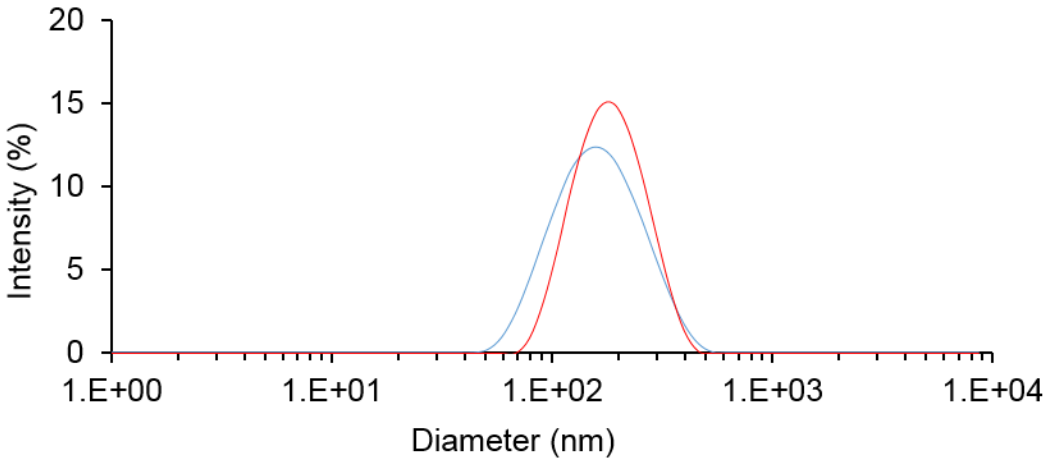

Figure 4.3: Size distribution of the empty liposomes (blue) and proteoliposomes (red) by DLS analysis.

4.2.4 Orientation of the protein into proteoliposomes

To determine if AmtB was inserted right-side-out (RSO - C-terminal tail located inside the liposome) or inside-out (IO - C-terminal tail located outside the liposome) the following methods were used:

1- Immobilised Metal Affinity Chromatography (IMAC) as described by Vitrac and co-workers (Vitrac *et al*., 2013).
2- TEV protease digestion assay as described by Wacker *et al.* (Wacker *et al*., 2014).

4.2.4.1 Orientation of the protein using IMAC matrix

Proteoliposomes were incubated in batch with Sepharose 6 matrix loaded with nickel. AmtB is fused at the C-terminal cytoplasmic tail with a hexa-His tag. If all AmtB proteins are inserted in a right-side-out (RSO) orientation in a liposome, the C-terminal affinity tags should not be accessible, hence the proteoliposomes should flow through the IMAC matrix. By contrast, if an AmtB protein is inserted inside-out (IO) in the proteoliposomes the His-tag should be accessible and the proteoliposomes are expected to bind to the matrix and thus be present in the elution fraction. As a control, I treated the proteoliposomes in parallel with DDM to solubilise AmtB and analyse it by IMAC using identical conditions as for the analysis of the proteoliposomes without DDM. The proteoliposomes (5 mg/mL) were treated with or without 2% DDM and incubated with the Ni-sepharose 6 affinity resin at 4ºC for 1 hour. The supernatant was collected after centrifugation and the resin was washed 4 times with non-activated buffer (**Chapter 2, Table 2.6**). The proteoliposomes were eluted in non-activated (NA) buffer containing 500 mM imidazole (**see Chapter 2 for details**). The flow through, wash and elution fractions were analysed by SDS-PAGE (**Figure 4.4**).

When the liposomes were treated with DDM, AmtB was almost exclusively present in the elution fraction as expected. Without DDM treatment, however, more than half of AmtB is present in the flowthrough (**Figure 4.4, FT minus condition**). This result indicated that in more than 50% of the proteoliposomes not a single protein is IO oriented (**Figure 4.4**).

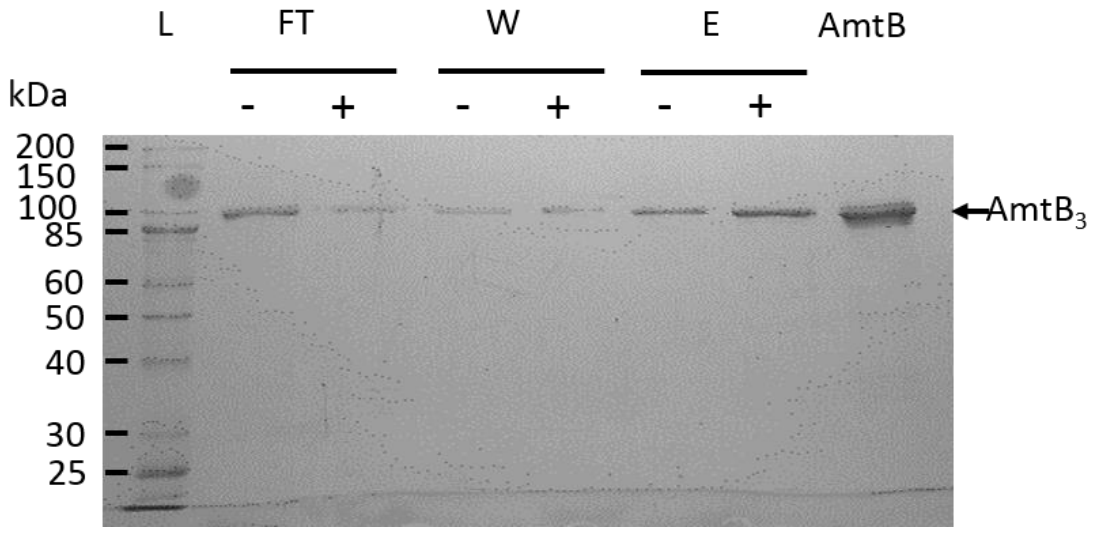

Figure 4.4: Determination of AmtB orientation in the proteoliposomes by IMAC. SDS-PAGE Coomassie Blue-stained gel the lipososmes purified by IMAC after DDM treatment (+) or in absence of DDM (-). L; ladder, FT; flow through, W; wash, E; elution fraction, AmtB; 5 µg of pure AmtB used for the reconstitution in the proteoliposomes.

4.2.4.2 Orientation of the protein using TEV protease digestion analysis

A chimeric AmtB protein containing a TEV cleavable site inserted between the C-terminal tail and the hexa-his tag (**Chapter 2, Table 2.3**) was inserted into liposomes according to the procedure described in **Chapter 2, section 2.3.1**. The proteoliposomes were treated with the TEV protease. As a control the same digestion experiment was done using pure AmtB protein and proteoliposomes solubilised by 1.25% of Triton X100.

The different reactions were analysed after digestion by SDS-PAGE. If AmtB inserted into proteoliposomes is orientated IO, the TEV protease will cleave the His-tag (~20 amino-acids lacking) leading to the shortening of the protein visualised on SDS-PAGE.

Only a light intensity band corresponding to non-digested AmtB was observed on the SDS-PAGE analysis indicating that the majority of AmtB was digested by the TEV (**Figure 4.5, Label 2**). This result shows that the majority of AmtB was inserted IO (**Figure 4.5**). Surprisingly both “IMAC” and “TEV protease” approaches gave contradicting results. It is therefore difficult to precisely quantify the amount of AmtB oriented RSO or RSO/IO. I can only conclude that there is a mixture of RSO/IO protein in the proteoliposomes. Therefore, a complementary experiment was undertaken to compare the activity of AmtB measured by SSME using a mixture of RSO/IO or pure RSO proteoliposomes. (see **section 4.3.1**).

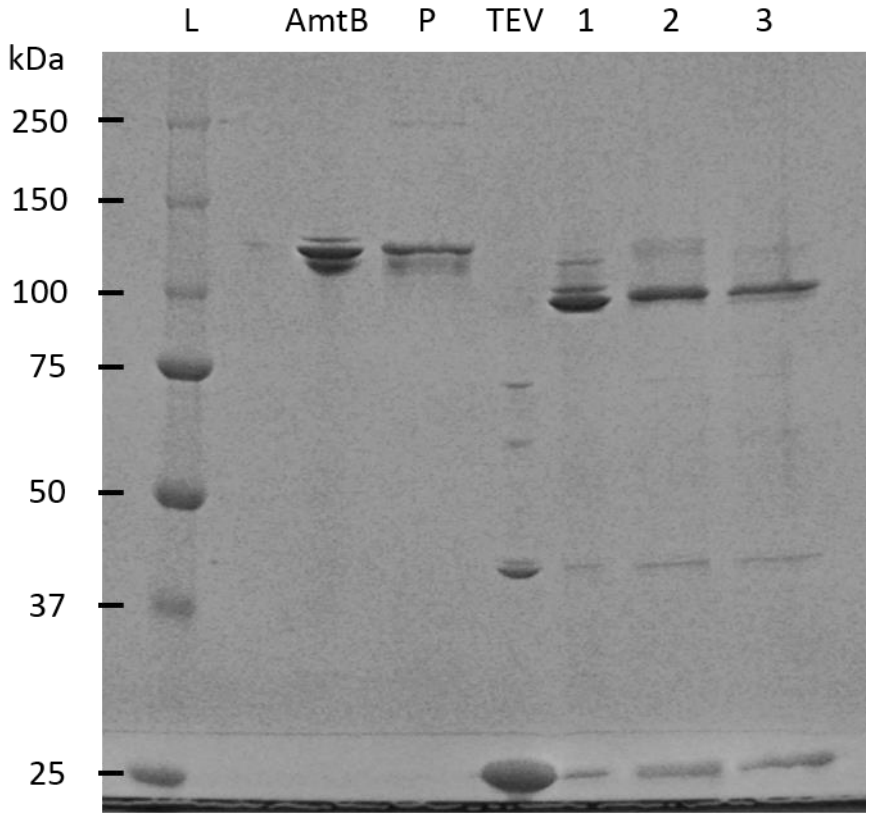

Figure 4.5: Determination of AmtB orientation in the proteoliposomes using TEV protease. SDS-PAGE Coomassie Blue-stained gel of 5 µg of pure AmtB used for the reconstitution in the proteoliposomes (AmtB), proteoliposomes (P), 5 µg of purified TEV (TEV), pure AmtB digested with TEV (1), proteoliposomes digested with TEV (2) and proteoliposomes solubilised by 1.25% Triton X-100 and digested with TEV (3).

4.3 Characterisation of AmtB activity using the Solid Supported Membrane Electrophysiology Technique (SSME)

4.3.1 Electrophysiological measurements on proteoliposomes at different lipid protein ratios

After an ammonium pulse of 100 mM to the proteoliposomes containing AmtB, a fast positive transient current of 3.3 nA was measured by SSME whereas no current was recorded for empty liposomes. I show a representative trace in **Figure 4.6, panel A** but It should be noted that the amplitude of the transient current differs from sensor to sensor because the number of proteoliposomes coated on the solid supported membrane (SSM) varies (Bazzone *et al.*, 2017). The average transient current peak measured in multiple sensors for a pulse of 100 mM ammonium at LPR (Lipid protein ratio) 10 was 3.37±0.26 nA. The current measured by SSME is transient because the charge displacement inside the proteoliposomes creates an outwardly directed negative membrane potential that progressively inhibits the transport cycle. Thus, a typical SSME trace possessed two phases 1- a rapid increase of the current followed by 2- an exponential decrease characterised by a decay time. The decay time of the second phase measures the velocity at which the membrane potential is created. This fast transient current measures both pre-steady-state charge displacement, corresponding to the interaction of ammonium with AmtB, and steady-state charge displacement, describing the continuous turnover during the complete transport cycle of AmtB (Bazzone *et al.*, 2017).

The proteoliposomes contained a mixture of RSO/IO oriented AmtB as presented in **section 4.2.4**. To estimate the effect of AmtB orientation on the transient current measured by SSME, I have measured the charge displacement on a majority of RSO proteoliposomes. To collect the proteoliposomes in which AmtB is mainly RSO orientated, I incubated the mixed RSO/IO proteoliposomes with IMAC resin and collected the flow through. A majority of RSO oriented AmtB are present in the flow through. The transient currents measured after an ammonium pulse of 100 mM in

proteoliposomes containing AmtB mainly oriented RSO or RSO/IO were normalised and compared (**Figure 4.7**). The overall shape of both transient currents was the same, thus I hypothesised that it is justified not to purify the proteoliposomes before each SSME measurement.

To further confirm that the transient currents correspond to the translocation of ammonium into the proteoliposomes, rather than a simple interaction between the substrate and the transporters, I have investigated the effect of varying the number of transporters per proteoliposome on the charge displacement. It is expected that the decay time is prolonged with increasing protein density in the liposomes if the current represents a complete transport cycle, while it should be independent if the current reflects a simple interaction between the substrate and the protein (Zuber *et al.,* 2005). To test this, I have reconstituted AmtB into liposomes at LPR 50, 10 and 5 (w/w). To confirm the variation of AmtB density in the proteoliposomes prepared at various LPR, the same quantity of proteoliposomes, for each LPR condition, was loaded on a SDS-PAGE. The SDS-PAGE confirmed that the protein density in the proteoliposomes changed in agreement with the LPR (**Figure 4.6, B**). After a pulse of 100 mM ammonium, the maximum amplitude of the transient current between LPR 50, 10 and 5 increased from 0.47±0.02 nA to 3.37±0.26 and 7.90±0.35, respectively. More importantly, the decay rate constant of the second phase increased from 9.5±0.7 s^{-1} to 13.4±1.6 s^{-1} and 18.7±1 s^{-1} (**Figure 4.6**).

Taken together, these results showed that:

1- A charge displacement specific to AmtB can be detected.
2- The transient current describes the complete transport cycle.

I conclude that AmtB is an electrogenic transporter acting as a NH_3/H^+ symporter or NH_4^+ uniporter.

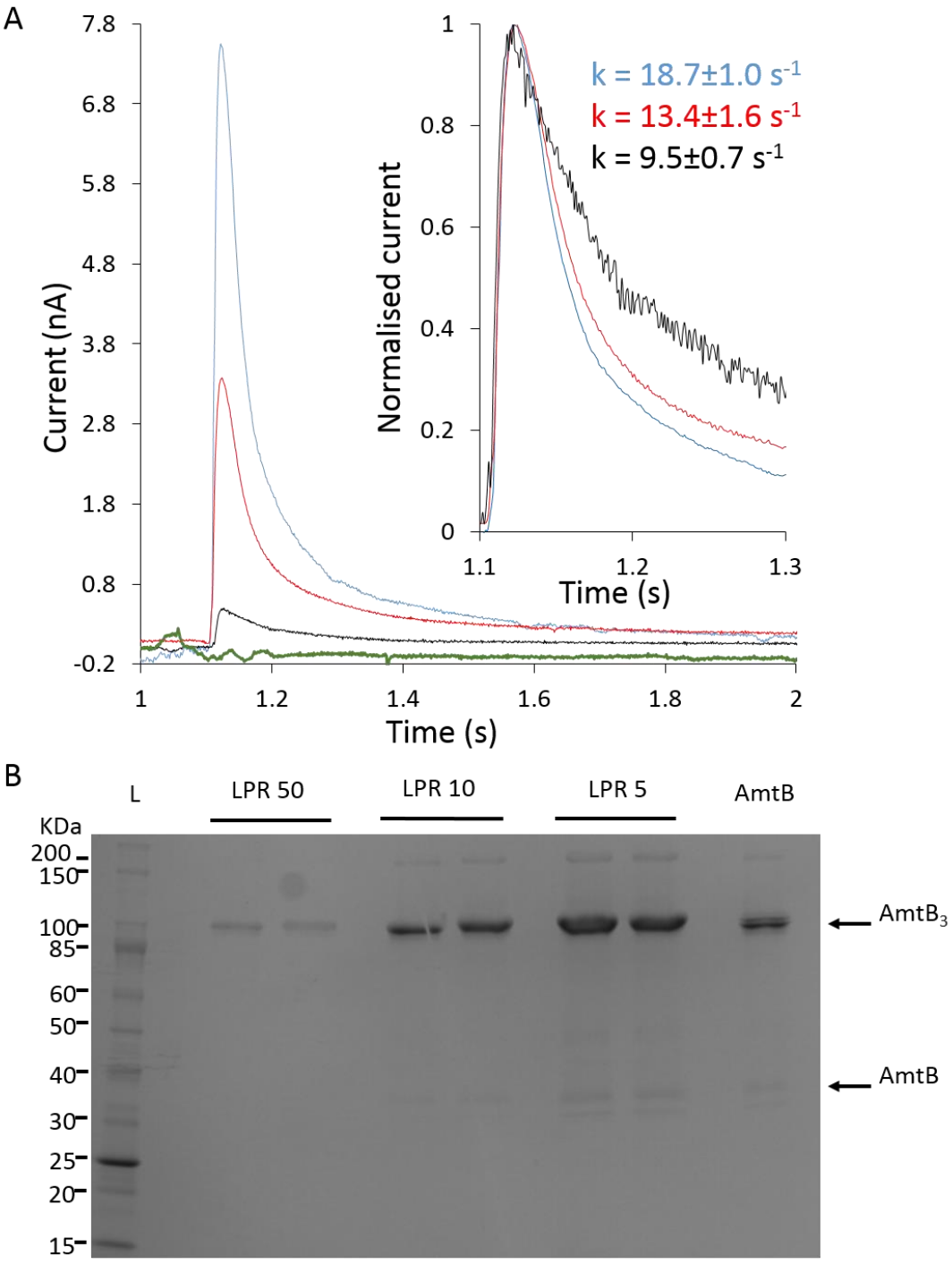

Figure 4.6: Characterisation of AmtB activity. **(A)** Transient current measured after a 100 mM ammonium pulse in empty liposomes (green) or proteoliposomes containing AmtB at a LPR50 (black), 10 (red) or 5 (blue). (***Insert***): Normalised current measured in proteoliposomes containing AmtB at a LPR50 (black), 10 (red) or 5 (blue). **(B)** SDS-PAGE Coomassie Blue-stained gel of proteoliposomes containing AmtB at a LPR 50, 10 and 5, AmtB; 5 mg of pure AmtB used for the reconstitution in the proteoliposomes.

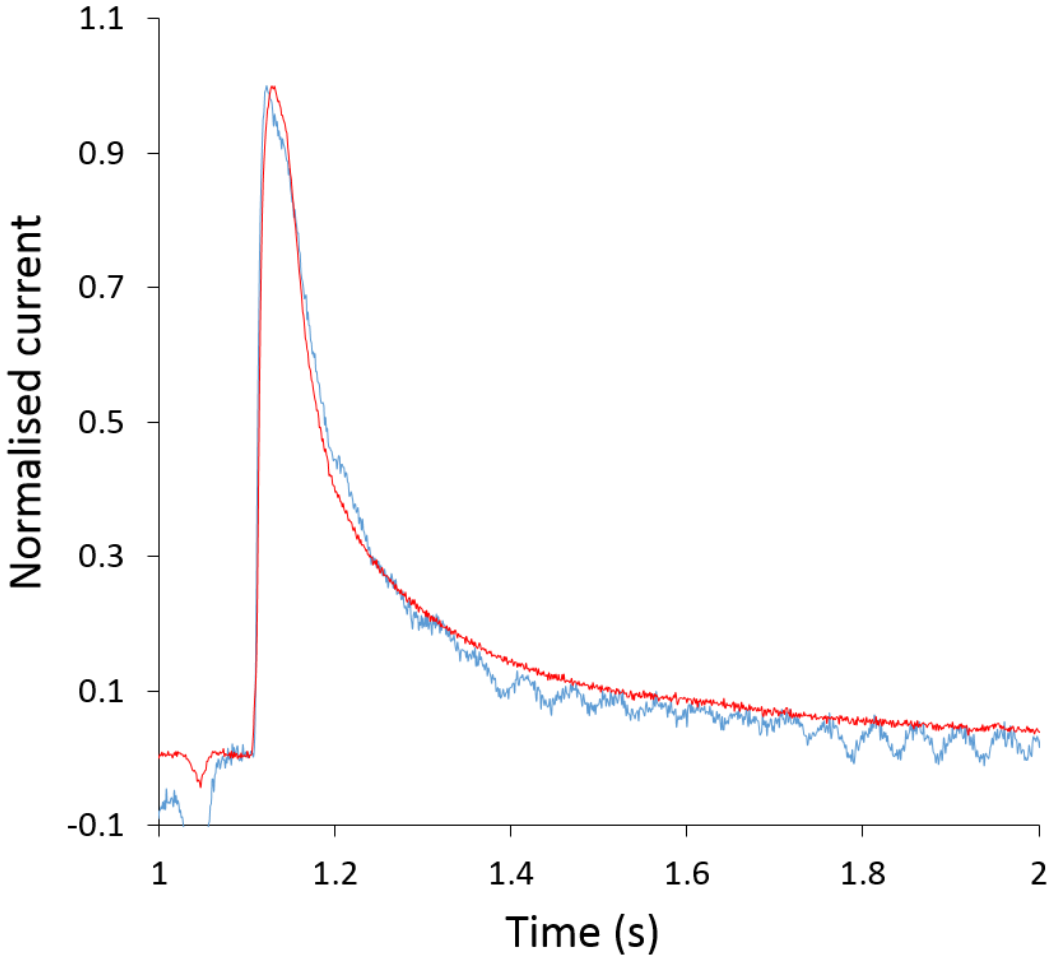

Figure 4.7*:* Functional characterisation of different AmtB orientations. Normalised current measured in proteoliposomes containing a mixed orientation of AmtB (red) or proteoliposomes containing AmtB orientated RSO (blue).

4.3.2 Substrate specificity

To characterise the specificity of AmtB towards monovalent cations, I measured the current after pulses of Na^+ and K^+. The ionic radii of Na^+ (0.116 nm), and K^+ (0.152 nm) are similar to the size of NH_4^+ ion (0.151 nm) (Shannon, 1976). Despite this, a pulse of 100 mM Na^+ or K^+ did not trigger any charge displacement which shows that these ions neither interact, nor are translocated through AmtB (**Figure 4.8**).

Next, I investigated the specificity of AmtB for ammonium versus methylammonium (MeA). MeA has been widely used to measure ammonium transport activity (for review see Javelle *at al*., 2007 and references herein). Here, I show that a pulse of 100 mM MeA triggers a transient current of 0.50±0.02 nA, compared to 3.37±0.26 nA for ammonium, while the decay constant is 4 times lower (**Figure 4.8**). To characterise the kinetics of ammonium and MeA translocation, the transient currents were measured in proteoliposomes reconstituted at LPR10, following ammonium or MeA pulses ranging from 0.024 mM to 100 mM. The peak current is saturated between ammonium pulses of 25-50 mM. Therefore, I normalised our recordings against the maximum current measured at 100 mM for ammonium. The data were then fitted according to the Michaelis-Menten equation (r^2=0.99) and a K_m of 0.8±0.1 mM was calculated for ammonium (**Figure 4.9**). A K_m 70 times higher (55.8 mM) was calculated for MeA uptake (**Figure 4.9**). Taken together, these results showed that AmtB is highly specific for ammonium which indicates that MeA is a poor substrate analogue not suited to elucidate the mechanistic details of AmtB activity.

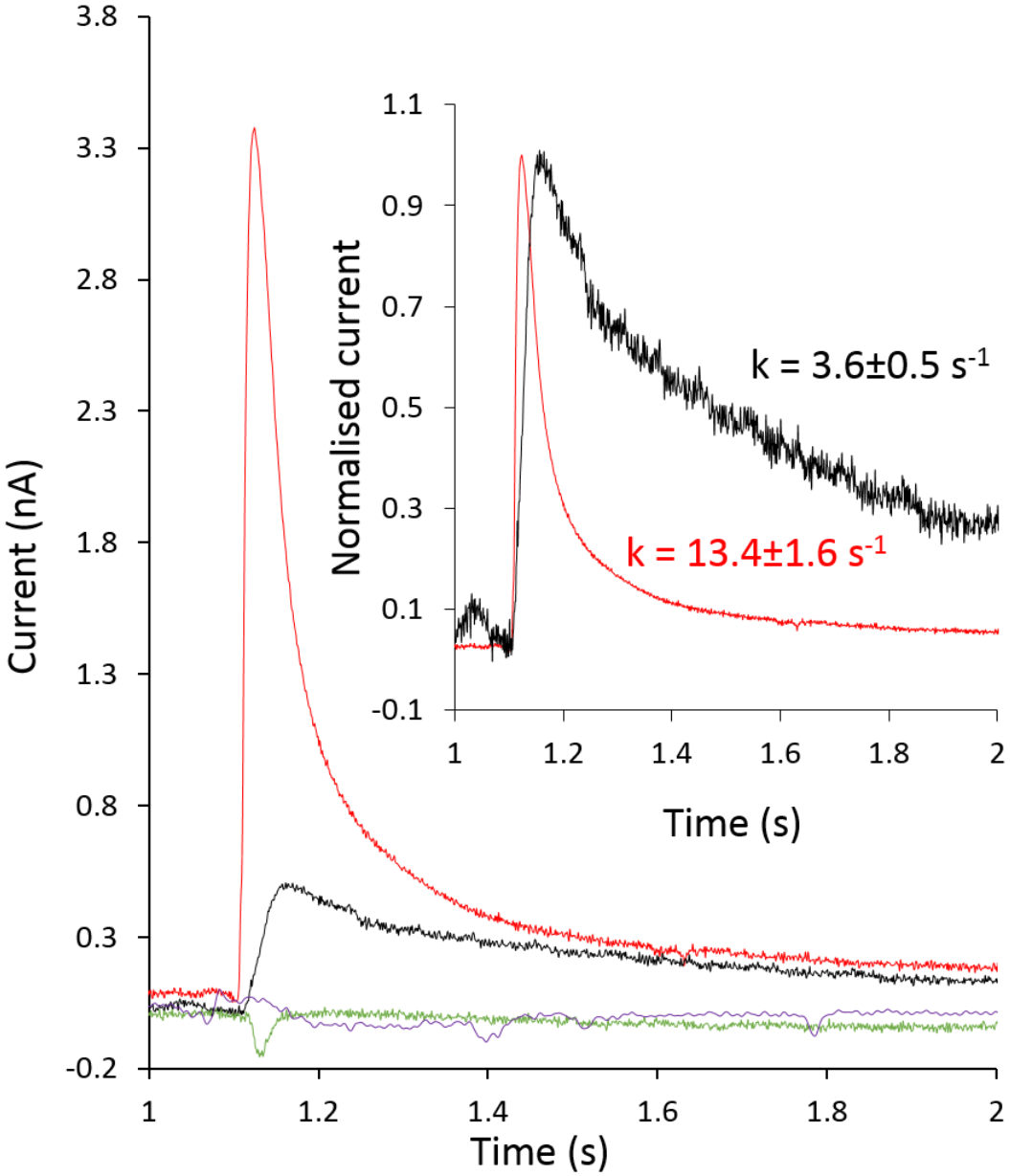

Figure 4.8*:* Specificity of AmtB activity: Transient current measured on proteoliposomes containing AmtB at a LPR10 after a 100 mM substrate pulse. Ammonium (Red), methylammonium (black), potassium (green) or sodium (purple). **(*Insert*)** Normalised current after a 100 mM substrate pulse ammonium (red) and methylammonium (black).

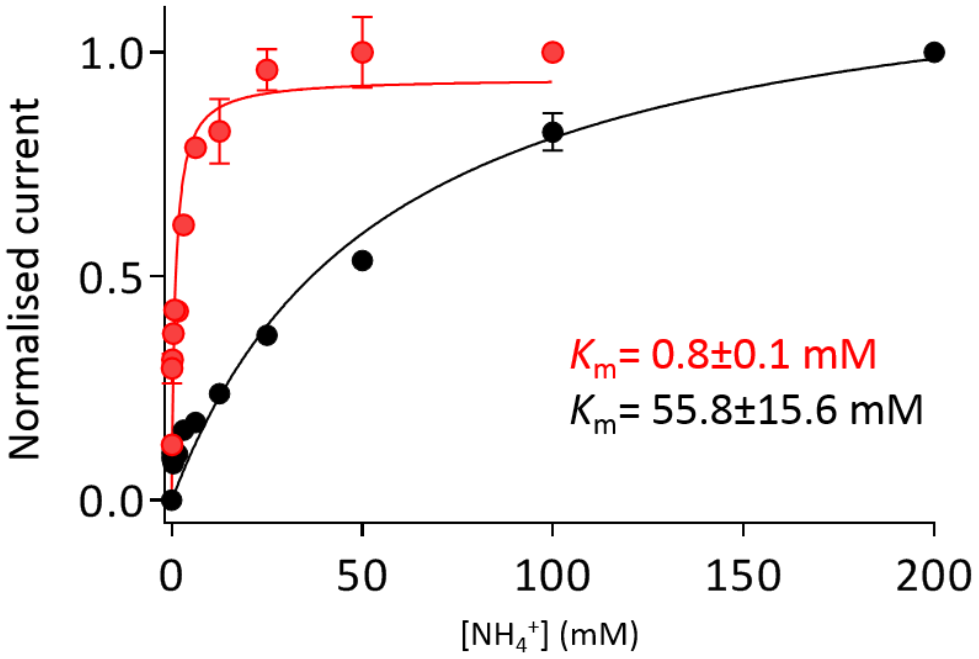

Figure 4.9: Kinetics analysis for the translocation of ammonium (red) or MeA (black) through AmtB. The currents were normalised against the maximum amplitude measured after a substrate pulse of 100 mM.

4.3.3 Current reconstruction

The transient current measures both pre-steady and steady state charge displacement. However, the steady state current which describes the full turnover of the transport activity can be reconstructed by analysing the system as an electrical circuit (Mager *et al.*, 2011). The detailed procedure for the current reconstruction is described in **Chapter 2, section 2.4.2.5**.

An ammonium or MeA pulse of 100 mM triggered a steady-state current of ~4 nA, or ~0.5 nA respectively (**Figure 4.10**). This shows that both MeA and ammonium are transported by AmtB, but MeA is translocated at a greatly reduced rate. These results show further that MeA is a poor substrate analogue, not suited to elucidate the mechanistic details of AmtB activity. The implication is that all previous analyses, aiming at answering mechanistic questions about AmtB using MeA should be re-evaluated with care.

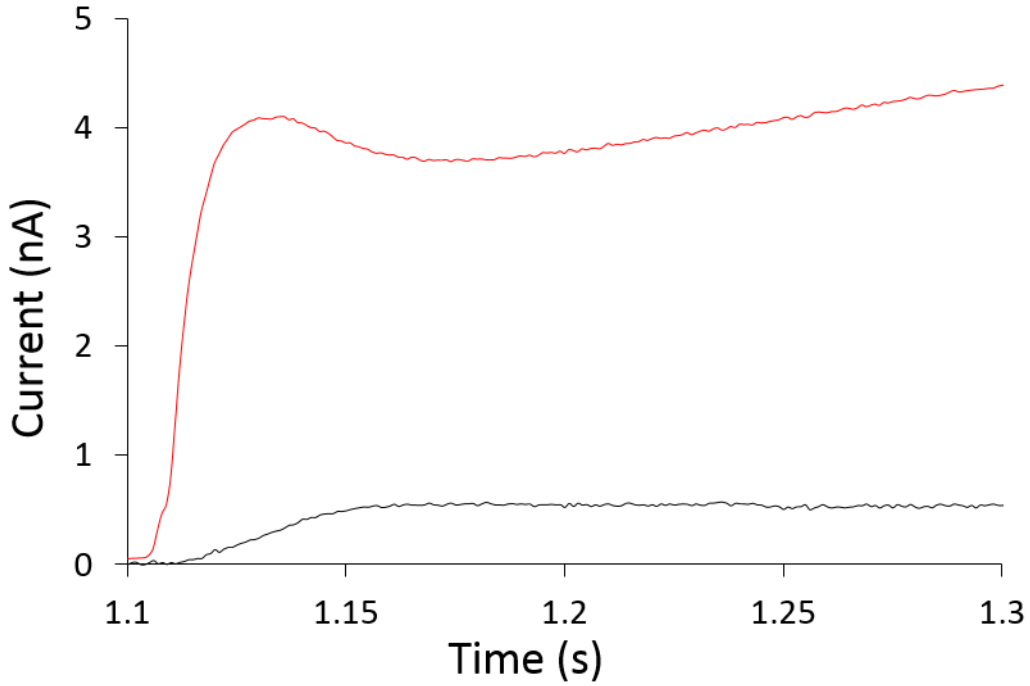

Figure 4.10: Reconstructed current using circuit analysis after a 100 mM pulse of ammonium (red) or methylammonium (black).

4.4 Characterisation of AmtB variants activities

I have previously demonstrated that it was possible to “mathematically” disconnect the steady state from the pre-steady state current associated with AmtB activity (see **section 4.3.3**). This indicates that there are at least two steps in the transport mechanism: 1- substrate/protein interaction and 2- substrate translocation. This is perhaps not surprising but it rules out a simple channel-like mechanism as previously proposed (Soupene *et al.,* 2002). In this section my aim was to experimentally show the existence of the two steps. To this end, I have disconnected the pre-steady state (substrate-protein interaction) and steady state (continuous turnover of the transport cycle) current by analysing numerous variants. Previous structural and functional analyses have shown that the residue Ser219 in the S1 site and the twin-His motif His168/His318 in the hydrophobic pore were particularly important for NH_4^+ recruitment and translocation respectively (Hall and Kustu, 2011, Javelle *et al.*, 2008, Javelle *et al.*, 2006). However, these functional data were collected using the non-suitable substrate analogue MeA. I have therefore analysed the activity of AmtB Ser219Ala, His168Ala/His318Ala and His168Ala/Ser219Ala/His318Ala variants using the real substrate (ammonium) and a combination of *in vivo* (**section 4.4.1**) and *in vitro* (**section 4.4.2**) techniques.

4.4.1 *In vivo* characterisation of AmtB variants in *S. cerevisiae*

First, I took advantage of the very clear ammonium-dependent growth phenotype of *S. cerevisiae* lacking all three *MEP* genes to characterise the phenotype associated with the activity of the AmtB variants (Wang *et al*., 2013). The wild-type and the variants Ser219Ala, His168Ala/His318Ala and His168Ala/Ser219Ala/His318Ala were expressed from the pDR195 plasmid in the *S. cerevisiae* strain 31019b (*ΔMEP1-3*). Growth phenotype analysis (**Figure 4.11**) showed that the *S. cerevisiae ΔMEP1-3* strains expressing or not Mep1, Mep 2, AmtB wild type/variants grew equally well on medium

containing glutamate as the sole nitrogen source, showing that the expression in trans of Mep1, 2 and AmtB is non-toxic to the cells. The *ΔMEP1-3* strain did not grow after 5 days at 30°C when 1 or 3 mM NH_4Cl was used as sole nitrogen source. The *ΔMEP1-3* strain expressing Mep1 or Mep2 or AmtB wild type/AmtB^{Ser219Ala} grew equally well on medium containing 1 or 3 mM ammonium as the sole nitrogen source but no growth was observed when the cells expressed AmtB$^{His168Ala/His318Ala}$ and AmtB$^{His168Ala/Ser219Ala/His318Ala}$ (**Figure 4.11**). This *in vivo* data shows that substituting only one residue in the S1 site does not prevent translocation of ammonium but changing both residues in the twin-his motif in the pore does impair ammonium translocation in yeast cells.

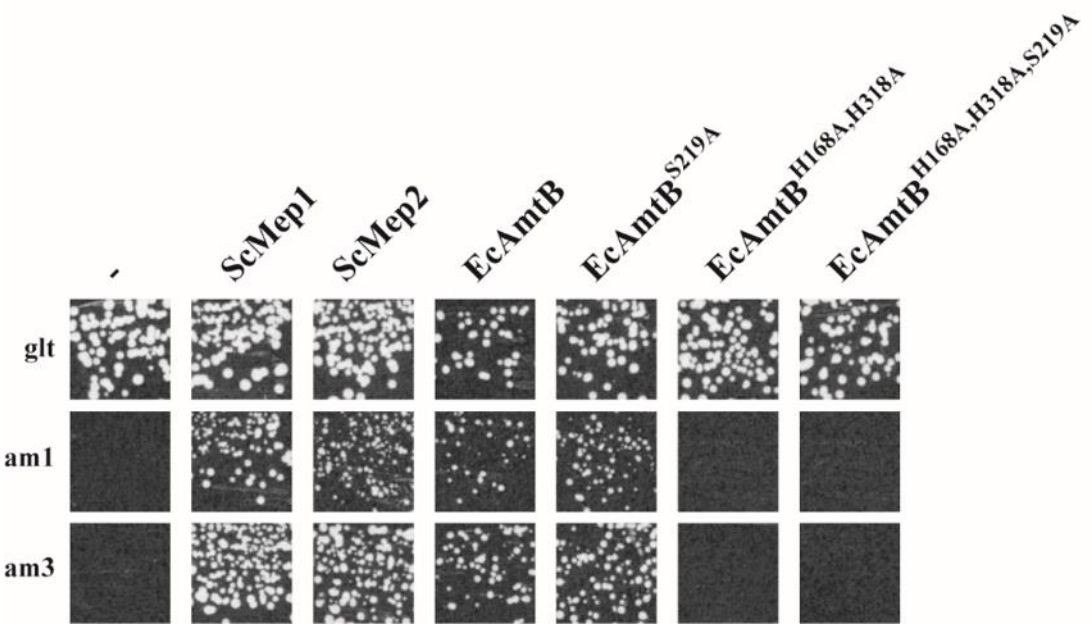

Figure 4.11*:* Growth tests of *Saccharomyces cerevisiae* yeast cells on solid medium. Medium containing, as the sole nitrogen source, ammonium 1 or 3 mM (Am1, Am3), or glutamate 0.1% (Glt, positive growth control). Triple-*MEPΔ* (*MEP1Δ MEP2Δ MEP3Δ*, 31019b) cells were transformed with an empty vector (-, pDR195), with a low-copy-number plasmid YCpScMep1, or YCpScMep2, or with a multi-copy plasmid pDR195EcAmtB, pDR195EcAmtB^{Ser219Ala}, pDR195EcAmtB$^{His168Ala/His318Ala}$, or pDR195EcAmtB$^{His168Ala/Ser219Ala/His318Ala}$. Cells were incubated for 3 days at 29°C.

4.4.2. *In vitro* SSME study on AmtB variants

To compare the qualitative result of the *in vivo* complementation test with the SSME *in vitro* assay, I next measured the transient current produced in response to ammonium pulses in proteoliposomes containing the Ser219Ala, His168Ala/His318Ala or His168Ala/Ser219Ala/His318Ala variants.

To be able to directly compare the transient current measured in the proteoliposomes containing the different variants, I have characterised their size distribution and the quantity of protein per proteoliposomes using DLS and SDS-PAGE analysis respectively (**Figure 4.12 and Figure 4.13, panel A upper insert**). The DLS and SDS-PAGE confirmed that the size of the liposomes and the quantity of the protein reconstituted were equivalent for all AmtB variants (**Figure 4.12 and Figure 4.13, panel A**).

4.4.2.1 Ser219Ala variant

To assess the influence of the S1 site on AmtB activity, I have measured the current associated with a Ser219Ala variant. After a 100 mM ammonium pulse, an $AmtB^{Ser219Ala}$ variant triggered a transient current with a maximum amplitude of 1.86±0.04 nA which is ~2 times lower than the wild-type (**Figure 4.13, panel A**). To ensure that this transient current corresponds to the complete translocation cycle, the effect of the protein density on the decay time was investigated. To this end I have reconstituted $AmtB^{Ser219Ala}$ at LPR 50, 10 and 5. An ammonium pulse of 100 mM did not trigger a measurable transient current at LPR 50, however the decay time constant increased from 15.0±0.6 s^{-1} at LPR 5 to 22.9±1.4 s^{-1} at LPR10 (**Figure 4.13, B left panel**). This data showed that the Ser219Ala variant completed the full transport cycle and translocated ammonium into the proteoliposomes but the transport rate is lower compared to the wild type protein. Surprisingly, the kinetics analysis showed that the K_ms calculated for AmtB and $AmtB^{Ser219Ala}$ were similar (0.8 vs 1 mM respectively). This counterintuitive result indicates that the K_m associated with AmtB activity does not represent the binding of NH_4^+ at

the S1 site and that a higher thermodynamic barrier associated with ammonium translocation exists below the S1 site.

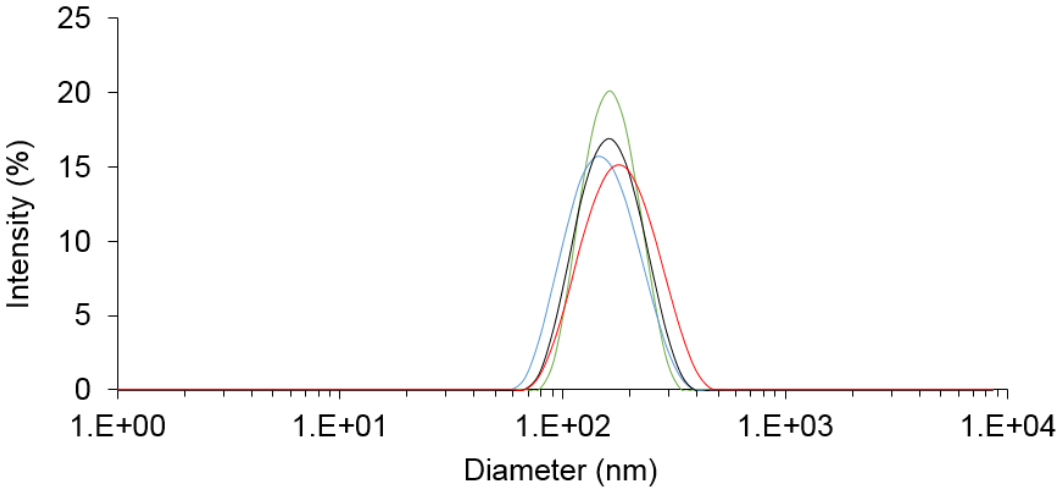

Figure 4.12: Size distribution of the proteoliposomes containing AmtB WT (red), AmtB^{Ser219Ala} (blue), AmtB$^{His168Ala/His318Ala}$ (black), AmtB$^{Ser219Ala/His168Ala/His318Ala}$ (green) by DLS analysis.

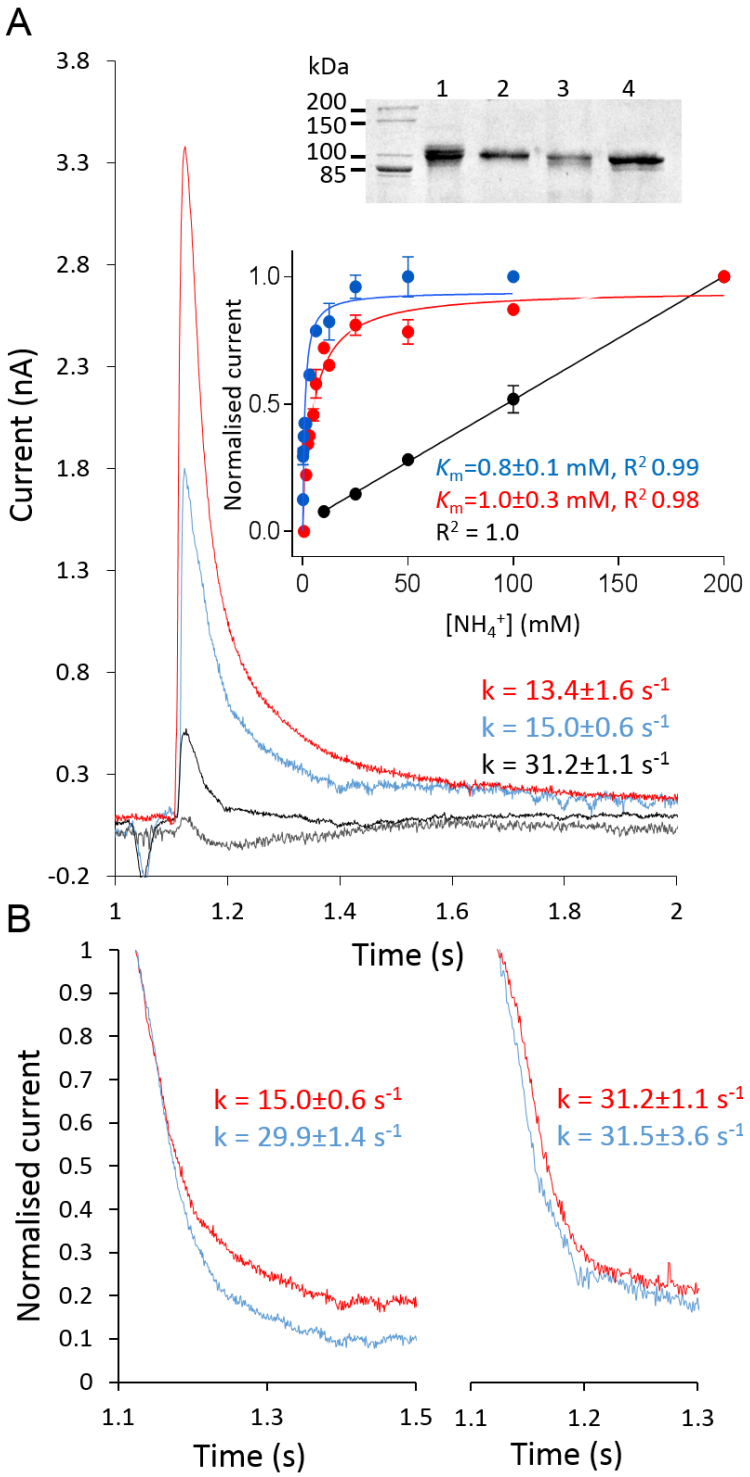

Figure 4.13: Activity analysis of AmtB variant. **(A)** Transient current (100 mM ammonium pulse) measured on proteoliposome containing AmtB (red), AmtB^{Ser219Ala} (blue), AmtB$^{His168Ala/His318Ala}$ (black), AmtB$^{Ser219Ala/His168Ala/His318Ala}$ (grey). (***Insert*): *Upper panel*** SDS-PAGE Coomassie Blue-stained gel of 5mg of pure AmtB (Lane 1), proteolipososmes (50 mg of lipids loaded in each lane) containing AmtB^{Ser219Ala} (lane 2), AmtB$^{His168Ala/His318Ala}$ (lane 3), AmtB$^{Ser219Ala/His168Ala/His318Ala}$ (lane 4). ***Lower panel,*** ammonium dependence of the maximum amplitude of the transient current for proteoliposome containing AmtB (red), AmtB^{Ser219Ala} (blue), AmtB$^{His168Ala/His318Ala}$ (black). **(B)** Normalised current after a 100mM ammonium pulse in liposomes containing AmtB^{Ser219Ala} (**left panel**) *or* AmtB$^{His168Ala/His318Ala}$ (**right panel**). Blue; LPR5, red; LPR10.

4.4.2.2 His168Ala/His318Ala variant:

In proteoliposomes containing AmtB$^{His168Ala/His318Ala}$, an ammonium pulse of 100 mM triggered a transient current with a maximum amplitude of 0.52±0.04 nA (compared to 3.37 for wild type AmtB) (**Figure 4.13, panel A**). Moreover, no signal was observed following an ammonium pulse below 12.5 mM and the current decay constant increased by more than 2 when compared to the current associated with the activity of wild type (**Figure 4.13, panel A**). This result show that the activity of the variant His168Ala/His318Ala was ~7 times lower than the WT.

To understand whether the AmtB$^{His168Ala/His318Ala}$ completed the full transport cycle, I have investigated the impact of the protein density on the current decay time. To this end I have reconstituted AmtB$^{His168Ala/His318Ala}$ at LPR50, 10 and 5. No charge displacement was measured at LPR50 after an ammonium pulse at 100 mM, however, the decay time associated with the charge displacement at LPR10 and 5 was similar and within error (31.2±1.1 s^{-1} vs. 31.5±3.6 s^{-1}) (**Figure 4.13, B left panel**) indicating that AmtB$^{His168Ala/His318Ala}$ variant generated only a pre-steady state current. The kinetics of the pre-steady-state charge displacement associated with AmtB$^{His168Ala/His318Ala}$ activity was not saturable in an ammonium concentration range of 12.5-200 mM (**Figure 4.13, panel A**).

From these results, I conclude that the current associated with AmtB$^{His168Ala/His318Ala}$ characterised a weak ammonium interaction with AmtB, most probably at the S1 site, but ammonium is not translocated through the hydrophobic pore. To validate my hypothesis, I have measured the current associated with the activity of a triple His168Ala/Ser219Ala/His318Ala variant in which the S1 site and the hydrophobic pore are altered. As shown in **Figure 4.13, panel A**, a pulse of 100mM ammonium does not trigger a measurable charge displacement above background, confirming that the current associated with AmtB$^{His168Ala/His318Ala}$ activity was due to the interaction of NH_4^+ at the S1 site.

4.5 Discussion

AmtB is an electrogenic transporter: A plethora of functional studies aimed at elucidating the mechanism of ammonium transport by Amt proteins have led to considerable controversy due to the lack of an *in vitro* assay characterising the activity of Amt proteins using ammonium as substrate (Andrade and Einsle, 2007, Javelle *et al*., 2007). The elegant work of Wacker *et al*., showed that two ammonium transporters from *Archaeoglobus fulgidus* activity are electrogenic (Wacker *et al.,* 2014). My study shows that the activity of AmtB, the archetypal Amt/Mep/Rh protein, is also associated with charge translocation across the membrane, which suggests that electrogenic transport may be a general feature for Amt proteins. The SSME analysis also demonstrated that, contrary to *A. fulgitus* Amt1, AmtB highly discriminates between MeA and ammonium as substrates. While in *Af*Amt1, MeA triggers a transient current amounting to 87% of the current elicited by ammonium (Wacker *et al*., 2014), the current induced by MeA in AmtB is less than 15% of that observed for ammonium (see **Figure 4.7**). The structural basis of this discrepancy is not yet clear since the three principal conserved features, namely the S1 binding site, the “Phe gate” and the pore twin-His motif (**see Chapter 1, section 1.3**) are conserved between both proteins. However, this functional difference, at the molecular level, between eubacterial and archaeal Amts raises important questions about the universality of the transport mechanism in microbial ammonium transporters. In this context, I have shown that *S. cerevisiae* Mep2 transporter may not acts as an electrogenic transporter (see **Chapter 6**).

I have hypothesised that ammonium transport across AmtB is electrogenic, thus AmtB acts as a NH_4^+ uniporter or NH_3/H^+ symporter. In recent work in yeast, Ariz *et al*. demonstrated, experimentally and for the first time, that the translocation of NH_4^+ was associated with deprotonation, ruling out the hypothesis of a direct NH_4^+ translocation (Ariz *et al.*, 2018). As already discussed, the hydrophobicity of the pore does not allow charge passage raising the question of how the proton is translocated by the protein. I will now

present the hypothesis we have developed concerning this intriguing and crucial mechanistic question.

Importance of the S1 binding site:

I have shown that a Ser219Ala variant is still able to generate a transient current ~2 times lower than the WT. In contrast, Javelle and co-workers observed a Ser219Ala variant possessed a higher transport activity compared to the WT using the *in vivo* MeA uptake assay (Javelle *et al.,* 2008). Hence, the author concluded that a thermodynamic barrier was present at the S1 site (Javelle *et al.,* 2008). However, it is important to point out that

1- I suggested, using SSME, that MeA is not a good substrate analogue to characterise Amt proteins and the same conclusion was also obtained in previous work (Hall and Kustu, 2011, Wang *et al*., 2013). It is therefore not surprising to obtain contradictory results depending on whether *in vivo* MeA- or *in vitro* ammonium- uptake assay are used to answer mechanistic questions concerning AmtB activity.
2- The K_ms of AmtB and AmtB^{Ser219Ala} for ammonium are similar, suggesting that the highest thermodynamic barrier for ammonium transport is not at the S1 binding site but further down the translocation pathway.

Interestingly, potential mean force calculations on AmtB for NH_4^+ and NH_3 conductions revealed that the deprotonation mechanism of NH_4^+ does not happen at the S1 binding site but in between the S1 and S2 site, supporting the hypothesis of a rate limited step after the initial ammonium-AmtB interaction (Bostick and Brooks, 2007).

Taken together these results clearly indicate that ammonium binding at the S1 site does not represent a rate limiting step in the transport activity, thus it is not a high affinity binding site. Additionally, I concluded that Ser219 is not involved in the deprotonation of NH_4^+ as previously proposed (Ishikita and Knapp, 2007). Further investigations are needed to define the role of Ser219 and the S1 site as a whole in the transport mechanism. The hypothesis currently

developed between Dr. Arnaud Javelle and Dr. Ulrich Zachariae is that the electrostatic micro-environment at the S1 site lowers the pKa for NH_4^+/NH_3 which favours the deprotonation event, optimising AmtB transport rate (Williamson *et al., in preparation*).

Importance of the twin-His motif in the translocation mechanism:

In the first published crystal structure of AmtB, non-protein electron densities were identified at the positions S1, S2, S3 and S4 in the hydrophobic pore when AmtB was crystallised in the presence of ammonium (**see Chapter 1, section 1.3**) (Khademi *et al.*, 2004). The authors concluded that these densities were due to the presence of well-defined NH_3 positions in the hydrophobic pore. However, it was later demonstrated that these electronic densities were also present when AmtB was crystallised in the absence of NH_4^+ (Javelle *et al*., 2007, Javelle *et al*., 2006, Zheng *et al*., 2004). This indicates that these densities are due to the presence of water and not NH_3 molecules (Javelle *et al*., 2007, Javelle *et al*., 2006, Zheng *et al*., 2004). Using MD simulations, the presence of 3 water molecules in the hydrophobic pore, precisely at the position S2-S4 have been confirmed (Lamoureux *et al*., 2007). The water wire was also observed by MD simulations done in collaboration with Dr. Ulrich Zachariae (Williamson *et al., in preparation*). Previous structural analyses have shown that no electronic densities were present in the hydrophobic pore of the $AmtB^{His168Ala/His318Ala}$ variant (Javelle *et al*., 2006). I have demonstrated that the His168Ala/His318Ala variant is not active. Taken together these results indicate a clear relationship between the activity of the transporter and the hydration of the pore. I conclude that the twin-His motif in the hydrophobic pore stabilises the water wire hence is essential for AmtB activity. I developed further the role of the pore hydration for AmtB activity in the paragraph below: "**A new deprotonation/translocation mechanism suggested**".

This hypothesis can reconcile many data that lead to the seemingly inconsistent proposals of how members of the Amt/Mep family work. However functional studies of variants at the position of His168 have concluded that the

twin-His motif was non-essential. In my opinion this is due to the fact that none of these studies have been done using a pure *in vitro* assay with ammonium as substrate.

The AmtB His168Ala variant is still active:

In vivo experiments revealed that AmtB^{His168Ala} was able to complement the growth defect of a *⊿MEP* yeast strain on ammonium, demonstrating that the protein was active (Wang *et al.*, 2013). This somewhat puzzling result can be explained by previous structural analysis that show a diffuse electronic density peak extending over sites S2 and S3 in the His168Ala variant (Javelle *et al.,* 2006). Thus the non-polar cavity generated by the His to Ala substitution can trap water molecules that are not localised at defined positions. This explains why a His168Ala variant is still able to translocate ammonium although at lower rate compared to the wild type. These results challenged the hypothesis of His168 being involved in NH_4^+ deprotonation (Lamoureux *et al*., 2007).

The AmtB His168Glu variant is super active:

As previously described in **Chapter 1**, the twin-His motif of AmtB is highly conserved amongst the Amt/Mep/Rh protein family (Javelle *et al*., 2006, Conroy *et al*., 2005). However, in *S. cerevisiae*, Mep2 possesses the twin-His motif but in the Mep1 and Mep3 transporter the first histidine (equivalent of His168 of AmtB) is replaced by a Glu residue. Very interestingly, the substitution His194Glu increases Mep2 activity by a factor 4 (Boeckstaens *et al.,* 2008). In the same studies, it was shown that an AmtB His168Glu variant can complement the growth defect of a *⊿MEP* strain on ammonium and that its activity increased by a factor 2. However, these results have been obtained using MeA and we have already seen that MeA is a bad substrate analogue. Very recently, using SSME, Mr. Gordon Williamson showed that this AmtB variant is ~4 times more active than the WT using ammonium as a substrate (Williamson *et al., in preparation*). Thus, the substitution of the first conserved His into Glu residue seems to increase the transport activity of Amt/Mep proteins. My hypothesis is that the carboxyl group of the Glu stabilises and connects the two water wires identified by MD simulations (see section below),

which might explain why the AmtB^{His168Glu} has a better transport activity than the WT.

A new deprotonation/translocation mechanism suggested:

A surprising fact is that all the *in vivo and in vitro* studies mentioned above did not demonstrate experimentally that NH_4^+ deprotonation was associated with the activity of the Amt/Mep/Rh protein. In a very recent and elegant work in yeast, Ariz *et al*. demonstrated that the translocation of NH_4^+ in Mep proteins was associated with deprotonation, closing the debate of direct NH_4^+ translocation (Ariz *et al.*, 2018). To demonstrate this, the authors used the fact that the equilibrium between NH_4^+ and NH_3/H^+ for a ^{15}N isotope can be discriminated from the ^{14}N. At high ammonium concentration, they showed that the expression in trans of *Sc*Mep2 protein in a *ΔMEP* yeast strain was still able to fractionate the isotope. Hence the NH_3 was present during the transport mechanism indicating that a deprotonation event occurred during the translocation (Ariz *et al.,* 2018).

To elucidate the deprotonation mechanism, molecular dynamic simulations were undertaken in collaboration with Dr. Giuilia Tamburrino and Dr. Ulrich Zachariae (University of Dundee). In these simulations, an aqueous pocket is observed in the pore extending from the cytoplasm to His168 (water wire 1 in **Figure 4.14, panel A**). Crucially, the formation of a second water channel, which opens from the periplasmic side of the protein towards its centre is observed (Williamson *et al., in preparation*) (water wire 2, **Figure 4.14, panel A**). This newly discovered water wire 2 connects the periplasmic solution to the twin-His motif in the hydrophobic pore. Notably, this water chain is formed alongside the sidechain of Asp160. This residue is conserved and has previously been shown to be essential for ammonium transport in AmtB by a number of experimental and computational studies (Thomas *et al.,* 2000, Marini *et al.*, 2006, Luzhkov *et al.*, 2006, Javelle *et al.,* 2004). The main significance of these findings lies in the establishment of a potential pathway for proton transfer from the NH_4^+ binding site to the cytoplasmic vestibule, which is distinct from the generally accepted pathway for NH_3 transport (**Figure**

4.14). Hence, the current hypothesis is that the electrostatic microenvironment at the S1 site lowers the pKa of NH_4^+/NH_3 favouring ammonium deprotonation, with the residue Asp160 acting as the proton acceptor. The proton is transferred from Asp160 to the cytoplasmic vestibule through the interconnected water wire 1 and 2 using a Grotthuss mechanism while NH_3 diffused through another pathway in the hydrophobic pore (Williamson *et al., in preparation*) (**Figure 4.14, right panel**).

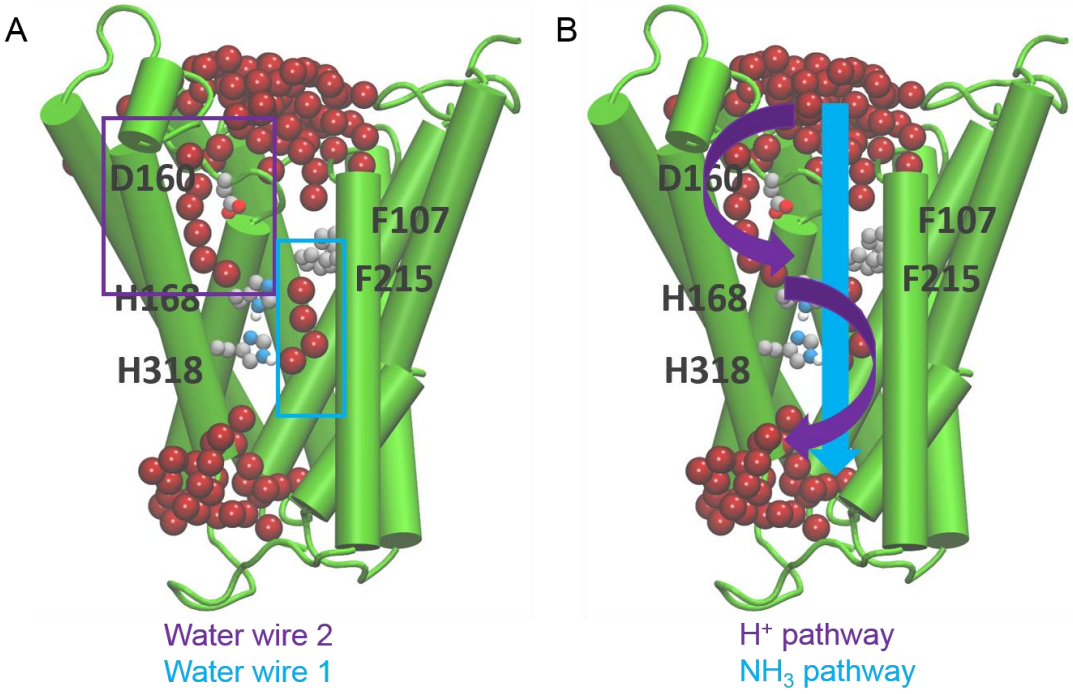

Figure 4.14: Proposed mechanism from ammonium transport. (A) Position of the new water wire (water wire 2) found (purple box) and previous water wire (water wire 1) isolated (blue box) from the crystal structure of AmtB using MD simulations. (B) Deprotonation and translocation mechanism in which H^+ is stripped and transported down to His168 through the newly found water wire (purple arrows), while NH_3 can diffuse through the hydrophobic gate (blue arrow) (adapted from Dr. Giulia Tamburinno, personal communications). The read beads are corresponding to water molecules.

Chapter 5: Effect of the lipid environment on AmtB activity

Aims and objectives:

In 2014, using mass spectroscopy, it was shown that 1-palmitoyl-2-oleoyl phosphatidylglycerol (PG) lipid can help to stabilise AmtB in contrast to anionic lipid such as phosphatidic acid (PA), phospho-L-serine (PS) or zwitterionic lipid such as phosphatidylcholine (PC) and phosphatidylethanolamine (PE) (Laganowsky *et al.,* 2014). Additionally, the authors obtained a structure of AmtB co-crystallised with PG which reveals specific PG binding sites in the upper leaflet (Laganowsky *et al.,* 2014). Unfortunately, to date, no functional studies have been undertaken to assess the effect of lipids on Amt activity. I have used a combination of experimental and computational approaches to investigate whether PG can affect AmtB activity. The MD simulations, carried out by our collaborators (Dr. Giulia Tamburrino and Dr. Ulrich Zachariae), have been informed by, and in turn feedback information to, my experimental studies in order to generate hypotheses concerning the molecular impact of PG binding on Amt activity.

The work presented in this Chapter has been published in *FASEB Journal* (see **appendix B**):

> **Dias Mirandela G**, Tamburrino G, Hoskisson PA, Zachariae U, and Javelle A. (2018) The lipid environment determines the activity of the *E.coli* ammonium transporter, AmtB. *FASEB J. in press. doi: 10.1096/fj.201800782R*

5.1 Introduction

During the last decade, it became evident that the lipid environment has a direct impact on membrane protein structure and function (Denning and Beckstein, 2013). For example, it has been demonstrated that the stability and activity of G-protein coupled receptors (GPCR) proteins is dependent on the intrinsic curvature of the membrane (Botelho *et al.*, 2006) or that the activity of the SecYEG (channel conducting preprotein) was maintained by the anionic properties of the phospholipid hydrophilic heads (van der Does *et al.*, 2000). For an excellent review summarising studies on how lipids are influencing membrane proteins see (Denning and Beckstein, 2013) and references therein.

Recently, a mass spectrometric analysis coupled with structural studies defined eight specific binding sites in AmtB for the PG head group (Laganowsky *et al.*, 2014). The X-ray structure of the AmtB-PG complex reveals subtle conformational changes which reposition some amino-acid side chains that interact with lipids. More recently, it has been shown that PG can allosterically regulate the interaction between AmtB and the signal transduction protein GlnK (Cong *et al.*, 2017). In spite of these findings, a direct functional role for PG on AmtB activity remains unclear.

Here I combine the SSME *in vitro* assay that I presented in Chapter 4 with MD simulations to analyse the effect of the lipid environment on AmtB activity. I show that PG is important for AmtB activity and that in the absence of PG, AmtB cannot complete its full translocation cycle. To my best knowledge, this is the first report highlighting the functional importance of specific lipids for AmtB activity.

5.2 Reconstitution of AmtB in various lipid environment

I have reconstituted AmtB into liposomes containing a mixture of PA/PC at a weight ratio of 1:9, or ternary mixtures of PA/PC and PG (**Table 5.1**). The PA/PC mixtures were chosen because **1-** no interactions have been detected between PA/PC and AmtB (Laganowsky *et al.,* 2014), and **2-** I have demonstrated that AmtB was correctly inserted in this lipid mixture but did not translocate ammonium (**see section 5.3.1**). Hence the PA/PC lipid mixture is very well suited to assess a potential functional role of PG on AmtB activity. The ternary mixture was chosen such that the quantity of PG (16.5% w/w) matched the standard composition used for the standard SSME experiments presented Chapter 4 (*E. coli* polar lipids/PC 2/1 w/w). The three different lipid compositions will be referred as condition 1-3 (**Table 5.1**).

Table 5.1: Lipid composition in liposomes and total PG content**.**

lipid condition	lipid content-ratio (w/w)	%PG
1	*E.coli* polar/POPC 2/1	16.5
2	POPA/POPC 1/9	0
3	POPA-POPC/POPG 5/1	16.5

5.2.1 Insertion of AmtB into liposomes containing various lipids mixtures

To insert AmtB in proteoliposomes containing the lipid mixture 1, 2 and 3 (**Table 5.1**), I destabilised the liposomes using Triton X-100 and determined the R_{sat} and R_{sol} parameters. To experimentally determine R_{sat} and R_{sol}, 1 µL of Triton X-100 at 25% was sequentially added to 500 µL of liposomes (5 mg/mL) and the absorbance at 400 nm was monitored (**Figure 5.1**)**.** The R_{sat} was reached for lipid compositions 1 and 3 (**Table 5.1**) when 4 µL of 0.39 M Triton X-100 was used while 3 µL was required for the liposome containing the lipid composition 2 (**Table 5.1**). After reaching R_{sat}, the addition of detergent decreased the absorbance until total solubilisation of the liposomes (R_{sol}). Therefore, the optimum amount of Triton X-100 for AmtB insertion was 1.56 µM per mg of lipid for liposome conditions 1 and 3. The shift in the maximum absorbance between condition 2 and conditions 1/3 (**Figure 5.1**) indicates that the liposomes made without PG are more easily destabilised. Therefore, 1.17 µM of Triton X-100 per mg of lipid was used to reconstitute AmtB in lipid condition 2.

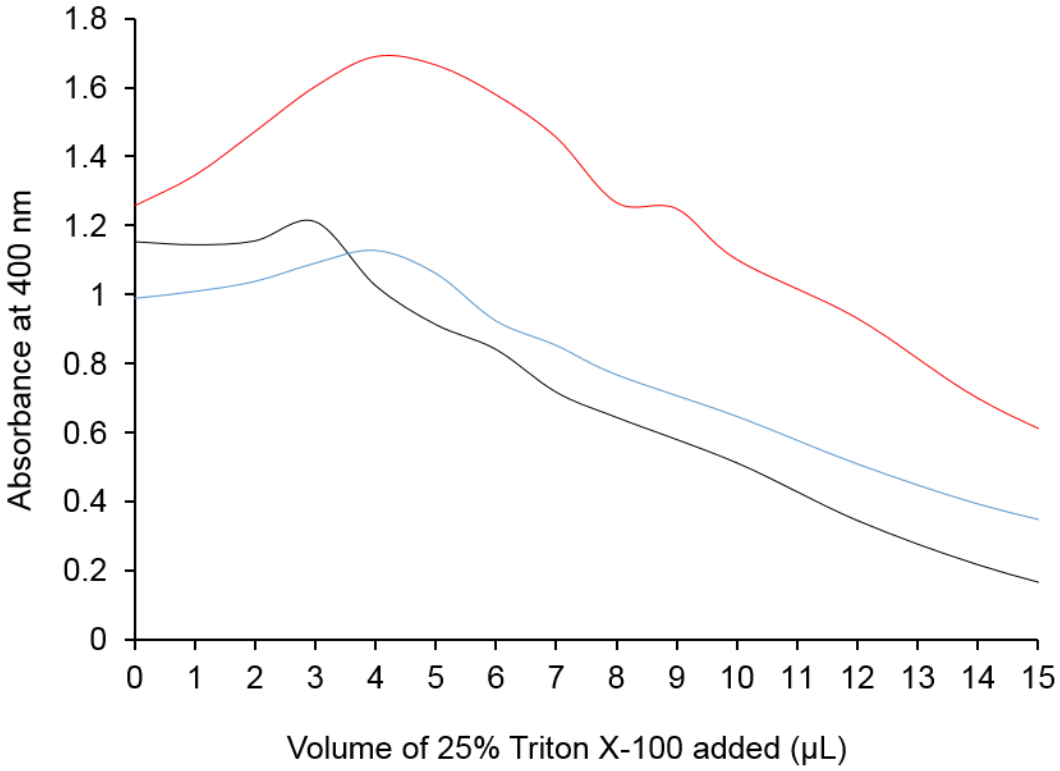

Figure 5.1 R_{sat} and R_{sol} determination of proteoliposomes containing the lipid mixture 1 (red), 2 (black) and 3 (blue) (see **Table 5.1**) using Triton X-100 at 25%.

5.2.2 Determination of the size distribution of the proteoliposomes and protein orientation in the proteoliposomes

5.2.2.1 Size distribution of the different liposome conditions

I used dynamic light scattering (DLS) to assess the size distribution of proteoliposomes prepared using the three different lipid conditions. The method is explained in **Chapter 2** and analysed in **Chapter 4, section 4.2.3**. The DLS analysis demonstrates that AmtB inserted in liposomes prepared using lipid compositions 1, 2 and 3 possessed the same unimodal distribution with a mean diameter of 110 nm (**Figure 5.2, panel A**). Hence, I was able to directly compare the transient charge displacement measured in all lipid conditions

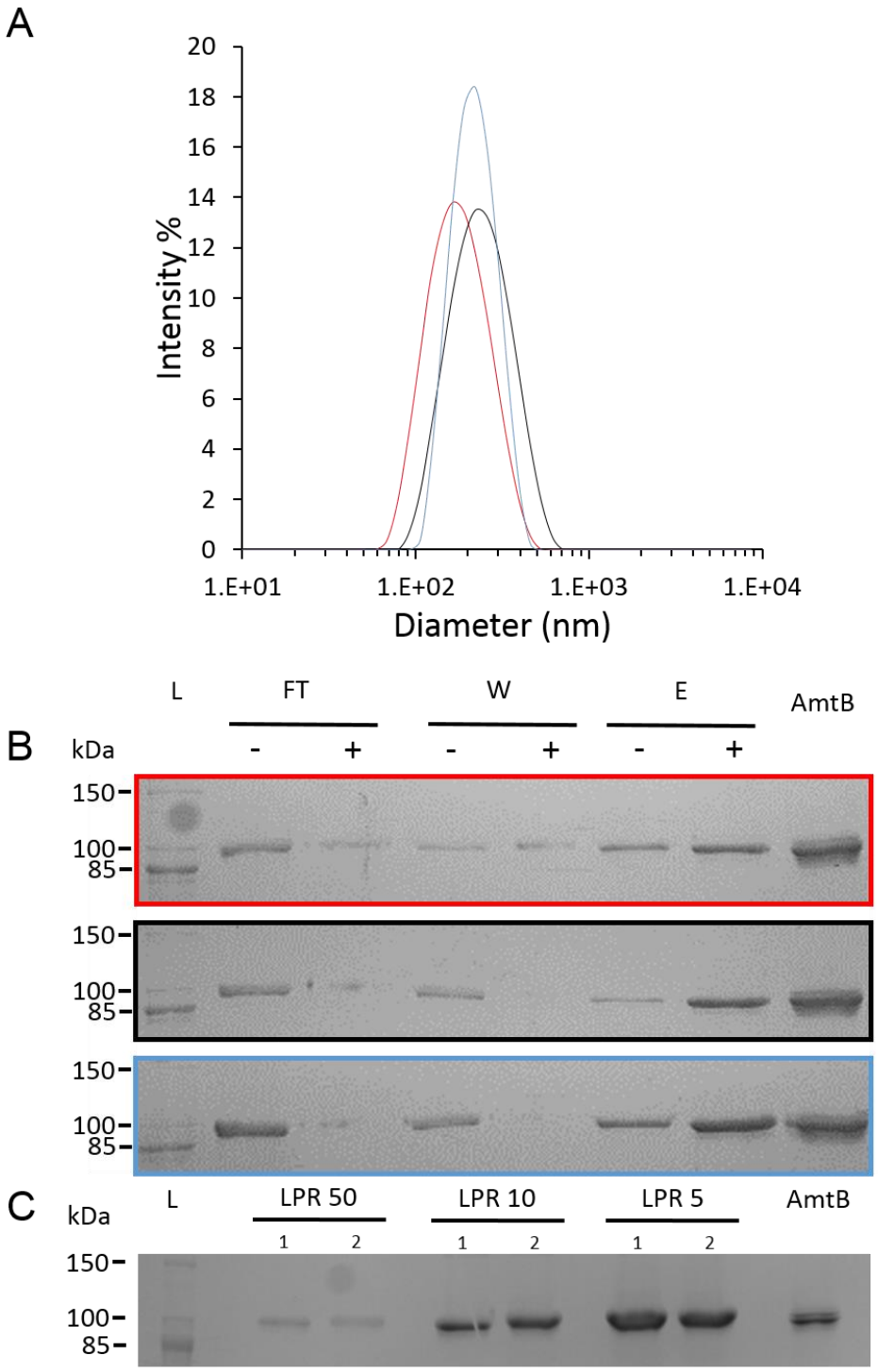

Figure 5.2*:* Characterisation of proteoliposomes prepared using different lipid composition. **(A)** DLS analysis of the proteoliposomes made using lipid condition 1 (red), 2 (black) or 3 (blue) (**Table 5.1**) at LPR 10. **(B)** SDS-PAGE Coomassie Blue-stained gel of the proteoliposomes made using lipid condition 1 (red boxed), 2 (black boxed) and 3 (blue boxed) purified by IMAC after DDM treatment (+) or in absence of DDM (-). L: ladder; FT; flow through, W; wash, E; elution fraction, AmtB; 5mg of pure AmtB used for the reconstitution in the proteoliposomes. **(C)** Comparison of the proteins content in proteoliposomes prepared under condition 1 and 2 (**Table 5.1**) at LPR 50, 10 and 5 (w/w). 10 µL of liposomes at 5 ml/mL have been loaded on the gel. AmtB: 5 µg of pure AmtB.

5.2.2.2 Protein orientation

To examine the orientation of AmtB, I analysed the proteoliposomes by Immobilised Metal Affinity Chromatography (IMAC) as described in **Chapter 4 section 4.2.4.1**. The SDS PAGE analysis showed that the orientation of AmtB in the proteoliposomes containing the lipid mixtures 1-3 is similar: in each condition more than half of AmtB is present in the flowthrough (**Figure 5.2, panel B**).

I have reconstituted AmtB at LPR 5, 10 and 50 following the procedure presented **Chapter 4, section 4.3.1** in liposomes containing lipid mixture 1, 2 and 3 (**Table 5.1**). In the SDS-PAGE analysis, the same quantity of lipid from the different LPRs were loaded on the gel and conditions 1 and 2 were compared (**Figure 5.2, panel C**). The quantity of protein at each different LPR in between conditions 1 and 2 was comparable (**Figure 5.2, panel C**) and equivalent to condition 3, see **Figure 4.6, Chapter 4**.

Taken together, DLS measurements, IMAC and SDS-PAGE gel analysis showed that the size of the liposomes, the protein orientation inside the membrane and the quantity of protein inserted were equivalent for all lipid conditions and at different LPR (**Figure 5.2**), hence I can directly compare the SSME measurements in the three lipid conditions.

5.3 Assessing the effect of PG on AmtB using SSME

5.3.1 Effect of PG on the pre-steady state and steady state current

For the proteoliposomes containing the three different lipid mixtures I have

1- Compared the activity of AmtB after a pulse of 100 mM NH_4^+ (**Figure 5.3, panel A**).

2- Determined AmtB affinity (apparent K_m) for ammonium (**Figure 5.3, panel A insert**).

3- Assessed whether AmtB was able to complete the full transport cycle (**Figure 5.3, panel B**).

In the absence of PG (condition 2), a 100 mM ammonium pulse triggered a transient current of 0.42±0.04 nA, compared to 3.37±0.26 nA in the presence of PG (condition 1) (**Figure 5.3, panel A**). Remarkably, in the presence of 16.5% PG in an otherwise pure PA/PC condition (condition 3) a current of 2.24±0.06 nA was measured, which is 5 times higher than in the absence of PG (condition 2) (**Figure 5.3, panel A**).

Next, I determined the apparent K_m by measuring the transient current after an ammonium pulse in the range 0.02-50 mM and the decay time after an ammonium pulse of 100 mM for the different liposome conditions. In the presence of PG (conditions 1 and 3) K_m*s* and decay time constants were similar and remained within experimental error (**Figure 5.3, panel A**). In contrast, in the absence of PG (condition 2), the decay rate and the *K*m increased by 1.6 and 7-fold, respectively, compared to conditions 1 and 3 (**Figure 5.3, panel A**). Taken together these results clearly show that PG lipids are important for AmtB activity.

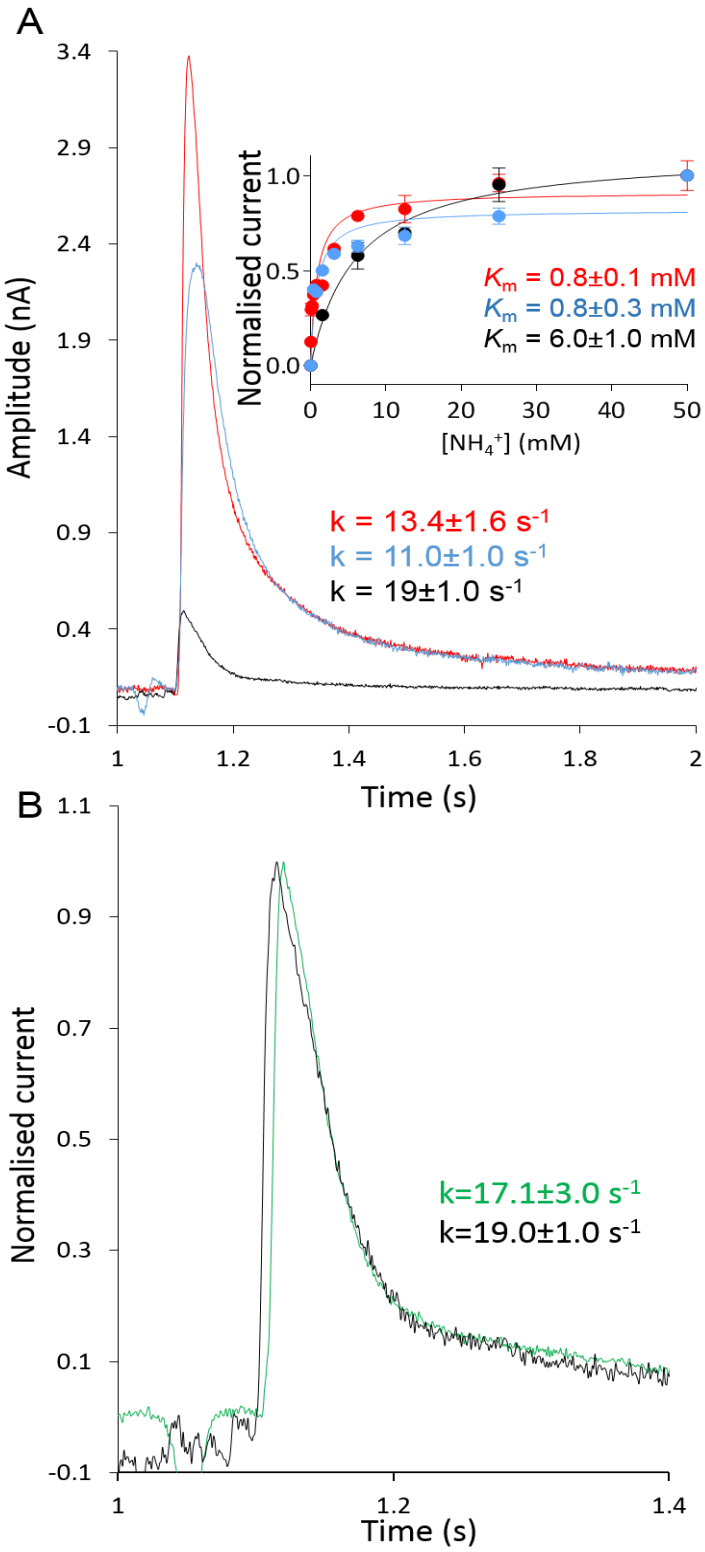

Figure 5.3*:* Phosphatidylglycerol is important for AmtB activity. **(A)** Transient current measured after a 100 mM ammonium pulse in proteoliposomes containing the lipid conditions 2 (black), 3 (blue), 1 (red). ***(Insert):*** Ammonium dependence of the maximum amplitude of the transient current for proteoliposomes containing the lipid conditions 2 (black), 3 (blue), 1 (red). **(B)** Normalised transient current measured in AmtB-containing proteoliposomes that does not contained PG (condition 2) at LPR10 (black) or 5 (green).

To further determine whether AmtB completes the full transport cycle in the absence of PG, I have reconstituted the protein in condition 2 (without PG, **Table 5.1**) at LPRs of 50, 10 and 5 (w/w) (**Figure 5.3, panel B**). Under condition 2, an ammonium pulse of 100 mM did not trigger a measurable transient current at LPR 50; however, at LPR 10 and 5, the decay time was similar and within the experimental error (19.0±1.0 s-1 vs. 17.1±3.0 s-1 respectively; **Figure 5.3, panel B**). This result clearly indicates that the current measured without PG reports only an ammonium-AmtB interaction. I concluded that in the absence of PG, AmtB is not able to complete the full transport cycle.

5.3.2 Is AmtB misfolded in absence of PG?

To ensure that the loss of AmtB activity in the liposomes under condition 2 (without PG) was not due to misfolding, I have treated the proteoliposomes in 2% DDM to re-solubilise AmtB and analysed the protein by Size Exclusion Chrotamography (SEC) on a Superdex 200 10/300 column. The SEC profile of AmtB solubilised from the liposome without PG was compared to the profile of AmtB before insertion (**Figure 5.4, panel A**). The SEC analysis showed that both proteins elute as a single monodisperse peak with the same retention time (11.6 mL) prior to and after reconstitution under condition 2 (**Figure 5.4, panel A**). This result shows that the hydrodynamic radii of AmtB before and after insertion using condition 2 (without PG) did not change.

To ensure that AmtB previously inserted into liposomes under condition 2 was still active, I subsequently re-inserted AmtB solubilised from condition 2 (without PG) into proteoliposomes using condition 1 (with PG). An ammonium pulse of 100 mM in the latter proteoliposomes triggered a transient current of 3.18±0.09 nA with a decay constant of 11.5±2.4 s-1 (**Figure 5.4, panel B**), and the kinetic analysis revealed a *K*m of 1.3±0.3 mM (**Figure 5.4, panel B insert**). These results showed that AmtB reconstituted under condition 2 (without PG) regains the original activity parameters (maximum current intensity, decay time

and *K*m) when reconstituted in liposomes under condition 1 (with PG). These data confirmed the correct folding of AmtB in the proteoliposomes without PG (condition 2). Taken together, these findings show that PG is important for AmtB activity and furthermore indicates that in the absence of PG AmtB exhibits a defective transport cycle.

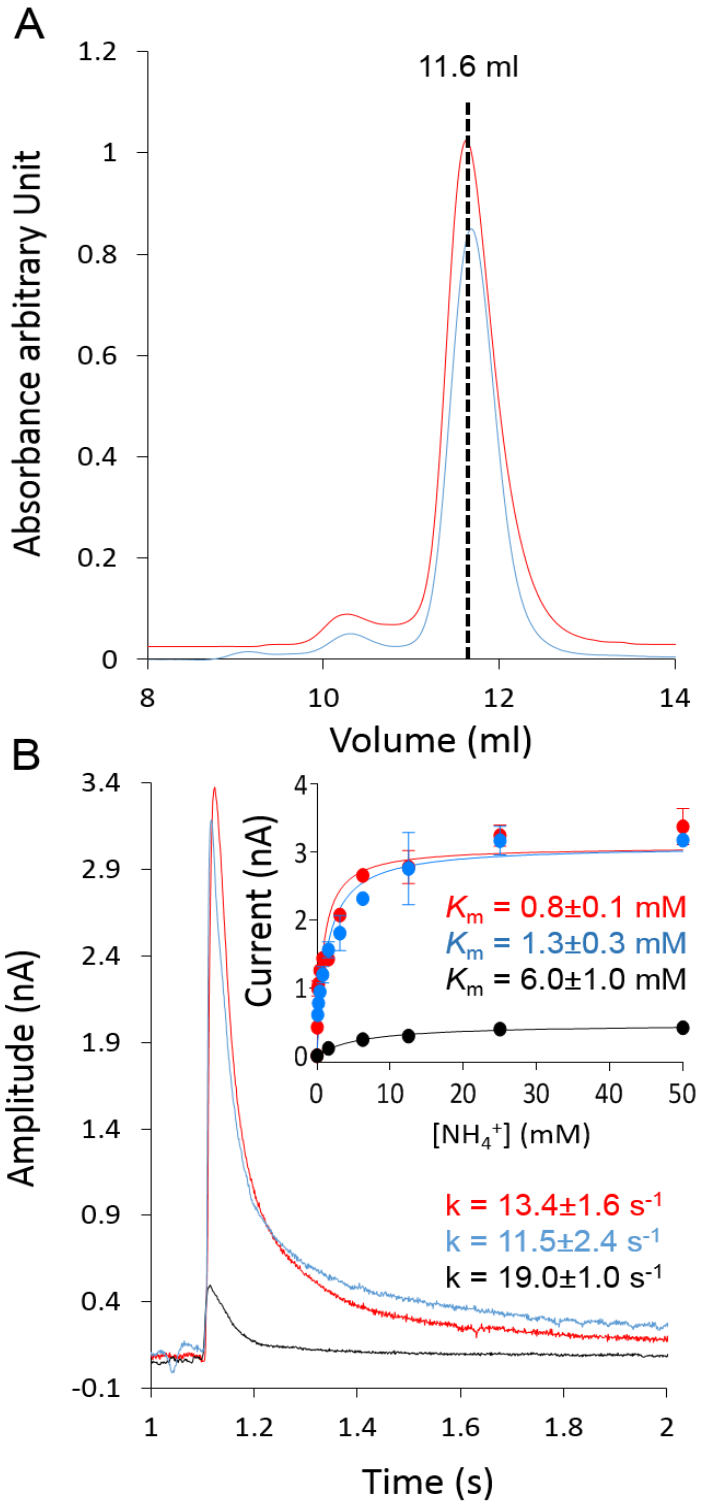

Figure 5.4: Phosphatidylglycerol is important for AmtB activity. **(A)** Gel filtration trace (Superdex 200 10/300 increase) of AmtB before (red) insertion in proteoliposomes under condition 2 and after (blue) solubilisation from proteoliposomes under lipid condition 2. **(B)** Transient current measured after a 100 mM ammonium pulse in proteoliposomes under condition 2 (black), under condition 1 containing AmtB re-inserted after solubilisation from proteoliposomes under condition 2 (condition 4-blue) and under condition 1 (red). ***(Insert):*** Ammonium dependence (raw data) of the maximum amplitude of the transient current in proteoliposomes under condition 1 (red), 2 (black) or 4 (blue).

5.4 MD simulations

5.4.1 Determination of PG lipid binding on AmtB using MD simulations

In collaboration with Dr. Giulia Tamburrino and Dr. Ulrich Zachariae from the University of Dundee, we next applied atomistic molecular dynamics (MD) simulations to study the interaction of PG lipids with AmtB in membranes at the molecular level. Although this work has not been done directly by myself, the MD simulation have been informed by, and in turn feedback information to, my experimental studies in order to generate hypotheses concerning the molecular impact of PG binding on Amt activity. Hence it is important to present these results to have a full understanding of the impact of this work on the Amt/Mep/Rh field.

Figure 5.5 shows the simulation systems containing an AmtB trimer embedded within PA/PC/PG (1:9:10), PA/PC (1:9), and PA/PC/PG (1:9:2) mixed lipid membranes, respectively. The colour maps on the right and bottom of each of these figures displays the density of PA/PC and PG, respectively, each derived from 0.7 μs simulations (**Figure 5.5, panel A**). The slices representing the lipid density in the periplasmic and cytoplasmic leaflets were taken at the average z-axis position of the phosphorus atoms within the lipid head groups of each membrane leaflet (**Figure 5.5, panel B and C**).

Although specific AmtB interactions with PG had previously been crystallographically detected for the extracellular membrane leaflet (Laganowsky *et al.,* 2014), our PA/PC/PG (1:9:10) simulations reveal additional PG binding sites (site 4, 5 and 6) on the intracellular side of the membrane (**Figure 5.5, blue square panel B and C**). PG lipids preferentially occupy sites on the AmtB trimer located near the interfaces between the monomers, both within the periplasmic and intracellular membrane leaflets (**Figure 5.5, blue square panel C**). Specifically, we observe three high-density lipid interaction sites per subunit in the periplasmic leaflet, one at the monomer

interface (site 1) and two in its vicinity (sites 2 and 3) (**Figure 5.5, blue square panel C**). Within the intracellular leaflet, about two high-density lipid sites are seen per subunit, in which lipids interact with interfacial helices of AmtB in both cases (site 4 and 5, **Figure 5.5, blue square panel C**), and an additional high-density region, in which we observe PG clustering (site 6, **Figure 5.5, blue square panel C**).

In contrast, the density maps recorded for the PA/PC lipid mixture (**Figure 5.5, black square**) show no binding hotspots of AmtB for PA and PC within the periplasmic membrane leaflet, while some lipid accumulation is observed within the intracellular leaflet close to the AmtB PG binding sites 1 and 2 (**Figure 5.5, black square panel B**). The PG density maps obtained from the PA/PC/PG (1:9:2) simulation (**Figure 5.5, red square**) show that, due to the lower PG concentration in this simulation system, the binding regions observed in the PA/PC/PG (1:9:10) simulation are only partially occupied by PG (**Figure 5.5, red square panel B and C**).

To assess whether the protein was structurally stable along the MD simulation process at the different lipid conditions, the Cα Root Mean Square Deviation (RMSD) of the AmtB structure was calculated all along the MD simulations in the presence of the different lipid conditions for 700 ns (**Figure 5.6, panel A**) or for 250 ns with independent simulations (**Figure 5.6, panel B**). The RMSD remained well below 2.5 Å in all simulations. The average RMSD for AmtB was found to be 1.51±0.22 Å for PA/PC, 1.60±0.21 Å for PA/PC/PG (1:9:2) and 1.51±0.16 Å for PA/PC/PG (1:9:10) (**Figure 5.6**). This shows that, regardless of the membrane composition, the protein was stable and maintained its overall conformation during the simulations.

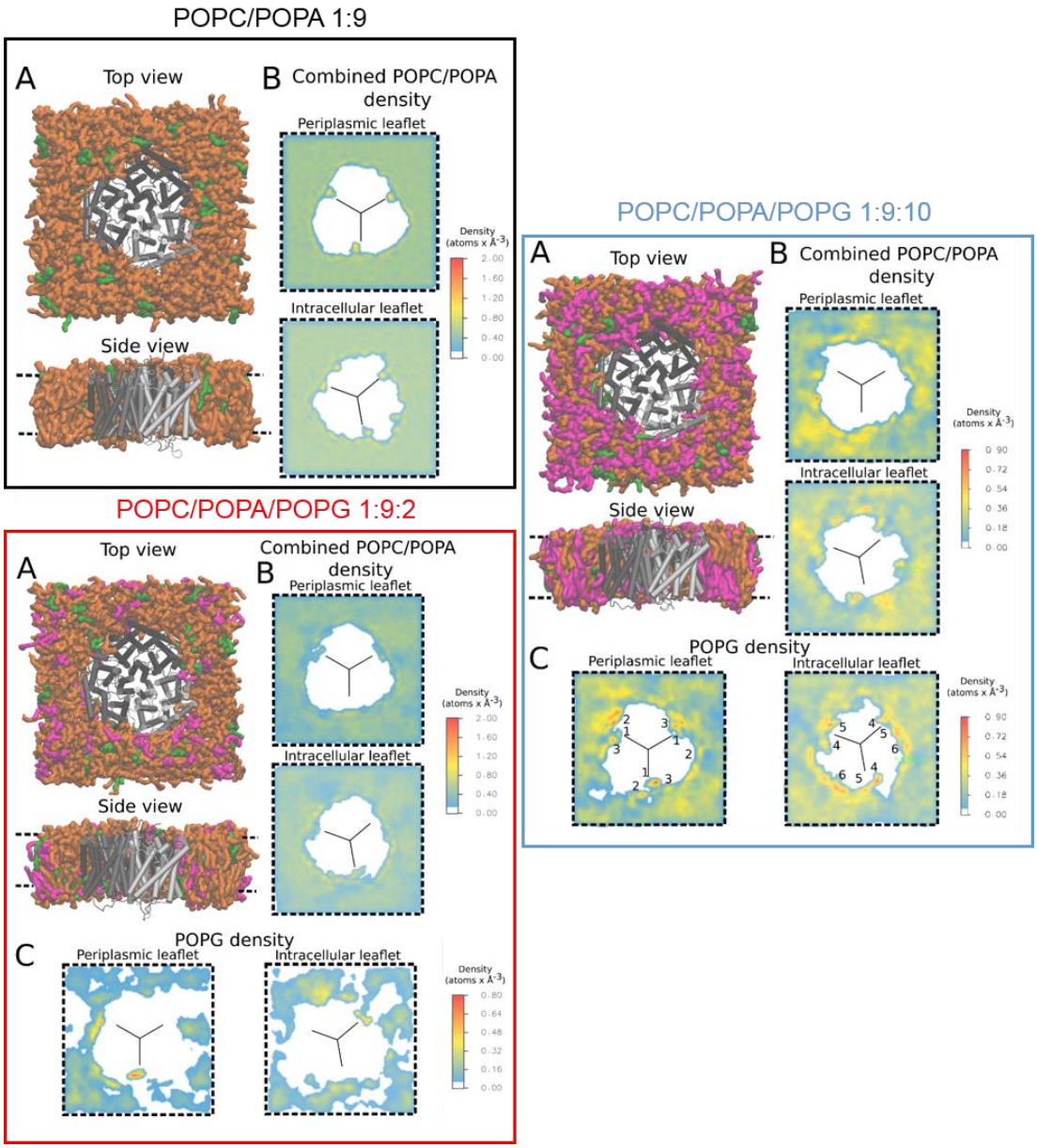

Figure 5.5: Trimeric AmtB in the PA/PC (1:9) (black square), PC/PA/PG 1:9:2 (red square) and PC/PA/PG 1:9:10 (blue square) system and lipid density plots. **(A)** Final frame of the simulation system, seen from the periplasm (top) and from the side (bottom). The protein is shown in grey, the PC lipid molecules in orange, PA in green. **(B)** Volumetric analysis of PC and PA combined average densities over the whole trajectory. **(C)** Volumetric analysis of PG average densities over the whole trajectory. The black lines in the density plots mark the approximate monomer interfaces. Specific binding sites are labelled in the density plots. A comparison of the 2-D density maps shows that PG tends to localise preferably close to the monomer interfaces.

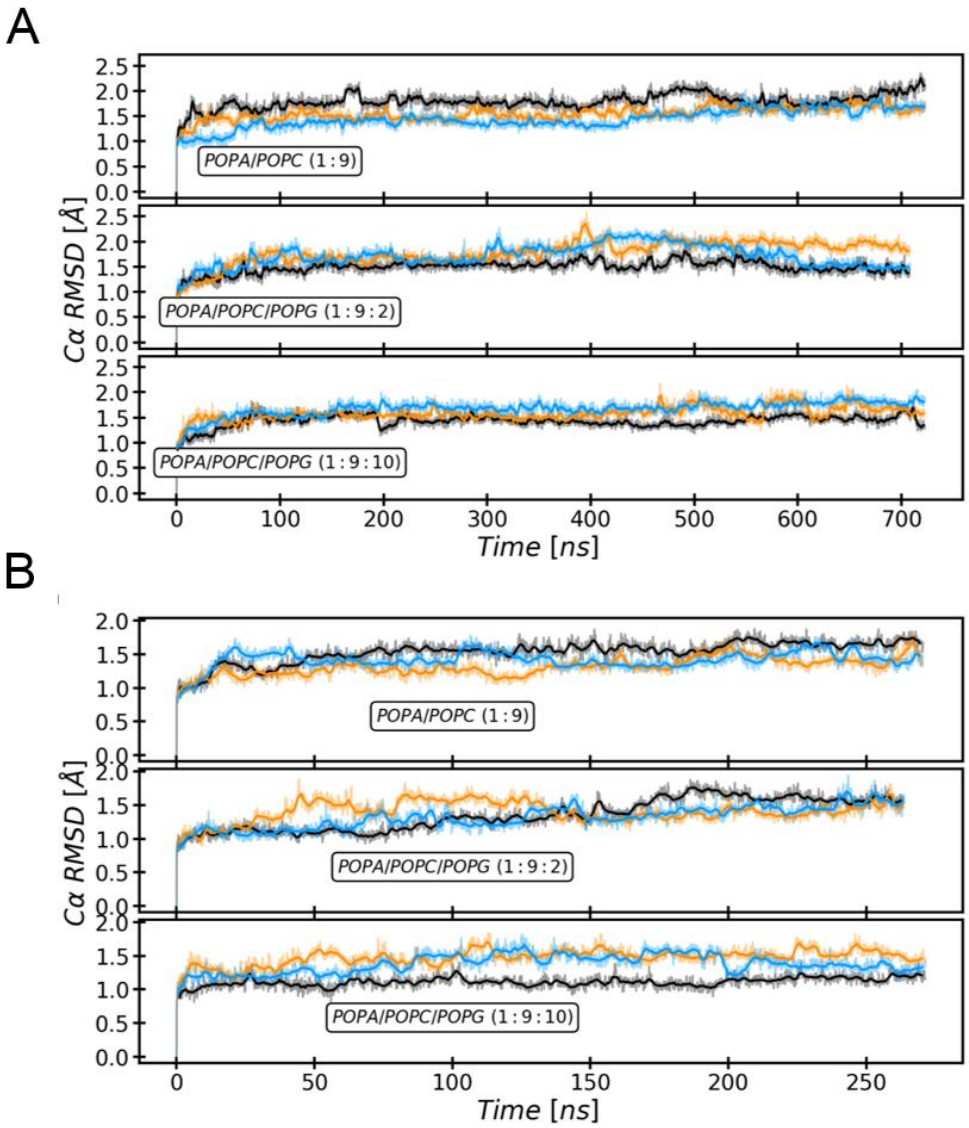

Figure 5.6: Cα RMSD of AmtB during the simulations in various lipid mixture: **(A)** Displays the RMSD over 700-ns simulations and **(B)** shows the RMSD during independent 250-ns simulations.

5.4.2 Visualisation of PG lipid binding on AmtB

To visualise the position of the specific lipid binding sites found during the MD simulations, close-up images highlighting the interaction sites between PG lipids and the AmtB subunits are shown in **Figure 5.7**. The close-up images were taken from AmtB simulated in PA/PC/PG (1:9:10) lipid conditions. The binding sites 1, 2 and 3 observed in our MD simulations within the periplasmic leaflet are in good agreement with crystallographically defined sites (Laganowsky *et al.*, 2014) (**Figure 5.7**). Interestingly, new intracellular interaction sites labelled 4, 5 and 6 were located at the interface region between the AmtB subunits (**Figure 5.7, panel B and C**).

In order to assess which type of lipid was occupying the specific binding sites during MD simulations, **Figure 5.8** shows the time evolution of the occupancy of all the suggested AmtB lipid binding sites by each lipid type. The MD simulations were done using data from two independent simulations of AmtB in a PA/PC/PG (1:9:10) membrane. As can be seen, the sites we identified preferentially interact with PG lipids. Preference for occupancy by PG molecules is seen for all of the binding sites. Additionally, to characterise which type of interaction existed between PG and the protein, an analysis of the number of hydrogen bonds formed between the lipid head groups and the protein (**Figure 5.9, panel A**) was done. As well, the radial distribution of the lipids around the protein was carried out (**Figure 5.9, panel C**). **Figure 5.9** showed that PG tends to localise closer to the protein surface compared to the PA and PC lipids and to form more hydrogen bond contacts. The average number of hydrogen bonds between each protein residue and the lipid head groups is displayed in **Figure 5.9 panel B**. This confirms that PG lipids generally establish more hydrogen bonds, in particular near residues that form the reported binding sites (numbered from 1 to 6 in **Figure 5.7**).

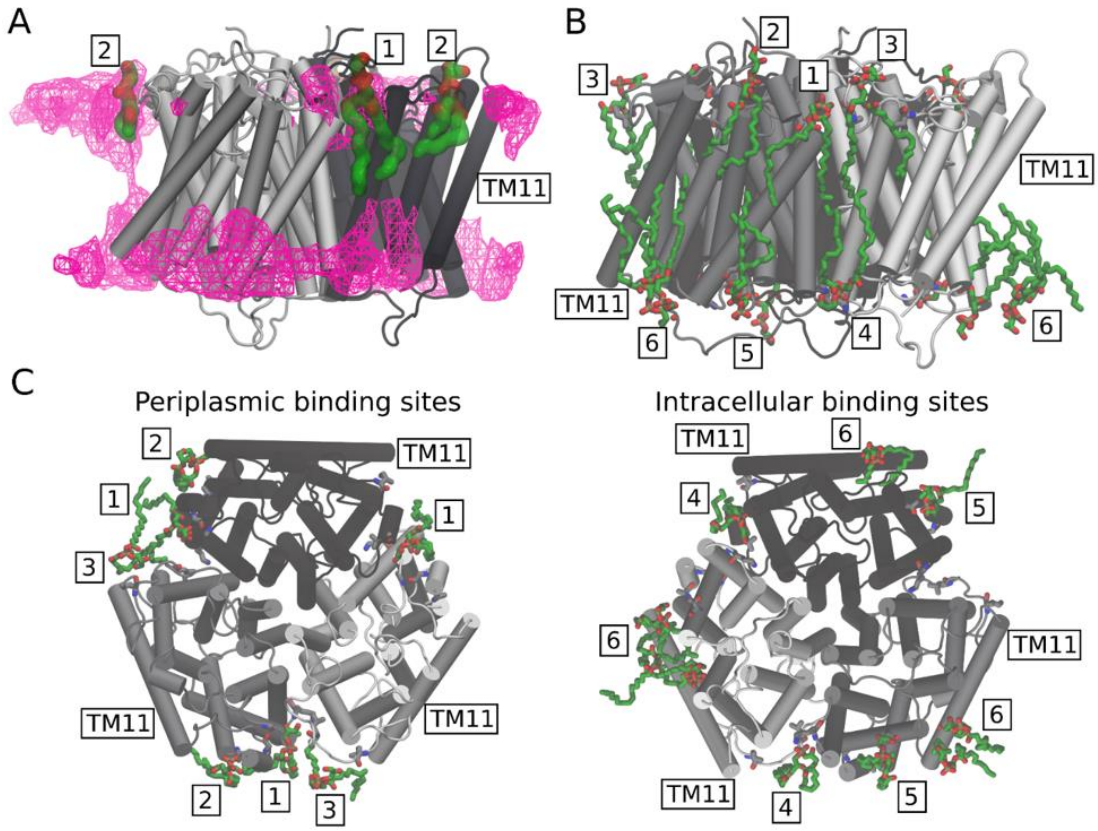

Figure 5.7*:* The images highlight the PG binding locations observed in the PA/PC/PG (1:9:10) simulations. The binding sites located in the periplasmic leaflet are numbered 1, 2 and 3, while the intracellular ones are labelled 4, 5 and 6. The same numbering scheme has been adopted for the volumetric maps shown in Figure S2 and S3. **(A)** Volumetric map of the average PG density obtained from a 700-ns simulation (magenta mesh surface, isovalue = 0.38) is compared to the PG binding sites which were previously resolved in the x-ray structure (PDB ID: 4nh2; lipids in green). Generally, good agreement between the experimental and the simulation sites is observed, especially for binding site 1. **(B)** Side view; **(C, left)** periplasmic; and **(C, right)** intracellular views of the PG binding sites taken from a representative simulation frame from the PA/PC/PG (1:9:10) mixture. Generally, PG tends to bind close to the monomer interface.

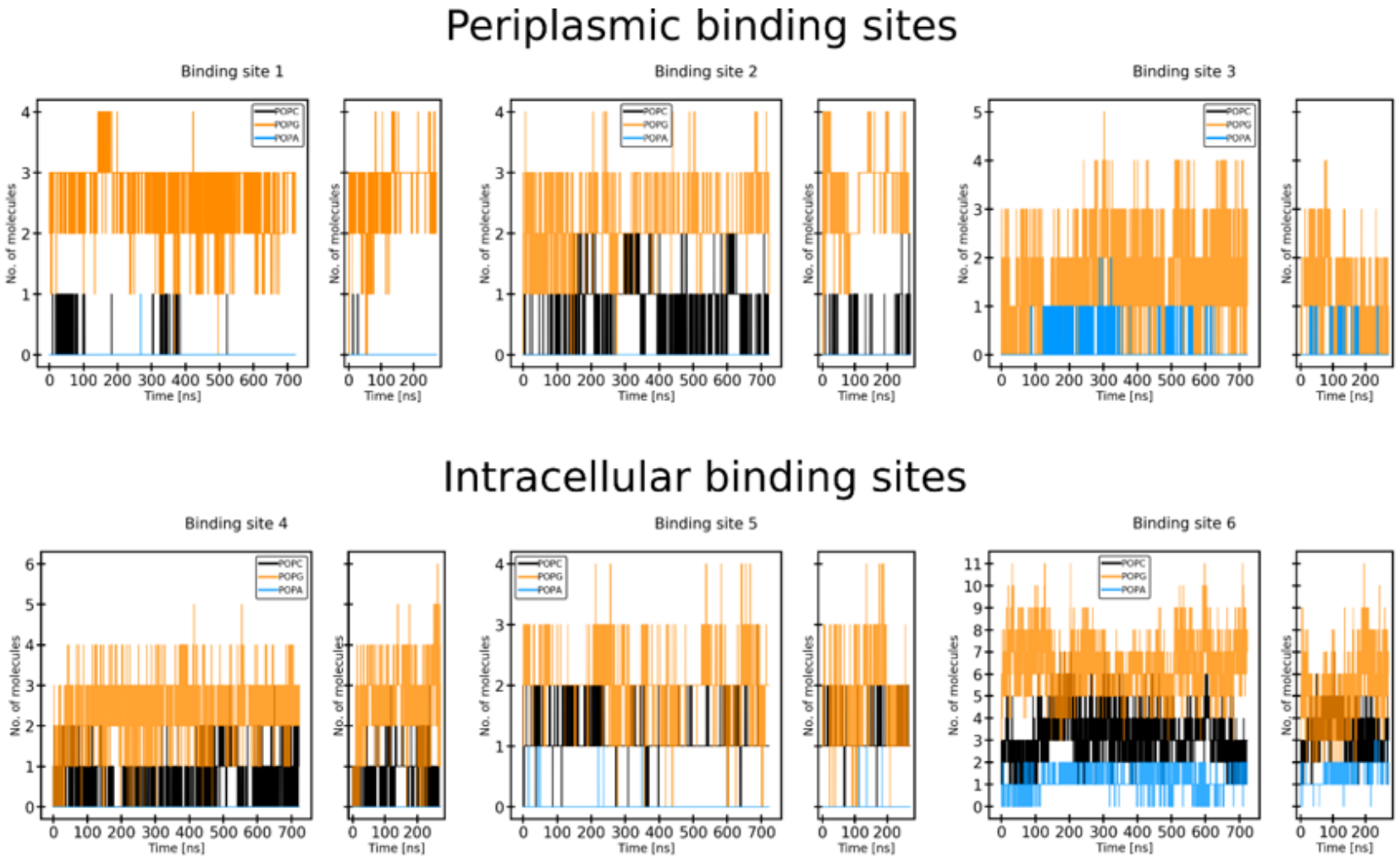

Figure 5.8: Timeline of the occupancy of the PG binding sites. Occupancy for the periplasmic leaflet (top) and the intracellular leaflet (bottom) with the lipid PA (blue), PC (black) and PG (orange).

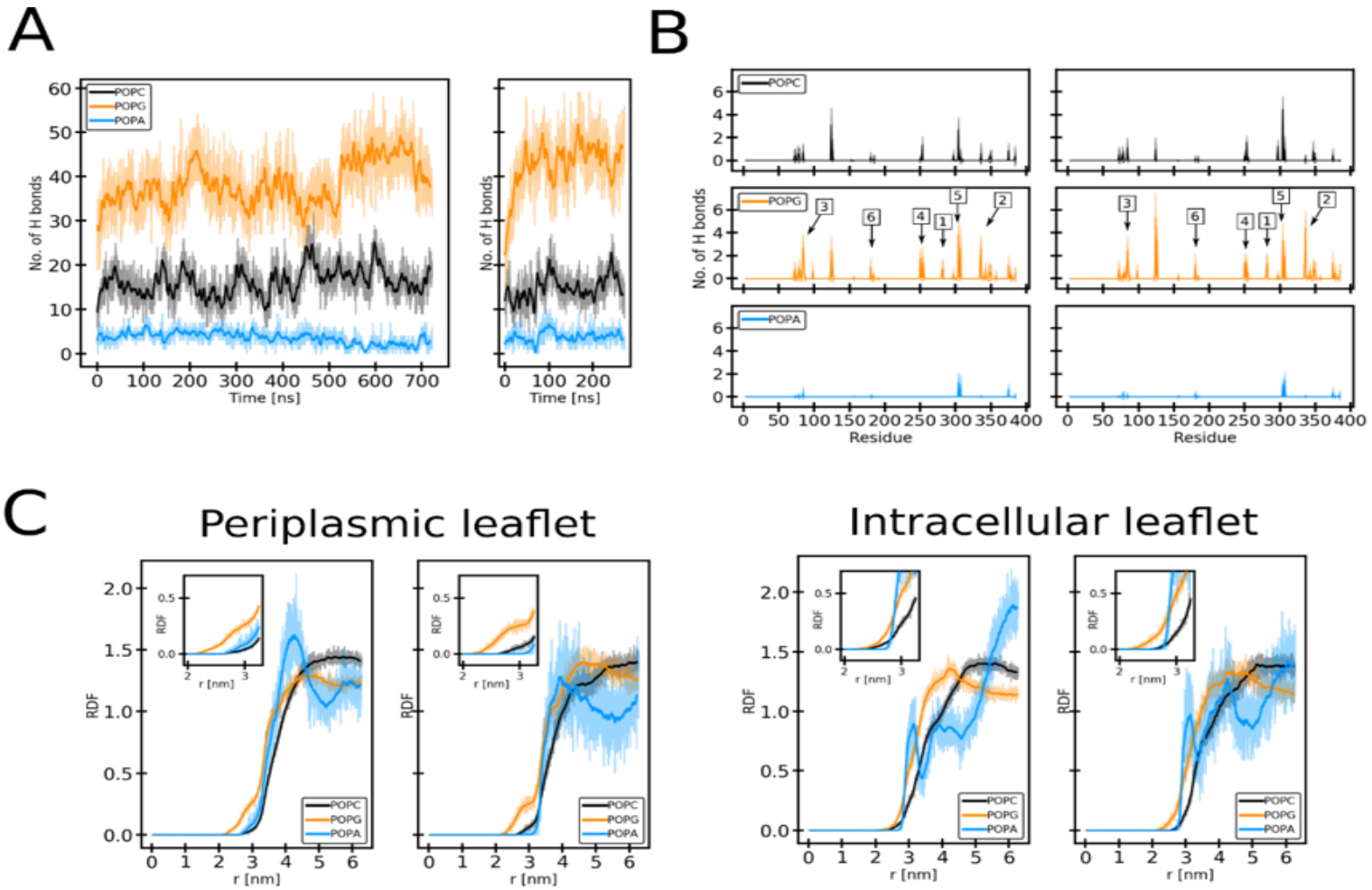

Figure 5.9*:* Interactions between PA (blue), PC (black), PG (orange) and AmtB. **(A)** Timeline of the total number of hydrogen bonds made between the protein and each lipid type, shown for the PA/PC/PG (1:9:10) simulations. Shaded lines show raw data, bold lines represent a running average using 5-ns windows. **(B)** Average number of hydrogen bonds for each AmtB residue (standard deviation in shaded colours). The PG binding sites observed in the simulations are labelled. **(C)** Radial distribution function (RDF) of each lipid for the periplasmic (left) and the intracellular (right) leaflets. Shaded lines show the raw data, bold lines represent a running average using 2.5-ns windows.

5.4.3 Small conformational change associated with PG binding

The most conspicuous conformational change we find to be induced by PG binding in AmtB on the time scale of the simulations is the preferred formation of a short helix within a periplasmic loop region (residues 77–81) following binding of the charged PG head group. The propensity of this region to form an alpha helix is shown in **Figure 5.10**. The simulations containing PG (both in the ratios 1:9:2 and 1:9:10) **(Figure 5.10, panel B and C)** exhibit a significantly increased propensity of this loop region to form a helical structure compared to simulations in the absence of PG **(Figure 5.10, panel A)**. This short region is part of a loop, which Laganowsky *et al.* (Laganowsky *et al*., 2014) showed to adopt a slightly different conformation upon PG binding, compared to the unbound structure, albeit without formation of a helix. Although the detailed mechanism of ammonium transport in AmtB is still unclear, this finding might link PG binding to AmtB structure and function.

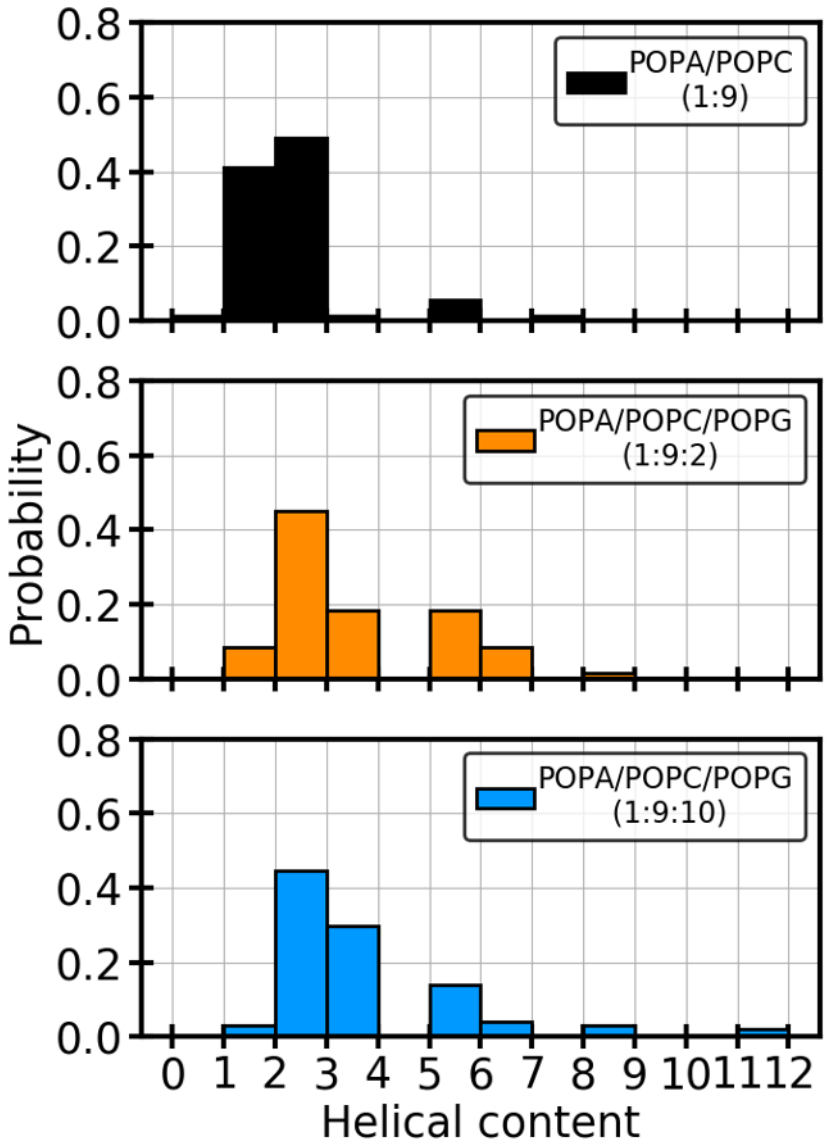

Figure 5.10: Helix-forming propensity of AmtB residues 77-81. Data from the two simulations conducted for each membrane lipid mixture was aggregated. The simulations containing PG show a significantly raised tendency of this region to form a short alpha-helix (p-value<10-7).

5.5 Discussion

It is well established that lipids can impact membrane protein structure and function through bulk membrane effects, by direct but transient annular interactions with the bilayer-exposed surface of protein, or by specific lipid binding to protein sites (for review see (Denning and Beckstein, 2013)). Altogether eight molecules of PG have been resolved in a recent crystal structure of AmtB, interacting at specific binding sites within the extracellular membrane leaflet (Laganowsky *et al.*, 2014). Our molecular dynamics simulations identify further interactions of PG molecules in the inner leaflet of the membrane.

However so far, no functional relationships have been reported to link PG binding with the activity of AmtB. My study shows that in the absence of PG, AmtB is non-functional as a transporter and unable to complete the full translocation cycle. Our simulations do not indicate substantial conformational changes in the S1 periplasmic binding site nor in the pore, suggesting that the molecular basis of the PG effect on AmtB activity could involve novel mechanistic sites. In this context, it is interesting to compare my findings with the lactose permease LacY in *E. coli*, the most extensively studied secondary transporter in the context of lipid-protein interactions. In the absence of phosphatidylcholine (PC) and/or phosphatidyethanolamine (PE), LacY is unable to support active transport, although substrate binding to the protein is unaffected (Bogdanov and Dowhan, 1995). This is similar to my observations for AmtB in the absence of PG lipids. LacY is known to undergo drastic topological rearrangements, which may explain the effect of PC/PE on its activity (Bogdanov *et al.*, 2002). In the case of AmtB, no topological rearrangements were observed upon PG binding and I have shown that, in the absence of PG, AmtB was folded correctly in the proteoliposomes, such that a major change in the AmtB topology is unlikely to explain the functional role of PG. However, changes in the dynamics of AmtB subunits were observed, which locate particularly the loop regions at the periplasmic face of the protein. It has previously been shown that the periplasmic loop regions include

functionally important residues (Cao *et al*., 2007, Bostick and Brooks, 2007, Luzhkov *et al.,* 2006, Javelle *et al.,* 2004). Once a more detailed picture of the overall transport mechanism of AmtB has been obtained, the role of these effects may emerge in greater clarity.

Several lines of evidence point towards functional cooperativity between the three subunits in the Amt/Mep transporters. Firstly, in *S. cerevisiae*, it has been demonstrated that expression of a non-functional Mep1 protein inhibits the transport activity of Mep2 and Mep3, indicating cross-talk between different Mep transporters (Marini *et al*., 2000). Similar observations have been reported for ammonium transporters of *Aspergillus nidulans* (Monahan *et al*., 2002). Secondly, co-expressed non-functional monomers cross-inhibit transport in plant Amts, and a genetic screen has identified several mutations at the subunit interface of the *Arabidopsis thaliana* AMT1;2 transporter which inactivates the translocation activity (Neuhäuser *et al*., 2014, Neuhäuser *et al*., 2007). Thirdly, extensive site-directed mutagenesis of the C-terminal tail of AmtB has led to the hypothesis that the three subunits function in a cooperative manner (Severi *et al.*, 2007). All of these findings indicate functional coupling between the adjacent subunits. Previous structural data and our MD simulations show that PG molecules bind mainly to sites at the vicinity of the subunit interfaces. It is therefore attractive to hypothesise that PG molecules act as wedges, which mediate the functional interaction between the subunits. In line with this hypothesis, a model in which various AmtB conformations may be favoured upon specific lipid binding has been proposed (Cong *et al.*, 2017).

Finally, it has been shown recently that other lipids, including PE and cardiolipin, can bind AmtB allosterically, indicating that transporters may recruit their own micro-lipidic environment (Patrick *et al.*, 2018). Whether these binding events are important to modulate the activity of AmtB remains a question to be addressed. A broad spectrum systematic screening has been undertaken in the laboratory to identify other potential lipids that are important for AmtB activity, in particular cardiolipin.

Chapter 6: General conclusions and future work

During my PhD, I successfully developed a biochemical and a biophysical approach to functionally and structurally characterise the ammonium transporter AmtB from *E.coli*.

In collaboration with Prof. Jochen, Dr. Ivanovic, Dr. Zachariae, Dr. Tamburrino, Dr. Gabel and under the supervision of Dr. Javelle, I successfully developed a modelling approach, using SAXS and SANS at different contrast match points, to accurately distinguish the hydrophobic tail and hydrophilic heads of DDM detergent molecules in the corona surrounding AmtB (**Chapter 3**). Next I combined my SAXS/SANS measurements with MD simulation and I have obtained a full atomistic model for the AmtB-DDM complex (**Chapter 3**).

It is my belief that this new methodological approach will be applied to characterise conformational changes associated with the activity of Amt/Mep/Rh proteins in solution. In future work, the methodology developed in **Chapter 3** could be used to:

1- **Measure experimental scattering data upon substrate, inhibitor, or co-factor binding**

As presented in **Chapter 1, section 1.3 and 1.4,** the x-ray crystal structures of AmtB obtained in the presence or absence of ammonium revealed no structural rearrangement. However, previous structural studies on AmtB, AMT1 from *A. thaliana* and Mep2 from *S. cerevisiae* have demonstrated that Amt/Mep proteins can undergo significant conformational change during the translocation cycle (Inwood *et al.,* 2009, De Michele *et al.,* 2013). A functional and structural study carried out by Dr. Javelle and co-workers demonstrated that 0.5 mM of thallium was capable of inhibiting AmtB-dependent MeA uptake by binding at the S1 site (Javelle *et al.*, 2008). However, the occupancy of the S1 site by thallium in the crystal lattice was around 10% which may explain why no significant conformational rearrangement was observed in AmtB upon thallium binding (Javelle et *al.,* 2008). Therefore, it would be interesting to

measure and compare x-ray/neutron scattering (at different contrast match points) for AmtB in the presence or absence of thallium. In combination with MD simulations, we will be able to generate computational models driven by the experimental scattering data, allowing us to observe potential conformational re-arrangements of AmtB.

2- To characterise conformational rearrangement of AmtB variants

I have purified different AmtB variants and noticed that their size-exclusion chromatography (SEC) profiles differ from the wild type protein (**Figure 6.1**). This shows that the hydrodynamic radii of the variants are different. However, the x-ray crystal structures obtained for some of the same variants were similar (Javelle *et al*., 2006, Javelle *et al*., 2008). This information indicates that the similarity of the crystal structure of AmtB variants and WT may be due to the propensity of the protein to crystallise in a unique thermodynamically stable conformation. In addition, these hydrodynamic radii difference could account for a particular re-organisation of the protein when mutated. Therefore, we are interested in characterising the structural rearrangement of the AmtB variants in solution by applying the same approach as described in the previous paragraph.

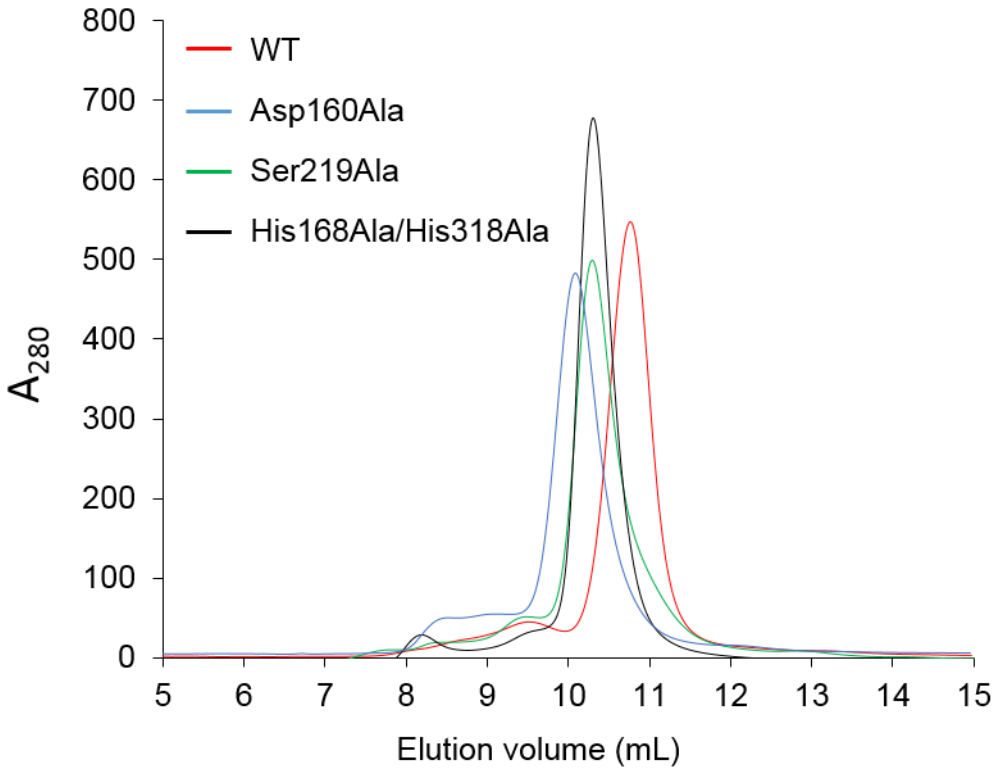

Figure 6.1 AmtB variants possessed different hydrodynamic radii. Size-exclusion chromatography profiles of AmtB variants. WT: Wild-type.

In **Chapter 4**, I demonstrated that AmtB is an electrogenic transporter and that MeA was not a suitable substrate analogue to elucidate functional questions. Using SSME in combination with MD simulations, I have shown that the modification of the S1 binding site has no effect on the K_m of AmtB for ammonium. My hypothesis is that a thermodynamic barrier for translocation exists below the S1 binding site. Additionally, I have demonstrated that the twin-His motif presented in the hydrophobic pore is essential for ammonium translocation. We propose a new mechanism to describe ammonium translocation *via* two water wires: an upper one linking the periplasmic vestibule to the hydrophobic pore *via* the residues Asp160 and His168 and a lower one alongside the hydrophobic pore. Thus variants at these positions designed to destabilise the water wire are currently being characterised in the laboratory.

To explore whether the mechanism I propose for AmtB is common in the Amt/Mep/Rh protein family, I have extended the functional study using SSME to bacterial Rh and fungal Mep proteins.

1- I have purified and measured the activity of the Rh protein from *Nitrosomonas europaea* (*Ne*Rh50). Preliminary data suggested that after an ammonium pulse, *Ne*Rh50 generates a transient charge displacement ~4 times lower than AmtB (0.69±0.08 versus 3.37±0.26 respectively) (**Figure 6.2, panel A**). The kinetic analysis revealed a K_m of 16.46 mM for *Ne*Rh50 compared to 0.8 mM observed for AmtB (**Figure 6.2, panel B**). The decay time observed for *Ne*Rh50 is 39.3±5.6 s^{-1} (13.4±0.6 s^{-1} for AmtB, **see Figure 4.6, Chapter 4**). As a current was measured after an ammonium pulse, the only firm conclusion that I can draw is that *Rh* proteins are not NH_3 "gas channels" as previously hypothesised (Soupene *et al.*, 2004, Hub *et al.*, 2010). However, the exact mode of action of *Ne*Rh50 is not clear. The transient current observed after an ammonium pulse could be due to a simple substrate-protein interaction or describe the continuous turnover of the ammonium translocation cycle. Recording the transient current associated with *Ne*Rh50 activity at various lipid protein ratios (LPR) in liposomes will help to discriminate between these two hypotheses. If the decay time measured after an ammonium pulse

depends on the density of *Ne*Rh50 in the proteoliposomes, we would be able to conclude that the transient current is describing the full translocation of ammonium, thus that the protein acts as an NH_4^+ or NH_3/H^+ transporter.

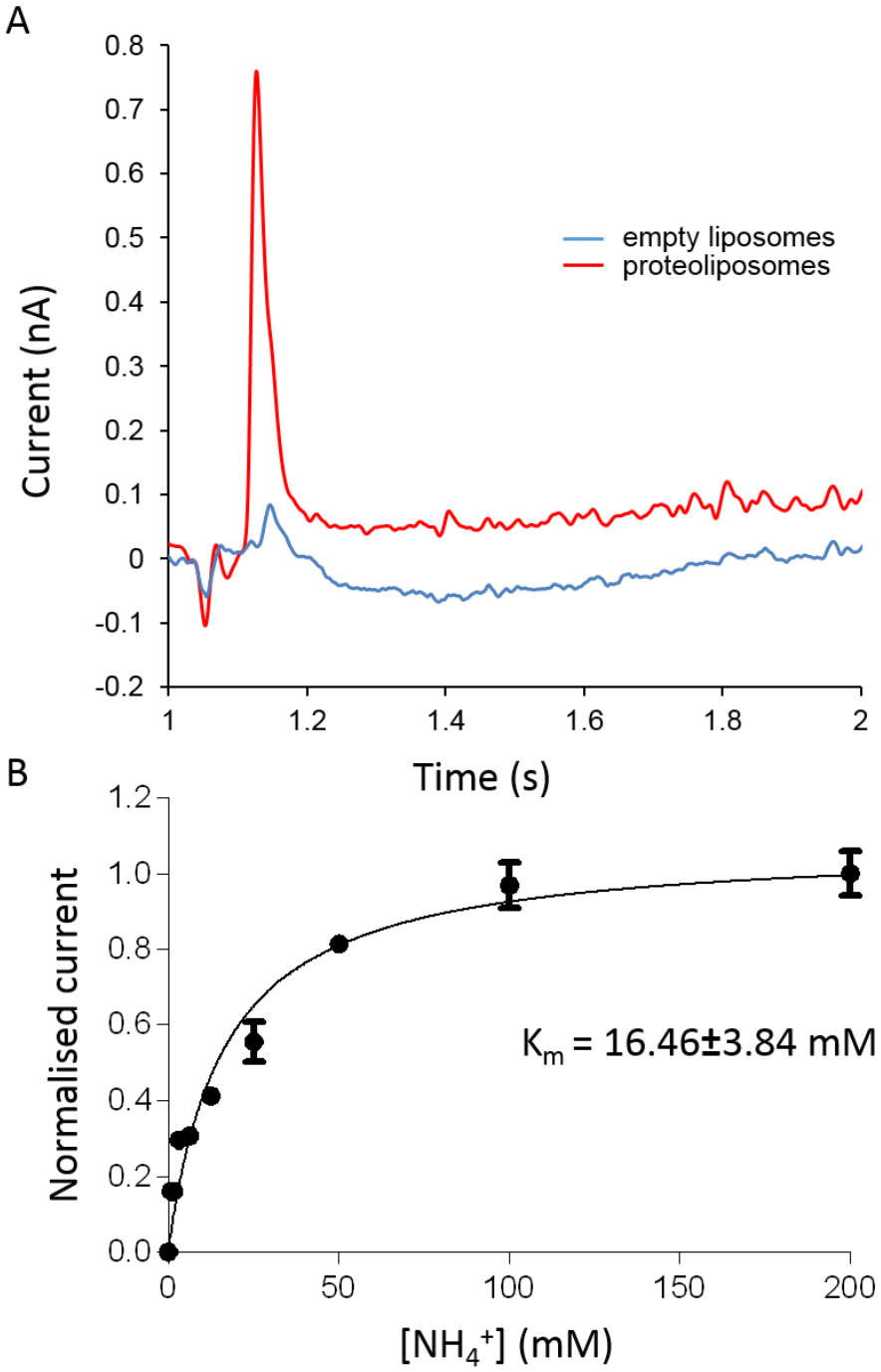

Figure 6.2 *Ne*Rh50 functional characterisation. **(A)** Transient current measured on empty liposomes (blue) or proteoliposomes containing Rh50 at LPR 10 (red) after a 100 mM ammonium pulse **(B)** Ammonium dependence of the normalised maximum amplitude of the transient current.

2- In collaboration with Dr. Anne Marie Marini, I have started to study the Mep2 protein from *S. cerevisiae.*

In pathogenic fungi, filamentation is a dimorphic change associated with virulence (see **section 1.2.5, Chapter 1**). Similarly to pathogenic fungi, *S. cerevisiae* is capable to develop pseudohyphae and Mep2 is essential in this process (Lorenz and Heitman, 1998). There are currently two hypotheses concerning the role of Mep2 in the signalling pathway leading to the pseudohyphal growth: **1-** "*The signal transduction pathway*": Mep2 act as a sensor in the filamentation *via* a signal transduction cascade involving various proteins or **2-** "*The functional signal*": Mep2 act as a sensor by transporting ammonium using a different transport mechanism compared to Mep1/3. Two facts support this latter hypothesis. Under nitrogen starvation conditions 1- The expression of the hyperactive variant (*Sc*Mep2$^{Asn4Gln/Gly349Cys}$) in trans in a *ΔMEP* yeast strain is associated with hyperfilamentation (Boeckstaens *et al.,* 2007) 2- In contrast, the same *ΔMEP* yeast strain expressing an inactive Mep2 variant (*Sc*Mep2^{Asp186Asn}) is unable to filament (Marini *et al.,* 2006). Thus it seems clear that the sensor function and the transport activity of Mep2 are closely linked.

In collaboration with Dr. Mélanie Boeckstaens and Dr. Anna-Maria Marini, we have successfully purified and inserted *Sc*Mep2 into liposomes. We have suggested that the protein is electroneutral (contrary to AmtB) (**Figure 6.3**). However further experiments will be required to confirm *Sc*Mep2 electroneutral mechanism. Using patch clamp in oocytes expressing the Mep2 and Mep1 transporters, Dr. Mélanie Boeckstaens, in collaboration with Prof. Von Wiren, obtained preliminary data indicating that Mep2 activity was not associated with a measurable current, supporting our SSME data. Inversely, Mep1 seems to act electrogenically (Dr. Mélanie Boeckstaens, personal communications). Therefore, it will be interesting to measure the activity of Mep1 using SSME technology. This will confirm whether Mep1 acts as an electrogenic transporter contrary to Mep2 supporting the "*the functional signal*" hypothesis concerning the role of Mep2 in the pseudohyphal growth signalling pathway.

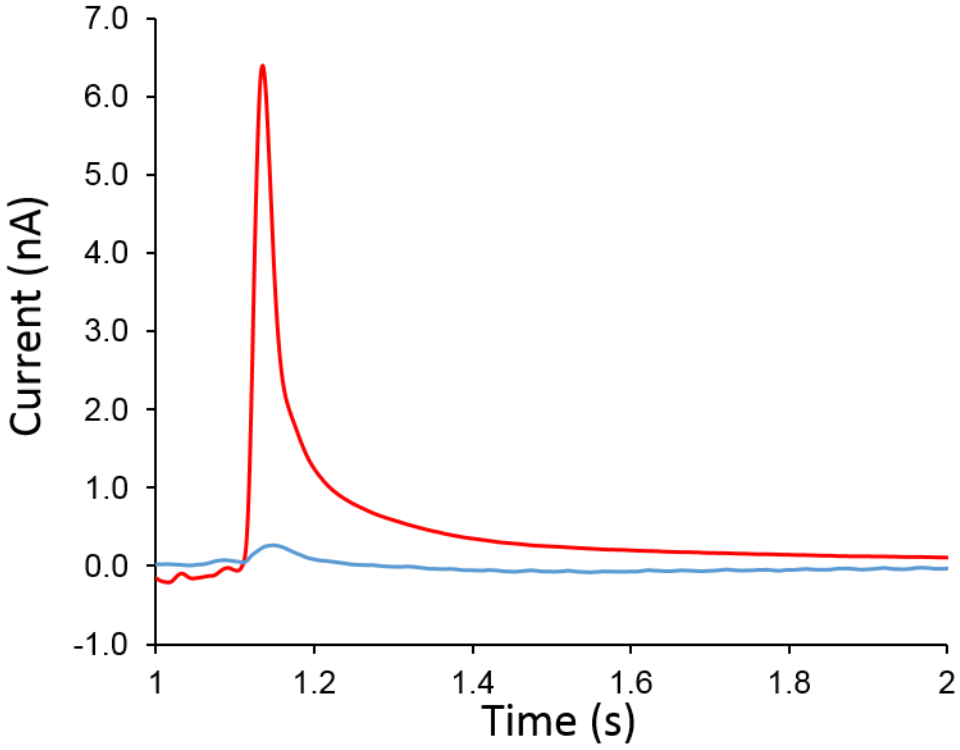

Figure 6.3 *Sc*Mep2 is electroneutral. Transient current measured on AmtB (red) or Mep2 (blue) at LPR 10 after a 100 mM ammonium pulse.

In **Chapter 5**, I have shown that PG is important for AmtB function. Interestingly, the structural analysis of AmtB-bound with PG shows that the residues Asn72 and Asn79 were in direct interaction with PG, forming a specific binding site (Laganowsky *et al*., 2014). Therefore, I have generated a double Asn72Ala/Asn79Ala variant by site directed mutagenesis. A functional study of this variant in the presence and absence of PG will demonstrate if these residues are functionally essential for the AmtB-PG complex formation. More recently, it has been demonstrated, using mass spectrometry, that PE and cardiolipin specifically binds to AmtB allosterically (Patrick *et al.,* 2018). Thus a functional study (similar to the one presented in **Chapter 5**) on PE and cardiolipin would be of high interest to further characterise the importance of the native lipid environment for AmtB.

A small conformational change in one of the extracellular loop regions (residues 70-81) was observed when AmtB was co-crystallised with PG (Laganowsky *et al*., 2014). However as discussed in the introduction (**section 1.3.3 and 1.3.5.2.2, Chapter 1**) x-ray crystallography is not the appropriate tool to characterise the full dynamics associated with AmtB activity. It is therefore necessary to use alternative high resolution structural techniques.

It is now possible, using cryo-electron microscopy (Cryo-EM), to experimentally describe the dynamics of membrane proteins in complex with lipids. More specifically, lipid disc technology (nanodisc or lipodisc), associated with Cryo-EM represents an excellent approach to capture high resolution structures of membrane proteins in native lipidic environment (see two excellent reviews from (Mio and Sato, 2018, Sgro and Costa, 2018)). Nanodiscs are lipid discs formed by apolipoprotein called Membrane Scaffold Protein (MSP) encapsulating a disc of lipid bilayer. The membrane protein of interest can be inserted into the nanodics following similar method than the one use for proteoliposome formation (Bayburt *et al.,* 2002).

I therefore started to use nanodisc technology to study AmtB by Cryo-EM in collaboration with Dr. Kyle Dent and Dr. Martin Walsh (Diamond Light Source, Oxford).

I have optimised the protocol described in (Ritchie *et al.*, 2009, Sligar *et al.,* 2009) to purify the MSP protein variant MSP1E3D1. I have used an *E.coli* polar lipid/PC mixture at a ratio 2/1 (w/w) for the nanodisc formation (same lipid composition previously used to form liposomes, see **Table 5.1, Chapter 5**). The molar ratio of MSP/AmtB/lipid/ used for nanodisc formation was 2/3/130.

The nanodics were subsequently injected onto a Superdex 200 10/300 gel filtration column, the elution profile presented three main peaks (**Figure 6.4, panel A**) and each of them was analysed using SDS-PAGE. The SDS-PAGE analysis revealed that AmtB and MSP were present in the three peaks (**Figure 6.4, panel B**) which suggests that AmtB was inserted into the nanodiscs and that the nanodiscs possessed a wide “size” distribution in solution. This type of SEC profile has been commonly observed for membrane proteins reconstituted into nanodisc (Grushin *et al.*, 2016, Hagn *et al.*, 2018) and it was shown that by varying the quantity of lipid per disc it is possible to improve sample homogeneity (Mors *et al.*, 2013).

In order to select the best condition for Cryo-EM, the nanodiscs present in the three SEC fractions were analysed by negative staining Electron Microscopy (EM). An EM negative staining image of the nanodiscs present in the peak 3 is presented **Figure 6.4, panel C**. The image revealed that the size of the nanodiscs particles is uniform which is ideal for particle averaging analysis by Cryo-EM.

It will now be of interest to 1- change the quantity of lipid used per nanodisc to optimise the sample homogeneity and quality and 2- to add an affinity chromatography step (IMAC) after the SEC to selectively purify nanodiscs containing AmtB prior to Cryo-EM experiments.

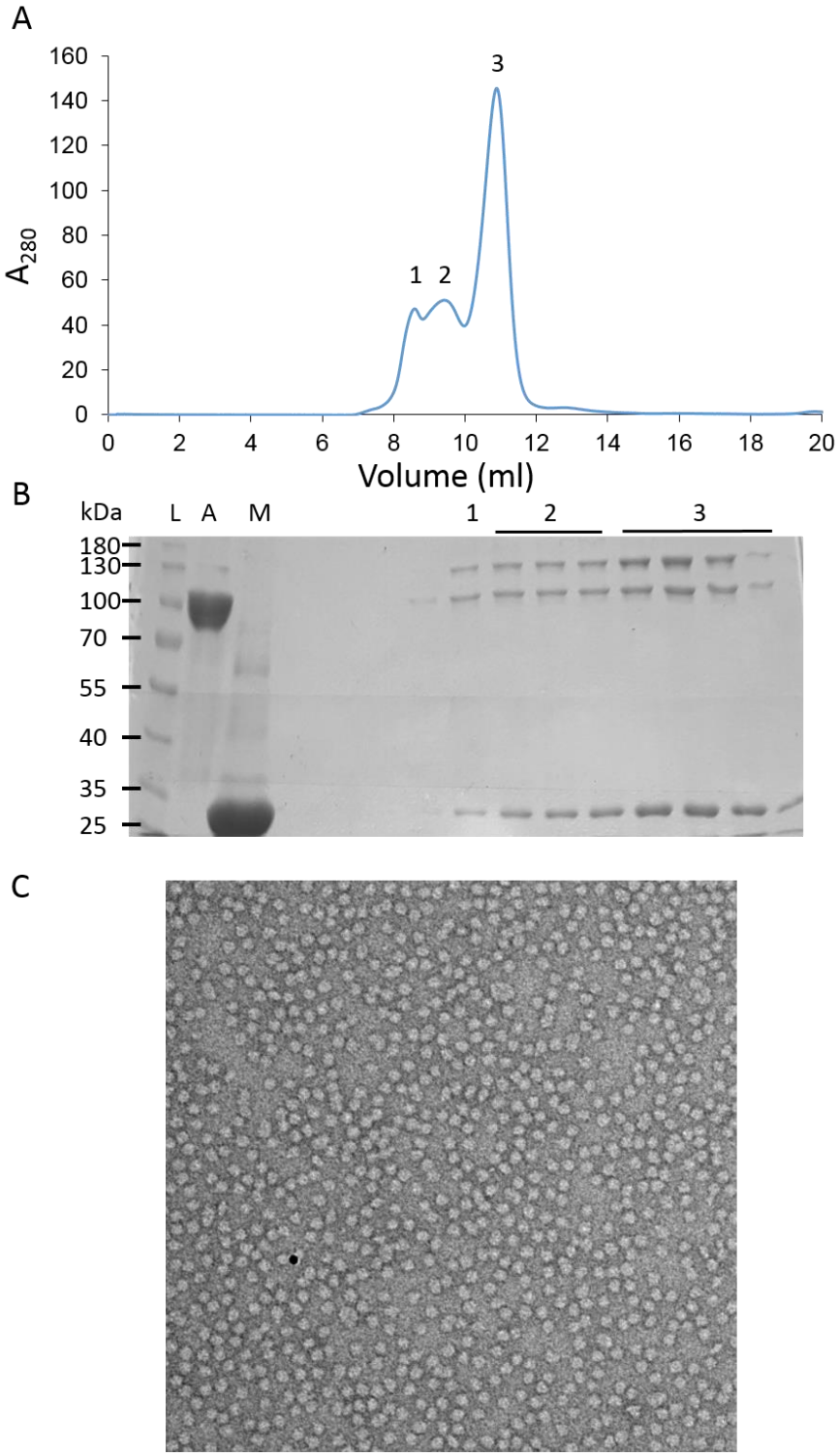

Figure 6.4 Characterisation of the nanodisc containing AmtB. **(A)** SEC elution profile of the complex AmtB-nanodisc (2/3/130 MSP/protein/lipid, molar ratio) **(B)** SDS-PAGE analysis of the three SEC elution peaks (L: Ladder, A: purified AmtB, M: purified Membrane scaffold protein) **(C)** Negative staining of AmtB inserted into nanodisc. The negative staining was done on the SEC peak 3. The particle size distribution is around 12 nm and the image resolution is 2.58 Å/pixel.

As a proof of concept, a first simulation of 2D particle averaging of the nanodiscs based on AmtB structure was generated (**Figure 6.5**). The 2D class average simulation image demonstrates that it should be possible to obtain a resolution high enough to observe some conformational changes on AmtB when inserted into nanodiscs.

Finally, it has been shown that it is possible to measure the activity of a transporter inserted into nanodics by SSME (Henrich *et al.*, 2017). Thus it should be possible to characterise AmtB activity using SSME and resolving potential structural rearrangements by Cryo-EM using the same nanodisc sample.

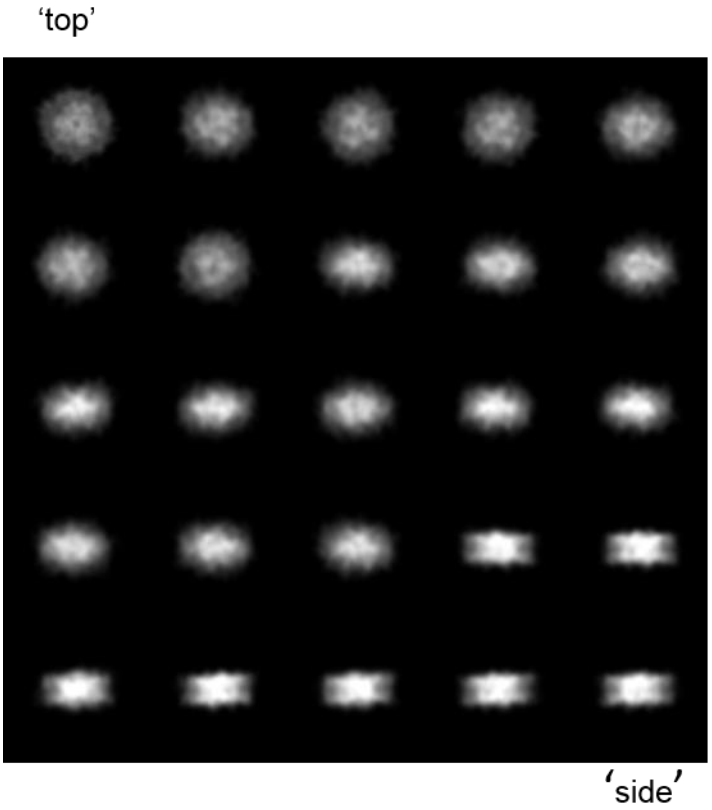

Figure 6.5 Cryo-EM simulation of AmtB inserted into nanodiscs. 2D classification prediction of AmtB-nanodisc particles using volta phase plate technology. Image resolution: 4.64Å/pixel.

References

Agre, P. & Cartron, J. P. (1991). Molecular biology of the Rh antigens. *Blood,* **78**, 551-63.

Alberts, B., Johnson, A., Lewis, J., Raff, M., Roberts, K. & Walter, P. (2002). *Molecular Biology of the Cell, Fourth Edition*, Garland Science.

Andrade, S. L., Dickmanns, A., Ficner, R. & Einsle, O. (2005). Crystal structure of the archaeal ammonium transporter Amt-1 from *Archaeoglobus fulgidus*. *Proc. Natl. Acad. Sci. U.S.A.,* **102**, 14994-9.

Andrade, S. L. & Einsle, O. (2007). The Amt/Mep/Rh family of ammonium transport proteins. *Mol. Membr. Biol.,* **24,** 357-65.

Apweiler, R., Bairoch, A., Wu, C. H., Barker, W. C., Boeckmann, B., Ferro, S., Gasteiger, E., Huang, H., Lopez, R., Magrane, M., Martin, M. J., Natale, D. A., O'donovan, C., Redaschi, N. & Yeh, L. S. (2004). UniProt: the Universal Protein knowledgebase. *Nucleic Acids Res.,* **32,** D115-9.

Ariz, I., Boeckstaens, M., Gouveia, C., Martins, A. P., Sanz-Luque, E., Fernández, E., Soveral, G., Von Wirén, N., Marini, A. M., Aparicio-Tejo, P. M. & Cruz, C. (2018). Nitrogen isotope signature evidences ammonium deprotonation as a common transport mechanism for the AMT-Mep-Rh protein superfamily. *Sci. Adv.,* **4**.

Avent, N. D. & Reid, M. E. (2000). The Rh blood group system: a review. *Blood,* **95,** 375-87.

Avent, N. D., Ridgwell, K., Tanner, M. J. & Anstee, D. J. (1990). cDNA cloning of a 30 kDa erythrocyte membrane protein associated with Rh (Rhesus)-blood-group-antigen expression. *Biochem. J.,* **271,** 821-5.

Baaske, P., Wienken, C. J., Reineck, P., Duhr, S. & Braun, D. (2010). Optical thermophoresis for quantifying the buffer dependence of aptamer binding. *Angew. Chem. Int. Ed. Engl.,* **49,** 2238-41.

Bakouh, N., Benjelloun, F., Hulin, P., Brouillard, F., Edelman, A., Cherif-Zahar, B. & Planelles, G. (2004). NH_3 is involved in the NH_4^+ transport induced by the functional expression of the human Rh C glycoprotein. *J. Biol. Chem.,* **279,** 15975-83.

Bates, R. G. & Pinching, G. D. (1950). Dissociation Constant of Aqueous Ammonia at 0 to 50° from E. m. f. Studies of the Ammonium Salt of a Weak Acid. *J. Am. Chem. Soc.,* **72,** 1393-6.

Bayburt, T. H., Grinkova, Y. V. & Sligar, S. G. (2002). Self-Assembly of Discoidal Phospholipid Bilayer Nanoparticles with Membrane Scaffold Proteins. *Nano. Letters,* **2,** 853-6.

Bazzone, A., Barthmes, M. & Fendler, K. (2017). SSM-Based Electrophysiology for Transporter Research. *Methods Enzymol.,* **594,** 31-83.

Bazzone, A., Costa, W. S., Braner, M., Călinescu, O., Hatahet, L. & Fendler, K. (2013). Introduction to solid supported membrane based electrophysiology. *J. Vis. Exp.***,** e50230.

Benko, P. V., Wood, T. C. & Segel, I. H. (1969). Multiplicity and regulation of amino acid transport in *Penicillium chrysogenum*. *Arch. Biochem. Biophys.,* **129,** 498-08.

Berthaud, A., Manzi, J., Perez, J. & Mangenot, S. (2012). Modeling detergent organization around aquaporin-0 using small-angle X-ray scattering. *J. Am. Chem. Soc.,* **134,** 10080-8.

Biswas, K. & Morschhauser, J. (2005). The Mep2p ammonium permease controls nitrogen starvation-induced filamentous growth in *Candida albicans*. *Mol. Microbiol.,* **56,** 649-69.

Biver, S., Belge, H., Bourgeois, S., Van Vooren, P., Nowik, M., Scohy, S., Houillier, P., Szpirer, J., Szpirer, C., Wagner, C. A., Devuyst, O. & Marini, A. M. (2008). A role for Rhesus factor Rhcg in renal ammonium excretion and male fertility. *Nature,* **456,** 339-43.

Blakey, D., Leech, A., Thomas, G. H., Coutts, G., Findlay, K. & Merrick, M. (2002). Purification of the *Escherichia coli* ammonium transporter AmtB reveals a trimeric stoichiometry. *Biochem. J.,* **364,** 527-35.

Blanchet, C. E. & Svergun, D. I. (2013). Small-angle X-ray scattering on biological macromolecules and nanocomposites in solution. *Annu. Rev. Phys. Chem.,* **64,** 37-54.

Boeckstaens, M., Andre, B. & Marini, A. M. (2007). The yeast ammonium transport protein Mep2 and its positive regulator, the Npr1 kinase, play an important role in normal and pseudohyphal growth on various nitrogen media through retrieval of excreted ammonium. *Mol. Microbiol.,* **64,** 534-46.

Boeckstaens, M., Andre, B. & Marini, A. M. (2008). Distinct transport mechanisms in yeast ammonium transport/sensor proteins of the Mep/Amt/Rh family and impact on filamentation. *J. Biol. Chem.,* **283,** 21362-70.

Bogdanov, M. & Dowhan, W. (1995). Phosphatidylethanolamine is required for in vivo function of the membrane-associated lactose permease of *Escherichia coli*. *J. Biol. Chem.,* **270,** 732-9.

Bogdanov, M., Heacock, P. N. & Dowhan, W. (2002). A polytopic membrane protein displays a reversible topology dependent on membrane lipid composition. *EMBO J.,* **21,** 2107-16.

Boogerd, F. C., Ma, H., Bruggeman, F. J., Van Heeswijk, W. C., Garcia-Contreras, R., Molenaar, D., Krab, K. & Westerhoff, H. V. (2011). AmtB-mediated NH_3 transport in prokaryotes must be active and as a consequence regulation of transport by GlnK is mandatory to limit futile cycling of NH_4^+/NH_3. *FEBS Lett.,* **585,** 23-8.

Bornhorst, J. A. & Falke, J. J. (2000). Purification of proteins using polyhistidine affinity tags. *Methods Enzymol.,* **326,** 245-54.

Bostick, D. L. & Brooks, C. L., 3rd (2007). Deprotonation by dehydration: the origin of ammonium sensing in the AmtB channel. *PLoS Comput. Biol.,* **3,** e22.

Botelho, A. V., Huber, T., Sakmar, T. P. & Brown, M. F. (2006). Curvature and hydrophobic forces drive oligomerization and modulate activity of rhodopsin in membranes. *Biophys. J.,* **91,** 4464-77.

Breyton, C., Gabel, F., Lethier, M., Flayhan, A., Durand, G., Jault, J. M., Juillan-Binard, C., Imbert, L., Moulin, M., Ravaud, S., Härtlein, M. & Ebel, C. (2013). Small angle neutron scattering for the study of solubilised membrane proteins. *Eur. Phys. J. E. Soft Matter,* **36,** 71.

Bruce, L. J., Guizouarn, H., Burton, N. M., Gabillat, N., Poole, J., Flatt, J. F., Brady, R. L., Borgese, F., Delaunay, J. & Stewart, G. W. (2009). The monovalent cation leak in overhydrated stomatocytic red blood cells results from amino acid substitutions in the Rh-associated glycoprotein. *Blood,* **113,** 1350-7.

Cao, Z., Lin, M., Zhang, Q. & Mo, Y. (2004). Studies of Solvation Free Energies of Methylammoniums and Irregular Basicity Ordering of Methylamines in Aqueous Solution by a Combined Discrete-Continuum Model. *J. Phys. Chem. A,* **108,** 4277-82.

Cao, Z., Mo, Y. & Thiel, W. (2007). Deprotonation mechanism of NH_4^+ in the *Escherichia coli* ammonium transporter AmtB: insight from QM and QM/MM calculations. *Angew. Chem. Int. Ed. Engl.,* **46,** 6811-5.

Chen, P. C. & Hub, J. S. (2014). Validating solution ensembles from molecular dynamics simulation by wide-angle X-ray scattering data. *Biophys. J.,* **107,** 435-47.

Chen, P. C. & Hub, J. S. (2015). Structural Properties of Protein-Detergent Complexes from SAXS and MD Simulations. *J. Phys. Chem. Lett.,* **6,** 5116-21.

Cherezov, V., Liu, J., Griffith, M., Hanson, M. A. & Stevens, R. C. (2008). LCP-FRAP Assay for Pre-Screening Membrane Proteins for in Meso Crystallization. *Cryst. Growth Des.,* **8,** 4307-15.

Cherif-Zahar, B., Bloy, C., Le Van Kim, C., Blanchard, D., Bailly, P., Hermand, P., Salmon, C., Cartron, J. P. & Colin, Y. (1990). Molecular cloning and protein structure of a human blood group Rh polypeptide. *Proc. Natl. Acad. Sci. U. S. A.,* **87,** 6243-7.

Cherif-Zahar, B., Raynal, V., Gane, P., Mattei, M. G., Bailly, P., Gibbs, B., Colin, Y. & Cartron, J. P. (1996). Candidate gene acting as a suppressor of the RH locus in most cases of Rh-deficiency. *Nat. Genet.,* **12,** 168-73.

Chiasson, D. M., Loughlin, P. C., Mazurkiewicz, D., Mohammadidehcheshmeh, M., Fedorova, E. E., Okamoto, M., Mclean, E., Glass, A. D., Smith, S. E., Bisseling, T., Tyerman, S. D., Day, D. A. & Kaiser, B. N. (2014). Soybean SAT1 (Symbiotic Ammonium Transporter 1) encodes a bHLH transcription factor involved in nodule growth and NH_4^+ transport. *Proc. Natl. Acad. Sci. U. S. A.,* **111,** 4814-9.

Compton, E. L., Karinou, E., Naismith, J. H., Gabel, F. & Javelle, A. (2011). Low resolution structure of a bacterial SLC26 transporter reveals dimeric stoichiometry and mobile intracellular domains. *J. Biol. Chem.,* **286,** 27058-67.

Compton, E. L., Page, K., Findlay, H. E., Haertlein, M., Moulin, M., Zachariae, U., Norman, D. G., Gabel, F. & Javelle, A. (2014). Conserved structure and domain organization among bacterial Slc26 transporters. *Biochem. J.,* **463,** 297-307.

Cong, X., Liu, Y., Liu, W., Liang, X. & Laganowsky, A. (2017). Allosteric modulation of protein-protein interactions by individual lipid binding events. *Nat. Commun.,* **8,** 2203.

Cong, X., Liu, Y., Liu, W., Liang, X., Russell, D. H. & Laganowsky, A. (2016). Determining Membrane Protein-Lipid Binding Thermodynamics Using Native Mass Spectrometry. *J. Am. Chem. Soc.,* **138,** 4346-9.

Conroy, M. J., Bullough, P. A., Merrick, M. & Avent, N. D. (2005). Modelling the human rhesus proteins: implications for structure and function. *Br. J. Haematol.,* **131,** 543-51.

Conroy, M. J., Durand, A., Lupo, D., Li, X. D., Bullough, P. A., Winkler, F. K. & Merrick, M. (2007). The crystal structure of the *Escherichia coli* AmtB-GlnK complex reveals how GlnK regulates the ammonia channel. *Proc. Natl. Acad. Sci. U. S. A.,* **104,** 1213-8.

Conroy, M. J., Jamieson, S. J., Blakey, D., Kaufmann, T., Engel, A., Fotiadis, D., Merrick, M. & Bullough, P. A. (2004). Electron and atomic force microscopy of the trimeric ammonium transporter AmtB. *EMBO Rep.,* **5,** 1153-8.

Coutts, G., Thomas, G., Blakey, D. & Merrick, M. (2002). Membrane sequestration of the signal transduction protein GlnK by the ammonium transporter AmtB. *EMBO J.,* **21,** 536-45.

Couturier, J., Montanini, B., Martin, F., Brun, A., Blaudez, D. & Chalot, M. (2007). The expanded family of ammonium transporters in the perennial poplar plant. *New. Phytol.,* **174**, 137-50.

De Michele, R., Ast, C., Loqué, D., Ho, C. H., Andrade, S. L., Lanquar, V., Grossmann, G., Gehne, S., Kumke, M. U. & Frommer, W. B. (2013). Fluorescent sensors reporting the activity of ammonium transceptors in live cells. *Elife,* **2,** e00800.

Deisenhofer, J., Epp, O., Miki, K., Huber, R. & Michel, H. (1985). Structure of the protein subunits in the photosynthetic reaction centre of *Rhodopseudomonas viridis* at 3Å resolution. *Nature,* **318,** 618-24.

Denning, E. J. & Beckstein, O. (2013). Influence of lipids on protein-mediated transmembrane transport. *Chem. Phys. Lipids,* **169,** 57-71.

Dias Mirandela, G., Tamburrino, G., Ivanovic, M. T., Strnad, F. M., Byron, O., Rasmussen, T., Hoskisson, P. A., Hub, J. S., Zachariae, U., Gabel, F. & Javelle, A. (2018). Merging In-solution X-Ray and Neutron Scattering Data Allows Fine Structural Analysis of Membrane-protein Detergent Complexes. *J. Phys. Chem. Lett*., **9** (14), 3910-4

Dubois, E. & Grenson, M. (1979). Methylamine/ammonia uptake systems in *saccharomyces cerevisiae*: multiplicity and regulation. *Mol. Gen. Genet.,* **175,** 67-76.

Durand, A. & Merrick, M. (2006). *In vitro* analysis of the *Escherichia coli* AmtB-GlnK complex reveals a stoichiometric interaction and sensitivity to ATP and 2-oxoglutarate. *J. Biol. Chem.,* **281,** 29558-67.

Ebel, C. (2011). Sedimentation velocity to characterize surfactants and solubilized membrane proteins. *Methods,* **54,** 56-66.

Einstein, A. (1905). Über die von der molekularkinetischen Theorie der Wärme geforderte Bewegung von in ruhenden Flüssigkeiten suspendierten Teilchen. *Ann. Phys.,* **322,** 549-60.

Elbing, K. & Brent, R. (2002). Media preparation and bacteriological tools. *Curr. Protoc. Mol. Biol.,* **Chapter 1,** Unit 1.1.

Elbourne, L. D. H., Tetu, S. G., Hassan, K. A. & Paulsen, I. T. (2017). TransportDB 2.0: a database for exploring membrane transporters in sequenced genomes from all domains of life. *Nucleic Acids Res.,* **45,** D320-4.

Endeward, V., Arias-Hidalgo, M., Al-Samir, S. & Gros, G. (2017). $CO_{(2)}$ Permeability of Biological Membranes and Role of $CO_{(2)}$ Channels. *Membranes,* **7,** 61.

Franke, D., Petoukhov, M. V., Konarev, P. V., Panjkovich, A., Tuukkanen, A., Mertens, H. D. T., Kikhney, A. G., Hajizadeh, N. R., Franklin, J. M., Jeffries, C. M. & Svergun, D. I. (2017). ATSAS 2.8: a comprehensive data analysis suite for small-angle scattering from macromolecular solutions. *J. Appl. Crystallogr.,* **50,** 1212-25.

Gabel, F. (2015). Small-Angle Neutron Scattering for Structural Biology of Protein-RNA Complexes. *Methods Enzymol.,* **558,** 391-415.

Gabel, F., Lensink, M. F., Clantin, B., Jacob-Dubuisson, F., Villeret, V. & Ebel, C. (2014). Probing the conformation of FhaC with small-angle neutron scattering and molecular modeling. *Biophys. J.,* **107,** 185-96.

Galián, C., Manon, F., Dezi, M., Torres, C., Ebel, C., Lévy, D. & Jault, J.-M. (2011). Optimized Purification of a Heterodimeric ABC Transporter in a Highly Stable Form Amenable to 2-D Crystallization. *PLoS ONE,* **6,** e19677.

Garvin, J. L., Burg, M. B. & Knepper, M. A. (1988). Active NH_4^+ absorption by the thick ascending limb. *Am. J. Physiol.,* **255,** F57-65.

Gasteiger, E., Hoogland, C., Gattiker, A., Duvaud, S. E., Wilkins, M. R., Appel, R. D. & Bairoch, A. 2005. Protein Identification and Analysis Tools on the ExPASy Server. *In:* Walker, J. M. (ed.) *The Proteomics Protocols Handbook.* Totowa, NJ: Humana Press.

Geertsma, E. R., Chang, Y. N., Shaik, F. R., Neldner, Y., Pardon, E., Steyaert, J. & Dutzler, R. (2015). Structure of a prokaryotic fumarate transporter reveals the architecture of the SLC26 family. *Nat. Struct. Mol. Biol.,* **22,** 803-8.

Gimeno, C. J., Ljungdahl, P. O., Styles, C. A. & Fink, G. R. (1992). Unipolar cell divisions in the yeast *S. cerevisiae* lead to filamentous growth: regulation by starvation and RAS. *Cell,* **68,** 1077-90.

Grushin, K., Andrew White, M. & Stoilova-Mcphie, S. (2016). Reversible Stacking of Lipid Nanodiscs for Structural Studies of Clotting Factors. *Nanotech. reviews,* **6,** 139-48.

Gruswitz, F., Chaudhary, S., Ho, J. D., Schlessinger, A., Pezeshki, B., Ho, C. M., Sali, A., Westhoff, C. M. & Stroud, R. M. (2010). Function of human Rh based on structure of RhCG at 2.1 Å. *Proc. Natl. Acad. Sci. U. S. A.,* **107,** 9638-43.

Gruswitz, F., Connell, J. & Stroud, R. M. (2007). Inhibitory complex of the transmembrane ammonia channel, AmtB, and the cytosolic regulatory protein, GlnK, at 1.96 Å. *Proc. Natl. Acad. Sci. U. S. A.,* **104,** 42-7.

Hackette, S. L., Skye, G. E., Burton, C. & Segel, I. H. (1970). Characterization of an ammonium transport system in filamentous fungi with methylammonium-^{14}C as the substrate. *J. Biol. Chem.,* **245,** 4241-50.

Hagn, F., Nasr, M. L. & Wagner, G. (2018). Assembly of phospholipid nanodiscs of controlled size for structural studies of membrane proteins by NMR. *Nat. Protoc.,* **13,** 79-98.

Hall, J. A. & Kustu, S. (2011). The pivotal twin histidines and aromatic triad of the *Escherichia coli* ammonium channel AmtB can be replaced. *Proc. Natl. Acad. Sci. U. S. A.,* **108,** 13270-4.

Hanahan, D. (1983). Studies on transformation of *Escherichia coli* with plasmids. *J. Mol. Biol.,* **166,** 557-80.

Hediger, M. A., Clemencon, B., Burrier, R. E. & Bruford, E. A. (2013). The ABCs of membrane transporters in health and disease (SLC series): introduction. *Mol. Aspects Med.,* **34,** 95-107.

Heinrich, A., Woyda, K., Brauburger, K., Meiss, G., Detsch, C., Stulke, J. & Forchhammer, K. (2006). Interaction of the membrane-bound GlnK-AmtB complex with the master regulator of nitrogen metabolism TnrA in *Bacillus subtilis*. *J. Biol. Chem.,* **281,** 34909-17.

Henrich, E., Sormann, J., Eberhardt, P., Peetz, O., Mezhyrova, J., Morgner, N., Fendler, K., Dotsch, V., Wachtveitl, J., Bernhard, F. & Bamann, C. (2017). From Gene to Function: Cell-Free Electrophysiological and Optical Analysis of Ion Pumps in Nanodiscs. *Biophys. J.,* **113,** 1331-41.

Https://Www.Creative-Biostructure.Com/. *Mempro™ Membrane Protein Platform* [Online]. Available: https://www.creative-biostructure.com/mempro%E2%84%A2-membrane-protein-platform-447.htm [Accessed 01 July 2018].

Huang, C. H. (1998). The human Rh50 glycoprotein gene. Structural organization and associated splicing defect resulting in Rh(null) disease. *J. Biol. Chem.,* **273,** 2207-13.

Huang, C. H. & Peng, J. (2005). Evolutionary conservation and diversification of Rh family genes and proteins. *Proc. Natl. Acad. Sci. U. S. A.,* **102,** 15512-7.

Hub, J. S., Winkler, F. K., Merrick, M. & De Groot, B. L. (2010). Potentials of mean force and permeabilities for carbon dioxide, ammonia, and water flux across a Rhesus protein channel and lipid membranes. *J. Am. Chem. Soc.,* **132,** 13251-63.

Huergo, L. F., Chandra, G. & Merrick, M. (2013). $P_{(II)}$ signal transduction proteins: nitrogen regulation and beyond. *FEMS Microbiol. Rev.,* **37,** 251-83.

Hyman, M. R. & Arp, D. J. (1992). $^{14}C_2H_2$- and $^{14}CO_2$-labeling studies of the de novo synthesis of polypeptides by *Nitrosomonas europaea* during recovery from acetylene and light inactivation of ammonia monooxygenase. *J. Biol. Chem.,* **267,** 1534-45.

Inwood, W. B., Hall, J. A., Kim, K. S., Fong, R. & Kustu, S. (2009). Genetic evidence for an essential oscillation of transmembrane-spanning segment 5 in the *Escherichia coli* ammonium channel AmtB. *Genetics,* **183,** 1341-55.

Ishikita, H. & Knapp, E. W. (2007). Protonation states of ammonia/ammonium in the hydrophobic pore of ammonia transporter protein AmtB. *J. Am. Chem. Soc.,* **129,** 1210-5.

Javelle, A., Lupo, D., Li, X. D., Merrick, M., Chami, M., Ripoche, P. & Winkler, F. K. (2007). Structural and mechanistic aspects of Amt/Rh proteins. *J.Struct.Biol.,* **158,** 472-81.

Javelle, A., Lupo, D., Ripoche, P., Fulford, T., Merrick, M. & Winkler, F. K. (2008). Substrate binding, deprotonation, and selectivity at the periplasmic entrance of the *Escherichia coli* ammonia channel AmtB. *Proc. Natl. Acad. Sci. U. S. A.,* **105,** 5040-5.

Javelle, A., Lupo, D., Zheng, L., Li, X. D., Winkler, F. K. & Merrick, M. (2006). An unusual twin-his arrangement in the pore of ammonia channels is essential for substrate conductance. *J. Biol. Chem.,* **281,** 39492-8.

Javelle, A., Morel, M., Rodríguez-Pastrana, B. R., Botton, B., André, B., Marini, A. M., Brun, A. & Chalot, M. (2003). Molecular characterization, function and regulation of ammonium transporters (Amt) and ammonium-metabolizing enzymes (GS, NADP-GDH) in the ectomycorrhizal fungus *Hebeloma cylindrosporum*. *Mol. Microbiol.,* **47,** 411-30.

Javelle, A., Rodríguez-Pastrana, B. R., Jacob, C., Botton, B., Brun, A., André, B., Marini, A. M. & Chalot, M. (2001). Molecular characterization of two ammonium transporters from the ectomycorrhizal fungus *Hebeloma cylindrosporum*. *FEBS Lett.,* **505,** 393-8.

Javelle, A., Severi, E., Thornton, J. & Merrick, M. (2004). Ammonium sensing in *Escherichia coli*. Role of the ammonium transporter AmtB and AmtB-GlnK complex formation. *J. Biol. Chem.,* **279,** 8530-8.

Javelle, A., Thomas, G., Marini, A. M., Krämer, R. & Merrick, M. (2005). *In vivo* functional characterization of the *Escherichia coli* ammonium channel AmtB: evidence for metabolic coupling of AmtB to glutamine synthetase. *Biochem. J.,* **390,** 215-22.

Jeffries, C. M., Graewert, M. A., Blanchet, C. E., Langley, D. B., Whitten, A. E. & Svergun, D. I. (2016). Preparing monodisperse macromolecular samples for successful biological small-angle X-ray and neutron-scattering experiments. *Nat. Protoc.,* **11,** 2122-53.

Jerabek-Willemsen, M., André, T., Wanner, R., Roth, H. M., Duhr, S., Baaske, P. & Breitsprecher, D. (2014). MicroScale Thermophoresis: Interaction analysis and beyond. *J. Mol. Struct.,* **1077,** 101-13.

Jiang, P. & Ninfa, A. J. (2007). *Escherichia coli* P_{II} signal transduction protein controlling nitrogen assimilation acts as a sensor of adenylate energy charge in vitro. *Biochemistry,* **46,** 12979-96.

Jiang, P., Peliska, J. A. & Ninfa, A. J. (1998). The regulation of *Escherichia coli* glutamine synthetase revisited: role of 2-ketoglutarate in the regulation of glutamine synthetase adenylylation state. *Biochemistry,* **37,** 12802-10.

Kaiser, B. N., Finnegan, P. M., Tyerman, S. D., Whitehead, L. F., Bergersen, F. J., Day, D. A. & Udvardi, M. K. (1998). Characterization of an Ammonium Transport Protein from the Peribacteroid Membrane of Soybean Nodules. *Science,* **281,** 1202-6.

Khademi, S., O'connell, J., Remis, J., Robles-Colmenares, Y., Miercke, L. J. & Stroud, R. M. (2004). Mechanism of ammonia transport by Amt/MEP/Rh: structure of AmtB at 1.35 Å. *Science,* **305,** 1587-94.

Kleiner, D. (1982). Ammonium (methylammonium) transport by *Klebsiella pneumoniae*. *Biochim. Biophys. Acta,* **688,** 702-8.

Kleiner, D. & Fitzke, E. (1979). Evidence for ammonia translocation by *Clostridium pasteurianum*. *Biochem. Biophys. Res. Commun.,* **86,** 211-7.

Knight, C. J. & Hub, J. S. (2015). WAXSiS: a web server for the calculation of SAXS/WAXS curves based on explicit-solvent molecular dynamics. *Nucleic Acids Res.,* **43,** W225-30.

Koutsioubas, A. (2017). Low-Resolution Structure of Detergent-Solubilized Membrane Proteins from Small-Angle Scattering Data. *Biophys. J.,* **113,** 2373-82.

Krogh, A., Larsson, B., Von Heijne, G. & Sonnhammer, E. L. (2001). Predicting transmembrane protein topology with a hidden Markov model: application to complete genomes. *J. Mol. Biol.,* **305,** 567-80.

Kynde, S. A., Skar-Gislinge, N., Pedersen, M. C., Midtgaard, S. R., Simonsen, J. B., Schweins, R., Mortensen, K. & Arleth, L. (2014). Small-angle scattering gives direct structural information about a membrane protein inside a lipid environment. *Acta Crystallogr. D Biol. Crystallogr.,* **70,** 371-83.

Laane, C., Krone, W., Konings, W., Haaker, H. & Veeger, C. (1980). Short-term effect of ammonium chloride on nitrogen fixation by *Azotobacter vinelandii* and by bacteroids of *Rhizobium leguminosarum*. *Eur. J. Biochem.,* **103,** 39-46.

Laemmli, U. K. (1970). Cleavage of structural proteins during the assembly of the head of bacteriophage T4. *Nature,* **227,** 680-5.

Laganowsky, A., Reading, E., Allison, T. M., Ulmschneider, M. B., Degiacomi, M. T., Baldwin, A. J. & Robinson, C. V. (2014). Membrane proteins bind lipids selectively to modulate their structure and function. *Nature,* **510,** 172-75.

Lamoureux, G., Klein, M. L. & Berneche, S. (2007). A stable water chain in the hydrophobic pore of the AmtB ammonium transporter. *Biophys. J.,* **92,** L82-4.

Lande, M. B., Donovan, J. M. & Zeidel, M. L. (1995). The relationship between membrane fluidity and permeabilities to water, solutes, ammonia, and protons. *J. Gen. Physiol.,* **106,** 67-84.

Le Van Kim, C., Mouro, I., Cherif-Zahar, B., Raynal, V., Cherrier, C., Cartron, J. P. & Colin, Y. (1992). Molecular cloning and primary structure of the human blood group RhD polypeptide. *Proc. Natl. Acad. Sci. U. S. A.,* **89,** 10925-9.

Lo, H. J., Kohler, J. R., Didomenico, B., Loebenberg, D., Cacciapuoti, A. & Fink, G. R. (1997). Nonfilamentous *C. albicans* mutants are avirulent. *Cell,* **90,** 939-49.

Loqué, D., Lalonde, S., Looger, L. L., Von Wirén, N. & Frommer, W. B. (2007). A cytosolic trans-activation domain essential for ammonium uptake. *Nature,* **446,** 195-8.

Lorenz, M. C. & Heitman, J. (1998). The MEP2 ammonium permease regulates pseudohyphal differentiation in *Saccharomyces cerevisiae*. *EMBO J.,* **17,** 1236-47.

Ludewig, U. (2004). Electroneutral ammonium transport by basolateral rhesus B glycoprotein. *J. Physiol.,* **559,** 751-9.

Ludewig, U., Von Wiren, N. & Frommer, W. B. (2002). Uniport of NH_4^+ by the root hair plasma membrane ammonium transporter *Le*AMT1;1. *J. Biol. Chem.,* **277,** 13548-55.

Lupo, D., Li, X. D., Durand, A., Tomizaki, T., Cherif-Zahar, B., Matassi, G., Merrick, M. & Winkler, F. K. (2007). The 1.3-Å resolution structure of *Nitrosomonas europaea* Rh50 and mechanistic implications for NH_3 transport by Rhesus family proteins. *Proc. Natl. Acad. Sci. U. S. A.,* **104,** 19303-8.

Luzhkov, V. B., Almlof, M., Nervall, M. & Aqvist, J. (2006). Computational study of the binding affinity and selectivity of the bacterial ammonium transporter AmtB. *Biochemistry,* **45,** 10807-14.

Mager, T., Rimon, A., Padan, E. & Fendler, K. (2011). Transport mechanism and pH regulation of the Na^+/H^+ antiporter NhaA from *Escherichia coli*: an electrophysiological study. *J. Biol. Chem.,* **286,** 23570-81.

Mahieu, E. & Gabel, F. (2018). Biological small-angle neutron scattering: recent results and development. *Acta Crystallogr. D Struct. Biol.,* **74,** 715-26.

Maresca, B. & Kobayashi, G. S. (1989). Dimorphism in *Histoplasma capsulatum*: a model for the study of cell differentiation in pathogenic fungi. *Microbiol. Rev.,* **53,** 186-209.

Maric, S., Skar-Gislinge, N., Midtgaard, S., Thygesen, M. B., Schiller, J., Frielinghaus, H., Moulin, M., Haertlein, M., Forsyth, V. T., Pomorski, T. G. & Arleth, L. (2014). Stealth carriers for low-resolution structure determination of membrane proteins in solution. *Acta Crystallogr. D Biol. Crystallogr.,* **70,** 317-28.

Marini, A. M., Boeckstaens, M., Benjelloun, F., Cherif-Zahar, B. & Andre, B. (2006). Structural involvement in substrate recognition of an essential aspartate residue conserved in Mep/Amt and Rh-type ammonium transporters. *Curr. Genet.,* **49,** 364-74.

Marini, A. M., Soussi-Boudekou, S., Vissers, S. & Andre, B. (1997a). A family of ammonium transporters in *Saccharomyces cerevisiae*. *Mol. Cell. Biol.,* **17,** 4282-93.

Marini, A. M., Springael, J. Y., Frommer, W. B. & Andre, B. (2000). Cross-talk between ammonium transporters in yeast and interference by the soybean SAT1 protein. *Mol. Microbiol.,* **35,** 378-85.

Marini, A. M., Urrestarazu, A., Beauwens, R. & Andre, B. (1997b). The Rh (rhesus) blood group polypeptides are related to NH_4^+ transporters. *Trends Biochem. Sci.,* **22,** 460-1.

Marini, A. M., Vissers, S., Urrestarazu, A. & André, B. (1994). Cloning and expression of the MEP1 gene encoding an ammonium transporter in *Saccharomyces cerevisiae*. *EMBO J.,* **13,** 3456-63.

Matassi, G., Cherif-Zahar, B., Raynal, V., Rouger, P. & Cartron, J. P. (1998). Organization of the human RH50A gene (RHAG) and evolution of base composition of the RH gene family. *Genomics,* **47,** 286-93.

Maurel, C., Reizer, J., Schroeder, J. I., Chrispeels, M. J. & Saier, M. H., Jr. (1994). Functional characterization of the *Escherichia coli* glycerol facilitator, GlpF, in Xenopus oocytes. *J. Biol. Chem*., **269**, 11869-72.

Mcdonald, T. R., Dietrich, F. S. & Lutzoni, F. (2012). Multiple horizontal gene transfers of ammonium transporters/ammonia permeases from prokaryotes to eukaryotes: toward a new functional and evolutionary classification. *Mol. Biol. Evol.,* **29,** 51-60.

Mcdonald, T. R. & Ward, J. M. (2016). Evolution of Electrogenic Ammonium Transporters (AMTs). *Front. Plant. Sci.,* **7,** 352.

Meier-Wagner, J., Nolden, L., Jakoby, M., Siewe, R., Kramer, R. & Burkovski, A. (2001). Multiplicity of ammonium uptake systems in *Corynebacterium glutamicum*: role of Amt and AmtB. *Microbiology,* **147,** 135-43.

Merrick, M., Javelle, A., Durand, A., Severi, E., Thornton, J., Avent, N. D., Conroy, M. J. & Bullough, P. A. (2006). The *Escherichia coli* AmtB protein as a model system for understanding ammonium transport by Amt and Rh proteins. *Transfus. Clin. Biol.,* **13,** 97-102.

Mio, K. & Sato, C. (2018). Lipid environment of membrane proteins in cryo-EM based structural analysis. *Biophys. Rev.,* **10,** 307-16.

Miroux, B. & Walker, J. E. (1996). Over-production of proteins in *Escherichia coli*: mutant hosts that allow synthesis of some membrane proteins and globular proteins at high levels. *J. Mol. Biol.,* **260,** 289-98.

Monahan, B. J., Unkles, S. E., Tsing, I. T., Kinghorn, J. R., Hynes, M. J. & Davis, M. A. (2002). Mutation and functional analysis of the Aspergillus nidulans ammonium permease MeaA and evidence for interaction with itself and MepA. *Fungal.Genet.Biol.,* **36,** 35-46.

Moradi, M. & Tajkhorshid, E. (2013). Mechanistic picture for conformational transition of a membrane transporter at atomic resolution. *Proc. Natl. Acad. Sci. U. S. A.,* **110,** 18916-21.

Mors, K., Roos, C., Scholz, F., Wachtveitl, J., Dotsch, V., Bernhard, F. & Glaubitz, C. (2013). Modified lipid and protein dynamics in nanodiscs. *Biochim. Biophys. Acta,* **1828,** 1222-9.

Mouro-Chanteloup, I., Cochet, S., Chami, M., Genetet, S., Zidi-Yahiaoui, N., Engel, A., Colin, Y., Bertrand, O. & Ripoche, P. (2010). Functional reconstitution into liposomes of purified human RhCG ammonia channel. *PLoS One,* **5,** e8921.

Neuhäuser, B., Dynowski, M. & Ludewig, U. (2014). Switching substrate specificity of AMT/MEP/ Rh proteins. *Channels (Austin),* **8,** 496-502.

Neuhäuser, B., Dynowski, M., Mayer, M. & Ludewig, U. (2007). Regulation of NH_4^+ transport by essential cross talk between AMT monomers through the carboxyl tails. *Plant. Physiol.,* **143,** 1651-9.

Neverisky, D. L. & Abbott, G. W. (2015). Ion channel-transporter interactions. *Crit. Rev. Biochem. Mol. Biol.,* **51,** 257-67.

Ninnemann, O., Jauniaux, J. C. & Frommer, W. B. (1994). Identification of a high affinity NH_4^+ transporter from plants. *EMBO J.,* **13,** 3464-71.

Nygaard, T. P., Rovira, C., Peters, G. H. & Jensen, M. O. (2006). Ammonium recruitment and ammonia transport by *E. coli* ammonia channel AmtB. *Biophys. J.,* **91,** 4401-12.

Oliver, R. C., Pingali, S. V. & Urban, V. S. (2017). Designing Mixed Detergent Micelles for Uniform Neutron Contrast. *J. Phys. Chem. Lett.,* **8,** 5041-6.

Overington, J. P., Al-Lazikani, B. & Hopkins, A. L. (2006). How many drug targets are there? *Nat. Rev. Drug Discov.,* **5,** 993-6.

Pateman, J. A., Kinghorn, J. R., Dunn, E. & Forbes, E. (1973). Ammonium regulation in *Aspergillus nidulans*. *J. Bacteriol.,* **114,** 943-50.

Paternostre, M. T., Roux, M. & Rigaud, J. L. (1988). Mechanisms of membrane protein insertion into liposomes during reconstitution procedures involving the use of detergents. 1. Solubilization of large unilamellar liposomes (prepared by reverse-phase evaporation) by triton X-100, octyl glucoside, and sodium cholate. *Biochemistry,* **27,** 2668-77.

Patrick, J. W., Boone, C. D., Liu, W., Conover, G. M., Liu, Y., Cong, X. & Laganowsky, A. (2018). Allostery revealed within lipid binding events to membrane proteins. *Proc. Natl. Acad. Sci. U. S. A.,* **115,** 2976-81.

Pearson, R. G. (1986). Ionization potentials and electron affinities in aqueous solution. *J. Am. Chem. Soc.,* **108,** 6109-14.

Perez, J. & Koutsioubas, A. (2015). Memprot: a program to model the detergent corona around a membrane protein based on SEC-SAXS data. *Acta Crystallogr. D Biol. Crystallogr.,* **71,** 86-93.

Petoukhov, M. V. & Svergun, D. I. (2015). Ambiguity assessment of small-angle scattering curves from monodisperse systems. *Acta Crystallogr. D Biol. Crystallogr.,* **71,** 1051-8.

Pfluger, T., Hernandez, C. F., Lewe, P., Frank, F., Mertens, H., Svergun, D., Baumstark, M. W., Lunin, V. Y., Jetten, M. S. M. & Andrade, S. L. A. (2018). Signaling ammonium across membranes through an ammonium sensor histidine kinase. *Nat. Commun.,* **9,** 164.

Radchenko, M. V., Thornton, J. & Merrick, M. (2010). Control of AmtB-GlnK complex formation by intracellular levels of ATP, ADP, and 2-oxoglutarate. *J. Biol. Chem.,* **285,** 31037-45.

Rath, A., Glibowicka, M., Nadeau, V. G., Chen, G. & Deber, C. M. (2009). Detergent binding explains anomalous SDS-PAGE migration of membrane proteins. *Proc. Natl. Acad. Sci. U. S. A.,* **106,** 1760-5.

Rentsch, D., Laloi, M., Rouhara, I., Schmelzer, E., Delrot, S. & Frommer, W. B. (1995). NTR1 encodes a high affinity oligopeptide transporter in Arabidopsis. *FEBS Lett.,* **370,** 264-8.

Reyes, F. E., Schwartz, C. R., Tainer, J. A. & Rambo, R. P. (2014). Methods for using new conceptual tools and parameters to assess RNA structure by small-angle X-ray scattering. *Methods Enzymol.,* **549,** 235-63.

Rhee, S. G., Park, S. C. & Koo, J. H. (1985). The role of adenylyltransferase and uridylyltransferase in the regulation of glutamine synthetase in *Escherichia coli*. *Curr. Top. Cell. Regul.,* **27,** 221-32.

Rice, S. A. (1956). Small angle scattering of X-rays. A. Guinier and G. Fournet. Translated by C. B. Wilson and with a bibliographical appendix by K. L. Yudowitch. Wiley, New York, 1955. 268 pp. *J. Poly. Sci.,* **19,** 594.

Rigaud, J. L. & Levy, D. (2003). Reconstitution of membrane proteins into liposomes. *Methods. Enzymol.,* **372,** 65-86.

Rigaud, J. L. (2002). Membrane proteins: functional and structural studies using reconstituted proteoliposomes and 2-D crystals. *Braz. J. Med. Biol. Res.,* **35,** 753-66.

Rigaud, J. L., Paternostre, M. T. & Bluzat, A. (1988). Mechanisms of membrane protein insertion into liposomes during reconstitution procedures involving the use of detergents. 2. Incorporation of the light-driven proton pump bacteriorhodopsin. *Biochemistry,* **27,** 2677-88.

Rigaud, J. L., Pitard, B. & Levy, D. (1995). Reconstitution of membrane proteins into liposomes: application to energy-transducing membrane proteins. *Biochim. Biophys. Acta,* **1231,** 223-46.

Ripoche, P., Bertrand, O., Gane, P., Birkenmeier, C., Colin, Y. & Cartron, J.-P. (2004). Human Rhesus-associated glycoprotein mediates facilitated transport of $NH_{(3)}$ into red blood cells. *Proc. Natl. Acad. Sci. U. S. A.,* **101,** 17222-7.

Ritchie, T. K., Grinkova, Y. V., Bayburt, T. H., Denisov, I. G., Zolnerciks, J. K., Atkins, W. M. & Sligar, S. G. (2009). Chapter 11 - Reconstitution of membrane proteins in phospholipid bilayer nanodiscs. *Methods Enzymol.,* **464,** 211-31.

Roon, R. J., Even, H. L., Dunlop, P. & Larimore, F. L. (1975). Methylamine and ammonia transport in *Saccharomyces cerevisiae*. *J. Bacteriol.*, **122,** 502-9.

Sambrook, J., Fritsch, E. F. & Maniatis, T. (1989). *Molecular Cloning: A Laboratory Manual*, Cold Spring Harbor laboratory Press.

Schleifer, K. H. & Kandler, O. (1972). Peptidoglycan types of bacterial cell walls and their taxonomic implications. *Bacteriol. Rev.,* **36,** 407-77.

Schuck, P. (2000). Size-distribution analysis of macromolecules by sedimentation velocity ultracentrifugation and lamm equation modeling. *Biophys. J.,* **78,** 1606-19.

Severi, E., Javelle, A. & Merrick, M. (2007). The conserved carboxy-terminal region of the ammonia channel AmtB plays a critical role in channel function. *Mol. Membr. Biol.,* **24,** 161-71.

Sgro, G. G. & Costa, T. R. D. (2018). Cryo-EM Grid Preparation of Membrane Protein Samples for Single Particle Analysis. *Front. Biosci.,* **5,** 74.

Shannon, R. (1976). Revised effective ionic radii and systematic studies of interatomic distances in halides and chalcogenides. *Acta Crystallogr. A,* **32,** 751-67.

Shwu-Huey, L., Ichun, K. & David, E. (1995). Discovery of the ammonium substrate site on glutamine synthetase, A third cation binding site. *Protein Sci.,* **4,** 2358-65.

Siewe, R. M., Weil, B., Burkovski, A., Eikmanns, B. J., Eikmanns, M. & Kramer, R. (1996). Functional and genetic characterization of the (methyl)ammonium uptake carrier of *Corynebacterium glutamicum*. *J. Biol. Chem.,* **271,** 5398-403.

Silhavy, T. J., Kahne, D. & Walker, S. (2010). The bacterial cell envelope. *Cold Spring Harb. Perspect. Biol.,* **2,** a000414.

Singer, S. J. & Nicolson, G. L. (1972). The fluid mosaic model of the structure of cell membranes. *Science,* **175,** 720-31.

Skar-Gislinge, N., Kynde, S. A., Denisov, I. G., Ye, X., Lenov, I., Sligar, S. G. & Arleth, L. (2015). Small-angle scattering determination of the shape and localization of human cytochrome P450 embedded in a phospholipid nanodisc environment. *Acta Crystallogr. D Biol. Crystallogr.,* **71,** 2412-21.

Sligar, S. G., Bayburt, T. H., Schuler, M. A., Civjan, N. R., Grinkova, Y. V., Denisov, I. G. & Grimme, S. J. (2009). Membrane scaffold proteins. *Google Patents*.

Slotboom, D. J., Duurkens, R. H., Olieman, K. & Erkens, G. B. (2008). Static light scattering to characterize membrane proteins in detergent solution. *Methods,* **46,** 73-82.

Smith, D. G., Garcia-Pedrajas, M. D., Gold, S. E. & Perlin, M. H. (2003). Isolation and characterization from pathogenic fungi of genes encoding ammonium permeases and their roles in dimorphism. *Mol. Microbiol.,* **50,** 259-75.

Son, H. S. & Rhee, S. G. (1987). Cascade control of Escherichia coli glutamine synthetase. Purification and properties of P_{II} protein and nucleotide sequence of its structural gene. *J. Biol. Chem.,* **262,** 8690-5.

Soupene, E., He, L., Yan, D. & Kustu, S. (1998). Ammonia acquisition in enteric bacteria: physiological role of the ammonium/methylammonium transport B (AmtB) protein. *Proc. Natl. Acad. Sci. U. S. A.,* **95,** 7030-4.

Soupene, E., Inwood, W. & Kustu, S. (2004). Lack of the Rhesus protein Rh1 impairs growth of the green alga *Chlamydomonas reinhardtii* at high $CO_{(2)}$. *Proc. Natl. Acad. Sci. U. S. A.,* **101,** 7787-92.

Soupene, E., Lee, H. & Kustu, S. (2002). Ammonium/methylammonium transport (Amt) proteins facilitate diffusion of NH_3 bidirectionally. *Proc. Natl. Acad. Sci. U. S. A.,* **99,** 3926-31.

Soupene, E., Ramirez, R. M. & Kustu, S. (2001). Evidence that Fungal MEP Proteins Mediate Diffusion of the Uncharged Species $NH_{(3)}$ across the Cytoplasmic Membrane. *Mol. Cell. Biol.,* **21,** 5733-41.

Stadtman, E. R. (2001). The story of glutamine synthetase regulation. *J. Biol. Chem.,* **276,** 44357-64.

Stevenson, R. & Silver, S. (1977). Methylammonium uptake by *Escherichia coli*: evidence for a bacterial NH_4^+ transport system. *Biochem. Biophys. Res. Commun.,* **75,** 1133-9.

Streicher, S. L., Shanmugam, K. T., Ausubel, F., Morandi, C. & Goldberg, R. B. (1974). Regulation of Nitrogen Fixation in *Klebsiella pneumoniae*: Evidence for a Role of Glutamine Synthetase as a Regulator of Nitrogenase Synthesis. *J. Bacteriol.,* **120,** 815-21.

Studier, F. W. (2005). Protein production by auto-induction in high density shaking cultures. *Protein Expr. Purif.,* **41,** 207-34.

Sutherland, W. (1905). LXXV. A dynamical theory of diffusion for non-electrolytes and the molecular mass of albumin. *Philos. Mag.,* **9,** 781-5.

Svergun, D. (1992). Determination of the regularization parameter in indirect-transform methods using perceptual criteria. *J. Appl Crystallogr.,* **25,** 495-503.

Svergun, D., Barberato, C. & Koch, M. H. J. (1995). CRYSOL - a Program to Evaluate X-ray Solution Scattering of Biological Macromolecules from Atomic Coordinates. *J. Appl Crystallogr.,* **28,** 768-73.

Svergun, D. I. (1999). Restoring low resolution structure of biological macromolecules from solution scattering using simulated annealing. *Biophys. J.,* **76,** 2879-86.

Tartof, K. D. (1987). Improved media for growing plasmid and cosmid clones. *Bethesda Res. Lab. Focus,* **9,** 12.

Tate, R., Riccio, A., Merrick, M. & Patriarca, E. J. (1998). The *Rhizobium etli* amtB gene coding for an NH_4^+ transporter is down-regulated early during bacteroid differentiation. *Mol. Plant Microbe Interact.,* **11,** 188-98.

Thomas, G. H., Mullins, J. G. & Merrick, M. (2000). Membrane topology of the Mep/Amt family of ammonium transporters. *Mol. Microbiol.,* **37,** 331-44.

Tremblay, P. L. & Hallenbeck, P. C. (2009). Of blood, brains and bacteria, the Amt/Rh transporter family: emerging role of Amt as a unique microbial sensor. *Mol. Microbiol.,* **71,** 12-22.

Trewhella, J., Duff, A. P., Durand, D., Gabel, F., Guss, J. M., Hendrickson, W. A., Hura, G. L., Jacques, D. A., Kirby, N. M., Kwan, A. H., Perez, J., Pollack, L., Ryan, T. M., Sali, A., Schneidman-Duhovny, D., Schwede, T., Svergun, D. I., Sugiyama, M., Tainer, J. A., Vachette, P., Westbrook, J. & Whitten, A. E. (2017). 2017 publication guidelines for structural modelling of small-angle scattering data from biomolecules in solution: an update. *Acta Crystallogr. D Struct. Biol.,* **73,** 710-28.

Truan, D., Huergo, L. F., Chubatsu, L. S., Merrick, M., Li, X. D. & Winkler, F. K. (2010). A new $P_{(II)}$ protein structure identifies the 2-oxoglutarate binding site. *J. Mol. Biol.,* **400,** 531-9.

Van Den Berg, B., Chembath, A., Jefferies, D., Basle, A., Khalid, S. & Rutherford, J. C. (2016). Structural basis for Mep2 ammonium transceptor activation by phosphorylation. *Nat. Commun.,* **7,** 11337.

Van Der Does, C., Swaving, J., Van Klompenburg, W. & Driessen, A. J. (2000). Non-bilayer lipids stimulate the activity of the reconstituted bacterial protein translocase. *J. Biol. Chem.,* **275,** 2472-8.

Verma, R., Holmans, P., Knowles, J. A., Grover, D., Evgrafov, O. V., Crowe, R. R., Scheftner, W. A., Weissman, M. M., Depaulo, J. R., Jr., Potash, J. B. & Levinson, D. F. (2008). Linkage disequilibrium mapping of a chromosome 15q25-26 major depression linkage region and sequencing of NTRK3. *Biol. Psychiatry,* **63,** 1185-9.

Vitrac, H., Bogdanov, M. & Dowhan, W. (2013). *In vitro* reconstitution of lipid-dependent dual topology and postassembly topological switching of a membrane protein. *Proc. Natl. Acad. Sci. U. S. A.,* **110,** 9338-43.

Voegele, R. T., Sweet, G. D. & Boos, W. (1993). Glycerol kinase of *Escherichia coli* is activated by interaction with the glycerol facilitator. *J. Bacteriol.,* **175,** 1087-94.

Von Smoluchowski, M. (1906). Zur kinetischen Theorie der Brownschen Molekularbewegung und der Suspensionen. *Ann. Phys.,* **326,** 756-80.

Wacker, T., Garcia-Celma, J. J., Lewe, P. & Andrade, S. L. (2014). Direct observation of electrogenic $NH_4^{(+)}$ transport in ammonium transport (Amt) proteins. *Proc. Natl. Acad. Sci. U. S. A.,* **111,** 9995-10000.

Wang, J., Fulford, T., Shao, Q., Javelle, A., Yang, H., Zhu, W. & Merrick, M. (2013). Ammonium transport proteins with changes in one of the conserved pore histidines have different performance in ammonia and methylamine conduction. *PLoS One,* **8,** e62745.

Wang, J., Yang, H., Zuo, Z., Yan, X., Wang, Y., Luo, X., Jiang, H., Chen, K. & Zhu, W. (2010). Molecular Dynamics Simulations on the Mechanism of Transporting Methylamine and Ammonia by Ammonium Transporter AmtB. *J. Phys. Chem. B,* **114,** 15172-9.

Wang, M. Y., Siddiqi, M. Y., Ruth, T. J. & Glass, A. D. M. (1993). Ammonium Uptake by Rice Roots (II. Kinetics of $^{13}NH_4^+$ Influx across the Plasmalemma). *Plant Physiol.,* **103,** 1259-67.

Weiner, I. D. & Hamm, L. L. (2007). Molecular mechanisms of renal ammonia transport. *Annu. Rev. Physiol.,* **69,** 317-40.

Westhoff, C. M., Ferreri-Jacobia, M., Mak, D.-O. D. & Foskett, J. K. (2002). Identification of the erythrocyte Rh blood group glycoprotein as a mammalian ammonium transporter. *J. Biol. Chem.,* **277,** 12499-502.

Wickes, B. L., Edman, U. & Edman, J. C. (1997). The *Cryptococcus neoformans* STE12alpha gene: a putative *Saccharomyces cerevisiae* STE12 homologue that is mating type specific. *Mol. Microbiol.,* **26,** 951-60.

Winkler, F. K. (2006). Amt/MEP/Rh proteins conduct ammonia. *Pflugers Arch.,* **451,** 701-7.

Wirén, N. V. & Merrick, M. (2004). Regulation and function of ammonium carriers in bacteria, fungi, and plants. *Molecular Mechanisms Controlling Transmembrane Transport.* Berlin, Heidelberg: Springer Berlin Heidelberg.

Min, X., Siddiqi, M. Y., Guy, R. D., Glass, A. D. and Kronzucker, H. J. (2000). A comparative kinetic analysis of nitrate and ammonium influx in two early-successional tree species of temperate and boreal forest ecosystems. *Plant Cell Environ.,* **23,** 321-8.

Xie, X. & Zubarev, R. A. (2014). Effects of low-level deuterium enrichment on bacterial growth. *PLoS One,* **9,** e102071.

Yang, H., Xu, Y., Zhu, W., Chen, K. & Jiang, H. (2007). Detailed Mechanism for AmtB Conducting $NH_{(4)}^{(+)}/NH_{(3)}$: Molecular Dynamics Simulations. *Biophys. J.,* **92,** 877-85.

Zaccai, N. R., Sandlin, C. W., Hoopes, J. T., Curtis, J. E., Fleming, P. J., Fleming, K. G. & Krueger, S. (2016). Deuterium Labeling Together with Contrast Variation Small-Angle Neutron Scattering Suggests How Skp Captures and Releases Unfolded Outer Membrane Proteins. *Methods Enzymol.,* **566,** 159-210.

Zheng, L., Kostrewa, D., Bernèche, S., Winkler, F. K. & Li, X. D. (2004). The mechanism of ammonia transport based on the crystal structure of AmtB of *Escherichia coli*. *Proc. Natl. Acad. Sci. U. S. A.,* **101,** 17090-5.

Zidi-Yahiaoui, N., Mouro-Chanteloup, I., D'ambrosio, A. M., Lopez, C., Gane, P., Le Van Kim, C., Cartron, J. P., Colin, Y. & Ripoche, P. (2005). Human Rhesus B and Rhesus C glycoproteins: properties of facilitated ammonium transport in recombinant kidney cells. *Biochem. J.,* **391,** 33-40.

Zuber, D., Krause, R., Venturi, M., Padan, E., Bamberg, E. & Fendler, K. (2005). Kinetics of charge translocation in the passive downhill uptake mode of the Na^+/H^+ antiporter NhaA of *Escherichia coli*. *Biochim. Biophys. Acta,* **1709,** 240-50.

Appendix

Appendix A: Publication nº1: Merging in solution X-ray and Neutron Scattering Data Allows Fine Structural Analysis of Membrane-Protein Detergent Complexes

This is an open access article published under a Creative Commons Attribution (CC-BY) License, which permits unrestricted use, distribution and reproduction in any medium, provided the author and source are cited.

THE JOURNAL OF PHYSICAL CHEMISTRY Letters

Letter

Cite This: J. Phys. Chem. Lett. 2018, 9, 3910−3914

pubs.acs.org/JPCL

Merging In-Solution X-ray and Neutron Scattering Data Allows Fine Structural Analysis of Membrane−Protein Detergent Complexes

Gaëtan Dias Mirandela,[†] Giulia Tamburrino,[¶,‡,§] Miloš T. Ivanović,[¶,∥] Felix M. Strnad,[⊥] Olwyn Byron,[#] Tim Rasmussen,[▽] Paul A. Hoskisson,[†] Jochen S. Hub,[*,††,∥] Ulrich Zachariae,[††,‡,§] Frank Gabel,[*,††,○,◆] and Arnaud Javelle[*,†]

[†]Strathclyde Institute of Pharmacy and Biomedical Sciences, University of Strathclyde, Glasgow, G4 0RE, United Kingdom

[‡]Computational Biology, School of Life Sciences, University of Dundee, Dundee, DD1 5EH, United Kingdom

[§]Physics, School of Science and Engineering, University of Dundee, Dundee, DD1 4NH, United Kingdom

[∥]Theoretical Physics, Saarland University, Campus E2 6, 66123 Saarbrücken, Germany

[⊥]Institute for Microbiology and Genetics, University of Goettingen, Justus-von-Liebig-Weg 11, 37077 Göttingen, Germany

[#]School of Life Sciences, College of Medical, Veterinary and Life Sciences, University of Glasgow, Glasgow, G12 8QQ, United Kingdom

[▽]School of Medical Sciences, University of Aberdeen, Foresterhill, Aberdeen AB25 2ZD, United Kingdom

[○]Institut Laue-Langevin, 71 Avenue des Martyrs 38042 Grenoble, France

[◆]University of Grenoble Alpes, CEA, CNRS, IBS, 38000 Grenoble, France

S *Supporting Information*

ABSTRACT: In-solution small-angle X-ray and neutron scattering (SAXS/SANS) have become popular methods to characterize the structure of membrane proteins, solubilized by either detergents or nanodiscs. SANS studies of protein-detergent complexes usually require deuterium-labeled proteins or detergents, which in turn often lead to problems in their expression or purification. Here, we report an approach whose novelty is the combined analysis of SAXS and SANS data from an unlabeled membrane protein complex in solution in two complementary ways. First, an explicit atomic analysis, including both protein and detergent molecules, using the program WAXSiS, which has been adapted to predict SANS data. Second, the use of MONSA which allows one to discriminate between detergent head- and tail-groups in an *ab initio* approach. Our approach is readily applicable to any detergent-solubilized protein and provides more detailed structural information on protein−detergent complexes from unlabeled samples than SAXS or SANS alone.

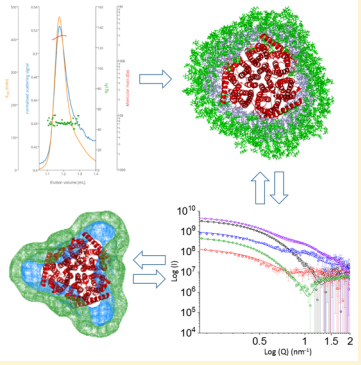

Downloaded via 2.219.24.201 on September 30, 2018 at 12:36:53 (UTC).
See https://pubs.acs.org/sharingguidelines for options on how to legitimately share published articles.

Integral membrane proteins form the entry and exit routes for nutrients, metabolic waste and drugs in biological cells, and they are involved in key steps of signaling and energy transduction. They thus play a central role in a variety of biological processes with exceptional medical relevance.[1] Structural information on membrane proteins has traditionally been obtained by X-ray crystallography aided by detergent molecules that replace the lipids during the purification and crystallization processes. Detergents stabilize membrane proteins by shielding the hydrophobic domains from the aqueous environment.[2] However, the translocation cycle underpinning membrane transporter activity requires substantial conformational variability and, in many cases, the static structural insight achieved by X-ray crystallography has proven insufficient to capture the essential functional information on these systems.[3] For this reason, there is considerable interest in the application of small angle scattering (SAS) methods to structurally characterize membrane proteins. Recently, efforts have been dedicated to develop combined in-solution small-angle X-ray/neutron scattering (SAXS/SANS) approaches to investigate membrane proteins stabilized by detergents or nanodiscs.[4−6] Further developments in these areas have faced important obstacles. Crucially, the electron density of the detergent shell encompassing the hydrophobic domains of membrane proteins differs from the electron density of the protein. Hence, it is difficult to obtain a model of a protein-detergent complex using *ab initio* SAXS-based methods, which typically assume a uniform electron density across the entire complex. To circumvent this problem, SANS experiments making use of contrast variation either by using deuterium-labeled proteins and/or detergent molecules have been employed. However, difficulties are often encountered in the expression and purification of deuterated proteins, as well as the limited availability of deuterated detergents.[4] To overcome these issues, we report a new methodology

Received: May 22, 2018
Accepted: June 25, 2018
Published: June 25, 2018

 © 2018 American Chemical Society

DOI: 10.1021/acs.jpclett.8b01598
J. Phys. Chem. Lett. 2018, 9, 3910−3914

that combines SAXS and SANS from unlabeled (i.e., non-deuterated) proteins and/or detergent samples to obtain detailed structural information on protein−detergent complexes. This approach is readily applicable to any detergent-solubilized protein.

We used the ammonium transporter AmtB from *Escherichia coli,* a structurally well-studied member of the ubiquitous and medically important Amt/rhesus family of proteins, to develop and validate our methodology.[7] To stabilize AmtB, the detergent n-dodecyl-β-D-maltoside (DDM) was used throughout the purification process (Supporting Information). Size exclusion chromatography in-line with multiangle light scattering (SEC-MALS) analysis showed that the AmtB-detergent complex comprises 285 ± 12 DDM molecules (Figure S1 and Table S1). Independently conducted analytical ultracentrifugation (AUC) experiments revealed a detergent shell of 321 ± 1 DDM molecules (Figure S2 and Table S1). Taken together, these independent findings indicate that the detergent corona around AmtB is likely to include between 260 and 320 DDM molecules.

We next exploited atomistic molecular dynamics (MD) simulations of the AmtB-DDM complex and scored the models against SAXS data to resolve the experimental uncertainty regarding the size of the detergent corona. AmtB in the physiologically functional trimeric form (PDB ID: 1U7G)[8] was simulated surrounded by DDM coronas of 260, 280, 300, 320, 340, and 360 molecules. A representative model obtained for a detergent corona containing 320 molecules of DDM is shown in Figure 1.

During the equilibration phase, the DDM molecules adopted the typical toroidal shape reported for other protein-detergent complexes,[9,10] with their hydrophilic heads facing the aqueous solution and their hydrophobic tails oriented toward the inside of the complex (Figure 1). As previously shown, the detergent corona further adapted to the shape of the transmembrane surface of the protein.[10] Our simulations indicate that the protein−detergent complexes are stable, and although some reorientation of DDM was observed, in particular during the first stages of the simulations, no dissociation of detergent molecules from the protein was detected after 20 ns of simulation time. We next computed SAS curves for the simulated complexes and compared them with experimental SAS measurements (Figure 2−3).

It has previously been shown that single structures extracted from MD trajectories do not fully capture the characteristics of the solution ensemble.[9] We therefore calculated the predicted SAXS curves from conformational ensembles comprising 9000 individual configurations as observed in 70−160 ns simulations of each differently sized complex. The SAXS curves were obtained using explicit-solvent calculations as implemented in the WAXSiS method, thereby taking into account accurate atomic models for both the hydration layer and the excluded solvent, and consequently avoiding any solvent-related fitting parameters (Figure 2).[11,12]

SAS experiments are very demanding in terms of requirements of sample quality,[13,14] therefore, before recording SAS data, we ascertained that our samples were monodisperse and that AmtB was pure, stable, and critically active in detergent (Supporting Information, Figure S1−S3). We subsequently collected experimental SAXS data following size-exclusion chromatography of the AmtB−DDM complex. The radius of gyration (R_g) was found to be constant across the elution peak (Figure S1), indicating the monodispersity of the complex and good data quality. Importantly, the scattering curves predicted

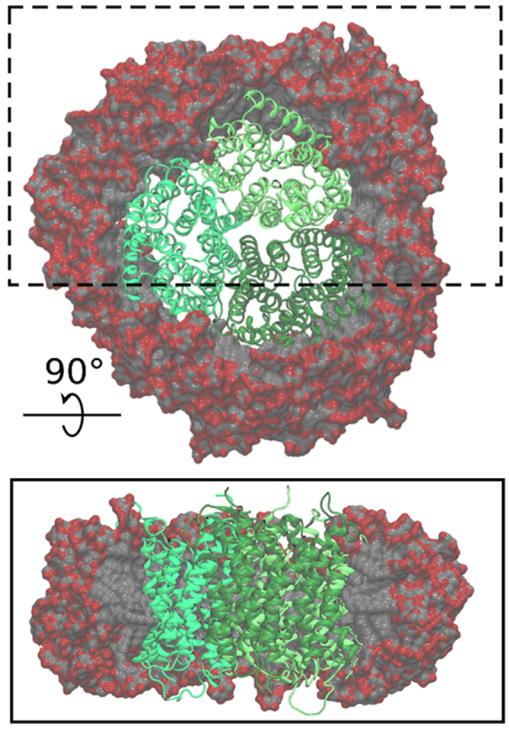

Figure 1. Atomistic model of the AmtB-DDM complex containing 320 DDM molecules. The model displays an equilibrated complex. In the trimer, each AmtB monomer is shown in a different shade of green, and the DDM carbon and oxygen atoms are shown in gray and red, respectively. The upper panel shows the complex seen from the top; the lower panel is a side-view of the complex where the DDM molecules outside of the box highlighted in the top panel are omitted, to illustrate the interior of the micelle.

for the models containing 260, 280, 300, 340, and 360 DDM molecules deviate slightly from the experimental data (Figures 2 and S4). By contrast, the curve computed for the MD model containing 320 DDM molecules was nearly indistinguishable from the experimental SAXS data (Figure 2 and S4). Furthermore, the values for R_g obtained by the Guinier approximation from the experimental data and from for the MD model containing 320 DDM molecules were in quantitative agreement (Table S3 and Figure S5). This suggests that the overall dimension of the simulated protein−detergent complex containing 320 molecules of DDM is identical to that in solution. It is important to note that the overall information content of SAXS is relatively low, and thus agreement between experimental and back-calculated curves may be insufficient to serve as unambiguous evidence for a structural model.[15] Specifically, in the context of a protein−detergent complex, SAXS data reports on the overall shape of the complex, whereas they do not provide independent information on the individual contributions from the protein and the detergent corona. Therefore, we employed SANS together with contrast variation to more firmly validate our computational model.

We collected SANS data at four contrast points (0%, 22%, 42% and 60% (v/v) D_2O) to differentiate between the individual components of the protein−detergent complex. To ensure that the samples were stable over the course of the SANS experiment, the hydrodynamic behavior of the proteins were analyzed before and after the SANS measurements by analytical size exclusion chromatography. No differences were observed in the elution profile, confirming the stability of the

DOI: 10.1021/acs.jpclett.8b01598
J. Phys. Chem. Lett. 2018, 9, 3910−3914

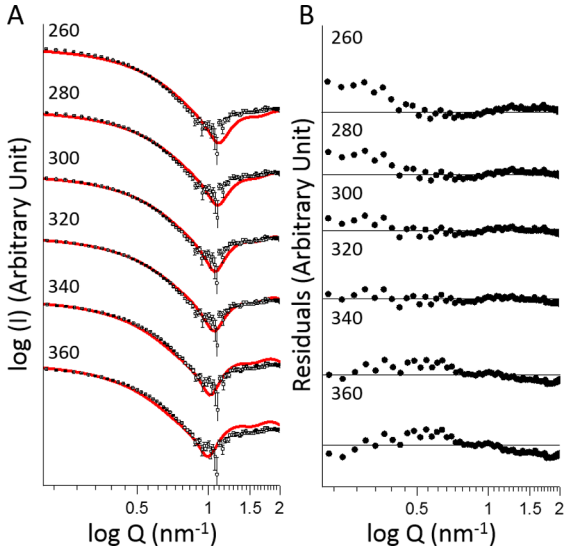

Figure 2. (A) Comparison of the experimental (symbols) and computed (red line) SAXS curves for the AmtB-DDM complex containing between 260 and 360 DDM molecules. For all plots, the maximum and minimum values for the *y*-axis are 10^{11} and 10^{5}. (B) Residual error plot expressed as the experimental minus computed scattering intensity. For all plots, the maximum and minimum values for the *y*-axis are 40 and −40. $Q = (4\pi \sin(\theta)/\lambda)$, where 2θ is the scattering angle.

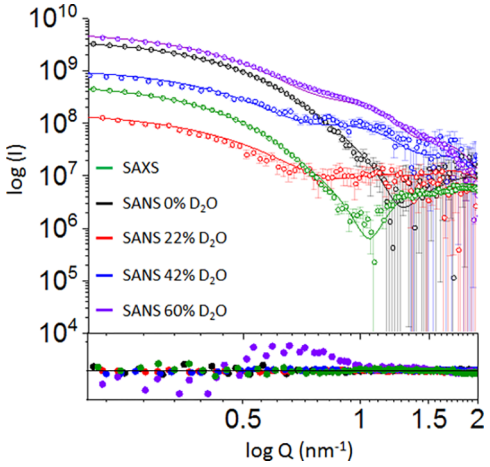

Figure 3. Comparison of the experimental (symbols) and computed (red line) SAXS/SANS curves for the model containing 320 DDM molecules. Residual error plot expressed as the experimental minus computed scattering intensity. The maximum and minimum values for the *y*-axis are 40 and −40, respectively.

protein during the SANS experiment (Figure S6). To ascertain the reproducibility and the quality of our measurements, two independent sets of SANS data were acquired, using two batches of AmtB purified independently. The two data sets were found to be identical within the limits of the observed experimental noise (Figure S7). It has previously been shown that in the absence of D_2O in the buffer, neutron scattering from DDM micelles originates primarily from the hydrophilic head groups.[16] We calculated (Supporting Information) the overall contrast match point of DDM to be at 22% D_2O, while the contrast match point for typical proteins is around 42% D_2O.[4,17] Consequently, the scattering contribution is dominated by the protein and the DDM hydrophilic headgroup in a buffer containing 0% D_2O, by the protein at 22% D_2O and by the complete detergent corona at 42% D_2O. To compare the experimental neutron scattering data with the MD-generated models, SANS curves were calculated using WAXSiS for 9000 individual configurations observed during 70−160 ns MD trajectories of each of the complexes. To this end, we extended the WAXSiS method, originally developed for SAXS predictions, to also allow SANS predictions with explicit-solvent models at various D_2O concentrations (Supporting Information). The experimental curves were fitted to the calculated curves following $I_{fit} = f \cdot I_{exp} + c$, thereby accounting for scattering contributions from the incoherent background with the fitting parameter *c*. However, neither the hydration layer nor the excluded volume were adjusted. Congruent with the analysis of the SAXS data, all SANS data sets were best fitted by the curves calculated for the model incorporating 320 molecules of DDM (Figure 3 and S8). Hence, the SANS and SAXS data consistently validate our MD model with 320 DDM molecules. Second, the excellent agreement we observe between the experimental and calculated SAXS curves shows that the overall organization of the complex is accurately reflected by the atomistic model. Finally, the good agreement between experimental and computed SANS curves indicates that the MD model describes accurately the hydrophobic and hydrophilic phase of the detergent ring as well as the position of AmtB inside the corona.

Importantly, the crystal structure of AmtB was used to produce our MD trajectories, which precludes the possibility of applying this combined MD/SAXS/SANS approach to membrane proteins of unknown structure. We therefore applied, in the final step, an independent "MD-free" approach to obtain a full *ab initio* model that captures detailed structural information on the complex without using the crystal structure of AmtB. To achieve this, we merged our complete SAXS and SANS data and conducted a multiphase volumetric analysis of the complex using MONSA[18,19] (Figure 4). Importantly, we

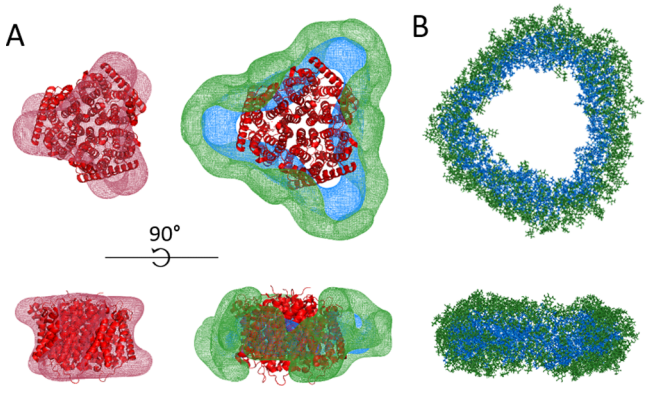

Figure 4. (A) MONSA multiphase modeling using experimental SAXS and SANS data. The phase corresponding to the protein is represented in red mesh, while the hydrophilic and hydrophobic detergent densities are represented in green and blue, respectively. (B) Molecular-dynamics generated model of the detergent corona (320 molecules) surrounding AmtB.

introduced two separate phases to describe the head and tail groups of the DDM detergent corona.

Assuming the volume of a DDM molecule to be 690 Å^3 (350 Å^3 and 340 Å^3 for the head and the tail, respectively),[4] we imposed a volume of 112 000 Å^3 and 108 800 Å^3 for the

DOI: 10.1021/acs.jpclett.8b01598
J. Phys. Chem. Lett. 2018, 9, 3910−3914

hydrophilic and hydrophobic phases of the 320 DDM molecules. The volume of AmtB (166 864 Å^3) was calculated based on its amino acid sequence alone (Supporting Information). Moreover, since the trimeric nature of AmtB in solution was confirmed by our SEC-MALS and AUC data (Figure S1−S2 and Table S1), we imposed a P3 symmetry on the complex. Crucially, all this information can be readily obtained for any membrane protein solubilized in detergent, using widely accessible and complementary biophysical techniques (e.g., SEC-MALS/AUC in this study). Ten MONSA runs (Figure S9) were performed yielding similar *ab initio* envelopes for AmtB. A representative MONSA model is shown in Figure 4, which faithfully reflects both the size and shape of the MD-generated model. The protein envelope is a good representation of the crystallographic structure of AmtB and is, furthermore, confined inside the detergent corona. Importantly, the joint use of both SAXS and multiple SANS data sets allowed us to distinguish the head- and tail-groups of the detergent corona and place them correctly with respect to the protein surface and solvent. Such detailed insight is usually not achieved with *ab initio* models unless additional contact restraints are applied:[20] the detergent ring fits the contours of the protein and the positions of the two detergent phases (head- and tail-groups) are particularly clear. The hydrophobic phase is strictly contained between AmtB and the hydrophilic ring, with only the tails of DDM being in contact with the hydrophobic surface of the transmembrane domain. Hence, without using deuterated protein or detergent, and without information about the 3D structure of AmtB, the combination of SAXS and SANS data capture the essential structural details contained in membrane−protein detergent complexes in solution.

In summary, there is considerable interest in developing SAS methodology further to allow routine investigation of membrane proteins. We have adapted WAXSiS to account for SANS data and therefore open up this software package for future projects including both types of scattering data. Using our methodology, based upon a combination of SAXS/SANS measurements and MD simulations, we have been able to propose an atomic model of a protein-detergent complex. Our integrative approach demonstrates that combining SAXS, SANS, and iterative simulations provides much more detailed structural information than each of the methods alone.

It is widely recognized that cryo-electron microscopy (cryo-EM) will revolutionize the structural analysis of membrane proteins in the near future.[21,22] It is our belief that a hybrid approach, combining in solution SAS techniques, *in silico* modeling, and cryo-EM will allow for better tracking and description of conformational changes of membrane proteins in solution, induced by ligand or cofactor binding. In this context, it was important to account accurately for the bound detergent molecules, which is greatly improved by combining SAXS and SANS data at various contrasts. Second, our multiphase analysis, which merges SAXS and SANS data, without using deuterated protein or detergent, allowed us to obtain unprecedented structural information on the phase density of the detergent, in particular to distinguish head- and tail-groups in the assembled membrane protein−detergent complexes. This is particularly relevant as deuterated media/detergents are often expensive and/or toxic for bacteria, leading to decreased protein yields.[23] Crucially, the multiphase analysis does not require information on the 3D structure of the protein, which opens up the possibility of applying this methodology to a wide range of important membrane proteins that have so far remained inaccessible to high resolution structural analysis. While SAS has become a popular technique among structural biologists, combinations of SANS, SAXS and MD simulations have remained underexploited by the community. In this context, our work represents a significant advancement in data acquisition, model validation, development of new software, and multiphase volumetric analysis to firmly establish SAS technology as a standard method for membrane protein structural biology.

■ ASSOCIATED CONTENT

Supporting Information

The Supporting Information is available free of charge on the ACS Publications website at DOI: 10.1021/acs.jpclett.8b01598.

Computational and methodological details, as well as three supporting tables and nine supporting figures (DOCX)

■ AUTHOR INFORMATION

Corresponding Authors

*E-mail: arnaud.javelle@strath.ac.uk.
*E-mail: frank.gabel@ibs.fr.
*E-mail: jochen.hub@physik.uni-saarland.de.

ORCID

Gaëtan Dias Mirandela: 0000-0001-5871-6288
Jochen S. Hub: 0000-0001-7716-1767
Ulrich Zachariae: 0000-0003-3287-8494
Arnaud Javelle: 0000-0002-3611-5737

Author Contributions

[¶]G.T. and M.T.I. contributed equally to this work.
[††]J.S.H., U.Z., and F.G. contributed equally to this work.

Notes

The authors declare no competing financial interest.

■ ACKNOWLEDGMENTS

G.D.M. and A.J. were supported by a Ph.D. and a Chancellor's Fellowship from Strathclyde University, respectively, G.T. and U.Z. acknowledge funding from the Scottish Universities' Physics Alliance (SUPA). P.A.H. acknowledges the support of the Natural Environment Research Council (NE/M001415/1) and A.J. the support of Tenovus Scotland (Project S17-07). M.T.I., F.M.S., and J.S.H. acknowledge support by the Deutsche Forschungsgemeinschaft (HU 1971-1/1, HU 1971-3/1, HU 1971-4/1). We thank the ILL Block Allocation Group (BAG) system for SANS beamtime at D22 and Dr A. Martel for help with the setup of the instrument. We acknowledge Diamond Light Source for time on Beamline B21. We thanks Dr. P. Soule (NanoTemper Technologies GmbH) and Dr. M. Tully (DIAMOND, U.K.) for help with the microscale thermophoresis experiments and SEC-SAXS data acquisition, respectively.

■ REFERENCES

(1) Dubyak, G. R. Ion homeostasis, channels, and transporters: an update on cellular mechanisms. *Adv. Physiol. Educ.* **2004**, *28*, 143−154.
(2) Werten, P. J.; Remigy, H. W.; de Groot, B. L.; Fotiadis, D.; Philippsen, A.; Stahlberg, H.; Grubmuller, H.; Engel, A. Progress in the analysis of membrane protein structure and function. *FEBS Lett.* **2002**, *529*, 65−72.
(3) Stahlberg, H.; Engel, A.; Philippsen, A. Assessing the structure of membrane proteins: combining different methods gives the full picture. *Biochem. Cell Biol.* **2002**, *80*, 563−568.
(4) Breyton, C.; Gabel, F.; Lethier, M.; Flayhan, A.; Durand, G.; Jault, J. M.; Juillan-Binard, C.; Imbert, L.; Moulin, M.; Ravaud, S.;

DOI: 10.1021/acs.jpclett.8b01598
J. Phys. Chem. Lett. 2018, 9, 3910−3914

Hartlein, M.; Ebel, C. Small angle neutron scattering for the study of solubilised membrane proteins. *Eur. Phys. J. E: Soft Matter Biol. Phys.* **2013**, *36*, 71−86.
(5) Kynde, S. A.; Skar-Gislinge, N.; Pedersen, M. C.; Midtgaard, S. R.; Simonsen, J. B.; Schweins, R.; Mortensen, K.; Arleth, L. Small-angle scattering gives direct structural information about a membrane protein inside a lipid environment. *Acta Crystallogr., Sect. D: Biol. Crystallogr.* **2014**, *70*, 371−383.
(6) Skar-Gislinge, N.; Kynde, S. A.; Denisov, I. G.; Ye, X.; Lenov, I.; Sligar, S. G.; Arleth, L. Small-angle scattering determination of the shape and localization of human cytochrome P450 embedded in a phospholipid nanodisc environment. *Acta Crystallogr., Sect. D: Biol. Crystallogr.* **2015**, *71*, 2412−2421.
(7) Merrick, M.; Javelle, A.; Durand, A.; Severi, E.; Thornton, J.; Avent, N. D.; Conroy, M. J.; Bullough, P. A. The *Escherichia coli* AmtB protein as a model system for understanding ammonium transport by Amt and Rh proteins. *Transfus. Clin. Biol.* **2006**, *13*, 97−102.
(8) Khademi, S.; O'Connell, J., III; Remis, J.; Robles-Colmenares, Y.; Miercke, L. J.; Stroud, R. M. Mechanism of ammonia transport by Amt/MEP/Rh: structure of AmtB at 1.35 Å. *Science* **2004**, *305*, 1587−1594.
(9) Chen, P. C.; Hub, J. S. Structural Properties of Protein-Detergent Complexes from SAXS and MD Simulations. *J. Phys. Chem. Lett.* **2015**, *6*, 5116−5121.
(10) Berthaud, A.; Manzi, J.; Perez, J.; Mangenot, S. Modeling detergent organization around aquaporin-0 using small-angle X-ray scattering. *J. Am. Chem. Soc.* **2012**, *134*, 10080−10088.
(11) Chen, P. C.; Hub, J. S. Validating solution ensembles from molecular dynamics simulation by wide-angle X-ray scattering data. *Biophys. J.* **2014**, *107*, 435−447.
(12) Knight, C. J.; Hub, J. S. WAXSiS: a web server for the calculation of SAXS/WAXS curves based on explicit-solvent molecular dynamics. *Nucleic Acids Res.* **2015**, *43*, 225−230.
(13) Trewhella, J.; Duff, A. P.; Durand, D.; Gabel, F.; Guss, J. M.; Hendrickson, W. A.; Hura, G. L.; Jacques, D. A.; Kirby, N. M.; Kwan, A. H.; Perez, J.; Pollack, L.; Ryan, T. M.; Sali, A.; Schneidman-Duhovny, D.; Schwede, T.; Svergun, D. I.; Sugiyama, M.; Tainer, J. A.; Vachette, P.; Westbrook, J.; Whitten, A. E. 2017 publication guidelines for structural modelling of small-angle scattering data from biomolecules in solution: an update. *Acta. Crystallogr. D. Struct. Biol.* **2017**, *73*, 710−728.
(14) Jeffries, C. M.; Graewert, M. A.; Blanchet, C. E.; Langley, D. B.; Whitten, A. E.; Svergun, D. I. Preparing monodisperse macromolecular samples for successful biological small-angle X-ray and neutron-scattering experiments. *Nat. Protoc.* **2016**, *11*, 2122−2153.
(15) Petoukhov, M. V.; Svergun, D. I. Ambiguity assessment of small-angle scattering curves from monodisperse systems. *Acta Crystallogr., Sect. D: Biol. Crystallogr.* **2015**, *71*, 1051−1058.
(16) Oliver, R. C.; Pingali, S. V.; Urban, V. S. Designing Mixed Detergent Micelles for Uniform Neutron Contrast. *J. Phys. Chem. Lett.* **2017**, *8*, 5041−5046.
(17) Zaccai, N. R.; Sandlin, C. W.; Hoopes, J. T.; Curtis, J. E.; Fleming, P. J.; Fleming, K. G.; Krueger, S. Deuterium Labeling Together with Contrast Variation Small-Angle Neutron Scattering Suggests How Skp Captures and Releases Unfolded Outer Membrane Proteins. *Methods Enzymol.* **2016**, *566*, 159−210.
(18) Reyes, F. E.; Schwartz, C. R.; Tainer, J. A.; Rambo, R. P. Methods for using new conceptual tools and parameters to assess RNA structure by small-angle X-ray scattering. *Methods Enzymol.* **2014**, *549*, 235−263.
(19) Svergun, D. I. Restoring low resolution structure of biological macromolecules from solution scattering using simulated annealing. *Biophys. J.* **1999**, *76*, 2879−2886.
(20) Koutsioubas, A. Low-Resolution Structure of Detergent-Solubilized Membrane Proteins from Small-Angle Scattering Data. *Biophys. J.* **2017**, *113*, 2373−2382.
(21) Vinothkumar, K. R. Membrane protein structures without crystals, by single particle electron cryomicroscopy. *Curr. Opin. Struct. Biol.* **2015**, *33*, 103−114.
(22) Rawson, S.; Davies, S.; Lippiat, J. D.; Muench, S. P. The changing landscape of membrane protein structural biology through developments in electron microscopy. *Mol. Membr. Biol.* **2016**, *33*, 12−22.
(23) Xie, X.; Zubarev, R. A. Effects of low-level deuterium enrichment on bacterial growth. *PLoS One* **2014**, *9*, e102071.

DOI: 10.1021/acs.jpclett.8b01598
J. Phys. Chem. Lett. 2018, 9, 3910−3914

Appendix B: Publication n°2: The lipid environment determines the activity of the *Escherichia coli* ammonium transporter AmtB

THE FASEB JOURNAL • RESEARCH • www.fasebj.org

The lipid environment determines the activity of the *Escherichia coli* ammonium transporter AmtB

Gaëtan Dias Mirandela,* Giulia Tamburrino,[†,‡] Paul A. Hoskisson,* Ulrich Zachariae,[†,‡] and Arnaud Javelle*[,1]

*Strathclyde Institute of Pharmacy and Biomedical Sciences, University of Strathclyde, Glasgow, United Kingdom; and [†]Computational Biology, School of Life Sciences, and [‡]Physics, School of Science and Engineering, University of Dundee, Dundee, United Kingdom

ABSTRACT: The movement of ammonium across biologic membranes is a fundamental process in all living organisms and is mediated by the ubiquitous ammonium transporter/methylammonium permease/rhesus protein (Amt/Mep/Rh) family of transporters. Recent structural analysis and coupled mass spectrometry studies have shown that the *Escherichia coli* ammonium transporter AmtB specifically binds 1-palmitoyl-2-oleoyl phosphatidylglycerol (POPG). Upon POPG binding, several residues of AmtB undergo a small conformational change, which stabilizes the protein against unfolding. However, no studies have so far been conducted, to our knowledge, to explore whether POPG binding to AmtB has functional consequences. Here, we used an *in vitro* experimental assay with purified components, together with molecular dynamics simulations, to characterize the relation between POPG binding and AmtB activity. We show that the AmtB activity is electrogenic. Our results indicate that the activity, at the molecular level, of Amt in archaebacteria and eubacteria may differ. We also show that POPG is an important cofactor for AmtB activity and that, in the absence of POPG, AmtB cannot complete the full translocation cycle. Furthermore, our simulations reveal previously undiscovered POPG binding sites on the intracellular side of the lipid bilayer between the AmtB subunits. Possible molecular mechanisms explaining the functional role of POPG are discussed.—Mirandela, G. D., Tamburrino, G., Hoskisson, P. A., Zachariae, U., Javelle, A. The lipid environment determines the activity of the *Escherichia coli* ammonium transporter AmtB. FASEB J. 33, 000–000 (2019). www.fasebj.org

KEY WORDS: Amt/Mep/Rh · protein–lipids interaction · molecular dynamics simulation · SSME

Ammonium is a vital source of nitrogen for bacteria, fungi, and plants and a toxic metabolic waste product for animals (1). Hence, ammonium transport across biologic membranes is a process of fundamental importance in all living organisms. In 1994, the first genes encoding ammonium transporters were identified in *Saccharomyces cerevisiae* [methylammonium permease (*Mep*)] (2) and *Arabidopsis thaliana* [ammonium transporter (*Amt*)] (3). Later, it was shown that the rhesus protein (Rh) is an ortholog of Amt in vertebrates (4) and, remarkably, that yeast *Mep* mutants can be complemented with the human Rh glycoprotein (5), demonstrating that the Rh protein is a functional ammonium transporter. Following those seminal findings, members of the Amt/Mep/Rh protein family were identified in almost all sequenced organisms, forming a unique and highly specific family of ammonium transporters (6, 7).

The functional context of Amt/Mep and Rh transporters is highly diverse: bacteria, fungi, and plants use Amt/Mep proteins to scavenge ammonium from their environments for biosynthetic assimilation, whereas mammals use the Rh proteins for ammonium detoxification in erythrocytes and kidney and liver tissues (1, 8, 9). Hence, members of the Amt/Mep/Rh family of proteins are associated with various fundamental biologic processes. In fungi, the dimorphic transition from yeast to filamentation is often related to the virulence of pathogenic species, such as *Candida albicans* (10), *Histoplasma capsulatum* (11), and *Cryptococcus neoformans* (12). Fungi possess multiple Mep proteins, and it has been shown that, in *S. cerevisiae* (13), the plant pathogens *Ustilago maydis* (14, 15), *Fusarium fujikuroi* (16), and the human pathogen *C. albicans* (17), the Mep2 transporters have a key role in the switch to filamentous growth.

ABBREVIATIONS: A, activated; Amt, ammonium transporter; AmtB, *Escherichia coli* ammonium transporter; DDM, *n*-dodecyl-β-D-maltoside; DLS, dynamic light scattering; IMAC, immobilized metal affinity chromatography; IO, inside-out; LPR, lipid-to-protein ratio; MD, molecular dynamics; MeA, methylammonium; Mep, methylammonium permease; NA, nonactivated; PDB, Protein Data Bank; POPA, 1-palmitoyl-2-oleoyl phosphatidic acid; POPC, 1-palmitoyl-2-oleoyl phosphatidylcholine; POPE, 1-palmitoyl-2-oleoyl phosphatidylethanolamine; POPG, 1-palmitoyl-2-oleoyl phosphatidylglycerol; Rh, rhesus protein; RSO, right-side-out; SEC, size-exclusion chromatography; SSM, solid supported membrane; SSME, solid supported membrane electrophysiology

[1] Correspondence: Strathclyde Institute of Pharmacy and Biomedical Sciences, 161 Cathedral St., Glasgow G4 0RE, United Kingdom. E-mail: arnaud.javelle@strath.ac.uk

doi: 10.1096/fj.201800782R
This article includes supplemental data. Please visit *http://www.fasebj.org* to obtain this information.

m www.fasebj.org by University of Strathclyde (130.159.234.44) on September 13, 2018. The FASEB Journal Vol. ${article.issue.getVolume()}, No. ${article.issue.getIssueNumber()},

In humans, Rh mutations are associated with numerous pathologies. RhAG mutations in red blood cells have been linked to recessive rhesus protein deficiency (18) and overhydrated hereditary stomatocytosis (19), a rare, dominant-inherited hemolytic anemia. In mouse kidneys, RhCG mutations impair ammonium homeostasis and are associated with distal renal tubular acidosis and male infertility (20). Finally, RhCG has been identified as a candidate gene for early onset major depressive disorder (21).

The *Escherichia coli* ammonium transporter AmtB is the most widely studied model system to investigate ammonium uptake in the ubiquitous Amt/Mep/Rh protein family (22). AmtB is well characterized structurally, with >20 high-resolution structures reported in the Protein Data Bank (PDB; Research Collaboratory for Structural Bioinformatics, *https://www.rcsb.org/*) to date. Despite this wealth of structural information, the ammonium transport mechanism has not yet been unraveled from those crystal structures because all the structures show a very similar conformation reflecting the inward-facing state of the protein, irrespective of the presence or absence of ammonium. Recently, mass spectrometry analysis coupled with structural studies defined 8 specific binding sites for the lipid 1-palmitoyl-2-oleoyl phosphatidylglycerol l (POPG) head group in AmtB, which increase protein stability (23). The X-ray structure of AmtB with bound POPG reveals distinct conformational changes, which reposition some of the protein residues that interact with lipids. More recently, it has been shown that POPG can allosterically regulate the interaction between AmtB and the signal transduction protein GlnK (24). In spite of those findings, a direct functional role for POPG on the transport of ammonium by AmtB has remained unclear.

Here, we couple an *in vitro* assay, based on protein reconstitution in liposomes and solid supported membrane electrophysiology (SSME) measurements with molecular dynamics (MD) simulations to illuminate the effect of lipid composition on AmtB activity. Our results indicate that the function of Amt in archaebacterial and eubacteria differs. We also show that POPG is an essential cofactor for AmtB activity and that, in the absence of POPG, AmtB cannot complete the full translocation cycle. To our knowledge, this is the first report highlighting the functional importance of specific lipids for AmtB activity and demonstrating that the high AmtB selectivity for POPG lipids is not only important for protein stability but also for the translocation cycle.

MATERIALS AND METHODS

Protein purification

AmtB(His_6), cloned into the pET22b vector, was overproduced and purified as previously described (9), except that 0.03% of *n*-dodecyl-β-D-maltoside (DDM) was used, instead of 0.09% *N*,*N*-dimethyldodecylamine-*N*-oxide in the final size-exclusion chromatography (SEC) buffer (Tris/HCl 50 mM, pH7.8, NaCl 100 mM, 0.03% DDM) (25). AmtB was kept in the SEC buffer at 4°C for subsequent characterization and insertion into proteoliposomes.

Reconstitution in liposomes

All lipids (Avanti Polar Lipids, Alabaster, AL, USA) were dried under nitrogen flow and resuspended at 5 mg/ml in non-activating (NA) buffer. The multilamellar liposomes were subsequently extruded 13 times with the miniextruder (Avanti Polar Lipids) mounted with a 0.1-μm filter pore. To facilitate the insertion of AmtB into liposomes, 1 μl Triton X-100 at 25% was sequentially added to 500 μl of liposomes, and the absorbance at 400, 500, 550, and 600 nm was measured to determine the saturation and solubilization constants. The liposomes were incubated for 5 min at room temperature. AmtB, stabilized in 0.03% DDM, was added at a lipid-to-protein ratio (LPR) of 5:1, 10:1, or 50:1 (w/w), and the mixture left for 30 min at room temperature. Three subsequent incubations with prewashed SM-2 Biobeads (Bio-Rad Laboratories, Hercules, CA, USA) at a beads-to-detergent ratio (w/w) of 20 were performed to ensure detergent removal and AmtB insertion. The average diameter of the liposomes/proteoliposomes was determined by dynamic light scattering (DLS) with a Zetasizer Nano ZS (Malvern Instruments, Malvern, United Kingdom) (Supplemental Fig. S1). Proteoliposomes were divided into 100-μl aliquots and frozen at −80°C.

AmtB orientation

Proteoliposomes (160 μl; 5 mg/ml) were treated with or without 2% DDM and incubated with 100 μl of Ni-Affinity Resin (Ni-Sepharose High Performance; GE Healthcare, Chicago, IL, USA) at 4°C for 1 h. The supernatant was collected, and the resin was washed 4 times using 50 μl of NA buffer (100 mM potassium phosphate pH 7, 300 mM KCl). The proteoliposomes were eluted in NA buffer containing 500 mM imidazole. Fifteen microliters of each fraction was mixed with 5 μl of loading blue buffer and analyzed by SDS-PAGE (**Fig. 1** and Supplemental Fig. S1). As a control, we next measured AmtB activity with the purified proteoliposomes containing only right-side-out (RSO)-inserted AmtB (Supplemental Fig. S2). The decay constant in the RSO-purified proteoliposomes or RSO/inside-out (IO) mixture was the same; hence, we concluded that it was justified not to purify the proteoliposomes before each SSME measurement.

Sensor preparation for SSME measurement

Three millimeters gold-coated sensors (Nanion Technologies, Munich, Germany) were prepared as previously described (26). Briefly, 50 μl of a 0.5 mM octadecanethiol solution prepared in isopropanol was used to coat a thiol layer on the gold surface of the sensor during 30 min. The sensors were rinsed with isopropanol and deionized water, dried, and subsequently, diphytanoyl-*sn*-glycerol-3-phosphocholin solution was dropped onto the surface. One hundred microliters of NA buffer was immediately added to the sensor to form the solid supported membrane (SSM). Proteoliposomes/empty liposomes were defrosted and sonicated in a sonication bath (U300H Ultrawave Precision Ultrasonic Cleaning; Ultrawave, Cardiff, South Wales, United Kingdom) at 35 W for 1 min, diluted 10 times in NA buffer, and 10 μl was added at the surface of the SSM on the sensor. After centrifugation, the sensors were stored at 4°C for a maximum of 48 h before electrophysiological measurements.

SSME measurements

The measurements were performed with a SURFE^{2}R N1 machine (Nanion Technologies, Munich, Germany) using default parameters (27). The quality of the sensor was assessed before any recording by determining its capacitance (value should be

m www.fasebj.org by University of Strathclyde (130.159.234.44) on September 13, 2018. The FASEB Journal Vol. ${article.issue.getVolume()}, No. ${article.issue.getIssueNumber()},

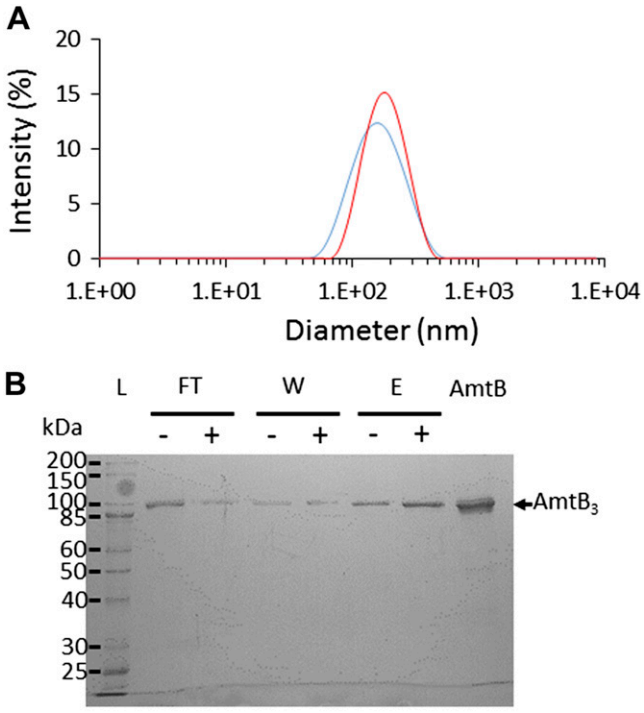

Figure 1. AmtB purification and reconstitution into liposomes (condition 1, table 1). *A*) DLS analysis of the empty liposomes (blue) and proteo-liposomes (red). *B*) SDS-PAGE Coomassie Blue–stained gel of the liposomes purified by IMAC after DDM treatment (+) or in absence of DDM (−). AmtB, 5 μg of pure AmtB used for the reconstitution in the proteoliposomes E, elution fraction; FT, flow through; W, wash.

between 15 and 30 nF) and conductance (value should be <5 nS). For the measurement, a single-solution exchange was used, which consisted of 3 phases of 1 s each; during which, NA, activating (A) (100 mM potassium phosphate pH 7, 300-X mM KCl, X mM of substrate -NH_4^+, MeA, Na^+, K^+-), and NA buffers were sequentially injected on the sensor over constant osmolality at a flow rate of 200 μl/s. The sample rate was set to 1000 Hz, and all the currents in the figures are presented at that rate, without filtering. The currents were amplified with a gain set to 10^9 V/A.

Wherever stated, the raw transient curves were normalized against the maximum current and for the kinetics against the maximum current recorded after a substrate pulse of 100 mM.

The measurements were conducted ≥2 times on each sensor and on 6 sensors prepared from 2 independent batches of AmtB purification. The decay constant was fitted using Origin (OriginLab, Northampton, MA, USA), and the kinetic analysis was performed using Prism 7 (GraphPad Software, La Jolla, CA, USA). The current reconstruction was performed as previously described (26).

Molecular dynamics simulations

The AmtB crystal structure at 1.35 Å resolution (PDB ID, 1U7G) (28) was used for all of our molecular dynamics simulations. The CHARMM-GUI web server graphical user interface (*http://www.charmm-gui.org/*) (29, 30) was applied to revert the mutations (S126P, K255L, F68S) present in the crystallographic construct in the PDB structure 1U7G back to its wild-type form. The protein termini were capped with acetyl and *N*-methyl moieties for the N and C terminus, respectively. The protein was then inserted into a 13 × 13-nm membrane patch constructed with the CHARMM-GUI web server interface. Three different membrane compositions were used: 1 containing 1-palmitoyl-2-oleoyl phosphatidic acid (POPA) and 1-palmitoyl-2-oleoyl phosphatidylcholine (POPC) lipids (POPA-to-POPC ratio, 1:9), and 2 containing POPA, POPC, and POPG lipids (POPA:POPC:POPG ratios, 1:9:2 and 1:9:10). K^+ and Cl^- ions were added to neutralize the system and to obtain a bulk ionic concentration of 150 mM. The CHARMM36 force field was used for the protein, lipids, and ions (31, 32). The water molecules were modeled with the TIP3P water model (33). Water bonds and distances were constrained by the Settle method (34), and all other bonds by the LINCS method (35). After a steepest-descent minimization, the system was equilibrated for ~5 ns by 6 consecutive equilibration steps (time ratio, 1:1:1:4:4:12) with decreasing position restraints on heavy atoms, ranging from 1000 to 200 kJ/mol/nm^2. We thereby followed a protocol recommended by the CHARMM_GUI web server to construct and equilibrate mixed lipid bilayer systems (36). The first 3 equilibration steps were performed in a NVT ensemble (constant temperature/constant volume ensemble) using a Berendsen thermostat (37) to keep the temperature at 310 K. The subsequent steps were conducted under a NPT ensemble (constant temperature/constant pressure ensemble), switching on a Berendsen barostat (37) with isotropic coupling, to keep the pressure at 1 bar. Production molecular dynamics simulations were performed with a Nosé–Hoover thermostat (38) with a time constant of 0.2 ps, and a Parrinello–Rahman barostat (39, 40) with semi-isotropic pressure coupling. An integration time step of 2 fs was used throughout the simulations. All simulations were performed with the Gromacs software, v.5.11 (*http://www.gromacs.org/*) (41). The Visual Molecular Dynamics (VMD) software (*https://www.ks.uiuc.edu/Research/vmd/*) (42) was used for the visualization of the trajectories and the generation of all structural images. We used the VMD VolMap plugin for the generation of the volumetric density maps, the DSSP program (43, 44) for secondary structure assignment, and in-house Python code for additional trajectory analysis.

RESULTS

Characterization of AmtB activity by SSME

To measure ammonium transport activity by SSME, we purified AmtB as previously described (45). The protein was incorporated into liposomes containing a mixture of *E. coli* polar lipids/POPC at a weight ratio of 2:1. AmtB was reconstituted at an LPR of 10 w/w). DLS analysis confirmed that liposomes and proteoliposomes follow a unimodal size distribution with a mean size of 110 nm (Fig. 1*A*). To examine the orientation of AmtB inserted in the liposomes, we analyzed the proteoliposomes by immobilized metal affinity chromatography (IMAC) (46). If all AmtB proteins are inserted in an RSO orientation in a liposome, none of the C-terminal affinity tags should be accessible; hence, the proteoliposome should flow through the IMAC matrix. By contrast, if the AmtB protein is inserted IO in the proteoliposome, then the His-tag should be accessible, and the proteoliposome is expected to bind the matrix and thus be present in the elution fraction. As a control, we treated the proteoliposomes in parallel with DDM to solubilize AmtB and analyze it by IMAC using conditions identical to those used for the analysis of the proteoliposomes without DDM. Our analysis showed that more than half of the proteoliposomes are present in the flow through, demonstrating that, in >50% of the proteoliposomes, not a single protein is IO oriented, which signifies that most AmtB is orientated RSO in the proteoliposomes (Fig. 1*B*).

m www.fasebj.org by University of Strathclyde (130.159.234.44) on September 13, 2018. The FASEB Journal Vol. ${article.issue.getVolume()}, No. ${article.issue.getIssueNumber()},

SSME analysis after an ammonium pulse of 100 mM revealed a fast, positive, transient current of 3.3 nA in proteoliposomes, whereas no current was recorded for protein-free liposomes (**Fig. 2**). We show a representative trace in Fig. 2; however, the amplitude of the transient current differs from sensor to sensor because the number of proteoliposomes coated on the SSM varies (27). In our standard experimental setup, we measured the current 2 times on 6 sensors produced from 2 independent protein preparations. The average transient current peak measured for a pulse of 100 mM ammonium at LPR10 was 3.37 ± 0.26 nA. SSME records transient currents, because the charge displacement caused by the translocation of ammonium inside the proteoliposomes creates an outwardly directed negative membrane potential that progressively inhibits the transport cycle. This fast, transient current measures both presteady-state charge displacement (corresponding to the interaction of ammonium with AmtB) and steady-state charge displacement (describing the continuous turnover during the complete transport cycle of AmtB) (27). To further confirm that the transient currents correspond to the translocation of ammonium into the proteoliposomes, rather than a simple interaction between the substrate and the transporters, we investigated the effect of varying the number of transporters/proteoliposome on the transient current. It was expected that the decay time would be prolonged with increasing protein in the liposomes if the current represents a complete transport cycle, whereas it should be independent of the number of transporters/liposome if the current reflects a simple binding interaction between the substrate and the protein (47). To test that, we reconstituted AmtB into liposomes at LPR values of 50, 10, and 5 (w/w). After a pulse of 100 mM ammonium, the maximum amplitude of the transient current between LPR 50, 10, and 5 increased from 0.47 ± 0.02 to 3.37 ± 0.26 and 7.90 ± 0.35 nA, respectively. Importantly, the decay rate constant of the second phase increased from 9.5 ± 0.7 to 13.4 ± 1.6/s and 18.7 ± 1/s (Fig. 2). Taken together, these results show that a charge displacement specific to AmtB can be detected, and that the current describes the continuous turnover of the complete transport cycle. To determine the transport kinetics, the transient currents were measured in proteoliposomes reconstituted at LPR10, after ammonium pulses ranging from 0.024 to 100 mM. The peak currents saturated between ammonium pulses of 25–50 mM; therefore, we normalized our recordings against the current measured at 100 mM. The data were then fitted according to the Michaelis–Menten equation and a K_m of 0.8 ± 0.1 mM was calculated ($r^2 = 0.99$) (**Fig. 3*B***).

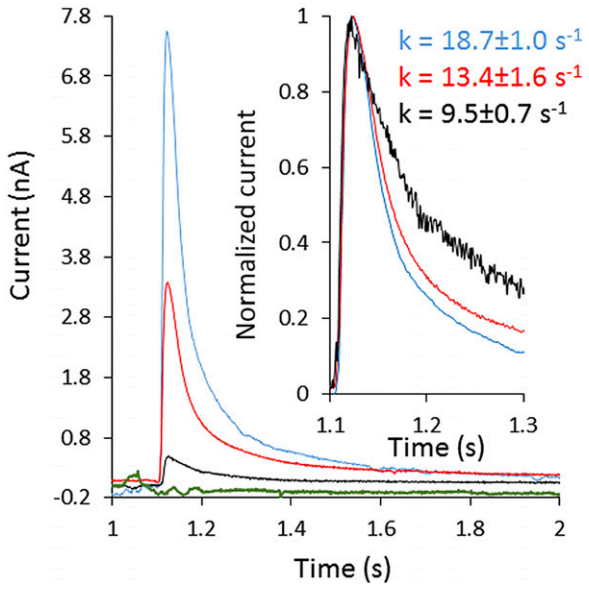

Figure 2. Characterization of AmtB activity. Transient current measured after a 100 mM ammonium pulse in empty liposomes (green) or proteoliposomes containing AmtB at an LPR of 50 (black), 10 (red), or 5 (blue). Inset: normalized current measured in proteoliposomes containing AmtB at an LPR of 50 (black), 10 (red), or 5 (blue).

To characterize the specificity of AmtB among monovalent cations, we measured the current after pulses of Na^+ and K^+. The ionic radii of Na^+ (0.116 nm), and K^+ (0.152 nm) are similar to the size of NH_4^+ ions (0.151 nm) (48). In spite of that, 100 mM Na^+ or K^+ pulses did not trigger any charge displacement (Fig. 3*A*). This shows that those ions do not interact with AmtB and are not translocated through the protein. These experimental observations agree with previous free-energy calculations, which have suggested a high energy barrier for the translocation of ions through AmtB because of the hydrophobicity of the pore (49–51).

Next, we investigated the specificity of AmtB for ammonium *vs.* methylammonium (MeA) transport. MeA has been widely used to measure ammonium transport activity because the radioactive tracer [^{14}C]MeA is commercially available. However, the suitability of MeA as an ammonium analog to characterize the kinetics, specificity, and energetics of Amt/Mep/Rh protein activity has been questioned (52, 53). Here, we show that a pulse of 100 mM MeA triggers a transient current of 0.50 ± 0.02 nA, compared with 3.37 ± 0.26 nA for ammonium, whereas the decay constant is 4 times lower (Fig. 3*A*). The currents recorded by SSME are intrinsically transient; however, the transporter steady-state components can be reconstructed by circuit analysis (54). Steady-state transport in AmtB associated with 100 mM ammonium caused a current of ~4 nA, whereas, for 100 mM MeA, it was ~0.5 nA. This shows that MeA is translocated through AmtB at a greatly reduced rate compared with ammonium (Fig. 3*C*). Furthermore, kinetic analysis reveals a K_m 70 times higher (55.8 mM) for MeA compared with ammonium, showing further that MeA is a poor substrate analog for AmtB, not well suited to elucidate the mechanistic details of AmtB activity (Fig. 3*B*).

POPG lipids are functionally required for full AmtB transport activity

Given that POPG has been shown to bind specifically to AmtB (23), we hypothesized that the lipid environment may also affect the protein's activity, the ammonium–AmtB interaction, and/or the translocation process. To test that question, we reconstituted AmtB into liposomes containing a mixture of POPA/POPC at a weight ratio of

m www.fasebj.org by University of Strathclyde (130.159.234.44) on September 13, 2018. The FASEB Journal Vol. ${article.issue.getVolume()}, No. ${article.issue.getIssueNumber()}

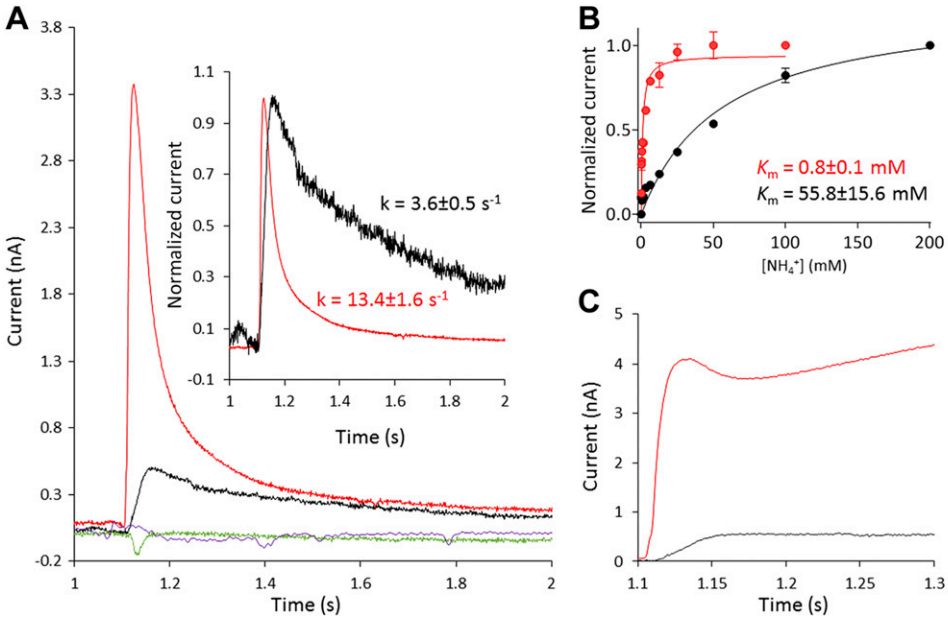

Figure 3. Specificity of AmtB activity. *A*) Transient current measured on proteoliposomes containing AmtB at LPR 10 after a 100 mM substrate pulse. Ammonium (red), methylammonium (black), potassium (purple), or sodium (green). Inset: normalized current after a 100-mM substrate jump. Ammonium (red), methylammonium (black). *B*) Substrate dependence [ammonium (red) or methylammonium (black)] of the maximum amplitude of the transient current. *C*) Reconstructed current using circuit analysis after a 100-mM pulse of ammonium (red) or methylammonium (black). SSME measures both presteady-state charge displacement (which corresponds to the binding of ammonium/MeA to AmtB) and steady-state charge displacement (which describes the continuous turnover of charge during the complete transport cycle of AmtB). It is possible, however, to isolate the steady-state (transport rate) current by analyzing the SSME system as an electric circuit describing the electrical properties of the compound membrane formed from the liposomes and the underlying SSM. This is important to clearly demonstrate that the rate of ammonium transport is larger than in the case of MeA.

1:9 or ternary mixtures of POPA/POPC and POPG (**Table 1**). The POPA/POPC mixtures were chosen because no strong interactions have been detected between POPA, POPC, and AmtB (23), and also because AmtB is correctly inserted in this lipids mixture but does not translocate ammonium (the decay rate does not change at various LPRs; **Fig. 4*B***). Hence, the POPA/POPC lipid mixture is very well suited to assess the specific role of POPG in AmtB activity. The ternary mixture was chosen such that the quantity of POPG (16.5% w/w) matched the standard composition used for the previous experiments (*E. coli* polar lipids/POPC; 2/1 w/w) (Table 1). DLS measurements and IMAC analysis showed that the size of the liposomes, the protein orientation inside the membrane, and the quantity of protein inserted were equivalent for all lipid conditions (Supplemental Fig. S1*A*, *B*). In the absence of POPG (condition 2, Table 1), a 100-mM ammonium pulse triggered a transient current of 0.42 ± 0.04 nA, compared with 3.37 ± 0.26 nA in the presence of POPG (condition 1, Table 1) (Fig. 4*A*). Remarkably, in the presence of 16.5% POPG in an otherwise pure POPA/POPC condition (condition 3, Table 1), a current of 2.24 ± 0.06 nA was measured, which is >5 times greater than in the absence of POPG (condition 2, Table 1) (Fig. 4*A*). The decay and the K_m constants measured in the presence of POPG (conditions 1 and 3, Table 1) were similar and remained within the experimental error (Fig. 4). In contrast, in the absence of POPG (condition 2, Table 1), the decay rate and the K_m increased by 1.6- and 7-fold, respectively, compared with conditions 1 and 3 (Fig. 4*A*). All of these findings clearly show that POPG lipids are important for the transport activity of AmtB.

TABLE 1. *Lipid composition in liposomes and total PG content*[a]

Lipid condition	Lipid content-ratio (w/w)	% PG
1	*E. coli* polar/PC - 2/1	16.5
2	PA/PC - 1/9	0
3	PA-PC/PG - 5/1	16.5

[a]We reconstituted AmtB in liposomes containing a mixture of phosphatidic acid (PA)/phosphatidylcholine (PC) at a weight ratio of 1/9 (condition 2) or in PA/PC-containing liposomes from condition 2 but also containing PG at a weight ratio of 5/1 (condition 3). Condition 3 was chosen such that the quantity of PG (16.5% w/w) matched the standard composition used for the previous experiments (*E. coli* polar lipids/PC 2/1 w/w; condition 1).

To determine whether AmtB completes a full transport cycle in the absence of POPG, we reconstituted the protein in condition 2 (without POPG, Table 1) at varying LPRs of 50, 10, and 5 (w/w). By SDS-PAGE analysis, we carefully checked that the quantity of protein in conditions 1 and 2 at the 3 LPRs were comparable (Supplemental Fig. S1*C*). Under condition 2, an ammonium pulse of 100 mM did not trigger a measurable transient current at LPR 50; however, at LPR 10 and 5, the decay time was similar and within the experimental error (19.0 ± 1.0/s *vs.* 17.1 ± 3.0/s respectively; Fig. 4*B*).

To ensure that AmtB was not misfolded in the liposomes under condition 2 (without POPG, Table 1), we solubilized the proteoliposomes in 2% DDM to extract AmtB and analyzed the protein by SEC on a Superdex 10/300 increase column (GE Healthcare). The SEC analysis showed that the protein elutes as a single monodispersed peak at the same retention time (11.6 ml) as before reconstitution under condition 2 (**Fig. 5*A***). We subsequently reinserted AmtB solubilized from condition 2 (without POPG, Table 1) into proteoliposomes using condition 1 (with POPG, Table 1). An ammonium pulse of 100 mM in these proteoliposomes triggered a transient current of 3.18 ± 0.09 nA with a decay constant of 11.5 ± 2.4/s, and the kinetic analysis revealed a K_m of 1.3 ± 0.3 mM (Fig. 5*B*). These results show that AmtB reconstituted under condition 2 (without POPG) regains the

m www.fasebj.org by University of Strathclyde (130.159.234.44) on September 13, 2018. The FASEB Journal Vol. ${article.issue.getVolume()}, No. ${article.issue.getIssueNumber()},

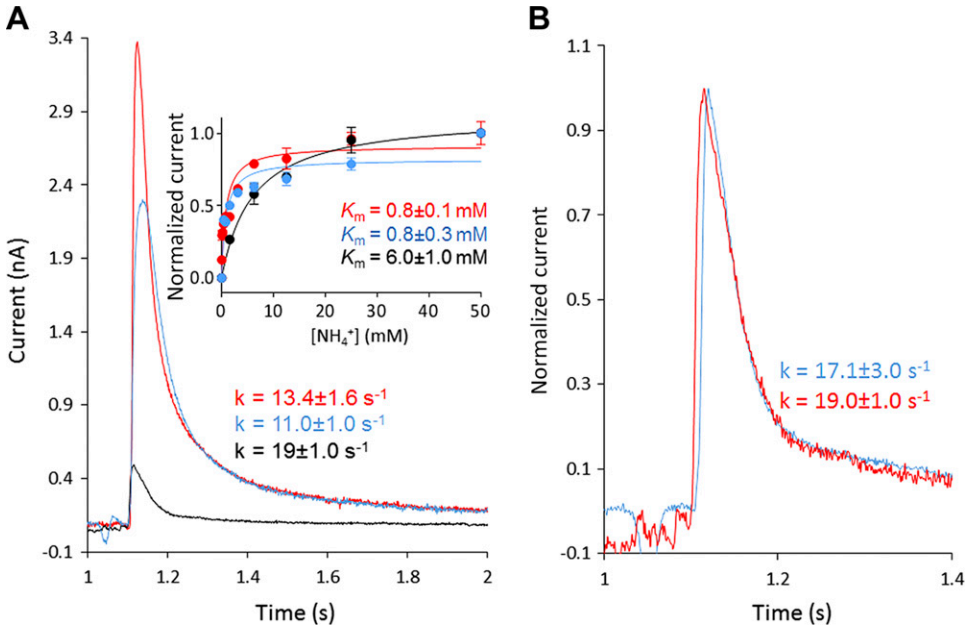

Figure 4. POPG is required for the full function of AmtB. *A*) Transient current measured after a 100-mM ammonium pulse in proteoliposomes containing the lipid conditions 2 (black), 3 (blue), and 1 (red). Inset: ammonium dependence of the maximum amplitude of the transient current for proteoliposomes containing the lipid conditions 2 (black), 3 (blue), and 1 (red). *B*) Normalized transient current measured in AmtB-containing proteoliposomes that do not contain POPG (condition 2) at LPR 10 (red) or 5 (blue).

original activity parameters (maximum current intensity, decay time, and K_m) when rereconstituted in liposomes under condition 1 (with POPG). These data confirm correct folding of AmtB in the proteoliposomes without POPG (condition 2). Taken together, these findings show that POPG is important for AmtB activity and furthermore indicate that, in the absence of POPG, AmtB exhibits a defective transport cycle.

Structural and dynamic investigation of POPG interacting with AmtB

We next applied atomistic MD simulations to study the interaction of POPG lipids with AmtB in membranes on the molecular level. **Figure 6*A*** and Supplemental Figs. S3*A* and S4*A* show the simulation systems containing an AmtB trimer embedded within POPA/POPC/POPG (1:9:10), POPA/POPC (1:9), and POPA/POPC/POPG (1:9:2) mixed lipid membranes, respectively. The color maps on the right and bottom of each of these figures display the density of POPA/POPC and POPG, respectively, each derived from 0.7-μs simulations. The slices representing the lipid density in the periplasmic and cytoplasmic leaflets were taken at the average *z* axis position of the phosphorus atoms within the lipid head groups of each membrane leaflet. The AmtB trimer remains stable in all the lipid environments we studied (Supplemental Fig. S5).

Although specific AmtB interactions with POPG had previously been detected crystallographically for the extracellular membrane leaflet (23), our simulations revealed additional POPG binding sites on the intracellular side of

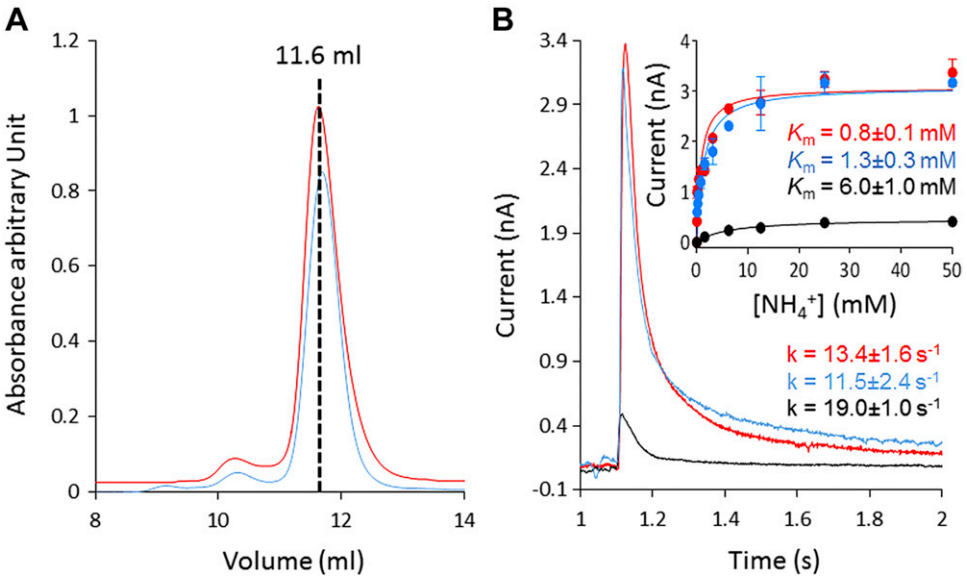

Figure 5. AmtB is correctly folded in the absence of POPG. *A*) Gel filtration trace (Superdex 200 10/300 increase) of AmtB before (red) insertion in proteoliposomes under condition 2 and after (blue) solubilization from proteoliposomes under lipid condition 2 (Table 1). *B*) Transient current measured after a 100 mM ammonium jump in proteoliposomes under condition 2 (black), under condition 1 containing AmtB reinserted after solubilization from proteoliposomes under condition 2 (blue), and under condition 1 (red) (Table 1). Inset: ammonium dependence (raw data) of the maximum amplitude of the transient current in proteoliposomes under condition 1 (red), 2 (black), or 4 (blue) (Table 1).

m www.fasebj.org by University of Strathclyde (130.159.234.44) on September 13, 2018. The FASEB Journal Vol. ${article.issue.getVolume()}, No. ${article.issue.getIssueNumber()},

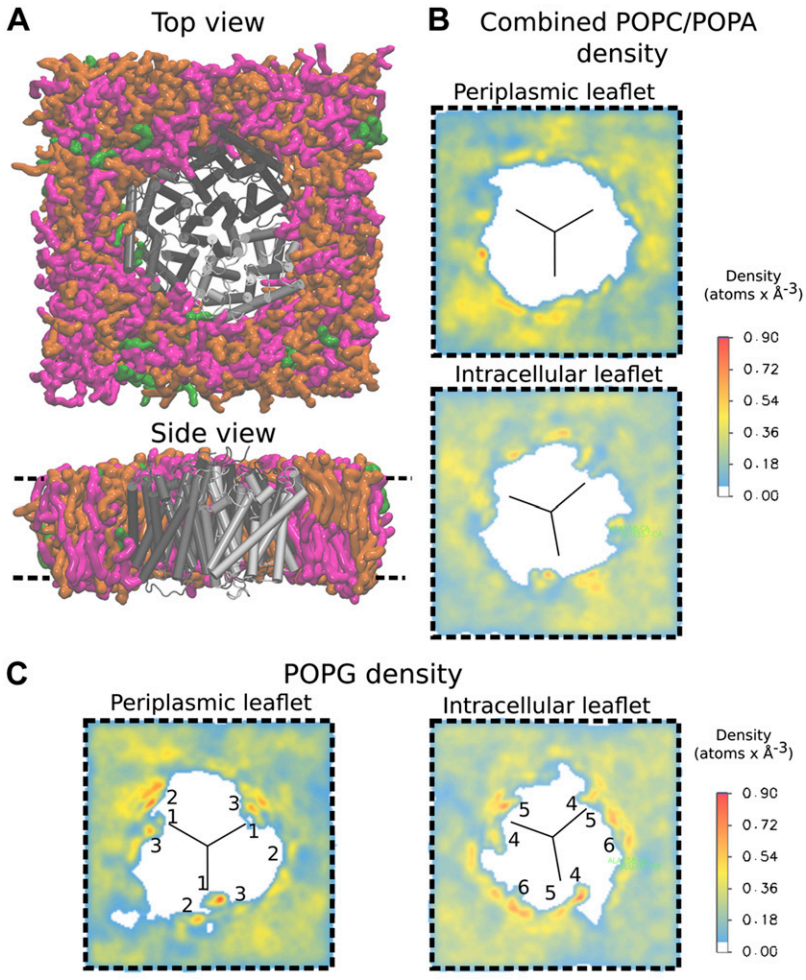

Figure 6. Trimeric AmtB in the POPA/POPC/POPG (1:9:10) system and lipid density plots. *A*) Final frame of the simulation system, seen from the periplasm (top) and from the side (bottom). The protein is shown in gray, the POPC lipid molecules in orange, POPA in green, and POPG in magenta. *B*) Volumetric analysis of the POPC and POPA combined average densities over the entire 700-ns trajectory. *C*) Volumetric analysis of POPG average densities over the entire trajectory. The black lines in the density plots mark the approximate monomer interfaces. Specific binding sites are labeled in the density plots. Comparison of the 2-dimensional density maps shows that POPG tends to localize preferentially close to the monomer interfaces.

the membrane (Fig. 6*B*, *C*). POPG lipids preferably occupy sites on the AmtB trimer located near the interfaces between the monomers, both within the periplasmic and intracellular membrane leaflets (Fig. 6*C*). Specifically, we observe 3 high-density lipid interaction sites/subunit in the periplasmic leaflet, 1 at the monomer interface (site 1) and 2 in its vicinity (sites 2 and 3). Within the intracellular leaflet, about 2 high-density lipid sites are seen per subunit, in which lipids interact with interfacial helices of AmtB in both cases (Fig. 6*C*; sites 4 and 5), and an additional high-density region, in which we observed POPG clustering (site 6). By contrast, the density maps recorded for the POPA/POPC lipid mixture show no binding hotspots of AmtB for POPA and POPC within the periplasmic membrane leaflet, whereas some lipid accumulation was observed within the intracellular leaflet close to the AmtB POPG binding sites 1 and 2 (Supplemental Fig. S3). The POPG density maps obtained from the POPA/POPC/POPG (1:9:2) simulation (Supplemental Fig. S4*C*) showed that, because of the lower POPG concentration in this simulation system, the binding regions observed in the POPA/POPC/POPG (1:9:10) simulation were only partially occupied by POPG. Close-up images highlighting the interaction sites between POPG lipids and the AmtB subunits are shown in **Fig. 7**. The binding sites observed in our MD simulations within the periplasmic leaflet are in good agreement with crystallographically defined sites (23) (Fig. 7*A*), whereas the new intracellular interaction sites also located to the interface region between the AmtB subunits (Fig. 7*B*, *C*).

Supplemental Figure S6 shows the time evolution of the occupancy of all the suggested AmtB lipid binding sites by each lipid type, using data from 2 independent simulations of AmtB in a POPA/POPC/POPG (1:9:10) membrane. As can be seen, the sites we identified preferably interact with POPG lipids. In addition, an analysis of the number of hydrogen bonds formed between the lipid head groups and the protein (Supplemental Fig. S7*A*), as well as the radial distribution of the lipids around the protein (Supplemental Fig. S7*C*), shows that POPG tends to localize closer to the protein surface, compared with the POPA and POPC lipids, and to form more hydrogen bond contacts. The average number of hydrogen bonds among each protein residue and the lipid head groups is displayed in Supplemental Fig. S7*B*, confirming that POPG lipids generally establish more hydrogen bonds, in particular, near residues that form the reported binding sites (1–6 in Fig. 7).

The most conspicuous conformational change we found to be induced by POPG binding in AmtB on the time scale of our simulations was the preferred formation of a short helix within a periplasmic loop region (residues 77–81) after binding of the charged POPG head group. The propensity of that region to form an α helix is shown in

m www.fasebj.org by University of Strathclyde (130.159.234.44) on September 13, 2018. The FASEB Journal Vol. ${article.issue.getVolume()}, No. ${article.issue.getIssueNumber()},

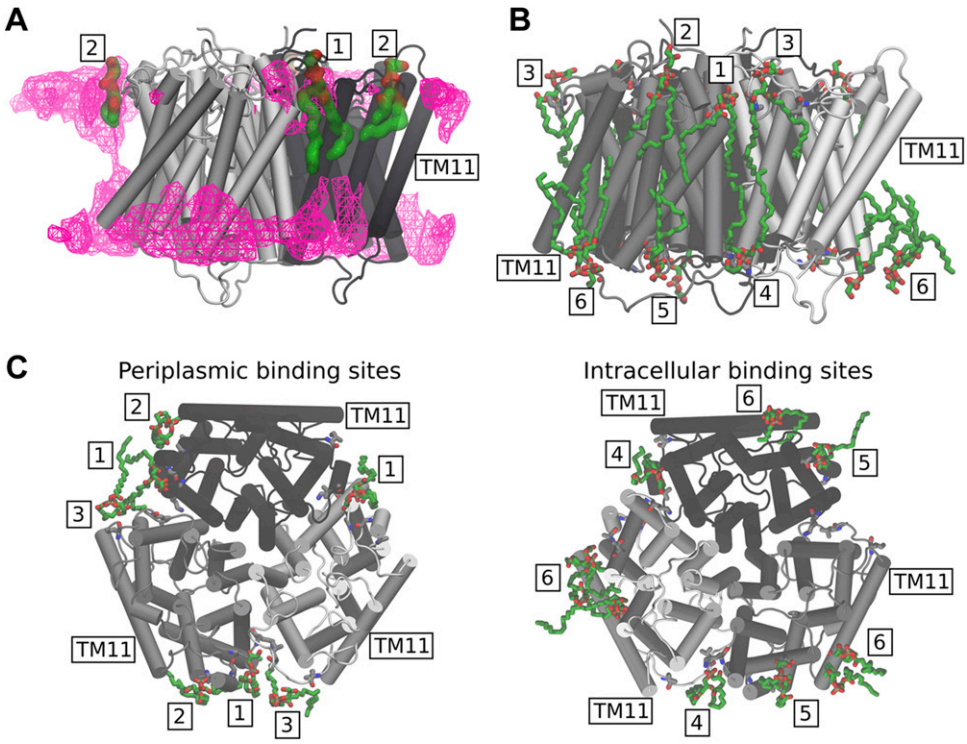

Figure 7. The images highlight the POPG binding locations observed in the POPA/POPC/POPG (1:9:10) simulations. The binding sites located in the periplasmic leaflet are numbered 1, 2, and 3, whereas the intracellular ones are labeled 4, 5, and 6. The same numbering scheme has been adopted for the volumetric maps shown in Supplemental Figs. S2 and S3. *A*) Volumetric map of the average POPG density obtained from a 700-ns simulation (magenta mesh surface, isovalue = 0.38) is compared with the POPG binding sites, which were previously resolved in the X-ray structure (PDB ID, 4nh2; lipids in green). Generally, good agreement between the experimental and the simulation sites was observed, especially for binding site 1. *B*, *C*) Side (*B*), periplasmic (*C*, left), and intracellular (*C*, right) views of the POPG binding sites taken from a representative simulation frame from the POPA/POPC/POPG (1:9:10) mixture. Generally, POPG tends to bind close to the monomer interface.

Supplemental Fig. S8. The simulations containing POPG (both in the ratios 1:9:2 and 1:9:10) exhibited a significantly increased propensity for this loop region to form a helical structure compared with simulations in the absence of POPG. That short region is part of a loop, which Laganowsky *et al.* (23) showed to adopt a slightly different conformation upon POPG binding, compared with the unbound structure, albeit without formation of a helix. Although the detailed mechanism of ammonium transport in AmtB is still unclear, this finding might link POPG binding to AmtB structure and function.

DISCUSSION

A plethora of functional studies aimed at elucidating the mechanism of ammonium transport by Amt proteins has led to considerable controversy because of the lack of an *in vitro* assay characterizing the activity of Amt proteins using ammonium as the substrate (1, 9). The elegant work of Wacker *et al*. (55) showed that 2 ammonium transporters from *Archaeoglobus fulgidus* activity are electrogenic (55). The work we present here shows that the activity of the archetypal Amt/Mep/Rh protein AmtB is also associated with charge translocation across the membrane, which suggests that electrogenic transport may be a general feature for these proteins. However, we also demonstrated that, contrary to *A. fulgidus* Amt1, AmtB highly discriminates between MeA and ammonium as substrates. Although in *A. fulgidus* Amt1, MeA triggers a transient current amounting to 87% of the current elicited by ammonium (55), the current induced by MeA in AmtB is <15% of that observed for ammonium. The structural basis for that discrepancy is not yet clear because the 3 principal conserved features, namely the S1 binding site, the "Phe gate," and the pore twin–His motif are structurally similar between both proteins. However, that functional difference, at the molecular level, between eubacterial and archaeal Amts raises important questions about the universality of the transport mechanism in microbial ammonium transporters. This is particularly relevant in the case of the Mep2-like protein, which has been assigned a sensor role in filamentous development, often related to the virulence of pathogenic fungi (13). There are 2 major hypotheses concerning the molecular mechanism of Mep2-mediated signaling. The first is that Mep2 is a sensor interacting with signaling partners, leading to induction of filamentation (56, 57), whereas the other posits that the transport mechanism of Mep2-like proteins may differ from other Mep proteins (58–60). Current evidence favors the second hypothesis given that signaling efficiency is closely linked to transport efficiency; however, further studies are needed to elucidate the exact mechanism, which may provide important information for the design of novel antifungal therapies.

It is well established that lipids can affect membrane protein structure and function through bulk membrane effects by direct, but transient, annular interactions with the bilayer-exposed surface of the protein or by specific lipid binding to protein sites (for review, see Denning and Beckstein (61). Altogether 8 molecules of POPG have been

m www.fasebj.org by University of Strathclyde (130.159.234.44) on September 13, 2018. The FASEB Journal Vol. ${article.issue.getVolume()}, No. ${article.issue.getIssueNumber()},

resolved in a recent crystal structure of AmtB, interacting at specific binding sites within the extracellular membrane leaflet (23). Our MD simulations identify further interactions of POPG molecules in the inner leaflet of the membrane. However, so far, no functional relationships have been reported to link POPG binding with the activity of AmtB. Here, we show that, in the absence of POPG, AmtB is nonfunctional as a transporter and unable to complete the full translocation cycle. Our experiments and simulations do not indicate substantial conformational changes in the S1 periplasmic binding site or in the pore, suggesting that the molecular basis of the POPG effect on AmtB activity could involve novel mechanistic sites. In this context, it is interesting to compare our findings with the lactose permease LacY in *E. coli*, the most extensively studied secondary transporter in the context of lipid–protein interactions. In the absence of POPC and/or phosphatidylethanolamine (POPE), LacY is unable to support active transport of the substrate into the cell, although the binding of the substrate to the protein is unaffected (62). This is similar to the observations we made for AmtB in the absence of POPG lipids. LacY is known to undergo drastic topological rearrangements, which may explain the effect of POPC/POPE on its activity (63). In the case of AmtB, no topological rearrangements were observed upon POPG binding, and we have shown that, in the absence of POPG, AmtB was folded correctly in the proteoliposomes, such that a major change in the AmtB topology is unlikely to explain the functional role of POPG. We did, however, observe changes in the dynamics of AmtB subunits, which located particularly to loop regions at the periplasmic face of the protein. The periplasmic loop regions have been shown to include functionally important residues (49, 50, 64, 65). Once a more detailed picture of the overall transport mechanism of AmtB has been obtained, the role of those effects may emerge into greater clarity.

Furthermore, several lines of evidence point toward functional cooperativity between the 3 subunits in the Amt/Mep transporters. First, in *S. cerevisiae*, it has been demonstrated that expression of a nonfunctional Mep1 protein inhibits the transport activity of Mep2 and Mep3, indicating crosstalk between different Mep transporters (66), and similar observations have been reported for ammonium transporters of *Aspergillus nidulans* (67). Second, coexpressed, nonfunctional monomers cross-inhibit transport in plant Amts, and a genetic screen has identified several mutations at the subunit interface of the *A. thaliana* Amt1/2 transporter, which inactivated the translocation activity (8, 68). Third, extensive site-directed mutagenesis of the C-terminal tail of *E. coli* AmtB has led to the hypothesis that the 3 subunits function in a cooperative manner (69). All of these findings indicate functional coupling among the adjacent subunits. Previous structural data and our MD simulations showed that POPG molecules bind mainly to sites at the vicinity of the subunit interfaces. It is, therefore, attractive to hypothesize that POPG molecules act as wedges, which mediate the functional interaction between the subunits. In line with that hypothesis, a model in which various AmtB conformations may be favored upon specific lipid binding has been proposed (24). Finally, it has recently been shown that other lipids, including POPE and cardiolipin, can bind AmtB allosterically, indicating that transporters may recruit their own microlipidic environment (70). Whether these binding events are important to modulating the activity of AmtB remains a question to be addressed in future studies. FJ

ACKNOWLEDGMENTS

The authors thank Dr. André Bazzone (Nanion Technologies, Munich, Germany) for helpful advice with SSME measurements. Special thanks to Prof. Iain Hunter (Strathclyde Institute of Pharmacy and Biomedical Sciences) for invaluable discussions and help during this project. G.D.M. was supported by a Ph.D. Studentship from the University of Strathclyde; A.J. was supported by a Chancellor's Fellowship from the University of Strathclyde; and G.T. and U.Z. acknowledge funding from the Scottish Universities' Physics Alliance (SUPA). A.J. acknowledges the support of Tenovus Scotland (Project S17-07), and P.A.H. acknowledges the support of the Natural Environment Research Council (Grant NE/M001415/1). The authors declare no conflicts of interest.

AUTHOR CONTRIBUTIONS

G. D. Mirandela, G. Tamburrino, U. Zachariae, and A. Javelle designed and performed the research and analyzed the data; and P. A. Hoskisson, U. Zachariae, and A. Javelle wrote the manuscript.

REFERENCES

1. Andrade, S. L., and Einsle, O. (2007) The Amt/Mep/Rh family of ammonium transport proteins. *Mol. Membr. Biol.* **24**, 357–365
2. Marini, A. M., Vissers, S., Urrestarazu, A., and André, B. (1994) Cloning and expression of the MEP1 gene encoding an ammonium transporter in *Saccharomyces cerevisiae*. *EMBO J.* **13**, 3456–3463
3. Ninnemann, O., Jauniaux, J. C., and Frommer, W. B. (1994) Identification of a high affinity NH_4^+ transporter from plants. *EMBO J.* **13**, 3464–3471
4. Marini, A. M., Urrestarazu, A., Beauwens, R., and André, B. (1997) The Rh (rhesus) blood group polypeptides are related to NH_4^+ transporters. *Trends Biochem. Sci.* **22**, 460–461
5. Marini, A. M., Matassi, G., Raynal, V., André, B., Cartron, J. P., and Chérif-Zahar, B. (2000) The human Rhesus-associated RhAG protein and a kidney homologue promote ammonium transport in yeast. *Nat. Genet.* **26**, 341–344
6. Huang, C. H., and Peng, J. (2005) Evolutionary conservation and diversification of Rh family genes and proteins. *Proc. Natl. Acad. Sci. USA* **102**, 15512–15517
7. McDonald, T. R., and Ward, J. M. (2016) Evolution of electrogenic ammonium transporters (AMTs). *Front. Plant Sci.* **7**, 352–360
8. Neuhäuser, B., Dynowski, M., and Ludewig, U. (2014) Switching substrate specificity of AMT/MEP/Rh proteins. *Channels (Austin)* **8**, 496–502
9. Javelle, A., Lupo, D., Li, X. D., Merrick, M., Chami, M., Ripoche, P., and Winkler, F. K. (2007) Structural and mechanistic aspects of Amt/Rh proteins. *J. Struct. Biol.* **158**, 472–481
10. Lo, H. J., Köhler, J. R., DiDomenico, B., Loebenberg, D., Cacciapuoti, A., and Fink, G. R. (1997) Nonfilamentous *C. albicans* mutants are avirulent. *Cell* **90**, 939–949
11. Maresca, B., and Kobayashi, G. S. (1989) Dimorphism in *Histoplasma capsulatum*: a model for the study of cell differentiation in pathogenic fungi. *Microbiol. Rev.* **53**, 186–209
12. Wickes, B. L., Edman, U., and Edman, J. C. (1997) The *Cryptococcus neoformans* STE12alpha gene: a putative *Saccharomyces cerevisiae* STE12 homologue that is mating type specific. *Mol. Microbiol.* **26**, 951–960

m www.fasebj.org by University of Strathclyde (130.159.234.44) on September 13, 2018. The FASEB Journal Vol. ${article.issue.getVolume()}, No. ${article.issue.getIssueNumber()},

13. Lorenz, M. C., and Heitman, J. (1998) The MEP2 ammonium permease regulates pseudohyphal differentiation in *Saccharomyces cerevisiae*. *EMBO J.* **17**, 1236–1247
14. Banuett, F. (1991) Identification of genes governing filamentous growth and tumor induction by the plant pathogen *Ustilago maydis*. *Proc. Natl. Acad. Sci. USA* **88**, 3922–3926
15. Smith, D. G., Garcia-Pedrajas, M. D., Gold, S. E., and Perlin, M. H. (2003) Isolation and characterization from pathogenic fungi of genes encoding ammonium permeases and their roles in dimorphism. *Mol. Microbiol.* **50**, 259–275
16. Teichert, S., Rutherford, J. C., Wottawa, M., Heitman, J., and Tudzynski, B. (2008) Impact of ammonium permeases mepA, mepB, and mepC on nitrogen-regulated secondary metabolism in *Fusarium fujikuroi*. *Eukaryot. Cell* **7**, 187–201
17. Dabas, N., and Morschhäuser, J. (2007) Control of ammonium permease expression and filamentous growth by the GATA transcription factors GLN3 and GAT1 in *Candida albicans*. *Eukaryot. Cell* **6**, 875–888
18. Agre, P., and Cartron, J. P. (1991) Molecular biology of the Rh antigens. *Blood* **78**, 551–563
19. Bruce, L. J., Guizouarn, H., Burton, N. M., Gabillat, N., Poole, J., Flatt, J. F., Brady, R. L., Borgese, F., Delaunay, J., and Stewart, G. W. (2009) The monovalent cation leak in overhydrated stomatocytic red blood cells results from amino acid substitutions in the Rh-associated glycoprotein. *Blood* **113**, 1350–1357
20. Biver, S., Belge, H., Bourgeois, S., Van Vooren, P., Nowik, M., Scohy, S., Houillier, P., Szpirer, J., Szpirer, C., Wagner, C. A., Devuyst, O., and Marini, A. M. (2008) A role for rhesus factor Rhcg in renal ammonium excretion and male fertility. *Nature* **456**, 339–343
21. Verma, R., Holmans, P., Knowles, J. A., Grover, D., Evgrafov, O. V., Crowe, R. R., Scheftner, W. A., Weissman, M. M., DePaulo, J. R., Jr., Potash, J. B., and Levinson, D. F. (2008) Linkage disequilibrium mapping of a chromosome 15q25–26 major depression linkage region and sequencing of NTRK3. *Biol. Psychiatry* **63**, 1185–1189
22. Merrick, M., Javelle, A., Durand, A., Severi, E., Thornton, J., Avent, N. D., Conroy, M. J., and Bullough, P. A. (2006) The *Escherichia coli* AmtB protein as a model system for understanding ammonium transport by Amt and Rh proteins. *Transfus. Clin. Biol.* **13**, 97–102
23. Laganowsky, A., Reading, E., Allison, T. M., Ulmschneider, M. B., Degiacomi, M. T., Baldwin, A. J., and Robinson, C. V. (2014) Membrane proteins bind lipids selectively to modulate their structure and function. *Nature* **510**, 172–175
24. Cong, X., Liu, Y., Liu, W., Liang, X., and Laganowsky, A. (2017) Allosteric modulation of protein-protein interactions by individual lipid binding events. *Nat. Commun.* **8**, 2203
25. Javelle, A., Lupo, D., Ripoche, P., Fulford, T., Merrick, M., and Winkler, F. K. (2008) Substrate binding, deprotonation, and selectivity at the periplasmic entrance of the *Escherichia coli* ammonia channel AmtB. *Proc. Natl. Acad. Sci. USA* **105**, 5040–5045
26. Bazzone, A., Costa, W. S., Braner, M., Călinescu, O., Hatahet, L., and Fendler, K. (2013) Introduction to solid supported membrane based electrophysiology. *J. Vis. Exp.* **75**, e50230
27. Bazzone, A., Barthmes, M., and Fendler, K. (2017) SSM-based electrophysiology for transporter research. *Methods Enzymol.* **594**, 31–83
28. Khademi, S., O'Connell III, J., Remis, J., Robles-Colmenares, Y., Miercke, L. J., and Stroud, R. M. (2004) Mechanism of ammonia transport by Amt/MEP/Rh: structure of AmtB at 1.35 Å. *Science* **305**, 1587–1594
29. Jo, S., Lim, J. B., Klauda, J. B., and Im, W. (2009) CHARMM-GUI membrane builder for mixed bilayers and its application to yeast membranes. *Biophys. J.* **97**, 50–58
30. Lee, J., Cheng, X., Swails, J. M., Yeom, M. S., Eastman, P. K., Lemkul, J. A., Wei, S., Buckner, J., Jeong, J. C., Qi, Y., Jo, S., Pande, V. S., Case, D. A., Brooks III, C. L., MacKerell, A. D., Jr., Klauda, J. B., and Im, W. (2016) CHARMM-GUI input generator for NAMD, GROMACS, AMBER, OpenMM, and CHARMM/OpenMM simulations using the CHARMM36 additive force field. *J. Chem. Theory Comput.* **12**, 405–413
31. Klauda, J. B., Venable, R. M., Freites, J. A., O'Connor, J. W., Tobias, D. J., Mondragon-Ramirez, C., Vorobyov, I., MacKerell, A. D., Jr., and Pastor, R. W. (2010) Update of the CHARMM all-atom additive force field for lipids: validation on six lipid types. *J. Phys. Chem. B* **114**, 7830–7843
32. Best, R. B., Zhu, X., Shim, J., Lopes, P. E., Mittal, J., Feig, M., and Mackerell, A. D., Jr. (2012) Optimization of the additive CHARMM all-atom protein force field targeting improved sampling of the backbone φ, ψ and side-chain χ_1 and χ_2 dihedral angles. *J. Chem. Theory Comput.* **8**, 3257–3273
33. Brooks, B. R., Brooks III, C. L., Mackerell, A. D., Jr., Nilsson, L., Petrella, R. J., Roux, B., Won, Y., Archontis, G., Bartels, C., Boresch, S., Caflisch, A., Caves, L., Cui, Q., Dinner, A. R., Feig, M., Fischer, S., Gao, J., Hodoscek, M., Im, W., Kuczera, K., Lazaridis, T., Ma, J., Ovchinnikov, V., Paci, E., Pastor, R. W., Post, C. B., Pu, J. Z., Schaefer, M., Tidor, B., Venable, R. M., Woodcock, H. L., Wu, X., Yang, W., York, D. M., and Karplus, M. (2009) CHARMM: the biomolecular simulation program. *J. Comput. Chem.* **30**, 1545–1614
34. Miyamoto, S., and Kollman, P. A. (1992) Settle: an analytical version of the SHAKE and RATTLE algorithm for rigid water models. *J. Comput. Chem.* **13**, 952–962
35. Hess, B., Bekker, H., Berendsen, H. J. C., and Fraaije, J. G. E. M. (1997) LINCS: a linear constraint solver for molecular simulations. *J. Comput. Chem.* **18**, 1463–1472
36. Jo, S., Kim, T., Iyer, V. G., and Im, W. (2008) CHARMM-GUI: a web-based graphical user interface for CHARMM. *J. Comput. Chem.* **29**, 1859–1865
37. Berendsen, H. J. C., Postma, J. P. M., van Gunsteren, W. F., DiNola, A., and Haak, J. R. (1984) Molecular dynamics with coupling to an external bath. *J. Chem. Phys.* **81**, 3684–3690
38. Evans, D. J., and Holian, B. L. (1985) The Nose–Hoover thermostat. *J. Chem. Phys.* **83**, 4069–4074
39. Parrinello, M., and Rahman, A. (1980) Crystal structure and pair potentials: a molecular-dynamics study. *Phys. Rev. Lett.* **45**, 1196–1199
40. Parrinello, M., and Rahman, A. (1981) Polymorphic transitions in single crystals: a new molecular dynamics method. *J. Appl. Phys.* **52**, 7182–7190
41. Abraham, M. J., Murtola, T., Schulz, R., Pálla, S., Smith, J. C., Hessa, B., and Lindahlad, E. (2015) GROMACS: high performance molecular simulations through multi-level parallelism from laptops to supercomputers. *SoftwareX* **1–2**, 19–25
42. Humphrey, W., Dalke, A., and Schulten, K. (1996) VMD: visual molecular dynamics. *J. Mol. Graph.* **14**, 33–38, 27–28
43. Touw, W. G., Baakman, C., Black, J., te Beek, T. A. H., Krieger, E., Joosten, R. P., and Vriend, G. (2015) A series of PDB-related databanks for everyday needs. *Nucleic Acids Res.* **43**, 364–368
44. Kabsch, W., and Sander, C. (1983) Dictionary of protein secondary structure: pattern recognition of hydrogen-bonded and geometrical features. *Biopolymers* **22**, 2577–2637
45. Blakey, D., Leech, A., Thomas, G. H., Coutts, G., Findlay, K., and Merrick, M. (2002) Purification of the *Escherichia coli* ammonium transporter AmtB reveals a trimeric stoichiometry. *Biochem. J.* **364**, 527–535
46. Vitrac, H., Bogdanov, M., and Dowhan, W. (2013) In vitro reconstitution of lipid-dependent dual topology and postassembly topological switching of a membrane protein. *Proc. Natl. Acad. Sci. USA* **110**, 9338–9343
47. Zuber, D., Krause, R., Venturi, M., Padan, E., Bamberg, E., and Fendler, K. (2005) Kinetics of charge translocation in the passive downhill uptake mode of the Na^+/H^+ antiporter NhaA of *Escherichia coli*. *Biochim. Biophys. Acta* **1709**, 240–250
48. Shannon, R. D. (1976) Revised effective ionic radii and systematic studies of interatomic distances in halides and chalcogenides. *Acta Crystallogr. A* **32**, 751–767
49. Luzhkov, V. B., Almlöf, M., Nervall, M., and Aqvist, J. (2006) Computational study of the binding affinity and selectivity of the bacterial ammonium transporter AmtB. *Biochemistry* **45**, 10807–10814
50. Bostick, D. L., and Brooks III, C. L. (2007) On the equivalence point for ammonium (de)protonation during its transport through the AmtB channel. *Biophys. J.* **92**, L103–L105
51. Wang, S., Orabi, E. A., Baday, S., Bernèche, S., and Lamoureux, G. (2012) Ammonium transporters achieve charge transfer by fragmenting their substrate. *J. Am. Chem. Soc.* **134**, 10419–10427
52. Wang, J., Fulford, T., Shao, Q., Javelle, A., Yang, H., Zhu, W., and Merrick, M. (2013) Ammonium transport proteins with changes in one of the conserved pore histidines have different performance in ammonia and methylamine conduction. *PLoS One* **8**, e62745
53. Hall, J. A., and Kustu, S. (2011) The pivotal twin histidines and aromatic triad of the *Escherichia coli* ammonium channel AmtB can be replaced. *Proc. Natl. Acad. Sci. USA* **108**, 13270–13274
54. Schulz, P., Garcia-Celma, J. J., and Fendler, K. (2008) SSM-based electrophysiology. *Methods* **46**, 97–103
55. Wacker, T., Garcia-Celma, J. J., Lewe, P., and Andrade, S. L. (2014) Direct observation of electrogenic NH_4^+ transport in ammonium transport (Amt) proteins. *Proc. Natl. Acad. Sci. USA* **111**, 9995–10000
56. Rutherford, J. C., Chua, G., Hughes, T., Cardenas, M. E., and Heitman, J. (2008) A Mep2-dependent transcriptional profile links

m www.fasebj.org by University of Strathclyde (130.159.234.44) on September 13, 2018. The FASEB Journal Vol. ${article.issue.getVolume()}, No. ${article.issue.getIssueNumber()},

permease function to gene expression during pseudohyphal growth in *Saccharomyces cerevisiae*. *Mol. Biol. Cell* **19**, 3028–3039
57. Van den Berg, B., Chembath, A., Jefferies, D., Basle, A., Khalid, S., and Rutherford, J. C. (2016) Structural basis for Mep2 ammonium transceptor activation by phosphorylation. *Nat. Commun.* **7**, 11337–11348
58. Boeckstaens, M., André, B., and Marini, A. M. (2007) The yeast ammonium transport protein Mep2 and its positive regulator, the Npr1 kinase, play an important role in normal and pseudohyphal growth on various nitrogen media through retrieval of excreted ammonium. *Mol. Microbiol.* **64**, 534–546
59. Boeckstaens, M., André, B., and Marini, A. M. (2008) Distinct transport mechanisms in yeast ammonium transport/sensor proteins of the Mep/Amt/Rh family and impact on filamentation. *J. Biol. Chem.* **283**, 21362–21370
60. Marini, A. M., Boeckstaens, M., Benjelloun, F., Chérif-Zahar, B., and André, B. (2006) Structural involvement in substrate recognition of an essential aspartate residue conserved in Mep/Amt and Rh-type ammonium transporters. *Curr. Genet.* **49**, 364–374
61. Denning, E. J., and Beckstein, O. (2013) Influence of lipids on protein-mediated transmembrane transport. *Chem. Phys. Lipids* **169**, 57–71
62. Bogdanov, M., and Dowhan, W. (1995) Phosphatidylethanolamine is required for in vivo function of the membrane-associated lactose permease of *Escherichia coli*. *J. Biol. Chem.* **270**, 732–739
63. Bogdanov, M., Heacock, P. N., and Dowhan, W. (2002) A polytopic membrane protein displays a reversible topology dependent on membrane lipid composition. *EMBO J.* **21**, 2107–2116
64. Javelle, A., Severi, E., Thornton, J., and Merrick, M. (2004) Ammonium sensing in *Escherichia coli*: role of the ammonium transporter AmtB and AmtB-GlnK complex formation. *J. Biol. Chem.* **279**, 8530–8538
65. Cao, Z., Mo, Y., and Thiel, W. (2007) Deprotonation mechanism of NH_4^+ in the *Escherichia coli* ammonium transporter AmtB: insight from QM and QM/MM calculations. *Angew. Chem. Int. Ed. Engl.* **46**, 6811–6815
66. Marini, A. M., Springael, J. Y., Frommer, W. B., and André, B. (2000) Cross-talk between ammonium transporters in yeast and interference by the soybean SAT1 protein. *Mol. Microbiol.* **35**, 378–385
67. Monahan, B. J., Unkles, S. E., Tsing I, T., Kinghorn, J. R., Hynes, M. J., and Davis, M. A. (2002) Mutation and functional analysis of the *Aspergillus nidulans* ammonium permease MeaA and evidence for interaction with itself and MepA. *Fungal Genet. Biol.* **36**, 35–46
68. Neuhäuser, B., Dynowski, M., Mayer, M., and Ludewig, U. (2007) Regulation of NH_4^+ transport by essential cross talk between AMT monomers through the carboxyl tails. *Plant Physiol.* **143**, 1651–1659
69. Severi, E., Javelle, A., and Merrick, M. (2007) The conserved carboxy-terminal region of the ammonia channel AmtB plays a critical role in channel function. *Mol. Membr. Biol.* **24**, 161–171
70. Patrick, J. W., Boone, C. D., Liu, W., Conover, G. M., Liu, Y., Cong, X., and Laganowsky, A. (2018) Allostery revealed within lipid binding events to membrane proteins. *Proc. Natl. Acad. Sci. USA* **115**, 2976–2981

Received for publication April 20, 2018.
Accepted for publication August 14, 2018.

m www.fasebj.org by University of Strathclyde (130.159.234.44) on September 13, 2018. The FASEB Journal Vol. ${article.issue.getVolume()}, No. ${article.issue.getIssueNumber()},